



DEPARTMENT OF MATERIALS ENGINEERING

A THESIS SUBMITTED TO MONASH UNIVERSITY AS FULFILMENT
FOR THE DEGREE OF DOCTOR OF PHILOSOPHY

**Micro-forming and Grain refinement: Effects
of Microstructural and Geometric Scale on
Metal Formability**

Chengfan Gu

Supervisors: Prof. Chris Davies (Monash University, Australia)

Prof. László S. Tóth (Université Paul Verlaine Metz, France)

(December 2010)

**To my late mother:
Professor Xia Chen
(18/11/1937-2/07/2008)**

ABSTRACT

The effects of grain size and geometric scale on metal processing were investigated for several processing techniques. The motivation for conducting this research was to improve our understanding of the microstructural evolution and thermo-mechanical behavior of UFG copper as a 'model material' used in micro-forming processes. Coarse grained (CG) copper was also investigated for comparison. The starting UFG material was obtained by equal channel angular pressing (ECAP). Micro deep-drawing and micro-extrusion were the two micro-forming processes investigated; geometry, crystallographic orientation effects and thermal stability were all examined. Crystallographic orientation was determined using electron back scattered diffraction (EBSD) and X-ray diffraction; grain size was determined by EBSD; and thermal stability was measured by differential scanning calorimetry and nano-indentation. Geometry effects were inferred from mechanical tests coupled with material characterization data. These experiments were supported by application of a grain fragmentation model coupled to a visco-plastic self consistent (VPSC) simulation in ECAP and micro-extrusion, and a VPSC simulation in micro-deep drawing.

In order to characterize the starting material a comparative study was conducted for different strain paths: ECAP and cold rolling. The refined grain size was significantly smaller in ECAP than in rolling. Grain fragmentation modeling demonstrated that these differences are attributable to the different lattice rotation rate in ECAP and cold rolling, and this provides important insight into the grain refinement process to obtain UFG structures.

EBSD measurements of ECAP-ed copper demonstrate that the misorientation distribution depends on the measurement plane. A new procedure is used which separates the misorientation distributions into two parts: a distribution that describes misorientations between subgrains *within* the original parent grain interior and a distribution that is measured *across* the original parent grain boundaries. The procedure permits us to track microstructure as it evolves from the original so-called 'parent grains'. It is based on measurements on two planes of misorientation, grain shape evolution; and subgrain size variations. The results obtained showed large misorientations in the boundary regions of the parent grains and mostly low misorientations for the new grains emerging in the interior of the parent grain.

In order to examine the effect of texture evolution on material behavior, micro deep drawing of ECAP-ed copper was investigated. Two blank thicknesses were investigated, and it was found experimentally that when the grain size was about one tenth of the thickness, the CG copper was less drawable. Through-thickness variations in the texture of the UFG copper were found by experiment and this was explained by simulations. It was shown that rigid body rotation during the drawing process play an important role in the evolution of the texture. Such variation is important in cup-forming if the grain size is very small.

Thermal stability during further processing is one of the main concerns in the application of UFG materials for micro-forming. Micro-extruded copper with a range of grain sizes, spanning from CG to UFG copper, have been studied at different extrusion speeds. It was clear that the grain size after micro-extrusion depends on the processing speed and was always larger than the grain size expected from purely geometrical considerations of the process. Differential scanning calorimetry, dislocation density measurements and hardness all support the occurrence of dynamic recrystallization (DRX) of the UFG copper – but importantly not the CG copper – during micro-extrusion at the highest extrusion speed of 25mm/min. The effect of recovery was incorporated in the grain refinement model by changing the curvature induced dislocation density represented by an adjustable parameter in model for CG copper at the extrusion speed of 1 mm/min. Good agreement with the experimental observation was obtained. Importantly, although the CG copper was micro-extrudable, the thermal stability of UFG copper was superior after high speed micro-extrusion because of the dynamic recrystallization and this justifies the use of UFG copper in this case.

DECLARATION STATEMENT

This thesis or any its portions thereof, does not contain material that has been submitted or accepted for the award of another degree, diploma or qualification of this or any other university or institution of learning.

Chengfan Gu

Under the Copyright Act 1968, this thesis must be used only under the normal conditions of scholarly fair dealing. In particular no results or conclusions should be extracted from it, nor should it be copied or closely paraphrased in whole or in part without the written consent of the author. Proper written acknowledgement should be made for any assistance obtained from this thesis.

I certify that I have made all reasonable efforts to secure copyright permissions for third-party content included in this thesis and have not knowingly added copyright content to my work without the owner's permission.

Copyright ©2010 by C. Gu. All rights reserved.

ACKNOWLEDGEMENTS

First and foremost I express my sincerest gratitude and appreciation to my enthusiastic supervisor Professor Chris Davies, whose erudition, constant encouragement, inspiration, guidance and support from the initial to the final stage enabled me to complete the research project. I attribute the level of my PhD degree to his supervision and effort, and this thesis would not have been possible without him.

I am heartily indebted to my supervisor Professor László Tóth (Laboratoire de Physique et Mécanique des Matériaux, Université Paul Verlaine de Metz, France) for his knowledge, supervision and support. This research project would not have made a significant progress without his mentoring, especially in crystal plasticity and grain fragmentation modeling.

I gratefully acknowledge the co-authors of my publications: Prof. Elena Pereloma, Drs. Tim Williams, Benoit Beausir, Prof. Yuri Estrin, Drs. Rimma Lapovok, Wenquan Cao, Andrey Molotnikov, Azdiar Gazder, Jean-Jacques Fundenberger and Ms. Mandana Arzaghi. I also appreciate Dr. Peter Thomson, Ms. Jane Moodie, Dr. Young Chun, Mr. Graham Prior, JiKang Zhong, Silvio Mattievich and Alan Holland for their great help.

I thank the Department of Materials Engineering at Monash University, Victorian Center for Advanced Materials Manufacturing, Australia and Université Paul Verlaine de Metz, France for providing the scholarship and research facilities for this project.

I express my deepest gratitude to my late mother Professor Xia Chen (1937-2008), who made many constructive suggestions at the beginning of this work, and to my family for their love and supports, both financial and moral.

PUBLICATIONS

JOURNAL PAPERS

1. C.F. Gu, L.S. Tóth, R. Lapovok and C.H.J. Davies, "Texture development and grain refinement of ultrafine-grained copper during micro-extrusion", *Philosophical Magazine A*, **91-2** (2011), 273-290.
2. C.F. Gu, L.S. Tóth, M. Arzaghi and C.H.J. Davies, "Effect of strain path on grain refinement in severely plastically deformed copper", *Scripta Materialia*, **64** (2011), 284-287.
3. L.S. Tóth, B. Beausir, C.F. Gu, Y. Estrin, N. Scheerbaum and C.H.J. Davies, "Effect of grain shape on next-neighbor misorientation distribution due to grain refinement in severe plastic deformation processes", *Acta Materialia*, **58** (2010), 6706-6716.
4. L.S. Tóth, R. Lapovok, A. Molotnikov, C.Gu, J-J. Fundenberger and C.H.J. Davies, "Texture evolution during micro drawing of ultrafine-grained copper", *Materials Science and Engineering A*, **527** (2010), 4633-4640.
5. C.F. Gu and C.H.J. Davies, "Thermal stability of ultrafine-grained copper during high speed micro-extrusion", *Materials Science and Engineering A*, **527** (2010), 1791-1799.
6. László S. Tóth, Yuri Estrin, Rimma Lapovok, Chengfan Gu, "A model of grain fragmentation based on lattice curvature ", *Acta Materialia*, **58** (2010), 1782-1794.
7. X. Ma, R. Lapovok, C. Gu, A. Molotnikov, Y. Estrin, E.V. Pereloma, C.H.J. Davies and P.D. Hodgson, "Deep drawing behaviour of ultrafine-grained copper: Modeling and Experiment," *Journal of Materials Science*, **44** (2009), 3807-3812.
8. W.Q. Cao, C.F. Gu, E.V. Pereloma and C.H.J. Davies, "Stored energy, vacancies and thermal stability of ultrafine-grained copper", *Materials Science and Engineering A*, **492** (2008), 74-79.

CONFERENCE PAPERS

9. C.F. Gu, L.S. Tóth, B. Beausir, T. Williams and C.H.J. Davies, "Grain fragmentation in equal channel angular pressed copper", *Materials Science Forum*, **654-656** (2010), 1570-1573.

10. A.A. Gazder, S.S. Hazra, C.F. Gu, W.Q. Cao, C.H.J. Davies, E.V. Pereloma, "Mechanical, microstructure and texture properties of interstitial-free steel and copper subjected to equal channel angular extrusion and cold-rolling", *Journal of Physics: Conference Series*: **240** (2010), 1742-6596.
11. T. Williams, C.F. Gu and X.Y. Fang, "EBSD from ultramicrotomed metal samples", *The 21st Australian Conference on Microscopy and Microanalysis (ACMM-21)*, 11-15th July 2010, Brisbane, Queensland, Australia.
12. L.S. Tóth, Y. Estrin, R. Lapovok, C. Gu, "A model of grain fragmentation based on lattice curvature", *15th International Conference on Strength of Materials (ICSMA15)*, 16-21st August 2009, Dresden, Germany.

CONTENTS

Abstract	I
Declaration Statement	III
Acknowledgments	IV
Publications	V
Contents	VII
List of Tables	XI
List of Figures	XIII
1 INTRODUCTION	1
1.1 Motivation.....	2
1.2 Objectives.....	2
1.3 Approach.....	2
1.4 Contribution to the Field	3
1.5 Thesis Structure.....	4
2 LITERATURE SURVEY	7
2.1 State of the Art in Micro-forming.....	7
2.1.1 Micro-extrusion.....	7
2.1.2 Micro deep drawing.....	8
2.2 Size Effect in Micro-forming.....	10
2.2.1 Microstructural effect.....	11
2.2.2 Geometry effect.....	12
2.2.3 Strain gradient effect.....	14
2.2.4 Boundary, surface and grain statistics effect.....	15
2.3 ECAP Technique for Obtaining UFG Materials.....	16
2.4 Microstructure, Texture and Thermo-mechanical Behaviors of UFG Materials.....	19
2.5 Grain Fragmentation for Obtaining UFG Materials.....	28
2.6 Summary.....	30
RESEARCH QUESTIONS.....	32
3 EXPERIMENTAL PROCEDURES AND MODELING METHODOLOGY	33
3.1 Deformation Processing.....	34
3.2 Samples Characterization	36

3.2.1 Electron backscattered diffraction.....	36
3.2.2 Textures.....	38
3.2.3 Uniaxial tensile test.....	39
3.2.4 Nano-indentation.....	40
3.2.5 Differential scanning calorimetry.....	40
3.2.6 X-ray diffraction for determining micro-strain and dislocation density.....	40
3.3 Grain Fragmentation Modeling Based on Lattice Rotation.....	41
3.3.1 Model description.....	41
3.3.1.1 Lattice distortion.....	41
3.3.1.2 Geometrically necessary dislocations associated with lattice curvature.....	43
3.3.1.3 Grain fragmentation.....	45
3.3.1.4 Polycrystal model.....	47
3.3.2 Numerical implementation.....	48
3.3.3 Summary	49
4 GRAIN FRAGMENTATION IN ECAP-ed COPPER.....	51
4.1 Experiments.....	51
4.1.1 Initial materials.....	51
4.1.2 Grain morphology after ECAP and rolling.....	52
4.1.3 Textures.....	57
4.1.4 Misorientation distributions.....	60
4.2 Grain Fragmentation Model Parameters.....	64
4.3 Grain Fragmentation Modeling Results for ECAP.....	66
4.3.1 Predicted textures.....	66
4.3.2 Predicted grain sizes.....	67
4.3.3 Predicted misorientation distribution.....	68
4.3.4 Predicted geometrically necessary dislocation associated with lattice curvature.....	69
4.4 Comparison of Grain Fragmentation Modeling between ECAP and Rolling.....	70
4.4.1 Elements of mechanics of ECAP and cold rolling	71
4.4.2 Simulation results.....	72
4.4.3 Lattice rotation versus strain path	73
4.5 Split of Misorientation Distribution.....	77

4.5.1 Background.....	78
4.5.2 Technique for obtaining the misorientation distributions.....	78
4.5.3 NNMD implementation.....	85
4.5.4 Discussions on NNMD.....	86
4.6 Summary	88
5 TEXTURE ANALYSIS DURING MICRO DEEP DRAWING.....	91
5.1 Deep Drawing Experiments.....	91
5.1.1 Tensile properties of ECAP-ed copper.....	91
5.1.2 Deep drawability of ECAP-ed copper.....	92
5.1.3 Initial thickness effect on deep drawability of ECAP-ed copper.....	97
5.2 Experimental Textures.....	100
5.2.1 Textures after ECAP and before micro drawing.....	100
5.2.2 Textures after micro drawing.....	104
5.3 Texture Modeling in Cup Drawing.....	110
5.4 Discussions.....	117
5.5 Summary.....	121
6 MICRO-EXTRUDED UFG AND CG COPPER.....	123
6.1 Force and Displacement during Micro-extrusion.....	123
6.2 Microstructure of UFG and CG after Micro-extrusion.....	124
6.3 Texture Evolution of UFG and CG Copper after Micro-extrusion.....	135
6.4 Differential Scanning Calorimetry.....	137
6.5 Nano-indentation.....	139
6.6 Flow Line Model.....	141
6.7 Polycrystal Modeling.....	145
6.8 Discussions.....	146
6.8.1 Textures.....	146
6.8.2 Thermo mechanical behaviour.....	150
6.9 Summary.....	158
7 SUMMARIES, CONCLUSIONS AND FUTURE WORK.....	161
7.1 Summaries.....	161
7.2 Conclusions.....	163
7.3 Future Work.....	165

REFERENCES.....169

LIST OF TABLES

Table 2-1. Experimental and calculated maximum drawing forces.....	9
Table 2-2. Ideal ECAP orientation and fibers for f.c.c. materials and a $\Phi=90^\circ$ die.....	20
Table 3-1. Starting materials used in the refinement study and micro-forming.....	33
Table 3-2. Mechanical characteristics for copper after N=0, 1, 4, 8, 12 and 16 passes....	40
Table 4-1. The average boundary length between two neighbouring grains, $\langle l_g^p \rangle$, and the average number of interconnected first neighbours around a grain, $\langle c_g^p \rangle$, measured from the EBSD maps on different planes of one-pass and three-pass deformed samples. The calculated 'internal' as well as the 'old boundary grain' type fractions are also indicated.....	83
Table 5-1. The von Mises accumulated strains from the FE simulations at six points in cup drawing tests.....	115
Table 6-1. Stored energy calculation from EBSD and XRD measurements of UFG and CG copper extruded at different speeds.....	154

LIST OF FIGURES

Figure 2-1. Illustration of two types scaling effects: grain size effect and geometry effect	11
Figure 2-2. Parameters of α and β , and their dependence on $n = D/d$ (D = sample size, d = grain size).....	14
Figure 2-3. ECAP rig at Monash University with a die angle of 90°	17
Figure 2-4. Ideal orientations of simple shear in a $\{111\}$ pole figure for f.c.c. metals.....	20
Figure 2-5. A schematic substructure evolution during the first pass of ECAP in (a) two grains with different crystal orientation; (b) both of which form cellular substructures early in the extrusion, but before they approach the intersection plane; (c) grain 1 has formed lamina sub boundaries not aligned with the main plane of simple shear, whereas grain 2 has formed lamella sub boundaries closely aligned with it; and (d) after passing through the deformation zone, both grains form sub boundaries on slip planes aligned closely with the intersection plane.....	24
Figure 2-6. Strain rate sensitivity (a) and apparent activation volume (b) as a function of the true stress for specimens subjected to 1,2,4,8 and 12 passes. (b) is plotted in logarithmic scale.....	26
Figure 2-7. Strain rate sensitivity m as a function of grain size for some b.c.c. metals as a function of grain size.....	27
Figure 3-1. Schematic diagram illustrating the main experimental and analytical procedures.....	33
Figure 3-2. Schematic drawing of ECAP die.....	34
Figure 3-3. Testing configuration for deep drawing and FE simulation (dimensions are in mm).....	35
Figure 3-4. Schematic diagram of the extrusion die (D : contained diameter, ϕ is 60°)....	36
Figure 3-5. True stress-strain curves for copper subjected to different number of ECAP passes, route Bc.....	39
Figure 3-6. Assumed distortion of a lattice plane in a crystal due to its grain boundary	42
Figure 3-7. Example of lattice curvature showing cumulative misorientation in a grain as moving away from its grain boundary in an Al-Si alloy; A2 and A3 indicate positions for scans.....	42

Figure 3-8. Schematic distortion of a crystallographic plane due to its position-dependent rotation in a cube-shaped crystal for the case when the lattice rotation is taking place perpendicular to a grain boundary (large arrow). The small vectors represent the local additional rotations produced by the ‘friction’ effect of the grain boundary.....	43
Figure 3-9. Schematic illustration of the parameters of the model.....	44
Figure 3-10. The ‘Rubik-cube’ representation of the grain fragmentation process. The fragmentation is continuous in each smaller cube in the same manner; three levels are considered.....	45
Figure 3-11. Relative position of the lattice rotation rate vector $\dot{\underline{\Omega}}$ and the resultant subgrain boundary normal vector $\underline{n}_{GND}^{(res)}$ in the deformed state.....	46
Figure 4-1. Representative orientation map and {111} pole figure of the as-received copper. The color code for the ED axis in the map is also shown in the unit triangle. The unit is micron in the orientation map.....	52
Figure 4-2. Examples of orientation maps after one ECAP pass in pure copper: (a) ED plane; (b) ND plane and (c) TD plane. Boundaries with at least 5° misorientation are marked with black lines. The color code for the orientations is also shown. Units are in micron (Zoom 1 refers to a later image, Figure 4-23).....	53
Figure 4-3. Inverse pole figure of deformation microstructure of OFHC copper deformed in route A ECAP in two passes. Grain boundaries with misorientation larger than 5° are depicted by black lines. Scale is in μm	54
Figure 4-4. EBSD orientation map after two passes of pure copper in Route Bc. Size of map: 80 × 100 μm	55
Figure 4-5. Measured grain size distribution for pure copper after two passes in route Bc.....	55
Figure 4-6. Orientation maps of 3 passes ECAP-ed copper: (a) TD plane and (b) ED plane. Boundaries with at least 5° misorientation are marked with black lines. The color code is the same as in Fig. 4-2, and scale is in micron (Zoom 2 refers to a later image, Figure 4-23).....	56
Figure 4-7. Deformation microstructure of OFHC copper deformed in rolling to a thickness reduction of 60% (a) and to 84% (b). Grain boundaries with misorientation larger than 5° are depicted by black lines. Scale is in μm	57
Figure 4-8. Measured textures for one-pass ECAP deformed copper in {111} pole figures by X-ray (a) and by EBSD on the TD plane (b) and from the ED plane (c). All three	

textures are expressed in the same sample reference system: pressing ('extrusion') direction ED is to the right, and normal direction ND is vertical. Isolevels: 0.7, 1, 1.2, 1.4, 1.6, 2, 2.5, 3, 3.5, 4.....58

Figure 4-9. X-ray measured texture for two-pass ECAP route Bc deformed copper in {111} pole figure. ED direction is to the right and normal direction ND is vertical. Isolevels: 0.7, 1, 1.2, 1.4, 1.6, 2, 2.5, 3, 3.5, 4.....59

Figure 4-10. Measured textures for three-pass ECAP deformed copper in {111} pole figures by X-ray (a) and by EBSD on the TD plane (b) and from the ED plane (c). All three textures are expressed in the same sample reference system: ED to the right and normal direction ND is vertical. Isolevels: 0.7, 1, 1.2, 1.4, 1.6, 2, 2.5, 3, 3.5, 4.....60

Figure 4-11. Comparison between pixel-to-pixel (light gray) and grain-to-grain (dark gray) misorientation distributions after one pass of copper in ECAP on the TD plane.....61

Figure 4-12. Grain-to-grain misorientation distributions measured on the TD as well as on the ED plane in pure copper deformed by ECAP after one pass. The minimum misorientation was set to 5° to identify grains.....62

Figure 4-13. Grain-to-grain misorientation distribution measured on the TD plane in pure copper deformed by ECAP in route Bc two passes. The minimum misorientation was set to 5° to identify grains.....63

Figure 4-14. Grain-to-grain misorientation distributions measured on the TD as well as on the ED plane in pure copper deformed by ECAP in three passes in route A. The minimum misorientation was set to 5° to identify grains.....64

Figure 4-15. Measured and simulated textures for copper deformed by ECAP in route Bc represented by {111} pole figures by X-ray. Pressing ('extrusion') direction ED is to the right, and normal direction ND is vertical. Isolevels: 0.7, 1, 1.2, 1.4, 1.6, 2, 2.5, 3, 3.5, 4. Open square symbols indicate a rotated cube position.....67

Figure 4-16. Predicted grain size distribution for pure copper after two passes in route Bc.....68

Figure 4-17. Comparison of predicted (black) and measured (gray) grain-to-grain misorientation distribution on the TD plane in pure copper deformed by ECAP in route Bc two passes. The minimum misorientation was set to 5° to identify grains.....69

Figure 4-18. Predicted density of curvature induced dislocations in route Bc ECAP of copper.....70

Figure 4-19. Simulated (continuous lines) and experimental (symbols) development of average grain size obtained in ECAP and rolling. Two simulations are shown for ECAP; the difference between them is the initial texture which was rotated by 90° for ECAP1....73

Figure 4-20. Analysis of the deformation processes in ECAP and rolling to show that the initial textures in the ECAP and rolling processes are 90° rotated with respect to the deformation (follow pink colored lines)	74
Figure 4-21. The average lattice rotation rate (a) and total lattice rotation (b) as a function of the equivalent strain obtained from the grain refinement simulation of ECAP as well as rolling	76
Figure 4-22. Schematic figure showing the trace of a boundary of an ‘old’ grain (broken line) together with the newly emerged finer grains represented by hexagons. New grains that are sitting at the old grain boundary are shaded	79
Figure 4-23. (a): Schematic illustration of the number of interconnected first neighbors around a grain for two “extreme” cases, the interconnections are indicated by short thick segments, and the blue line represents an old grain boundary; (b) and (c): Zooms in the EBSD map after 1 pass ECAP on the TD plane, and after 3 passes ECAP on the ED plane, respectively.....	81
Figure 4-24. Geometry of an old grain on the TD plane in ECAP.....	84
Figure 4-25. Split NNMDs for one pass (a) and three-pass (b) ECAPed copper; in light gray the old grain-interior frequency distribution ($\nu_{int}(\theta)$) and in dark gray the old boundary layer grain distribution ($\nu_{OBG}(\theta)$).....	86
Figure 5-1. Tensile strength (solid line) and tensile ductility (dash line) as a function of number of ECAP passes.....	92
Figure 5-2. Cups drawn from blanks with four different diameters from copper pre-processed by one and four ECAP passes.....	93
Figure 5-3. Load versus d/D for number of ECAP passes (experimental). Full and open symbols are used for non cracked and cracked samples, respectively.....	94
Figure 5-4. Limit drawing ratio versus number of ECAP passes (experimental).....	97
Figure 5-5. Load-displacement curves for CG (a) and UFG (b) copper at the different thicknesses of 0.4 mm and 0.2 mm (experimental).....	98
Figure 5-6. Experimental load versus drawing ratio for the 0-pass and for the 12-pass ECAPed samples at 0.4 and 0.2 mm sheet thicknesses. Full and open symbols are used for non cracked and cracked samples, respectively.....	99
Figure 5-7. Normalised yield stress vs thickness/grain size for ECAP-ed copper.....	100
Figure 5-8. Experimental textures in {111} pole figures after 1, 4, 8 and 16 ECAP passes of route Bc. Isolevels: 0.7, 1.0, 1.5, 2.0, 2.8, 4.0.....	102

Figure 5-9. Constant ODF sections of ECAP-ed copper (a) 1 pass, (b) 4 pass, (c) 8 pass and (d) 16 pass. Contour step size: 1.65 times.....	103
Figure 5-10. Textures ($\{111\}$ pole figures) measured by X-ray at the base of the cups after cup micro-drawing for the sample with initial blank diameter of 14.6 mm. The number of ECAP passes prior to drawing are indicated under each pole figure. Isolevels: 0.7, 1, 1.2, 1.4, 1.6, 2. The reference system is the same as in Fig. 5-8.....	104
Figure 5-11. Textures measured by EBSD after cup-drawing in $\{111\}$ pole figures for the 16-pass ECAP after cup micro-drawing for the sample with initial blank diameter of 14.6 mm at six selected points in the cup. The projection plane is ED, and ND and TD axes are at the top and on the left of each pole figure, respectively. Isolevels: 0.7, 1, 1.2, 1.4, 1.6, 2, 2.5.....	105
Figure 5-12. EBSD after cup-drawing for the 16-pass ECAP after cup micro-drawing for the sample with initial blank diameter of 14.6 mm at six selected points in the cup. Boundaries with at least 5° misorientation are marked with black lines. The colour code for the orientation of the axis perpendicular to the image is shown in an insert.....	107
Figure 5-13. Grain size distribution of the 16-pass ECAP after cup micro-drawing for the sample with initial blank diameter of 14.6 mm at six selected points in the cup.....	108
Figure 5-14. Neighbour-to-neighbour misorientation distribution of the 16-pass ECAP after cup micro-drawing for the sample with initial blank diameter of 14.6 mm at six selected points in the cup.....	109
Figure 5-15. FE predicted shape and von Mises strain map of the one-pass ECAPed sample with initial blank diameter of 9.5 mm. Numbers indicate the six points selected for texture simulation and measurement at their initial positions and after drawing. The rotation angle of the deformed surface with respect to the undeformed is indicated by α at point 2 (30°).....	111
Figure 5-16. Simulated textures in $\{111\}$ pole figures for the 0-pass ECAP cup-drawing as a function of blank diameter and position in the drawn cup. The projection plane is ED, and axes ND and TD are at the top and on the left of each pole figure, respectively. Isolevels: 0.7, 1, 1.2, 1.4, 1.6, 2, 2.5, 3, 3.5, 4.....	112
Figure 5-17. Simulated textures in $\{111\}$ pole figures for the 1-pass ECAP cup-drawing as a function of blank diameter and position in the drawn cup. The projection plane is ED, and axes ND and TD are at the top and on the left of each pole figure, respectively. Isolevels: 0.7, 1, 1.2, 1.4, 1.6, 2, 2.5, 3, 3.5, 4.....	113
Figure 5-18. Simulated textures in $\{111\}$ pole figures for the 16-pass ECAP cup-drawing as a function of blank diameter and position in the drawn cup. The projection plane is ED,	

and axes ND and TD are at the top and on the left, respectively. Isolevels: 0.7, 1, 1.2, 1.4, 1.6, 2, 2.5, 3, 3.5, 4.....	114
Figure 5-19. Simulated textures in the one-pass ECAP drawn cup compared to the initial texture that is simply rotated around the TD axis at four positions. Isolevels: 0.7, 1, 1.2, 1.4, 1.6, 2, 2.5, 3, 3.5, 4.....	119
Figure 6-1. Force-displacement response for micro-extruded UFG and CG copper.....	124
Figure 6-2. Examples of orientation maps after micro-extrusion in CG copper: (a) as-received; (b) C = 0.6 and (c) C = 0. Boundaries with at least 5° misorientation are marked with black lines. The colour code for the orientation of the axis perpendicular to the image is shown in an insert. Coordinates are in μm.....	125
Figure 6-3. Grain size (a) and neighbour-to-neighbour misorientation distribution (b) in CG as-received copper.....	126
Figure 6-4. (a) Grain size; (b) neighbour-to-neighbour misorientation distribution at position C = 0.6; (c) Grain size and (d) neighbour-to-neighbour misorientation distribution at C = 0 in CG copper after micro-extrusion.....	127
Figure 6-5. Microstructure of CG copper extruded at different speeds: (a) CG extruded at 0.1 mm/min; (b) at 10 mm/min and (c) at 25 mm/min. Scale bar and ED are the same as Fig. 6-2.....	129
Figure 6-6. Examples of orientation maps after micro-extrusion in UFG copper: (a) as-received, (b) at C = 0.6 and (c) at C = 0. Boundaries with at least 5° misorientation are marked with black lines. The colour code is shown in an insert. Coordinates are in μm.....	130
Figure 6-7. (a) Grain size and (b) neighbour-to-neighbour misorientation density distributions in UFG copper.....	131
Figure 6-8. (a) Grain size; (b) neighbour-to-neighbour misorientation distribution at position C = 0.6; (c) Grain size and (d) neighbour-to-neighbour misorientation distribution at position C = 0 in UFG copper after micro-extrusion.....	132
Figure 6-9. Microstructure of UFG copper extruded at different speeds: (a) UFG extruded at 0.1 mm/min; (b) at 10 mm/min and (c) at 25 mm/min. Scale bar and ED are the same as in Fig. 6-6.....	134
Figure 6-10. IPFs of CG as-received (a), and CG copper extruded at different speeds: (b) CG extruded at 0.1 mm/min; (c) at 1 mm/min; (d) at 10 mm/min and (e) at 25 mm/min.....	136
Figure 6-11. IPFs of UFG initial (a) and UFG copper extruded at different speeds: (b) UFG extruded at 0.1 mm/min; (c) at 1 mm/min; (d) at 10 mm/min and (e) at 25 mm/min.....	137

Figure 6-12. Exothermic DSC curves of UFG and CG copper extruded at 0.1, 1, 10, and 25 mm/min. Samples were scanned at linear heating rate of 10 K/min. (The very bottom scans are for the un-extruded starting materials).....	138
Figure 6-13. (a) Peak temperatures from DSC measurement for UFG and CG copper and (b) Stored energy from DSC measurement for UFG and CG copper. Values for the un-extruded starting material in both cases are shown as an extrusion speed of zero for comparison.....	139
Figure 6-14. Load and displacement curves from nano-indentation experiments performed at 100 μ N/sec: (a) UFG and (b) CG.....	140
Figure 6-15. Nano-indentation hardness variation for extruded UFG and CG copper. Values for the un-extruded starting material in both cases are shown as an extrusion speed of zero for comparison.....	141
Figure 6-16. Dislocation density calculation from XRD measurement for extruded UFG and CG copper. Values for the un-extruded starting material in both cases are shown as an extrusion speed of zero for comparison.....	141
Figure 6-17. Flow of the metal in the extrusion die obtained by finite element modeling: The analytical flow line entering at position $C = 0.6$ ($C = 0$ is the centre) is superimposed, identified by the arrow. R_1 and R_2 are the diameters of the extrudates before and after (micro-)extrusion.....	142
Figure 6-18. Evolution of the components of the velocity gradient as a function of time along the flow line selected at position $C = 0.6$ ($C = 0$ is the centre). The equivalent strain rate obtained from the FE simulation is superimposed (it corresponds to initial position $C = 0.62$).....	145
Figure 6-19. Experimental and predicted $\{100\}$ pole figures of $C = 0$ and $C = 0.6$ within the extrudates for CG; Isolevels: 1.2, 2.0, 2.5, 3.0, 3.5, 4, 8, 12, 20, 30.....	147
Figure 6-20. Experimental and Predicted $\{100\}$ pole figures of $C = 0$ and $C = 0.6$ within the extrudates for UFG copper; Isolevels: 1.2, 2.0, 2.5, 3.0, 3.5, 4, 8, 12, 20, 30.....	148
Figure 6-21. Comparison of the deformation induced dislocation densities in severe plastic deformed copper by X-ray measurement, DSC measurement and TEM.....	151
Figure 6-22. Variation of average misorientation for initial UFG and UFG copper extruded at different speeds.....	153
Figure 6-23. Variation of average misorientation for initial CG and CG copper extruded at different speeds.....	153

Figure 6-24. IPFs of UFG micro-extruded at 25 mm/min: (a) recrystallized component and (b) un-recrystallized component.....158

1

INTRODUCTION

1. INTRODUCTION

Micro-forming is the production of parts or structures with at least two dimensions in the sub-millimeter range [1]. It has a great potential to provide a cheaper and more efficient means for producing small parts, which can be used in variety of products such as mobile phones, laptops, personal digit assistants, environmental monitoring, biotechnology, and surgical equipment. However, investigations of the micro-forming process reveal significant differences in the forming behavior of metals at this geometric scale compared to conventional bulk metal forming. Among these differences are the reduced repeatability of the shape of the manufactured part, increased friction and decreased surface quality which prevent micro-forming being widely used [1-4]. Therefore, micro-forming is a challenging research topic, requiring forming characteristics to be re-investigated.

The use of metals with grain sizes that are comparable to the part size can be problematic when used in micro-devices [5, 6] because the relatively coarse grained (CG) structure of micro parts can lead to non-uniform material flow and lack of repeatability of products during micro-forming. Because of their small grain sizes, ultrafine-grained (UFG) materials are expected to behave differently compared to their CG counterparts in terms of plastic flow, shape representation and surface effects. In the past decade, various techniques for UFG or nanocrystalline (NC) materials have been used to investigate microstructural and thermal-mechanical behaviors. The studies are along with a range of grain sizes, and geometries produced by different deformation modes and heat treatments. UFG microstructures are commonly obtained by severe plastic deformation (SPD) processes such as equal channel angular pressing (ECAP), high pressure torsion, and accumulated roll bonding through introducing large strains into a polycrystalline aggregate [7-11]. Comparing with CG metals, the deformation microstructure is finer and the stored energy and high angle boundary fraction are much higher in UFG materials [12]. Ultrafine-grained metals typically have a grain size in the range from 0.15 μm [13] to 0.3 μm [14,15] and the assumption is that in typical micro-formed parts of dimensions in the hundreds of microns there ought to be sufficient grains to accommodate slip and allow for reproducibility of shape. Therefore, it is interesting to conduct this research to improve the understanding of microstructure and thermal mechanical behaviors for UFG materials used in micro-forming process.

1: Introduction

1.1 Motivation

Size effects have been shown to exist when part geometry and microstructural scale coincide and this usually occurs at part dimensions that are less than 10-15 grain diameters in width [16, 17]. The differing trend of experimental results for different grain sizes highlights the need for greater understanding of the specimen size effect by monitoring the mechanical properties over a range of grain sizes, especially in micro-size range, which are ideal to be used in micro-forming. Also the constitutive models that account for the size effect must be investigated and developed to adequately observe and predict microstructure behaviors and mechanical response of UFG materials used in micro-forming.

Geometrical influence is an important factor in micro-forming. Modeling the proportion of surface grains and their relative strength leads to the prediction that yield stress of copper would be reduced below a critical dimensional ratio of thickness / grain size of ~ 15 [16, 17]. Experimental work showed the yield stress of large grains follow the expected and modeled behavior but specimens with smaller grains displayed unexpected results [3, 18]. Therefore, the decreased size to the component size needs to be investigated to gain a greater understanding of the influence of geometry in micro-forming.

1.2 Objectives

The objectives of my PhD project are:

- i) This project will investigate fundamental issues concerning the grain fragmentation during SPD process which will be shown to be dependent on texture and lattice rotation;
- ii) Our research work [19] showed that improved formability was obtained from high strained ECAP copper after micro-deep drawing. However, the texture effect was not investigated. Therefore, the thesis will study the effect of texture evolution along the thickness in micro deep drawing of ECAP-ed copper in comparison with modeling prediction to understand to what extent texture will vary during micro-forming;
- iii) Using raw materials of different grain sizes the thesis will study the effect of different strain rates on the thermal stability of UFG and CG copper after micro-extrusion.

1.3 Approach

A grain refinement modeling based on lattice curvature [20] is explored to explain and analyze the experimental results obtained by severe plastic deformation. The modeling

1: Introduction

results give fairly precise prediction of grain size and grain orientation distribution. The crystallographic textures are well reproduced and the strength of the materials is reliably predicted based on modeling of dislocation density evolution coupled with texture development. The related lattice rotation and texture are the main elements of the grain refinement process and these two elements have been investigated in the UFG structure obtained by using three different deformation processing routes:

- ECAP 1, 2, 3 passes, route A copper to assess strain and texture effect on the grain refinement process;
- ECAP 1, 4, 8, 12, 16 passes, route Bc copper followed by micro deep drawing;
- ECAP, route Bc, 8 passes plus micro-extrusion to a strain of 2.77 under different strain rates of 0.1, 1, 10 and 25 mm/min.

The experimental work is conducted based on different SPD processes by using X-ray diffraction, EBSD, DSC and mechanical properties. Advanced theoretical models will be established based on computation and simulation analysis to interpret and analyze the experimental results. Thermal stability of micro-extruded UFG and CG copper were chosen to compare the microstructure and thermal mechanical properties of these two materials.

1.4 Contribution to the Field

The novelties contained in this thesis are:

- i) The key experimental findings provided an insightful understanding of grain size and its distribution, misorientation distribution and texture evolution during SPD processes. Grain fragmentation modeling based on lattice curvature were carried out to obtain physical information about the grain refinement process;
- ii) A new procedure based on EBSD orientation maps' was proposed to separate the next-neighbour misorientation distribution of UFG materials into two parts: the distribution of misorientations between newly emerged daughter grains within the original parent grain interior and the distribution of misorientations between grains adjacent to an original grain boundary on its opposite sides;
- iii) A thorough experimental investigation was carried out for determining size and geometric effects of UFG copper in micro-forming processes for the important variables: orientation and thermal stability. The results in different combination have demonstrated that texture plays an important role during micro deep drawing and

1: Introduction

thermal stability has been improved in UFG copper during high speed micro-extrusion.

1.5 Thesis Structure

This research studies fundamental issues of material characteristics associated with micro-forming through materials themselves, entry of forming and further simulation of these results. It aims to investigate the size and geometry effects on the microstructure and thermal mechanical behaviors of UFG and CG materials over a range of grain size.

In Chapter 2 a literature review is presented concerning processes to obtain UFG materials and their further processing in micro-forming.

Chapter 3 describes the experimental techniques used as well as the new grain fragmentation model based on lattice curvature. This new model captures within a single modeling frame all the main microstructural features of SPD process, including evolution of the grain size distribution, misorientation distribution and crystallographic texture. I wish to make it clear at this point that the grain fragmentation model development described in Chapter 3 is not part of the work I am presenting for my thesis.

My original contribution starts in Chapter 4 where extensive experimental results are first presented then modeled with the help of the new grain fragmentation model based on lattice curvature. The experimental and modeling studies presented in Chapter 4 provide further support for the grain refinement process to obtain UFG structures. In this chapter a new technique based on grain shape evolution and subgrain size variations during severe plastic deformation is also presented to separate next-neighbor misorientation distributions (NNMD) into two parts: the grain interior and boundary parts. The successful application of this technique for the first time in ECAP deformed copper creates new opportunities for the interpretation of the grain refinement process during large strain that lead to UFG materials.

Chapter 5 focuses on the textures during cup micro-forming because texture evolution is another important element in grain refinement.

Micro-extrusion has been studied in Chapter 6 to observe the predictive capacity of texture modeling in UFG with respect to CG materials in micro-forming conditions. The results of both finite element and analytic deformation models were used for this purpose

1: Introduction

and were shown to be predictive with respect to local materials behaviors. Thermal stability during further processing is also the main concerns in applications of UFG materials. It is shown clearly that the grain size after extrusion depends on the processing speed and is always larger than the one expected by pure geometry of the micro-extrusion process. During micro-extrusion, a grain coarsening was observed for UFG copper which was attributed to dynamic recrystallization (DRX). Other characteristics such as dislocation density and hardness also support the evidence of DRX during processing.

Finally, Chapter 7 concludes the thesis and discusses the future research work.

2

LITERATURE SURVEY

2. LITERATURE SURVEY

In this Chapter it will be shown how and why UFG metals are likely candidates for micro-forming by describing the state of the art in the micro-forming technology and by looking at experimental and simulation evidences in SPD obtained materials for the following aspects:

- Bulk production including micro extrusion and micro deep drawing;
- Scaling effect within the micro-forming process, including microstructural effects, geometry effect, strain gradient effect, boundary, surface and grain statistics effects;
- ECAP technique for obtaining UFG materials;
- Microstructure, texture and mechanical properties of UFG materials;
- Simulation prediction and analysis of scaling effects for SPD materials which are used to replace CG materials because CG materials may cause problems during micro-forming process when grain size is comparable to the part dimensions.

2.1 State of the Art in Micro-forming

Forming and micro-forming of metals can be divided into massive forming, sheet metal forming and profile forming. However, transferring macro-forming directly into the micro-forming is impossible due to the size effect when parts are minimized, such as the ratio of surface to volume increases and other effects like adhesion force and surface tension. The size effect plays an important role in micro-forming, and thus has received attention. Also, one of the main challenges remaining in micro-forming is to transfer the laboratory processes to the production line of industry. Such a process requires a fundamental understanding of the starting point, processes conditions and the interaction of these two. These aspects have to be understood from the raw materials up to the final products.

2.1.1 Micro-extrusion

Micro-extrusion, forward and/or backward, has been recently employed in a variety of manufacturing processes to obtain small-scale products. Examples of micro parts include connector pins, springs, micro-gears, screws and fasteners, just naming a few [21]. Apart from feasibility, the research of micro-forming also focuses on the suitability in mass-production. For example, some effects of the products scaling down from conventional macro-scale manufacturing processes for double-cup micro-extrusion [2, 22] demonstrating the ratio of the cup height and the length of the connection part increases with miniaturization in the fine sized grain of 4 μm . However, when the coarse sized grain

2: Literature Survey

of 120 μm is used, the ratio of the cup height and the length of the connection part do not increase. The observed results can be explained by the microstructure of the samples. The larger the ratio of the grain size and cup wall is, the more easily material flows into the connection part instead of the cup wall.

The effects of parts size and grain size on forming behavior as parts approach the sub-millimeter size range have seldom been investigated together. In numerical simulations friction increases dramatically as parts size is reduced [23] but in experiments total load is reduced when parts are scaled down to around 1 mm in diameter [24]. This can be explained by an increase of the ratio between the surface grains and the volume grains. Grains within the surface layer are less restricted than inner grains and thus show less hardening, resulting in a lower overall flow stress. A significant increase in friction (up to a factor of 20) was identified by decreasing specimen size when using extrusion oil as lubricant.

Similar research work was also investigated by using extruded micro-pins with diameters of 1.2 and 0.48 mm at meso-scale extrusion [25]. Three different grain sizes of 32, 80 and 200 μm of CuZn30 were used. The ram force was increased by decreasing the grain size, which was in agreement with the Hall-Petch equation [26]. Other investigations include the raw parts, which can be used for wire drawing or micro-extrusion if the parts are miniaturized to a certain point [27]. These studies indicate the importance of size effect in micro-extrusion in sub-millimeter pins. Coupled with inhomogeneous deformation of micro parts and location of individual grains effects, the deformation behavior highlights the necessity of investigating the crystallographic orientation, or texture by considering the starting materials, deformation condition and microstructure mechanism. In CG materials, equi-sized grains show different orientations and have a tendency to deform differently, and this could also likely contribute to non-uniform deformation. However, investigation of UFG materials, before and after micro-extrusion, using orientation mapping is needed to identify whether a preferential orientation contributes to the inhomogeneous deformation of micro-extruded parts [6, 28].

2.1.2 Micro deep drawing

As a basic process of manufacturing, deep drawing provides the potential application for the manufacturing of parts with complex shapes. Size effect makes impossible to transfer macro forming technology directly to the micro-forming [29], thus, micro deep drawing draws great attention when the forming parts are minimized. A comparison study of final parts from macro and micro deep drawing of 99.5% Al with punch diameter of 50, 1.0 mm

2: Literature Survey

and thickness of 1.0, 0.02 mm showed that wrinkles on the flange are almost absent on macro samples while very much present in the micro part [27]. A thin sheet low carbon steel sample below 0.2 mm thickness in micro deep drawing, and (or at) the ratio of a relative punch diameter D_p/t (D_p : punch diameter, and t : thickness of sheet metal) ranged from 10 to 100, were investigated under different conditions of blank holder pressure p and drawing ratio $\beta = D_s/D_p$ (D_s : specimen diameter). The results showed that with the overall increase of D_p/t from 10 to 100, the LDR (limiting drawing ratio) was decreased [30]. Similar results were observed for $D_p/t = 40$ and above. The drawing mechanism for $D_p/t = 20$ and below were different comparing to $D_p/t = 40$, and different drawing mechanism was also observed concerning the shape of the drawn cups. In contrast, for $D_p/t = 10$, the drawing process was like for sheet metals. In addition, the geometry similarity law was also studied on the mechanism of thin thickness of 0.05, 0.1 and 0.2 mm. The maximum force P_{exp} was measured. It was also calculated (P_{cal}) based on Hukui's and Yoshida's equation for deep drawing of thin sheets for D_p/t above 40 [30]. When D_p/t was below the value of 20, the effect of the die radius R_d became notable (Table 2-1).

Table 2-1. Experimental and calculated maximum drawing forces

D_p/t	D_p (mm)	P_{exp}/N		P_{cal}/N		P_{exp}/P_{cal}	
		$R_d = 2.5t$	$R_d = 5.0t$	$R_d = 2.5t$	$R_d = 5.0t$	$R_d = 2.5t$	$R_d = 5.0t$
100	10.0	1640	1620	1560	1520	1.05	1.05
50	5.0	767	686	767	725	1.00	0.90
40	4.0	668	618	597	555	1.12	1.11
30	3.0	470	471	426	384	1.10	1.23
20	2.0	274	258	256	214	1.07	121
15	1.5	190	160	171	128	1.11	1.25
10	1.0	111	88.2	85.3	43.1	1.30	2.07

A similar study was also reported by using punch diameter of 28-64 mm and different values D_p/t of 60-3200 and 60-300 [31, 32]. An investigation of thin foils in micro deep drawing experimental work was carried out by reducing thicknesses from 300 to 80 μm with punch diameters of 8 to 1 mm for CuZn37 foils [33]. The experimental work was further compared with Finite Element (FE) analysis to study the effect of parameters on drawability in terms of blank holder gap and friction coefficient. The material flow curve used in the FE models was obtained from the tensile stress-strain up to a maximum true strain of 0.22.

2: Literature Survey

During the micro-forming process, scaling effects do not appear within the process but must be taken into account in all the aspects of the manufacturing process, including the starting materials, characterization and deformation modes.

2.2 Size Effect in Micro-forming

Micro-forming has revolutionized numerous frontier fields by leading to the applications in micro-electro-mechanical system industries [25], however, the production of these parts is largely not by micro-forming; more likely it is by machining, which is wasteful. Comparing to the advantages of conventional forming such as the high production rate, minimization of the waste, and excellent mechanical properties [2, 27], handling of such small pieces within an appropriate time and precision is difficult. Also, the micro-scale technique cannot be analyzed by the same methods that are used to quantify conventional forming due to the size effect. At the micro scale, processes are only characterized by a few grains across the section of the deformed areas, and thus a material cannot be considered as a continuum any more. Large share of volume occupied by an individual grain, together with size and orientation, influences the flow of the material. Therefore, conventional materials properties will no longer be valid for accurate analysis at the micro level. Further, the deformation mechanisms change largely in response to materials when the ratio of grain size to dimension size is comparable. Friction and surface interactions are also predominant in micro-forming. In addition, the forming process is coupled with other physical behaviors, and thermal-mechanical behaviors need to be addressed when scaling the grain size down to the part dimensions. Several groups investigated the size effect by performing tensile tests, hydraulic bulge test and bending tests. Different deformation modes, such as micro-extrusion, and micro deep drawing, on materials with different grain sizes and with different ratio of grain size to geometry have been carried out [22, 23, 30].

Investigations in simulation of micro forming is challenging when the grain size is the same as the size of geometry, especially in the case when very small dimensions are considered in micro-forming. Since the conventional FE-program does not take the size effect into account, it is necessary to establish experimental techniques for investigation of the size effect and to use experimental results in mathematical models for predicting and analyzing the performance of micro-forming processes. Messner et al [24] presented a flow simulation of micro parts in which the scaling effect was taken into account and applied on simple upsetting tests of strain-hardened rods CuZn15 from 4.8 to 1.0 mm in diameter. The size effect could be roughly characterized by the ratio of geometry and grain size, surface topography and the condition of lubrication. The results showed no size

2: Literature Survey

effect in friction for dry condition, but a good agreement for the numerically calculated tool load.

The optical, mechanical and electrical properties of a material are determined by the structure or dimension of an internal feature or overall physical geometry of the material (Fig. 2-1). For metals, the size effect relating to the length scale changes are readily observed and are often exploited for commercial usage. As a result, conventional continuum mechanics are no longer valid when only a grain is presented in the thickness of the materials. In addition, the applied force shows great difference along the thickness when a few grains are presented across the thickness of the material. The reproducibility of mechanical properties is also a difficult problem.

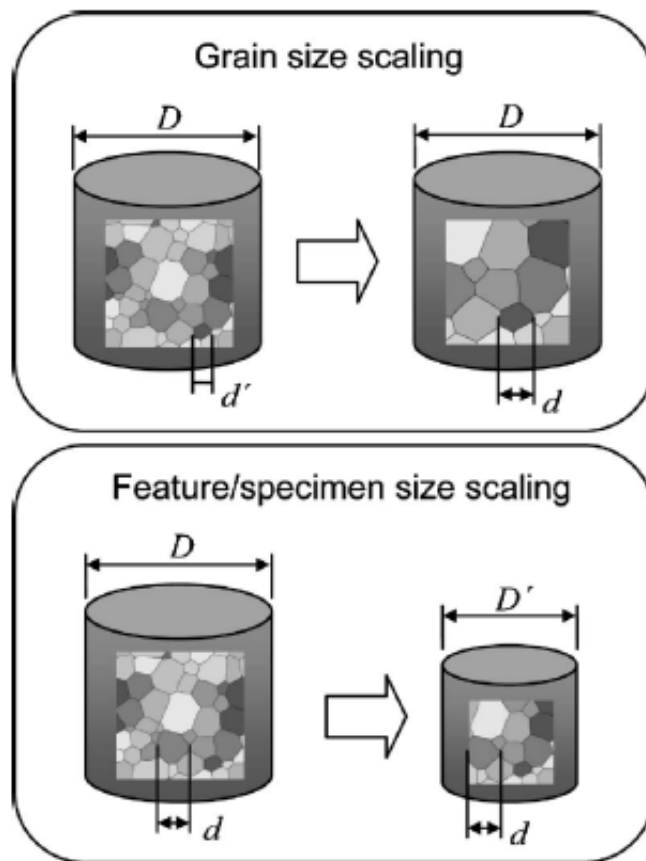


Figure 2-1. Illustration of two types scaling effects: grain size effect and geometry effect

2.2.1 Microstructural effect

Refinement of grain size can improve yield strength. The improvement is in agreement with the Hall-Petch relationship, where the yield strength is proportional to the inverse square root of the average grain diameter. The contribution from the grain interior and

2: Literature Survey

boundary on the overall flow stress can be separated. Large yield strengths can be obtained by reducing the grain size of a material in terms of the propagation of slip from one grain to adjacent grains through the cross-section of the sample. Similar investigations on the structural evolution and the validity of the Hall-Petch relationship were also conducted at micron grain size. Wang et al [34] reported that for an average grain size of $\sim 0.2 \mu\text{m}$ and $0.09 \mu\text{m}$ Al-3%Mg obtained by ECAP and torsion, an increase in micro hardness with decreasing grain size was identified experimentally at $\sim 90 \text{ nm}$. To explain the phenomenon, a pile-up model and a grain boundary dislocation source model [35,36] were introduced. When dislocation piles up behind the grain boundary, the stress concentration at the tip of the slip plane increases and eventually causes neighbor grain to yield.

2.2.2 Geometry effect

The microstructural features and grain size effect are not the same as expected in bulk materials. 'Bulk' material behavior is observed in metals with grain sizes in the order of microns to tens of microns when the thickness of a tensile specimen exceeds about ~ 10 - 15 times the grain size [3, 4, 37, 38]. The size effect on yield stress was first documented in 1977 [18], in which the combined ratio of grain size to sample diameter size for high purity Al was investigated by testing cylindrical samples with a small diameter relative to grain size to observe the stress-strain behavior. The results showed the strengthening for smaller grains is in line with the Hall-Petch relationship [39, 26]. As mentioned previously, a study on the effect of varying the shapes of specimens shows that down scaling the specimen dimensions changes the overall mechanical behaviors, which is called the geometry effect. Geiger et al [40] reported that in upsetting tests on cylindrical billets of CuZn alloys the flow stress dropped by decreasing the diameter. Similar results were obtained by tension of Al, Cu and Cu-13 at. wt.%Al and CuZn alloys [3, 37, 38], bulging of CuZn alloys [4], and bending of Al and CuZn alloys [37, 38], confirming a significant variation in the flow stress by downsizing the billets. Based on the experimental data for tensile tests of brass sheet (CuZn36) with different thickness and grain size, Michel et al [4] proposed a scaling procedure:

$$\sigma_k = K(\varepsilon_0 + \bar{\varepsilon})^n \quad (2-1)$$

$$\bar{\sigma} = \sigma_k F(\lambda, \bar{\varepsilon}) \quad (2-2)$$

$$F(\lambda, \bar{\varepsilon}) = 1 - \exp(-\alpha\lambda + b)(-c\varepsilon + d) \quad (2-3)$$

2: Literature Survey

where the flow stress $\bar{\sigma}$ is related to the equivalent strain $\bar{\varepsilon}$ and a size factor λ (the thickness effect), with a , b , c and d being positive parameters. For a thickness of 0.5 mm of CuZn36 alloy, $K = 718$ Mpa, $\varepsilon_0 = 0.11$ and $n = 0.18$. $F(\lambda, \bar{\varepsilon}) \rightarrow 1$ when $\lambda \rightarrow 0.5$.

Eqs. (2-2) and (2-3) show that the flow stress decreases when λ decreases, and the variation in flow stress decreases when $\bar{\varepsilon}$ increases. For CuZn36 specimen, the reference behavior not showing size effect, that are independent of the flow stress, can be obtained from experimental measurements with large specimen and thick thickness to obtain the parameters K , ε_0 and n . Size effects dependence of flow stress can be obtained by small and thin samples. With this model, size effect has been taken into account for tensile and bulging tests and can be easily integrated in a FE package to simulate the metal forming and found no thickness effect for very thick sheets [4]. However, some studies on grain size effect for thin films show inconsistent results [16], or even opposite results [17], such as for micro-bending test of pure Ni [41] and micro-torsion of pure Cu [42] where it was shown that strength rises by decreasing specimen size. Kim et al [43] proposed a model which quantifies the relationship between the size effect and geometry effect based on tensile testing of sheet metals by introducing two new parameters (α, β) to modify the Hall-Petch equation:

$$\sigma(\varepsilon) = M^\alpha \tau_R(\varepsilon) + K(\varepsilon) \beta d^{-0.5} \quad (2-4)$$

where M is the orientation factor, τ_R is the resolved shear stress, $\beta = 0$ for single crystal, and $\alpha = \beta = 1$ for polycrystal. M can be determined by crystal plasticity modeling. For the grain size of 40 μm , samples with the range of the thickness of 1.0, 0.5 and 0.1 mm were used to evaluate the scaling parameters in Eq. (2-4) (Fig. 2-2). The results showed that α and β increased when n decreased. At the limit of $n = 15$ ($n = D/d$, $D =$ sample size, $d =$ grain size), the size effect may start, and this value corresponds to the case when a significant drop in α and β is observed [18]. Three sets of predicted results reproduced the experimental data very well, validating the scaling in the form given by this model. The limitation of this model is that it is largely empirical and all the variables except for the orientation factor are determined by experimental data.

In addition to theoretical interpretations, the different grain sizes and length scales along with the different trend from the experimental results highlights the need for greater understanding of the specimen size effect by monitoring the mechanical properties over a

2: Literature Survey

range of grain sizes. When investigating the materials strength over a range of grain sizes, the grain and dislocation boundary strengthening mechanisms must be taken into account [44].

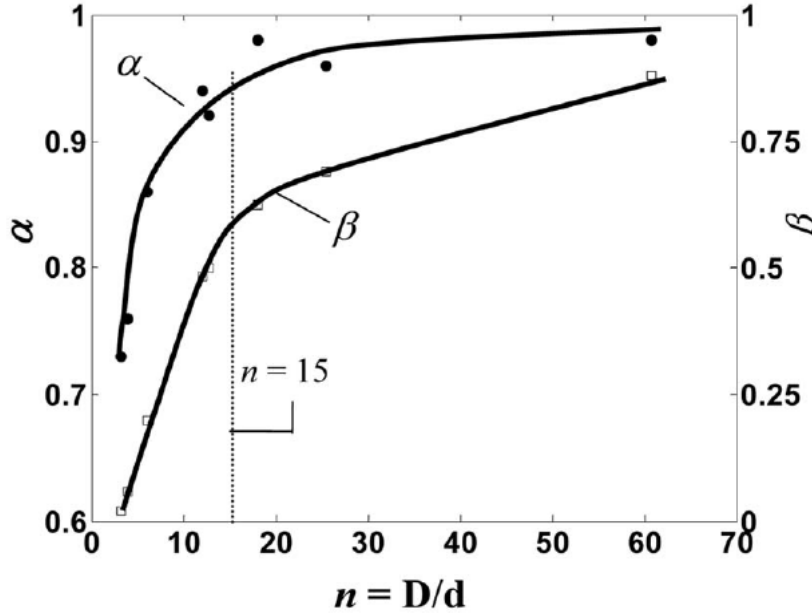


Figure 2-2. Parameters of α and β , and their dependence on $n = D/d$ ($D =$ sample size, $d =$ grain size) [43]

2.2.3 Strain gradient effect

To explain the different phenomenon due to the size and geometry effect, strain gradient plasticity theory [42] has become a significant feature of SPD modeling. A number of gradient plasticity models have been reported [42, 45-47]. The prevailing view in the solid mechanics community is that the influence of strain gradient effects needs to be included in the formulation of the constitutive behavior of materials at the micro-scale. Gradient plasticity theory is based on the Ashby’s concept of geometrically necessary dislocations (GND), which is used in conjunction with the Taylor’s equation:

$$\sigma = M\alpha Gb\sqrt{\rho_T} \tag{2-5}$$

where σ is the flow stress, ρ_T is the total dislocation density, M is the Taylor factor, α is a numerical constant, G is the shear modulus and b is the magnitude of the dislocation’s Burgers vector. In Ashby’s approach the total dislocation density can be represented as the sum of the GND density ρ_G and the statistically stored dislocation

2: Literature Survey

density ρ_s , the latter considered to be more or less randomly distributed. ρ_G is important to maintain strain compatibility across the material. Usually small geometry specimen displays a greater strain gradient hardening due to the accumulation of GNDs. Size dependence appears at a scale of a micron to tens of microns. At a scale of non-homogeneous deformation, this so-called strain gradient effect is mainly due to the appearance of lattice curvature which has to be accommodated by GNDs. Other approaches including both first-order and second-order gradient terms [48, 49] were applied to simulate highly non-uniform deformation processes in terms of microstructural characteristics of materials. However, strain-gradient effects on the mechanical behaviors are ruled out when deformation is macroscopically homogeneous. For nanomaterials, however, the observed strain rate sensitivity plays an important role in the plasticity of the material [50] and the idea that the observed rate sensitivity of stress can be explained in terms of thermally assisted activation of Frank-Read sources in grain boundaries is not supported by the available experimental data. Further studies into the mechanisms underlying strain rate sensitivity of the flow stress are needed.

2.2.4 Boundary, surface and grain statistics effect

Grain refinement leads to an increase in strength due to the increase in the number of grain boundaries and dislocation boundaries. The effect of grain boundaries during SPD of metals varies the properties of UFG materials significantly depending on the regimes and routes of processing. The grain boundaries can be high or low angle boundaries. For thin film/small structures, the physical boundaries - a dimensional constraint - are close to the sample surfaces, and the dimensional constraint plays a similar role as the microstructural constraints. Grains in the surface region have a different deformation behavior than grains within the volume of the material. It is because the "surface grain" is less constrained during deformation by the neighboring grains thus, appears to be weaker. When the thickness of the specimen decreases, the fraction of grains with a free surface increases and the flow stress decreases.

The ratio of the thickness of the sample to the grain size and the volume fraction of grains with a free surface are the parameters that are used to study the free surface effect; they determine the volume fraction of the surface area f with respect to the whole sample:

$$f = 1 - \frac{(w - 2d)(t - 2d)}{wt} \quad (2-6)$$

2: Literature Survey

where w is the width of the sample, d is the grain size and t is the thickness. In the range of thicknesses of hundreds of microns, investigations have been carried out in a certain range of grain size [40, 51]. It was shown that the flow stress decreases by decreasing the specimen thickness when the ratio of specimen thickness to the average grain size is smaller than a critical value. By increasing the grain size and the stacking fault energy, this critical ratio increases. The weakening effect of specimen geometry on copper and copper-aluminium over a range of large grain size has been reported in [3]. The results for both materials followed the trend found by Hansen that the flow stress at 20% strain decreased with decreasing ratio of the thickness on grain size. A comprehensive investigation of the geometry size effect is necessary to fully understand the underlying mechanisms.

2.3 ECAP Technique for Obtaining UFG Materials

As an effective method of fabricating bulk UFG/nano-grained (NG) structures of samples and billets, ECAP has been successful in various metals for refinement through the simple shear deformation of the process. As one of the major severe plastic deformation (SPD) method, ECAP was employed in a large amount of research to produce nano- and submicro-crystalline structures in various metals and alloys [7, 8 11, 52-54]. The grain structure obtained by ECAP is characterized by an average grain size between 250 nm and 1 μm , high angle grain boundaries (60-70% for Al [12], 40-70% for copper [55]), a continuous increase of misorientation across subgrain boundaries [56], and large vacancy concentration [57, 58]. This method also overcomes the difficulties resulted from residual porosity in compacted samples and impurities from ball milling, which are inherent problems in other nanostructured materials processing methods.

The main principle of ECAP is to press a metal billet through an angular channel which introduces intense plastic strain into the material without changing the cross section area of the billet. It is also a repetitive deformation process. The process consists of two die channels of equal cross-section (Fig. 2-3), intersecting at an inner angle of 2θ ($2\theta = 90^\circ$ or 120°) and outer corner angle of ψ . Large shear deformation is produced in the shear zone where the entrance and exit parts of the channel meet. Subsequent ECAP passes, together with the rotation of the billet about the pressing direction between the passes, results in growing accumulation of dislocations, and increases the misorientation angles between subgrains.

2: Literature Survey

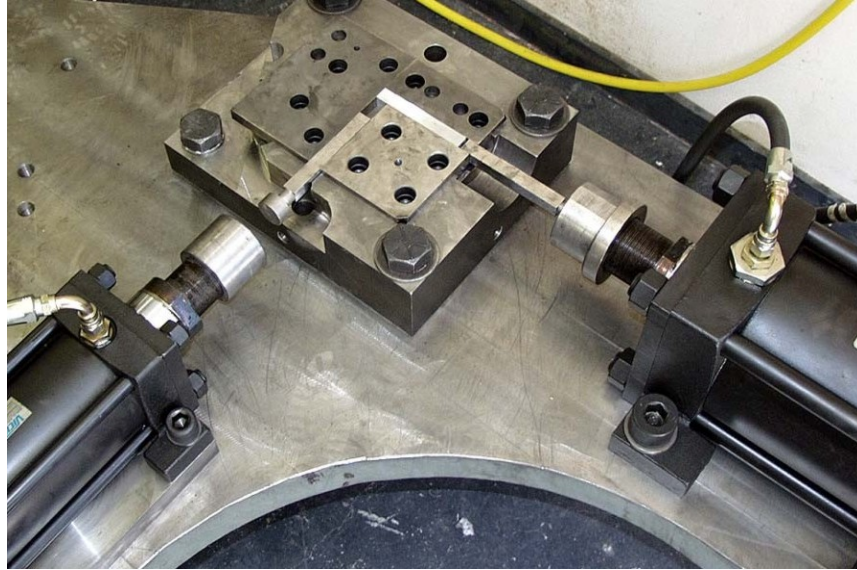


Figure 2-3. ECAP rig at Monash University with a die angle of 90°

ECAP can also be conducted at elevated temperatures for hard-to-deform materials. When the outer angle $\psi = 0^\circ$, (Fig. 2-3) the increment of shear strain in one pass can be calculated from the following relation [8]:

$$\Delta\varepsilon_i = \frac{2}{\sqrt{3}} \times \cot \frac{\phi}{2} \quad (2-7)$$

As the billet can be pressed several times, the total strain value is

$$e_N = N \times \Delta\varepsilon_i \quad (2-8)$$

where N is the number of passes. An equivalent strain of about 1.16 can be achieved for a single pass when the die angle is 90°.

The strain value of the billet during the ECAP process for N passes can be obtained by the following general relationship [8]:

$$e_N = N \left\{ \frac{2 \cot(\Phi/2 + \Psi/2) + \Psi \operatorname{cosec}(\Phi/2 + \Psi/2)}{\sqrt{3}} \right\} \quad (2-9)$$

The ECAP process has been successfully used to produce a variety of metallic materials with UFG or NC microstructures at relatively low melting temperatures. These include pure f.c.c. metals such as Al, Cu, Ni, b.c.c. metals such as Fe, hcp metals such as Ti, and

2: Literature Survey

alloys such as steels and Al alloys [59-66]. During ECAP, the initial large equi-axed grains become elongated and turn into lamellar-type structures or elongated microstructures which are made up of cells and/or sub grains by low angle boundaries together with shear bands. These cells and subgrains develop into a new grain structures with high angle grain boundaries and stabilize to form UFG structures. Consequently, those UFG structures act as hereogeneous nucleation sites for recrystallization of fine grains when the ECAP-ed materials are annealed.

Route A, B_C, B_A and C have been achieved by rotations around the long axis between successive passes amounting to 0°, +90° and ±180°:

- A – no rotation between consecutive pressings;
- B_C – rotation by +90° after each pressing;
- B_A – rotation by ±90° after each pressing;
- C – rotation by 180° after each pressing.

During ECAP, the orientation of the shear plane with respect to the sample varies for each route mentioned above [67]. Furuka et al [68] studied the shape change of a material element for different routes for the case of $\phi = 90^\circ$ and $\psi = 0^\circ$ without taking into account the effect of friction. FE analyses showed that the shape change agrees well in the central part of well lubricated samples where friction is negligible.

The theoretical shear plane is shown in [68] as a shaded plane at the channel intersection, where the X, Y and Z planes define three mutually orthogonal planes. The shape change of a cubic element contained within the sample during the ECAP passage through a die is shown. The planes that are considered are chosen to be perpendicular to the longitudinal axis of the pressed sample and parallel either to the side faces or to the top face of the sample at the point of exit from the die, respectively. The results show that routes have effects on the distortion of the rhombohedron, which comes from the die shear [68]. Following pressings lead to further change of shapes of an analyzed cubic element.

It is known that traditional rolling can also produce fine grained structure. A cellular type structure with low angle boundaries can be obtained by the induced recovery of subgrains when annealing at a low temperature after heavy deformation by cold rolling. Recently, asymmetric rolling (ASR) has attracted much attention due to the capability of producing

2: Literature Survey

UFG structure with high angle boundaries on annealing. Other SPD techniques, such as cyclic extrusion and compression (CEC) [10], accumulated rolling-bonding (ARB) [69], high pressure torsion (HPT) [7], repetitive corrugation and straightening (RCS) [70], multi-directional forging (MDF) [71] and twist extrusion (TE) [72] are also able to produce UFG/NG materials.

2.4 Microstructure, Texture and Thermo-mechanical Behaviors of UFG Materials

The UFG obtained by SPD process refers to grain sizes between 100 nm and 1 μm . Although such grain sizes are slightly beyond the 100 nm limit which is usually used to define NC materials, the SPD materials can be considered to be “nanostructured”. This is because the microstructural features, such as subgrains and domain structures separated by low-angle boundaries, are of the scale of 100 nm and below [63, 73-75]. UFG structure has a non-equilibrium nature and a recovery to an equilibrium structure can be observed by an increase of temperature [76]. Recrystallization happens when increasing temperature to a certain level, which provides thermal energy to nucleate new strain-free grains that subsequently grow to take the entire structure. Recrystallization also reduces the stored energy produced by dislocations and interfaces. For pure copper, dynamic recrystallization occurs when deformed to high strain, such as SPD, and heat treatment can further enable the static recrystallization of the microstructure [77, 78].

Microstructure changes have been investigated for a pure Aluminium with starting grain size of ~ 1 mm and reduced to ~ 4 μm deformed by ECAP, and elongated band structure of subgrains separated by low angle grain boundaries were observed [67]. A gradual decrease in grain size was observed as strain increased, and a band structure was visible after 4 passes and route A. For route Bc, the band structure vanished after 3 passes and was not visible after 4 passes due to the continuous change of the shear plane. Route Bc has been proven to be more efficient in refining the microstructure. The efficiency for microstructure refinement for routes A and C were compared. The result showed that the 180° rotation between each pressing leads to quicker elimination of elongated subgrains, enhances the evolution of low angle subgrain boundaries into high angle grain boundaries, and reaches similar microstructure for both routes after 10 passes. It has been reported that Route Bc is more efficient than route C to develop high angle grain boundaries (HAB) [79] in pure Al. After 8 passes, the fraction of HABs for route Bc was 65% while 38% for route C. The HAB fraction is an important parameter for describing the microstructure of SPD processed materials. It is useful in explanation of ultrafine-grain

2: Literature Survey

formation and can have a dramatic effect on mechanical behavior of the processed materials. For example, different distribution from HAB by introducing the boundary segregations was approved to have an effect to the embrittlement behavior of UFG Ni [80].

Strain path changes usually lead to dramatic changes in texture, and are often influence materials strength, work hardening, plastic anisotropy, formability, grain refinement and fracture. For SPD process, structural properties cannot be completely understood without the knowledge of texture. Most SPD processes involve simple shear, and simple shear texture depend on crystal structures and their ideal components. F.c.c. ideal orientations of simple shear can be described by two partial fibres with $(111) \parallel$ shear plane (SP) (A fiber) and $\langle 110 \rangle \parallel$ shear direction (SD) (B fiber). The A fiber contains the ideal components A_1, A_2, A, \bar{A} , while B fiber contains B, \bar{B}, A, \bar{A} and C (Fig. 2-4). These two fibers are connected at A and \bar{A} orientations in a (111) pole figures. The f.c.c. ideal ECAP components for the $\Phi = 90^\circ$ die angle are listed in Table 2-2 [81].

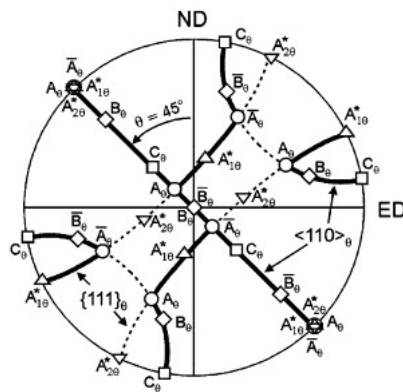


Figure 2-4. Ideal orientations of simple shear in a $\{111\}$ pole figure for f.c.c. metals [81]

Table 2-2. Ideal ECAP orientations and fibers for f.c.c. materials for a $\Phi=90^\circ$ die

Notation	Euler angles ^a (°)			Miller indices ^b			Fibers it belongs to
	φ_1	φ	φ_2	ND	ED	TD	
$A_{1\phi}^*$	80.26/260.26	45	0	$[81\bar{1}]$	$[1\bar{4}4]$	$[011]$	$\{111\}_\phi$
	170.26/350.26	90	45				
$A_{2\phi}^*$	9.74/189.74	45	0	$[1\bar{4}4]$	$[81\bar{1}]$	$[011]$	$\{111\}_\phi$
	99.74/279.74	90	45				
A_ϕ	45	35.26	45	$[914]$	$[111\bar{5}]$	$[\bar{1}12]$	$\{111\}_\phi, \langle 110 \rangle_\phi$
\bar{A}_ϕ	225	35.26	45	$[\bar{1}\bar{1}\bar{1}5]$	$[\bar{9}\bar{1}\bar{4}]$	$[\bar{1}12]$	$\{111\}_\phi, \langle 110 \rangle_\phi$
B_ϕ	45/165/285	54.74	45	$[15411]$	$[726\bar{1}9]$	$[\bar{1}11]$	$\langle 110 \rangle_\phi$
\bar{B}_ϕ	105/225/345	54.74	45	$[\bar{7}\bar{2}\bar{6}19]$	$[\bar{1}\bar{5}\bar{4}\bar{1}\bar{1}]$	$[\bar{1}11]$	$\langle 110 \rangle_\phi$
C_ϕ	135/315	45	0	$[334]$	$[22\bar{3}]$	$[\bar{1}10]$	$\langle 110 \rangle_\phi$
	45/225	90	45				

^a Given in the $\varphi_2 = 0^\circ$ and 45° sections only.

^b Approximate values.

2: Literature Survey

Texture develops even after 1 pass, and crystal orientations normally approach the ideal positions after large plastic strain imposed by ECAP (Fig. 2-4 and Table 2-2). For simple shear texture development, monoclinic symmetry of the texture after 1 pass has been observed in samples when the initial texture was random or had monoclinic symmetry. No monoclinic symmetry will be observed if the initial texture is relatively strong and does not have monoclinic symmetry. Since non-random texture can happen easily for metals containing large-sized (0.1 to 1 mm) grains or metals that experienced pre-processing, initial texture effects can be non-negligible and have to be taken into consideration.

ECAP route and pass number significantly impact texture evolution, and the influence has been studied comprehensively in cubic materials. In route Bc and Ba, the monoclinic symmetry is lost in subsequent passes after one pass. This is because the texture is rotated between passes around an axis which is not a texture-symmetry-axis of the process. The so-called “texture-symmetry-axis” is the TD axis.

Using both ODFs and $\{111\}$ pole figures in neutron diffraction measurements from a 90° die, the texture development for an example of f.c.c. copper was observed [82].

It is apparent that all the ECAP ideal components appear except for a weak $A_{2\phi}$, and the main orientation fibres $f_1 - f_3$ can be identified after 1 pass. In both route A and Bc, the main components change along the passes. Some changes are strong in 1 pass, and disappear with further processing and others remain similar after 8 and 16 passes. Textures of route Bc are difficult to characterize due to the complexity of this route. This has been overcome by [82], in which texture evolution up to 16 passes was well understood and characterized based on the main orientation fibres $f_1 - f_3$ and the changes of these fibres with passes and routes were analyzed in terms of location and variation of orientations.

Deviations from ideal positions are not surprising in ECAP process because these have also been observed in torsion processing. In some cases, the comparison with torsion tests can be only applied when the condition of ideal simple shearing is achieved. Precise measurements of the tilts are only possible in an ODF representation of the texture because the tilts in ECAP textures can be relatively small of a few degrees and depend on the components. Apart from the observed physical tilts, other source of information can be gained from polycrystal modeling. Texture simulated by the viscoplastic self-consistent

2: Literature Survey

(VPSC) models using the simple shear deformation mode leads to more tilts of the texture around the TD axis than the one simulated by the Full Constraints Taylor (FC) model, improving the agreement with measurements [28].

Texture strength is another feature of texture analysis, which is defined as:

$$T = \int [f(g)]^2 dg \quad (2-10)$$

where $f(g)$ is the orientation density function and g is the orientation defined by the Euler angles: $g = (\varphi_1, \Phi, \varphi_2)$. T is usually represented as a function of number of passes and routes. Texture strength is sensitive to local heterogeneities in the measured samples, measurement techniques, areas/volumes scanned, number of measured grains and initial texture. Usually, the strength of ECAP texture does not vary dramatically with the number of passes and routes unless it starts with a strong initial texture. Sometimes it is difficult to find out the meaningful trend because the maximum values of intensity are sensitive to many factors. Also, it is possible that texture evolution can saturate after many passes (after 4 passes to 8 passes) to a steady-state texture which is specific to processing routes. Saturation means that the texture after many passes becomes very similar with the repetition of the deformation path, although grains have to rotate near to a stable orientation during each pass. The apparent stability of the texture is surprising as the texture is always rotated between passes from a nearly stabilized orientation into an unstable position [83].

One of materials properties, i.e. stacking fault energy (SFE), varies in pure metals and can be lowered by alloying. Low SFE f.c.c. materials include gold (45 mJ/m²) and silver (19-22 mJ/m²). High to medium SFE includes Al (167.5 mJ/m²), Ni (128 mJ/m²), and Cu (78 mJ/m²). It has been found that different stacking fault energy results in different torsion textures, and high to medium SFE materials tend to have their slip directions (<110>) aligned with the shear direction leading to strong B fibres. Cross slip, climb, stacking fault formation, subgrain formation, shear banding and twinning are all affected by SFE. Large misorientations across boundaries mostly come from twinning and shear banding. As a consequence, texture changes significantly in two ways: i) a small volume of grains are re-orientated because of the above mentioned mechanism; and ii) boundaries act as barriers to dislocation slip, leading to anisotropic hardening of a grain, change slip activity, and in turn, texture evolution.

2: Literature Survey

To date, the effect of slip is well observed and understood in texture evolution. However, the deformation by both slip and twinning is yet to be understood. Twinning has been observed in SPD processed metals, usually in nano-sized grains or close to regions of concentrated strain, such as shear bands in low stacking fault metals. Further, the texture evolution of SPD metals under low temperature and high deformation rate for promoting twinning is yet systematically analyzed.

Two generic length scales are developed in subgrain microstructure during SPD by ECAP. Shear bands are at the order of 10-100 μm in thickness, and are arranged into cellular pattern in long extended sub boundaries, spanning approximately 0.1-1 μm . Texture evolution is associated with both substructures either directly by reorienting a volume fraction of grains and/or indirectly by creating directional barriers for slips. Different slip systems usually appear when the substructure elements do not deform independently from their neighbourhood. Consequently, the misorientation across sub-boundaries can increase with severe plastic straining. Usually, measured texture intensities are lower than those predicted by polycrystal models and can be explained by lower-scale substructure evolution. Higher-scale deformation bands and shear bands generally influence texture as the misorientation may become high, and both can provide high-angle boundaries which contribute to grain refinement and possible recrystallization. The coupling between the texture and subgrain structure gets stronger at large strains. Texture influences the morphology of the substructure, in turn, substructure affects directional hardening and slip activities and hence grain re-orientation [28].

The effect of strain path changes along ECAP passes on the textures has yet to be determined for different types of initial textures and subgrain morphologies. The strain path change causes the “entry texture” of each pass to be different from that produced at the end of the previous pass. Also, the “entry” microstructure changes from pass to pass. Grain orientation determines the new substructure through the old substructure. Fig. 2-5 shows the schematic progression of substructure development in two representative grain orientations, defined as A and B. The results show that the best grain orientations for grain refinement are those like grain A which promote a transition from planar slip on one plane to another during the process of extrusion [28].

2: Literature Survey

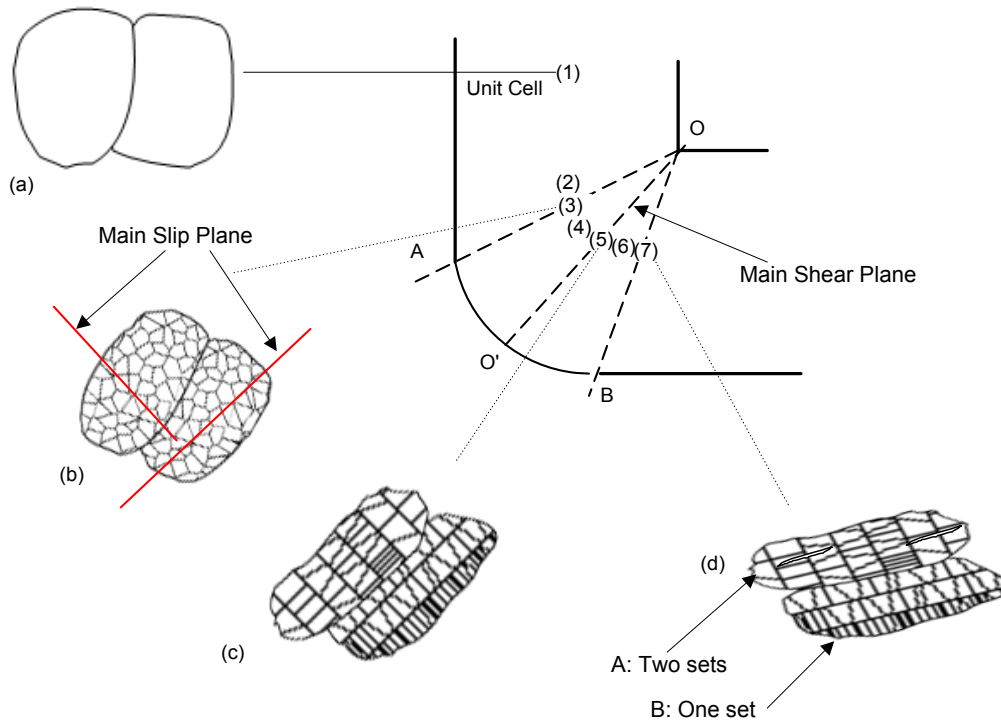


Figure 2-5. A schematic substructure evolution during the first pass of ECAP in (a) two grains with different crystal orientation; (b) both of which form cellular substructures early in the extrusion, but before they approach the intersection plane; (c) grain 1 has formed lamina sub boundaries not aligned with the main plane of simple shear, whereas grain 2 has formed lamella sub boundaries closely aligned with it; and (d) after passing through the deformation zone, both grains form sub boundaries on slip planes aligned closely with the intersection plane [28].

Another texture-related deformation mechanism which can aid grain refinement is twinning. Introducing highly misoriented twin boundaries and reorienting parts of the crystal favourable for slip cause grain refinement by twinning, therefore promoting slip-induced deformation microstructures [28]. With this in mind, it is found that the initial textures and strain path changes that place grains near to orientations that promote twinning – like A^*_1 in silver [84] play an important role in the grain refinement process.

Texture evolution during ECAP at elevated temperature effect has yet to be studied for cubic metals. Texture development slows down at higher temperatures as less dislocation slip is needed due to diffusion processes, and climbing are more important, which does not change orientation. Nonetheless, it should be emphasized that to achieve better grain refinement, lower processing temperature is recommended. The higher thermal energy enables dislocations to participate in plastic relaxation. This promotes the development of

2: Literature Survey

stress-free, low-energy and high angle boundary dislocation structure, and eventually forming large subgrains. Higher temperature can promote the dynamic recrystallization process which is operated by grain boundary motion and leads to even larger grain sizes in ECAP compared to lower temperature ECAP.

UFG metals are not without their own challenges. It is widely known that UFG materials show a high tensile strength, but this is accompanied by low ductility [63, 75, 85-87]. For instance, Valiev et al. [88] reported that the yield strength of UFG copper with a mean subgrain size of ~100 nm is six-times higher than its coarse grained counterpart, but that the ductility is ~5%. The low ductility, which is attributed to the absence of work hardening due to the exhaustion of dislocation accumulation [64], has restricted the commercialization of UFG materials.

Two criteria, i.e., necking instability and crack nucleation, have been used to explain the reduced ductility. Necking begins at the maximum load during tensile testing and the amount of uniform elongation depends on the strain, or the work hardening rate Θ which is defined as:

$$\Theta = \frac{1}{\sigma} \left(\frac{\partial \sigma}{\partial \varepsilon} \right)_{\dot{\varepsilon}} \quad (2-11)$$

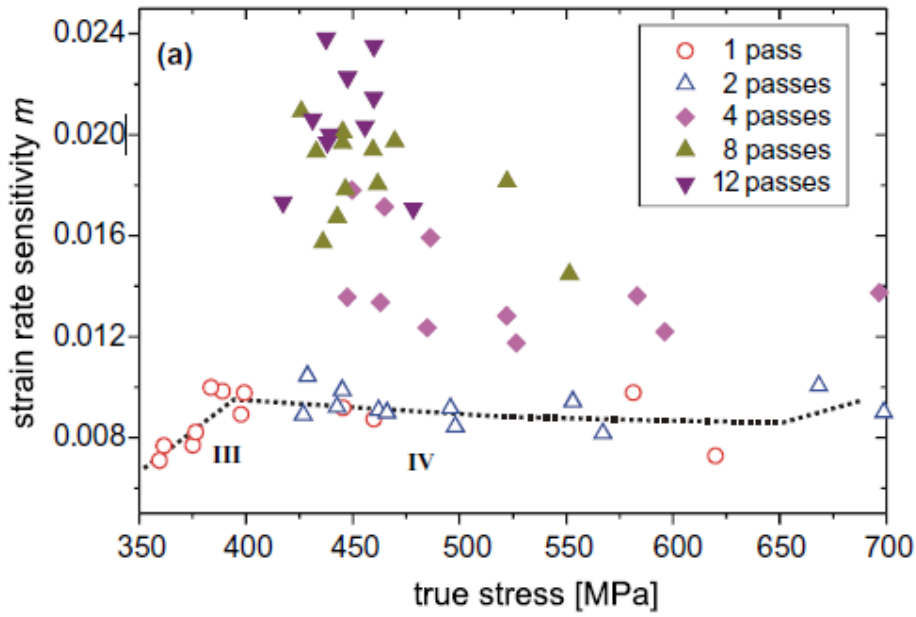
where σ is the true stress, $\dot{\varepsilon}$ is the strain rate, and ε is the true strain. Plastic instability is reached when $\Theta \leq 1$ for materials with low strain rate sensitivity. Insufficient strain hardening ability observed in NC metals would mainly lead to the onset of early necking, reducing homogeneous plastic deformation. Also, the mechanical behaviors are different at different strain rates. The strain rate sensitivity m (SRS) is defined as:

$$m = \left(\frac{\partial \ln \sigma}{\partial \ln \dot{\varepsilon}} \right)_{\varepsilon} \quad (2-12)$$

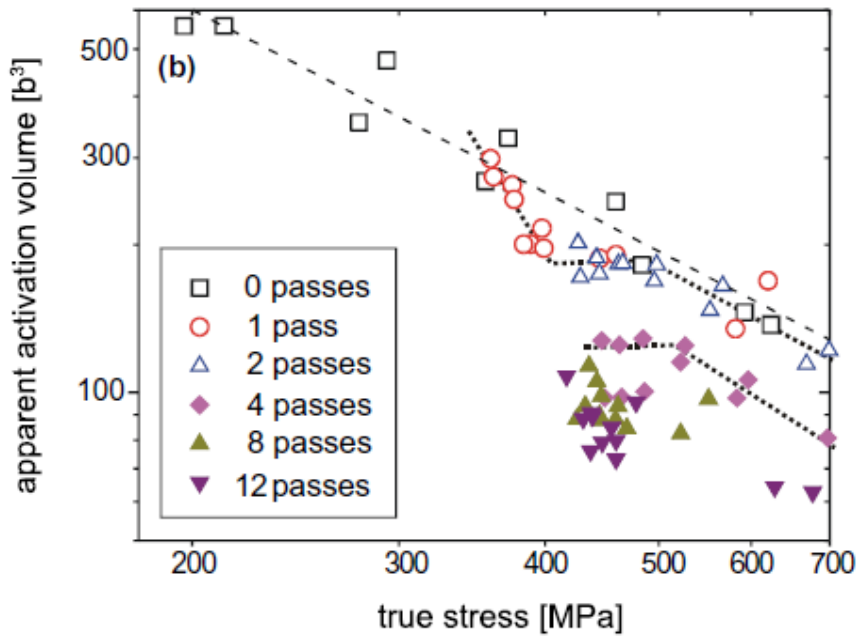
Kocks [89] demonstrated that m increases dramatically when the strain rates exceed $\sim 10^3$ /s in copper and other metals of f.c.c. structure. Dalla Torre et al [90] measured ECAP-ed copper and demonstrates that an increase in m with increasing number of passes and a decrease in apparent activation volume for copper processed by one to twelve passes ECAP (Fig. 2-6). Wei et al [91] studied m as a function of grain size for b.c.c. metals. (Fig. 2-7) shows results obtained for Fe prepared by ball milling and consolidation (Fig. 2-7). Some data are consistent but the uncertainties of unusually low

2: Literature Survey

m values need to be investigated. For f.c.c. metals, refined grain size down into UFG/NC regimes results in elevated SRS.



(a)



(b)

Figure 2-6. Strain rate sensitivity (a) and apparent activation volume (b) as a function of the true stress for specimens subjected to 1,2,4,8 and 12 passes. (b) is plotted in logarithmic scale [90].

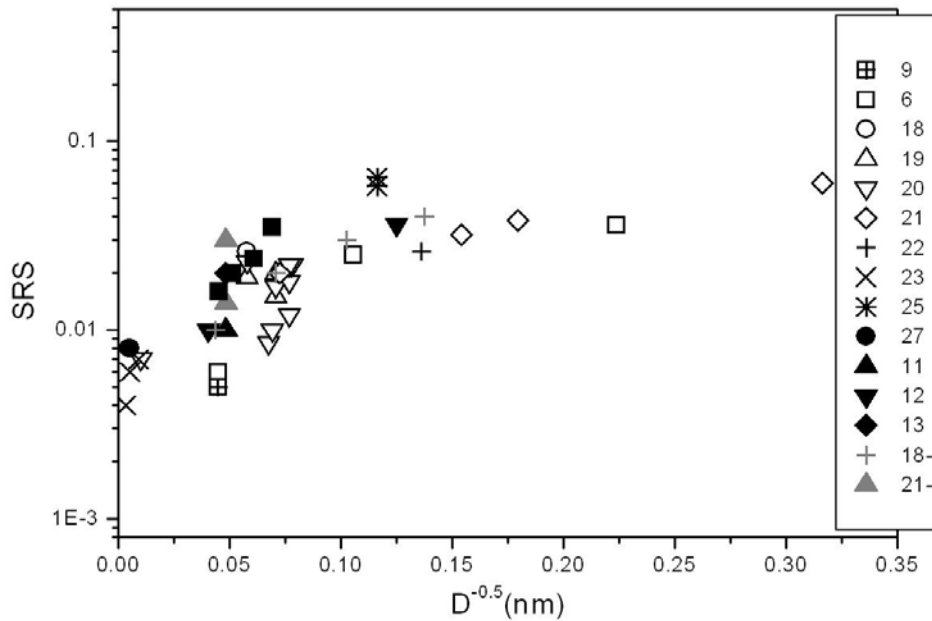


Figure 2-7. Strain rate sensitivity m as a function of grain size for some b.c.c. metals as a function of grain size. 9 [92]; 6 [93]; 18[94]; 19[91]; 20[90]; 21[95]; 22[96]; 23[89]; 25[97]; 27[98]; 11[99]; 12,13, 18[100]; 21[101].

Recently, development of new strategies for improving ductility has received great attention. For example, 95% cryodrawing of ECAP-ed copper followed by cryorolling to 96%, results in a tensile strength of 500 MPa, which is significantly higher than that of coarse-grained copper and 18% higher than that of ECAP-ed copper [23]. However, the uniform elongation (3.7%) is only slightly higher than of ECAP-ed copper (3.5%) [102]. A similar study shows that the tensile strength and strain to failure of 93% cryorolled copper (490 MPa, 18%) is higher than those in 95% cold rolled copper (400 MPa, 10%) [103]. Alternatively, cold rolling copper followed by high pressure torsion increases the high angle boundary fraction [104]. In contrast, the decrease of the dislocation density has little effect on the tensile strength of ~420 MPa, but improves uniform elongation and elongation to failure. Further, annealing cryorolled copper at 200°C for three minutes is reported for achieving high strength/ductility (UTS: 400 MPa; strain to failure: 60%) [103] because of a bimodal grain structure which arises from non-uniform coarsening [105, 106]. However, the mechanism of microstructure evolution is yet to be fully understood, and thus it is of interest to investigate the role of microstructural refinement, texture evolution and the distribution of boundary misorientation angles [107]. The large non-uniform plastic deformation (post necking elongation) is explained by the strain gradient plasticity theory [42, 45-47, 108]. The theory predicts significant strain hardening owing to

2: Literature Survey

an excessively large number of geometrically necessary dislocations that are forced to exist to accommodate the large strain gradient. Twinning is observed in the larger annealed grains, although twins have already been presented because of annealing.

An interesting and important issue in these studies is the observed twinning as a deformation mechanism. An important question is how twinning is nucleated in UFG materials? It has been found that twinning is nucleated by the high stresses caused by the small surrounded UFG grains. The role of twins in the deformation behavior of nano-scale microstructure has also been highlighted as a strengthening mechanism [109, 110], and the predictions of grain boundary engineering via twins have shown the deformation of twins during the annealing of severely deformed UFG metals and alloys [111-113].

2.5 Grain Fragmentation for Obtaining UFG Materials

Grain refinement by plastic deformation provides a potential solution for improving the mechanical properties of metallic materials. In recent investigations, extreme grain refinement down to micron and sub-micron range by SPD has been reported. The surveys of the research work in this area can be found in [12, 114]. While experimental work in this area has produced a significant body of knowledge with regard to microstructures and properties of SPD processed materials, the mechanisms for grain refinement which is crucial for the property improvement are far from being unraveled. Previous work on SPD induced microstructures [9, 115] suggests that a dislocation cell structure formed within a grain be considered as a precursor of the eventual grain structure. Estrin et al [116] quantified the notion (Eqs. (2-13) and (2-14)) that fine granularity is attained through gradual accumulation of misorientations across the dislocation cell boundaries with progressing straining.

$$\frac{d\theta}{d\gamma} = \frac{\chi}{2} \frac{1}{\theta} \quad (2-13)$$

$$\chi = 6\beta^* \xi \frac{b}{d} \frac{(1-f)^{2/3}}{f} \quad (2-14)$$

where γ is the plastic shear rate in the cell interior, d denotes the average dislocation cell size evolving during straining which is related to the total dislocation density, f the volume fraction of cell walls that decreases with strain and β^* a numerical constant. It should be noted that d and f are variables [117,118], which need to be considered in

2: Literature Survey

integrating Eq. (2-13). The average dislocation cell size d is related to the total dislocation density that is comprised by the densities of dislocations in the cell walls and cell interiors. The calculations of the increase of dislocation cell misorientations are consistent with the observed level of misorientations associated with the incidental grain boundaries (in the terminology of Pantleon and Hansen [119]), but cannot account for the occurrence of a very significant fraction of large-angle grain boundaries found experimentally, e.g. for ECAP.

In modeling of SPD process, the existing models based on dislocation density evolution [98, 117, 118] can account for strain hardening associated with SPD. However, there still is a need of accurate modeling for the process of grain refinement and the concomitant evolution of misorientations between neighboring grains. This also means that texture simulation of SPD needs to be addressed in a more rigorous way.

The existing attempts for understanding grain refinement have focused on the effects of the initial orientations of a grain and its neighbors as well as the effects of the deformation field itself. Barnett and Montheillet [120] and Raabe et al [121] used the asymmetric convergent/divergent nature of the rotation field in orientation space for simulation of the development of high angle grain boundaries from slightly disoriented single crystals. Actually, near ideal orientations in simple shear there always is a divergent region in which orientations that are initially near to each other will be drifted rapidly far away in orientation space during straining. In this way, the misorientation of adjacent grains increases converting them into grains with large angle grain boundaries. This mechanism, however, is expected to operate only under simple shear and for a limited population of grains. Other grains, however, with orientations situating in convergent part of the rotation field should decrease their misorientations with adjacent grains of similar orientations which is in contradiction with experimental observations. Raabe et al. [122] carried out finite element simulation, finding that grain refinement is much more dependent on the initial orientation of the grain than on the orientations of its neighboring grains.

To date, the gradual change of the grain population due to grain subdivision is not included in the simulation [28], so that an essential feature of the process is disregarded. The present research uses a model that does account for grain subdivision in considering microstructure evolution, including grain size and local misorientation distributions, overall texture and strain hardening. A main ingredient of the model, namely grain subdivision is treated as a result of the development of lattice curvature within an individual grain and constraints imposed by its neighborhood. The geometrically necessary dislocations

2: Literature Survey

associated with the lattice curvature are considered to give rise to grain subdivision. The methodology will be described in Chapter 3. This element of modeling is shown to give more than satisfactory predictions of all major features of microstructure and texture evolution, as well as the strain hardening behavior of SPD processed copper. Except for hardening, the present thesis examines texture evolution, grain size development and misorientation distribution.

2.6 Summary

The literature review shows that there is an increasing activity in the research of micro-forming, driven by the industrial demand for miniaturization and also by the scientific curiosity. This research has three major ingredients: i) deformation processing; ii) production of suitable starting material; and iii) study of the properties of the obtained products.

The deformation processing by micro-forming presents several new challenges of which some aspects have already been studied. In particular, the ratio of surface grains with respect to the bulk grains plays an important role in the mechanical behavior. The grain size itself is an important variable. Significant advances have been made in this direction by both modeling and experiments. However, the forming of micro parts requires the knowledge of the deformation field, and there has been very limited research conducted in these areas. One example is the plastic flow in micro extrusion, and thus an analytic modeling will be studied in the present work.

Concerning the starting material, very fine grained material is needed for parts obtained by micro-forming. This is why it is important to use an appropriate production route for producing bulk fine-grained structured materials. One of the most promising techniques for this purpose has been presented and discussed - ECAP process – which produces such materials by severe plastic deformation. In this field, modeling work was also conducted in order to uncover and understand the process that leads to the fragmentation of grains. These models, however, are far from completeness. As each model captures only partial elements of the process, rather than the whole, this thesis presents a thorough study on the grain fragmentation process, and provides extensive experimental data and application of the new model.

Finally, it is important to study the properties of the obtained micro-parts. One important physical parameter is the crystallographic texture of the deformed material. There is very

2: Literature Survey

little research in this field. The present thesis contributes to this field not only by experiments, but also by sophisticated grain fragmentation modeling as well. Also, the thermal stability during further processing is main concern in application of UFG materials. The stored energy and thermal stability of micro-extruded UFG copper were compared to CG copper as entry materials to validate the substantial refinement with respect to the micro-forming process.

RESEARCH QUESTIONS

The disciplines of micro-forming and SPD metals have been developing separately so far. However, taking into account the problems, such as the surface effect, friction effect and repeatability of micro-formed components associated with scaling down parts' dimension, the use of UFG metals in micro-forming seems to be a natural choice.

To understand the aspects of UFG characterization, we must first explore the role of grain refinement in UFG materials behaviors, such as: Does the texture development play a key role in the obtained average grain sizes? What is the role in grain refinement of the processing route itself during micro-forming? Can these two issues be explained on a single theoretical basis? The basic hypothesis of the grain refinement modeling presented in this thesis is that the lattice rotation induces lattice curvature which controls the grain refinement process. It is assumed that lattice rotation is a decisive factor of the rate of grain refinement process. The grain refinement changes very significantly the orientation of a subgrain with respect to the parent grain, and thus affects the evolution of the distribution of the crystallographic texture as well as its intensity.

If all what presented above is true, we should see that the crystallographic texture is an important ingredient of the behavior of the micro-formed part. This conditions the use of such components in commercial applications, because formability is strongly related to the evolution of the texture. During micro deep drawing, through-thickness variations in the texture are found by both simulation and experiments. Such variations are important in cup forming if the grain size is very small. We must investigate also the thermal mechanical behaviors of UFG materials because thermal stability during further processing is also one of main concerns for applications of UFG materials in micro-forming. The thermal stability has been shown to be improved in UFG copper during high speed micro-extrusion.

3

**EXPERIMENTAL PROCEDURES
AND MODELING METHODOLOGY**

3. EXPERIMENTAL PROCEDURES AND MODELING METHODOLOGY

This Chapter discussed the experimental procedures utilised for grain fragmentation and micro-forming processes as well as the employed grain refinement model. The methodology for micro-forming adopted for the data analysis obtained from electron backscatter diffraction (EBSD), X-ray diffraction, uniaxial tensile test, nano-indentation and differential scanning calorimetry (Fig. 3-1).

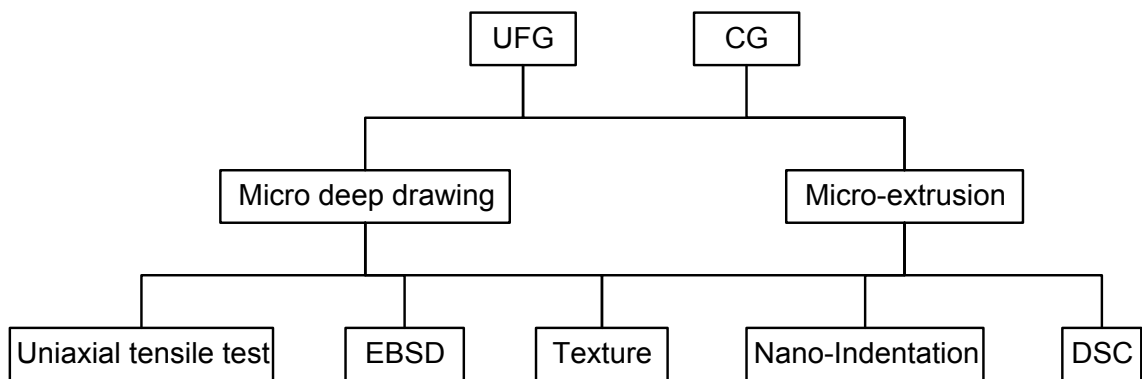


Figure 3-1. Schematic diagram illustrating the main experimental and analytical procedures

The material used in this project was oxygen free high conductivity (OFHC) copper which was prepared for the testing by the following treatments:

- OFHC copper was homogenized at 650°C for 2 hours under N₂ atmosphere, resulting in an equiaxed grain structure with a mean grain size of ~24 μm (CG);
- CG copper samples were processed by ECAP for 1, 2, 4, 8 and 16 passes, route Bc; and for 1, 2 and 3 passes, route A to produce UFG material.

The processing routes for the starting materials (UFG and CG) are shown in Table 3-1.

Table 3-1. Starting materials used in the refinement study and micro-forming

	ECAP A	ECAP Bc	CG
	Refinement	1, 2, 3	cold rolling
Micro-forming methods	Micro deep drawing	1, 4, 8, 16	as-received
	Micro-extrusion	8	as-received

3.1 Deformation Processing

The first step in the processing route was ECAP. Billets of the CG samples were machined to 20 mm square cross section and 120 mm length and placed into an ECAP die, within which three inserts were arranged to form an L-shaped channel (Fig. 2-3). Experiments were conducted at room temperature (RT) at $\Phi=90^\circ$ (Fig. 3-2) via route A (no rotation) and Bc (90° rotation around the billet's longitudinal axis between each pass). A back pressure of 25 MPa was applied and the forward speed was 2 mms^{-1} . The equivalent strain in one pass was ~ 1.15 . The die channel and billets were lubricated using graphite sprays then MoS_2 coating in order to reduce friction. The billets were subjected to up to 16 passes in route Bc and 3 passes in route A. The samples were ground back to their original sizes between each successive pass using water soluble oils as a lubricant and cooling medium (this operation was needed because the sample dimensions slightly increased due to hardening of the sample which produced a 'springback'). The coordinate system of ECAP is defined by the extrusion direction (ED), normal direction (ND), and transverse direction (TD), see Fig. 3-2.

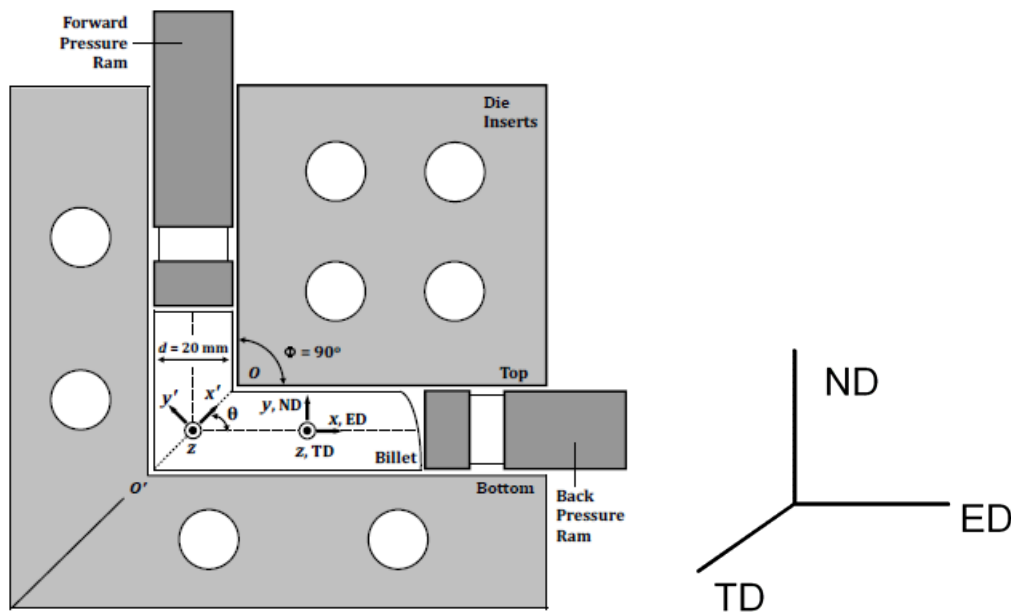


Figure 3-2. Schematic drawing of ECAP die

Cold rolling of CG copper with an initial thickness of 2.0 mm at room temperature was performed up to a true strain of ~ 1.06 and 2.12 (thickness reduction of 60% and 84%) in a rolling mill with roll diameter of 72 mm.

3: Experimental Procedures and Modeling Methodology

A small-scale Swift (flat-bottom) cup test was used to examine the drawability of the UFG material. UFG specimens were obtained from ECAP, route Bc, 1, 4, 8, 12 and 16 passes and cut from the ND-TD plane. A mini Swift test device was constructed with a 6 mm diameter punch, and round discs of diameters 9.6, 11.48, 13.16 and 14.6 mm. The obtained discs had been ground and polished to a required thickness of 0.4 mm (Fig. 3-3). Using the mini Swift test, the limiting drawing ratio (LDR), which is defined as the ratio of the largest blank diameter drawn without failure to the punch diameter, was determined for the ECAP processed copper. CG copper was mini-Swift tested under the same conditions for comparison.

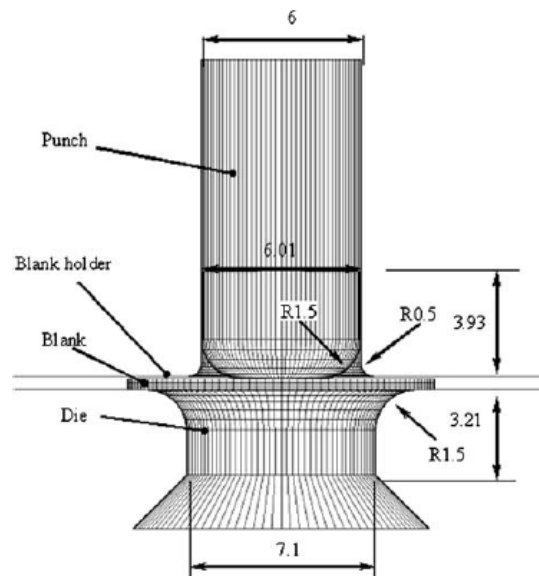


Figure 3-3. Testing configuration for deep drawing and FE simulation (dimensions are in mm)

For micro-extrusion, UFG specimens obtained from ECAP, route Bc and 8 passes were cut from the center of the ND-ED plane of the sample and were extruded through a conical die (Fig. 3-4) at four different speeds of 0.1, 1, 10 and 25 mm/min using a micro-extrusion device (billet diameter D_0 of 2 mm, extrudate diameter D_f of 0.5 mm and a homogeneous logarithmic strain of 2.77) in an Instron 5500R. After micro-extrusion, the samples were stored in a conventional freezer until further testing. Billets with CG structure were extruded under the same conditions for comparison.

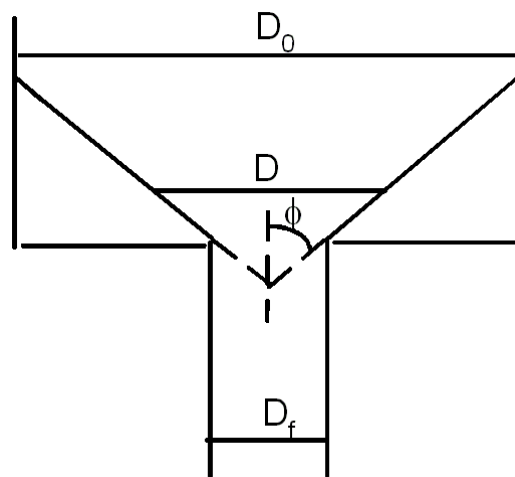
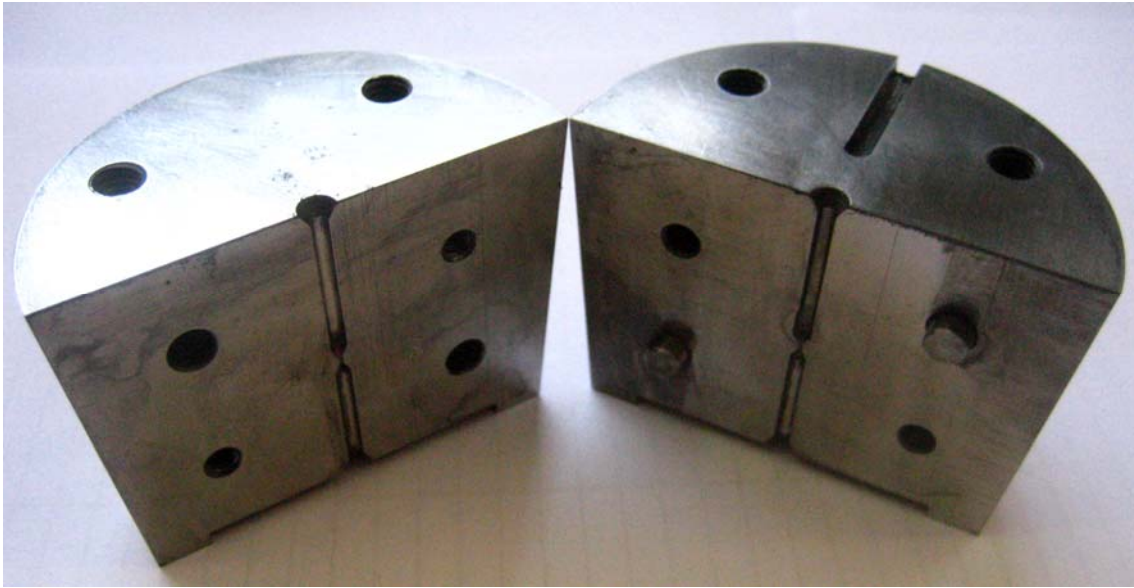


Figure 3-4. Schematic diagram of the extrusion die (D : contained diameter, ϕ is 60°)

3.2 Sample Characterization

3.2.1 Electron backscatter diffraction

A Scanning Electron Microscope (SEM) equipped with a backscatter diffraction camera was used in experimental operation of EBSD. A flat and well prepared crystalline specimen was inserted into the specimen chamber with a high tilt ($\sim 70^\circ$ from horizontal) towards the diffraction camera. The main effect of tilting the specimen is to reduce the path length of electrons which have been backscattered by the lattice plane when they enter into the samples, thus allowing a far greater proportion of electrons to undergo diffraction and contribute to the measurement intensity. The diffracted electrons produce a diffraction pattern, sometimes called an Electron Backscatter Pattern (EBSP), which often shows Kikuchi bands, provided that the surface material (top ~ 20 - 100 nm) is suitably crystalline. A suitable EBSD pattern is generated in a SEM by the following steps [83]:

3: Experimental Procedures and Modeling Methodology

- i) Tilt the specimen so that its surface makes an angle $\sim 70^\circ$ with the horizontal;
- ii) Turn off the scan coils to obtain a stationary beam;
- iii) Place a recording medium or device in the front of the tilted specimen to capture the diffraction pattern.

The EBSD scan in the following Chapters were performed on a Jeol 70001F field emission gun (FEG) and Leo 1530 FEG SEM equipped with Nordlys II detector and data were collected and analysed using HKL Channel 5 software. The deformed specimen (Chapter 4) was examined by EBSD on three different sections, ED, TD and ND (respectively: extrusion, transverse and normal direction) of the billet. A specimen was cut from the middle part of the sample and mechanically polished to 4000 grit by using SiC paper, and then electropolished for 20 seconds in an electrolyte of 25 pct orthophosphoric acid, 25 pct ethanol and 50 pct distilled water at 10V, 20°C with a current of ~ 150 mA. The step size was 0.2 μm . In order to have representative data, three or four maps 80 μm x 80 μm in size were measured for each plane.

The three-pass ECAP sample (Chapter 4) with dimensions of 100 mm x 10 mm x 10 mm was deformed using the ECAP rig at Metz University at room temperature with a cross-head speed of 1 mm/s in route A. The initial grain size was 18 μm and the texture was nearly random. Annealing twins were also present in the undeformed sample. For EBSD, specimens were prepared from the middle part of the ECAP-ed sample on the ED and TD planes. They were first mechanically ground on wet SiC paper (grit 220–2400) with Struers LaboPol-21 followed by electropolishing using Struers Lectropol-5 at 15°C with electrolyte D2 at a polishing voltage of 24 V. The electropolishing was conducted twice for 20 s each time. The EBSD measurements were carried out on a LEO 1530 scanning electron microscope equipped with a field emission gun. Automated orientation analyses of the Kikuchi patterns were performed with the CHANNEL 5 software package produced by HKL Technology. The map sizes were 80 μm x 100 μm on the TD and 80 μm x 110 μm on the ED plane.

Following micro-extrusion (Chapter 6), the samples for EBSD were cut from the centre of the extruded specimen and parallel to the longitudinal direction of extrusion with dimensions of diameter of 0.5 mm and length of 10 mm. The ECAP-ed plus extruded sample was cut along the ED – ND plane with ND being the normal direction in the ECAP testing. Another region was explored for the sample with the speed of 1 mm/s. at an intermediate position on the samples at about 0.3 mm from the centre for texture analysis.

3: Experimental Procedures and Modeling Methodology

Grains in the measured orientation maps were coloured according to inverse pole figures corresponding to the sample axis perpendicular to the plane of investigation. Grain boundaries were identified using a 5° criterion. Such criterion was chosen to avoid the detection of dislocation cells and really detect only the grain boundary. Three or more maps that covered at least 300 grains in total were measured for each UFG and CG extrudates. The raw EBSD data were processed by orientation averaging using the HKL software (Channel 5) to reduce orientation noise inherent in the data. After noise reduction, the angular resolution was improved to 5° . In determining the mean boundary intercept ($\Delta\theta \geq 5^\circ$) and misorientation (θ), boundaries with misorientation lower than 5° were excluded. Subgrain detection in post-EBSD analysis was performed using the new software of Beausir [123]. In this software, grains were identified first, and then their orientations were assigned as an average of the pixel-orientations composing a grain. Then inverse pole figure maps and misorientation frequency functions were generated from the so-defined grain distributions. The frequency distributions for both grain size and misorientation were normalized to a total integral of 1. This was done in order to avoid the dependence of the obtained frequency value on the adopted size of the intervals within which individual values were collected. For this reason, the calculated frequency distributions are frequency-density distributions meaning that the probability that a value lies in a given interval is equal to the integral of the obtained distribution within the specified interval. Therefore, local values can be larger than 1 (which is normal for density functions).

3.2.2 Textures

Texture analysis in this study was performed on $20 \times 20 \times 3 \text{ mm}^3$ size samples with normal direction ED using a GBC-MMA texture goniometer working at 40 KV and 25 mA equipped with a CuK_α anode and a polycapillary beam enhancer, resulting in a collimated beam of $10 \times 10 \text{ mm}^2$. Raw data in the form of incomplete pole figures (PFs) were measured in the range of $\chi = 0^\circ$ to 80° from the (111), (200) and (220) crystallographic plane reflections and were used to calculate the orientation distribution functions (ODFs) $f(g)$ using the spherical harmonic method without imposing any sample symmetry conditions. The notation $g = (\varphi_1 \Phi \varphi_2)$ refers to grain orientation denoted by the three Euler angles in Bunge's convention. All end-texture PFs and ODFs were subsequently rotated to the TD view and analyzed using the commercial software developed by Resmat Corp. Post processing was performed using procedures written in Matlab. Textures at the bottom flat parts of the cups after drawing described in Chapter 5 were also measured locally in several locations using a texture goniometer with a CoK_α anode in Metz, France.

3: Experimental Procedures and Modeling Methodology

A double pinhole collimator was used to get a 0.5 mm diameter parallel X-ray beam. The goniometer was driven in such a way that the illuminated area on the sample was kept inside a 3 mm diameter circle. After corrections (positions and volume absorption) the pole figure data were treated using the MTEX software [124] to obtain the ODF.

3.2.3 Uniaxial tensile test

A screw-driven universal Instron 4505 testing machine was used for tension testing. The Instron Bluehill software was used as an operating system and for recording data. A data acquisition time of 0.5 s was chosen for each tensile curve, resulting in more than 160 data points per curve. Strain was measured by using an extensometer with a gauge length of 25 mm and maximum travelling length of 12.5 mm. CG copper and UFG copper obtained by ECAP in 1, 4, 8, 12 and 16 passes were examined at room temperature at an operating strain rate of $1.6 \times 10^{-3} \text{ s}^{-1}$. Two tensile tests were performed on each sample condition except for the 16 pass sample, from which only one test could be performed due to the lack of sufficient material. The absolute error originating from the calibration of the load cell and extensometer together with the machine compliance was known to be around 10%. The gauge length and diameter of the tensile specimens were 25 and 4 mm diameter. Fig. 3-5 and Table 3-2 show the changes in the yield and total strength with increasing number of passes. The yield strength increases with number of passes up to 4 passes and shows slight decrease for subsequent passes.

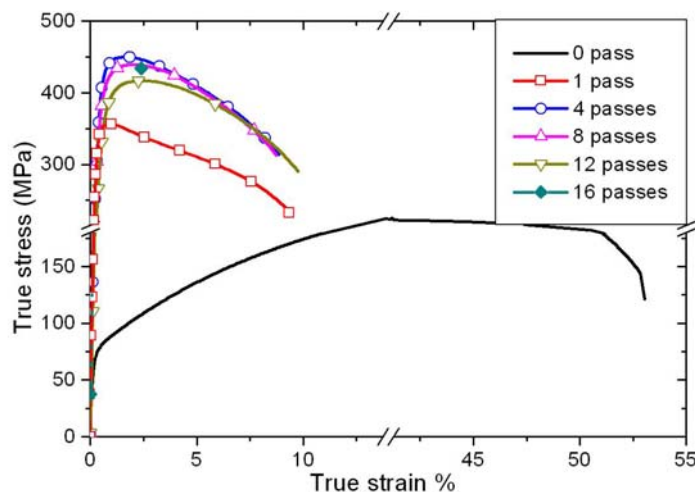


Figure 3-5. True stress-strain curves for copper subjected to different number of ECAP passes, route Bc [19].

3: Experimental Procedures and Modeling Methodology

Table 3-2. Mechanical characteristics for copper after N=0, 1, 4, 8, 12 and 16 passes

Mechanical Characteristics	Number of Passes					
	N=0	N=1	N=4	N=8	N=12	N=16
Yield Strength (0.2%) (MPa)	68±6	342±5	415±4	385±3	348±4	345
UTS (MPa)	332±13	358±2	455±4	449±1	423±8	407
Total elongation [%]	48.5	8.9±0.0	8.2±0.4	8.5±0.1	8.5±1.1	10.0
Uniform elongation [%]	28.7	0.75±0.1	1.6±0.3	2.5±0.1	2.5±0.5	2.2

3.2.4 Nano-indentation

The hardness of both micro-extruded CG and UFG specimens produced at different extrusion speeds was measured at a constant loading rate of 100 $\mu\text{N}/\text{sec}$ using a nano-indentation device (TriboLab, Hysitron Incorporated, USA) equipped with a diamond Berkovich tip. At least 20 indents were performed for each sample. The unloading curves were shifted to the end of the applied loads at the maximum of 5000 μN and fitted with a power law between 20%-80% of the maximum load when Young's modulus calculation was necessary.

3.2.5 Differential scanning calorimetry

Differential scanning calorimetry (DSC) is used to measure the heat release energy as a function of temperature. In DSC, there are two samples: one is the tested sample and another which serves as a reference. Both samples are subjected to identical temperature variations at a constant rate throughout the experiment. A Perkin Elmer DSC7 equipment was used under a constant heating rate of 10 K/min in N_2 atmosphere within a temperature range of 50-300°C. At least two samples were measured, each of weighing between 40-85 mg. The calorimeter was calibrated using standard Zinc and Indium samples prior to measurement. The stored energy and recrystallization temperature of the micro-extruded CG and UFG specimens at different extrusion speeds were determined. A fully recrystallized copper sample was scanned at the same heating rate to provide a baseline reference for each DSC run so that the heat release detected was only from the restoration processes taking place in each sample.

3.2.6 X-ray diffraction for determining micro-strain and dislocation density

A high resolution Phillips 1140 diffractometer operated at 40 KV and 25 mA using $\text{CuK}\alpha 1$ radiation ($\lambda = 0.1540\text{nm}$) was used to collect the X-ray peak data. The dislocation density measured in UFG and CG materials can be obtained from $\rho = 2 / \pi(b \times d)^2$ [125], where b is the Burgers vector (=0.256 nm) and d is the grain size.

3.3 Grain Fragmentation Modeling Based on Lattice Rotation

The grain fragmentation modeling work that was employed in the present thesis has been reported in *Acta Materialia* [20]. The core of this new approach is the concept that grain subdivision is associated with accumulation of lattice curvature during the deformation process. In order to assimilate the basic elements of the model, this section provides the background information about the fundamental issues associated with the physics of grain refinement modeling.

Grain refinement is a very important issue in SPD processes because the over-riding aim of SPD is to produce a very fine grain size. This is why many experimental studies are reported in the literature concerning the characterization of the microstructure and its refinement. Measurements prove that mechanical properties are improved dramatically with grain refinement. Although good progress has been achieved on the experimental side, simulation work is less developed.

The principles of the new grain fragmentation model are presented below. The model is based on the assumption that crystal rotation inherent in plastic deformation (for non-ideal orientations) is not uniform within a grain. In its grain boundary area, the lattice rotation is slowed down as an effect of the grain boundary, which is basically an effect of the neighboring grains. As this modeling is based on crystal rotation, a polycrystal plasticity model is used – the Taylor model – to obtain lattice rotations. In this way, the texture of the material is also taken into account, together with the possible slip systems of the crystal. The model permits us to introduce the initial grain size distribution, and predicts the same after large strain together with the texture development and other microstructure features, like next-neighbor grain misorientation distribution. Using a dislocation based hardening model, hardening can also be predicted together with dislocation densities and cell-wall misorientations (which will not be examined here). This model, however, is relatively simplified. The initial grain shapes are assumed to be cubic and their fragmentation is also of cubic shape. In spite of the simplifications, the model is able to predict several features at the same time.

3.3.1 Model description

3.3.1.1 Lattice distortion

As mentioned above, the basic idea of the model is to consider the distortion of crystallographic planes of a grain embedded in the polycrystal due to its grain boundary. The material is considered to be initially recrystallized, meaning that crystallographic

3: Experimental Procedures and Modeling Methodology

planes are not distorted; they are straight, as illustrated in Fig. 3-6. However, during large strain, crystal orientation is changing (texture development) meaning that the same planes appear in rotated positions. It is reasonable to assume that the rotation of a plane is not uniform within the grain; and the rotation is impeded near the grain boundaries. Two zones can be considered: the central zone of the grain where lattice plane distortion is negligible (because this zone is far from the grain boundary). The other zone is near to the GB where the plane becomes curved, see Fig. 3-6. Lattice distortions that are similar in nature to the one depicted in Fig. 3-6 are frequently observed experimentally [126-128]. One example is shown in Fig. 3-7 [126].

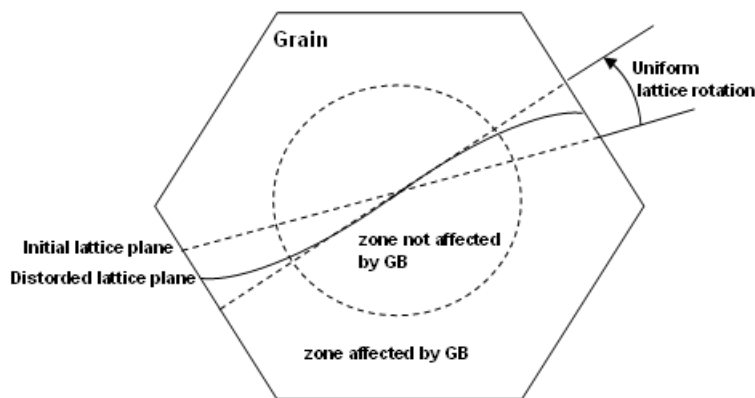


Figure 3-6. Assumed distortion of a lattice plane in a crystal due to its grain boundary

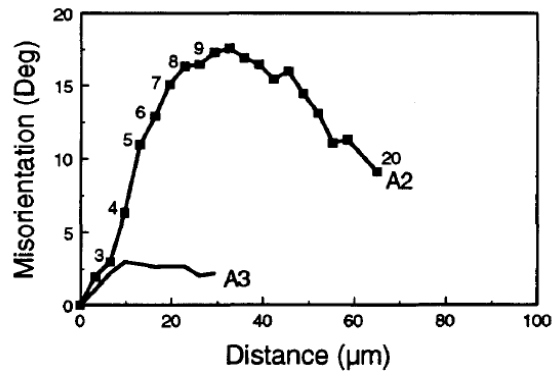


Figure 3-7. Example of lattice curvature showing cumulative misorientation in a grain as moving away from its grain boundary in an Al-Si alloy [126]; A2 and A3 indicate positions for scans.

While it is easy to imagine that a crystallographic plane should become S-shaped when it is looked at from the direction of its lattice rotation vector, in reality, the distortion is more complex because there are several grain boundaries, and their orientation is changing during strain, see Fig. 3-8. This figure shows the lattice rotation vector $\underline{\dot{\Omega}}_G$ as well as the

3: Experimental Procedures and Modeling Methodology

small additional rotation vectors at different locations on the plane. The grain boundaries are considered to remain plane during strain, which comes from the hypothesis of the Taylor deformation mode of the polycrystal. Their orientation is represented by the grain boundary normal vector \underline{n}_{GB} .

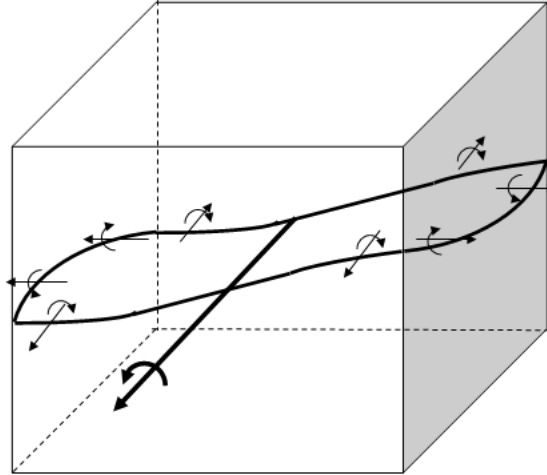


Figure 3-8. Schematic distortion of a crystallographic plane due to its position-dependent rotation in a cube-shaped crystal for the case when the lattice rotation is taking place perpendicular to a grain boundary (large arrow). The small vectors represent the local additional rotations produced by the ‘friction’ effect of the grain boundary.

3.3.1.2 Geometrically necessary dislocations associated with lattice curvature

The variation in curvature of a crystallographic plane is equivalent to a distribution of geometrically necessary dislocations (GNDs). A new GB can appear due to the GNDs if the lattice curvature is sufficiently large. These kinds of GNDs are called ‘curvature induced dislocations’ (CID) in the present grain refinement model. The CIDs are selected from the existing dislocations to build up subgrain boundaries that finally become large angle boundaries forming grains. The local curvature κ on a plane (i.e. in two dimensions), can be related to the dislocation density ρ_{CID} through the relation:

$$\kappa = \frac{1}{R} = \rho_{CID}b \quad (3-1)$$

where R is the radius of curvature and b the length of the Burgers vector [129]. It has been shown that the CID density ρ_{CID} can be measured with the help of EBSD experiments [130]. Some further simple assumptions are necessary to obtain reasonable

3: Experimental Procedures and Modeling Methodology

values for R in order to estimate ρ_{CID} . It is actually assumed that the curvature is constant in the grain boundary region so that locally the plane can be approximated by a sphere of radius R , see Fig. 3-9.

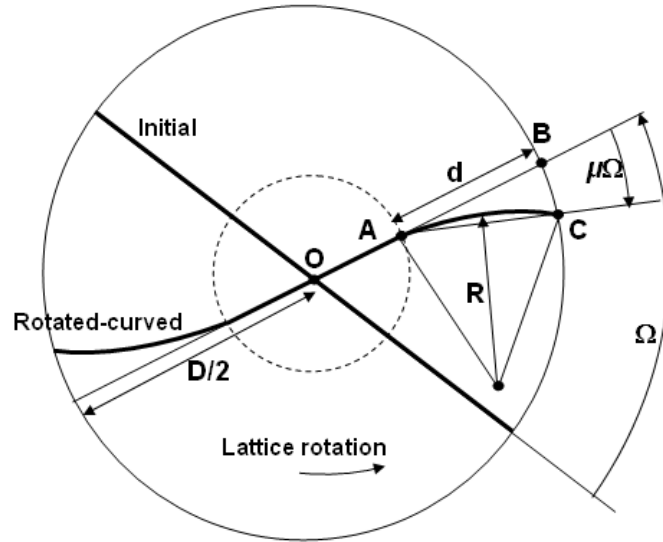


Figure 3-9. Schematic illustration of the parameters of the model

The initial position of a crystallographic plane is shown as a straight line (Fig. 3-9). For the subsequent calculations, a spherical grain shape is assumed with diameter D and with a GB affected zone of thickness d . The geometry of the process results in lattice curvature.

In order to simplify the calculations for R and ρ_{CID} , the diameter D of the grain is divided into three equal size zones; the middle part and two GB regions with equal thickness d leading to $d = D/3$. Observations of deformed microstructures show that this is actually a good working hypothesis: Mishra et al. [131] has found similar sizes for the two zones.

The lattice rotation Ω of the central part of the crystal can be obtained from crystal plasticity (the Taylor model). The retardation effect in rotation of the plane can be expressed by the parameter μ which could be called a 'GB-friction' coefficient and illustrated in Fig. 3-9 as the arc with angle of $\mu\Omega_G$. The value of μ can be varied between 0 and 1. The resultant average rotation of the lattice in the GB region will then be $\Omega - \mu\Omega$. Under these hypotheses one obtains the following formula for the curvature radius:

3: Experimental Procedures and Modeling Methodology

$$R = D \frac{-\cos(\mu\Omega) + \sqrt{\cos^2(\mu\Omega) + 8}}{12 \sin(\mu\Omega)} \quad (3-2)$$

Using this relation in Eq. (3-1), the CID density is determined by:

$$\rho_{CID} = k \frac{12 \sin(\mu\Omega)}{bD \left[-\cos(\mu\Omega) + \sqrt{\cos^2(\mu\Omega) + 8} \right]}, \quad k = 1, 2, \text{ or } 3. \quad (3-3)$$

The coefficient k is introduced here because the GB zone can be in contact with one, two, or three grain boundaries, each assuming to produce the same lattice distortion.

3.3.1.3 Grain fragmentation

Following the assumption that the three zones along a diagonal of the grain have equal sizes, one obtains an image of the ‘Rubik-cube’ for the fragmentation process, see Fig. 3-10.

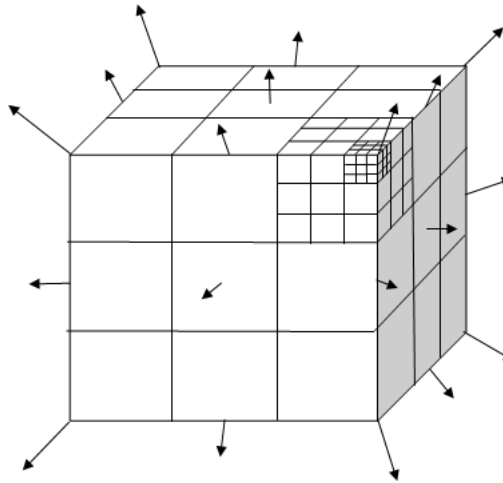


Figure 3-10. The ‘Rubik-cube’ representation of the grain fragmentation process. The fragmentation is continuous in each smaller cube in the same manner; three levels are considered.

The GB normals in the GB zones play an important role as each GB influences the distortion in the concerned GB cube element of the crystal. The resultant distortion-rotation vectors are represented by the vectorial sum of each n_{GB} vectors; they are depicted in Fig. 3-10. There is no extra rotation for the central part while there are different numbers of grain boundary vectors affecting the total distortion at different places in the

3: Experimental Procedures and Modeling Methodology

cube (on the facets or in the corners). Following the above arguments, the rotation of a given subgrain (i.e., a smaller cubic element) is defined by the relationship:

$$\dot{\underline{\Omega}}_{SG} = \dot{\underline{\Omega}}_G + \dot{\underline{\Omega}}_{SG}^{GB} \quad (3-4)$$

One has to also account for the relative position of the lattice spin vector and the so-called resultant GB normal vector. The latter can be defined as:

$$\underline{n}_{GB}^{(res)} = \sum_{i=1}^k \underline{n}_{GB}^{(i)}, \quad k = 1, 2, \text{ or } 3 \quad (3-5)$$

Actually, depending on crystal orientation, the lattice spin vector is not always positioned symmetrically, as depicted in Fig. 3-11.

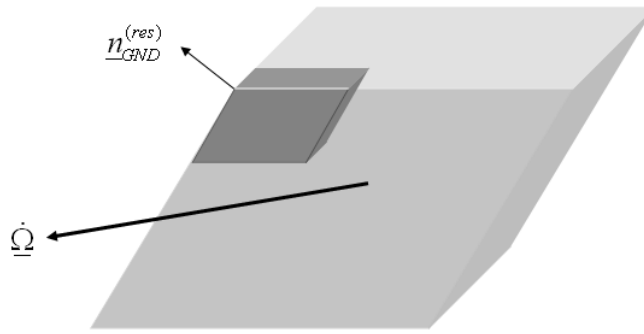


Figure 3-11. Relative position of the lattice rotation rate vector $\dot{\underline{\Omega}}$ and the resultant subgrain boundary normal vector $\underline{n}_{GND}^{(res)}$ in the deformed state.

Fig. 3-11 shows a deformed grain. Due to plastic deformation, the orientations of its grain boundaries change. Knowing the deformation gradient tensor $\underline{F} = \partial \underline{r} / \partial \underline{R}$ during the process, one can update the orientation of the GB using the formula:

$$\underline{n}_{GB_{deformed}}^{(i)} = \underline{F} \underline{n}_{GB_{initial}}^{(i)} \quad (3-6)$$

After updating the GB normals using Eq. (3-6), one obtains the ‘resultant GB vector’ from Eq. (3-5). The angle α between this vector and the lattice rotation rate vector $\dot{\underline{\Omega}}$ can be obtained as:

$$\alpha = \arccos \frac{\dot{\underline{\Omega}}_G \cdot \underline{n}_{GB}^{(res)}}{\left| \dot{\underline{\Omega}}_G \right| \left| \underline{n}_{GB}^{(res)} \right|} \quad (3-7)$$

3: Experimental Procedures and Modeling Methodology

It can be further assumed that when $\alpha = 90^\circ$ the GB retards the lattice rotation with a maximum efficiency. On the contrary, when $\alpha = 0$, there is no impeding effect of the GB. In order to quantify the effect, a simple scaling by a $|\sin \alpha|$ function with respect to the grain rotation rate $\dot{\underline{\Omega}}$ is assumed in the model. Taking into account this last hypothesis, the impeding part of the lattice rotation rate of a small cubic element (a 'subgrain' in the Rubik cube) can be calculated from:

$$\dot{\underline{\Omega}}_{SG}^{GB} = \text{sign}(p) |\sin \alpha| \left| \mu \dot{\underline{\Omega}}_G \right| \frac{n_{GB}^{(res)}}{\left| \frac{n_{GB}^{(res)}}{n_{GB}^{(res)}} \right|} \quad (3-8)$$

Here a sign function $\text{sign}(p)$ was needed to be introduced which is defined by:

$$\text{sign}(p) = -\text{sign} \left[\dot{\underline{\Omega}}_G n_{GB}^{(res)} \right] \quad (3-9)$$

The final formula for the lattice rotation is the following:

$$\dot{\underline{\Omega}}_{SG}^{GB} = -\text{sign} \left[\dot{\underline{\Omega}}_G n_{GB}^{(res)} \right] |\sin \alpha| \left| \mu \dot{\underline{\Omega}}_G \right| \frac{n_{GB}^{(res)}}{\left| \frac{n_{GB}^{(res)}}{n_{GB}^{(res)}} \right|} \quad (3-10)$$

Note that this is not the resultant lattice rotation of a subgrain; the total rotation is defined by Eq. (3-4).

3.3.1.4 Polycrystal model

A new parameter in the polycrystal model is the grain size which has to be assigned to the grains in addition to their orientation. For this purpose a special algorithm was developed to represent the initial state of the polycrystal (texture + grain size) with 500 grain orientations. For the grain size distribution, a lognormal type was used with average size of 24 μm . The grain sizes were ranging from 14 to 35 μm and the initial texture was nearly random, just like in the experimental copper material (the maximum intensity was 1.2 x random in the initial texture).

The Taylor viscoplastic polycrystal model was adopted. The main reason for this is that it permits to assume cubic shapes of the grains. Indeed, the more sophisticated self consistent viscoplastic (VPSC) model [132] could also be a candidate for this modeling,

3: Experimental Procedures and Modeling Methodology

however, the grain shape is ellipsoidal in VPSC and the computational part is much more complex than the Taylor model. For the first application, a simple model is more suitable. Also, the Taylor model is considered to be good enough for simulating texture development of polycrystals.

In the present modeling it is assumed that the grain boundaries of the initial grains are parallel to the axes of the reference coordinate system. As a consequence of straining, their orientation is changing which is updated according to Eq. 3-6.

Each initial grain was already subdivided into $27 \times 27 \times 27$ cubic elements in the very initial state, but with identical orientations. Each of these elements, however, changed their orientation during deformation according to the following procedure. First the lattice rotation was calculated from the Taylor model for the central part of the grain. This rotation was imposed to the central zone of the crystal but slightly different rotations were applied to the GB zones, depending on their positions with respect to the grain boundaries, see Eqs. (3-4) and (3-10). After each strain increment (as low as about 0.05), a misorientation study was carried out between the small cubic elements. Once a cell was misoriented more than 5° with respect to its neighbours, it was considered to be a new grain, thus, its own slip distribution and lattice rotation was computed. The same critical angle was employed in the analysis of the EBSD experiments of the real test. Three levels of subdivision processes were built into the initial cube. As described above, in the first level, the grain size could be decreased by a factor of three (Rubik-cube geometry). Once a subgrain appeared at the first level, its further subdivision was possible by a factor of three again. Finally, in the smallest scale, the grain size could go down to $1/27$ of the initial size.

3.3.2 Numerical implementation

The numerical computation required large computer memory as each initial grain could potentially broke up into $27 \times 27 \times 27 = 19,683$ small grains. Having 500 initial grains, the total population of grains can be $500 \times 19,683 = 9,841,500$ grains. Such computations have never done before in polycrystal modeling. For this reason, the Sun Grid computing facility in Monash University was used in FORTRAN language. Typical running time was about ~9 hours for 200 strain increments (9,841,500 grains treated in each increment). Continuous regions of neighbouring grains were identified having less than 5° misorientation to identify grain size. Care was taken to take into account the 24 symmetries of cubic crystals for the misorientation calculations; the smallest angle among all 24 misorientation angles was selected, just like in the software of the experimental EBSD facility.

3: Experimental Procedures and Modeling Methodology

A program was also constructed to carry out orientation analysis on virtual two dimensional sections of the polycrystal which was carried out on the computed results. A procedure similar to the TSL or HKL software was applied to determine grain sections. Grain sizes were assigned to such grains using the equivalent surface area criterion and grain size distributions were computed for comparison with experimental measurements.

3.3.3 Summary

The proposed grain fragmentation model adds the ongoing evolution of the grain population due to grain subdivision with the Taylor model of polycrystal plasticity. The core of this new element of modeling is the concept that grain subdivision is associated with accumulation of lattice curvature during the deformation process. The geometrically necessary dislocations produced as a result of the evolving lattice curvature are considered to build up boundaries of the emerging new grains. Despite the rough subdivision rule, the model is able to predict all aspects of large deformation of a polycrystal. The application of this model to ECAP process, which is described in the next chapter, demonstrates fairly precise predictions of grain size and grain misorientation distribution. It also demonstrates crystallographic textures are well reproduced, showing that texture development is an important element in the grain fragmentation process.

It is generally in good agreement with the experiments. There is, however, limitation of this on-going grain fragmentation modeling. As mentioned above, the coefficient (μ) and the width of the GB zone are the parameters to control the grain refinement. The width of the GB zone was taken to be equal to the size of the middle zone of a grain. This might be a rough approximation for grains with large size where it is expected that the effect of the GB is limited to a small region adjacent to the GB. Therefore, the present modeling is expected to be used for the application below a certain grain size and roughly to be 30 μm . In practice, each of the initial 500 grains having a particular orientation is subdivided into three level embedded cubic elements, and thus the final grain numbers are nearly 10 million (500×27^3). Modeling a polycrystal with such a large number of grain orientations needs supercomputer facilities to satisfy the memory and computational speeds. For grain size below 100nm, the diffusion component needs to be considered for the deformation mechanism together with slips of grain fragmentation. Also, the model is currently used for modeling large deformation of f.c.c. metals, and modifications accounting for specific deformation mechanisms of other crystallographic structures will be pursued in future work.

4

GRAIN FRAGMENTATION IN ECAP-ed COPPER

4. GRAIN FRAGMENTATION IN ECAP-ed COPPER

The grain fragmentation modeling in Chapter 3 highlighted within a single frame the main microstructural features of fine grained structure, including the evolution of the grain size distribution, misorientation distribution and crystallographic texture to simulate and analyze the observed experimental results. The present Chapter tests this modeling and places a strong emphasis on reliable determination of the model parameters within realistic limits. The experimental evidences for grain refinement are obtained from different strain and processing routes. In this way, the proposed grain fragmentation modeling is convincingly validated for ECAP-ed copper and in turn, the experiments provide details for analyzing grain fragmentation and understand the mechanism and materials behaviour after SPD process.

A special feature of the ECAP-refined microstructure is also investigated in this chapter in detail; the next neighbour misorientation distribution (NNMD). A new technique was developed to split the measured distribution to characterize two different populations of the new grains: the NNMD that belongs to the new grains within the old grains and another NNMD that describes the misorientations of the neighbours across the grain boundary of their respective parent grains. This is useful because the identification of the grain structure after SPD is of importance as it can provide quantitative measurement of the refined microstructure through the grain size distribution. The identified grains can be directly used in polycrystal plasticity modeling to assess the texture changes and mechanical behaviours.

4.1 Experiments

4.1.1 Initial materials

The average initial grain size of the material before ECAP processing was about 24 μm and the texture was nearly random (Fig. 4-1).

4: Grain Fragmentation in ECAP-ed Copper

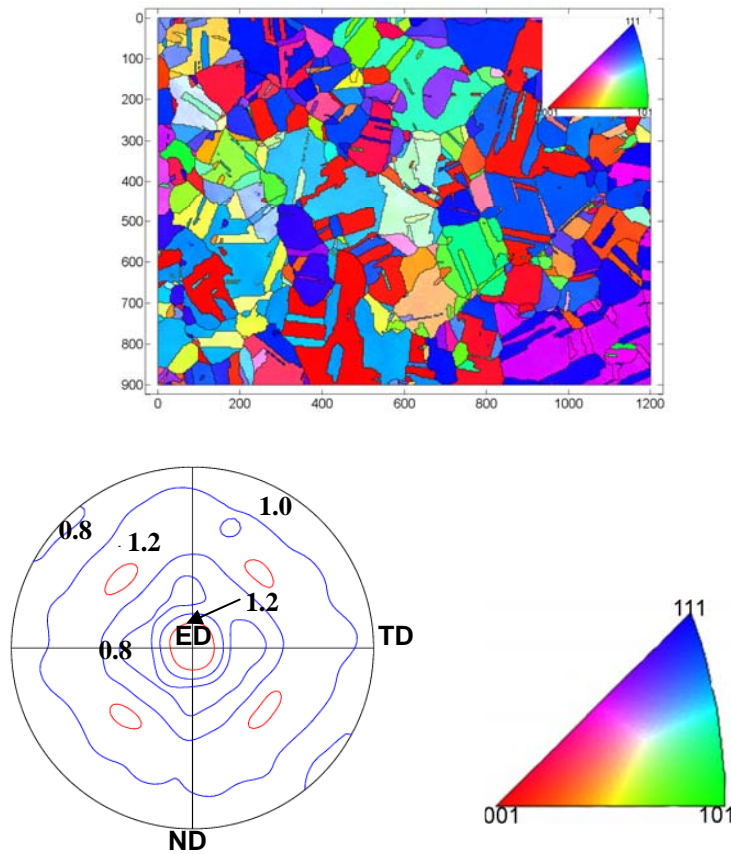


Figure 4-1. Representative orientation map and {111} pole figure of the as-received copper. The color code for the ED axis in the map is also shown in the unit triangle. The unit is micron in the orientation map.

4.1.2 Grain morphology after ECAP and rolling

For one-pass ECAP-ed copper, the microstructure of the CG copper became elongated on the ED and TD planes but not on the ND section, (Fig. 4-2). On the ED plane, the original grains were flattened perpendicular to the ND direction while on the TD plane, the grain axes were inclined at about 25° with respect to ED which is actually expected from the simple shear model of ECAP. The grain morphology was similar to the initial one on the ND plane (Fig. 4-2b) which is also a result of the simple shear process. The subgrain sizes after ECAP were in the range of 1.04 -1.86 μm obtained using the equivalent area formula $d = 2 \times \text{sqrt}(S / \pi)$ where S is the surface of the grain measured in a given plane. The microstructure was more refined on the ED and TD planes compared to the ND plane, Fig. 4-2.

4: Grain Fragmentation in ECAP-ed Copper

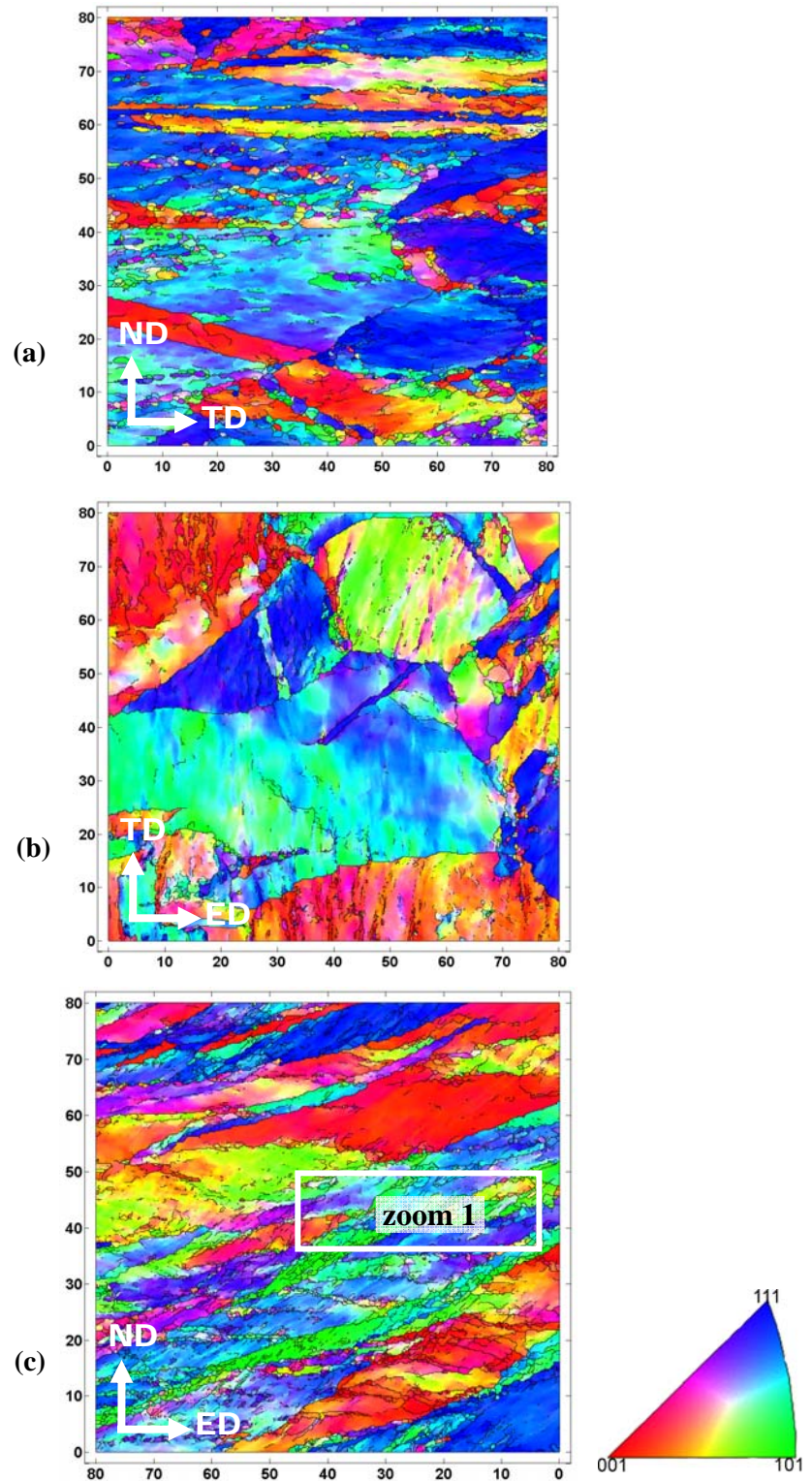


Figure 4-2. Examples of orientation maps after one ECAP pass in pure copper: (a) ED plane; (b) ND plane and (c) TD plane. Boundaries with at least 5° misorientation are marked with black lines. The color code for the orientations is also shown. Units are in micron (Zoom 1 refers to a later image, Figure 4-23).

4: Grain Fragmentation in ECAP-ed Copper

After two passes route A, the microstructure is shown in Fig. 4-3 taken on the TD plane, as the grain structure in this plane is more refined than the other two planes through the shear deformation (Fig. 4-2). The average grain size values further decreased to about $0.82 \pm 0.11 \mu\text{m}$, depending on the area studied (several maps were made; Fig. 4-3 is just an example).

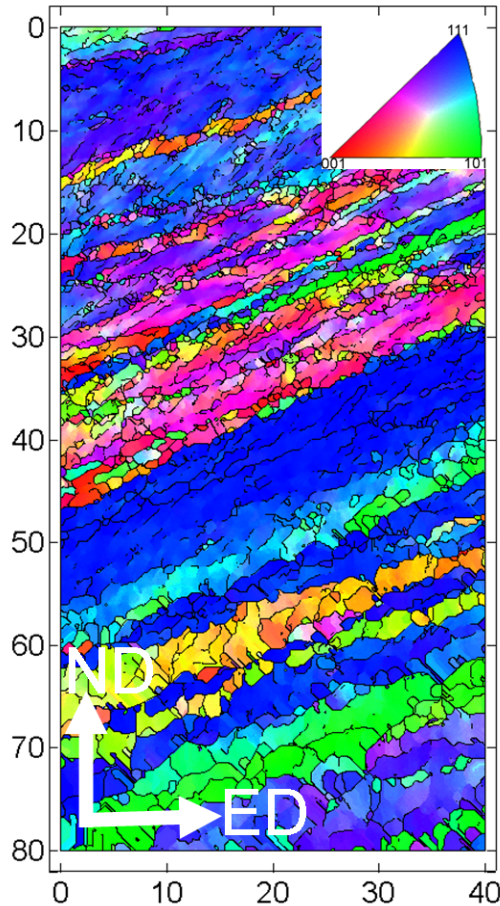


Figure 4-3. Inverse pole figure of deformation microstructure of OFHC copper deformed in route A ECAP in two passes. Grain boundaries with misorientation larger than 5° are depicted by black lines. Scale is in μm .

For route Bc, second pass, a typical microstructure is displayed in Fig. 4-4. The corresponding grain size distribution, shown in Fig. 4-5, presents a large and relatively narrow peak at about 1 micron. Note that this grain size frequency calculation was made by counting each grain (small or large) same irrespectively of its grain area. Some larger grains were also seen (in small number fractions) which are out of the region in size for Fig. 4-5. They are not refined at all, or only near to their grain boundary region.

4: Grain Fragmentation in ECAP-ed Copper

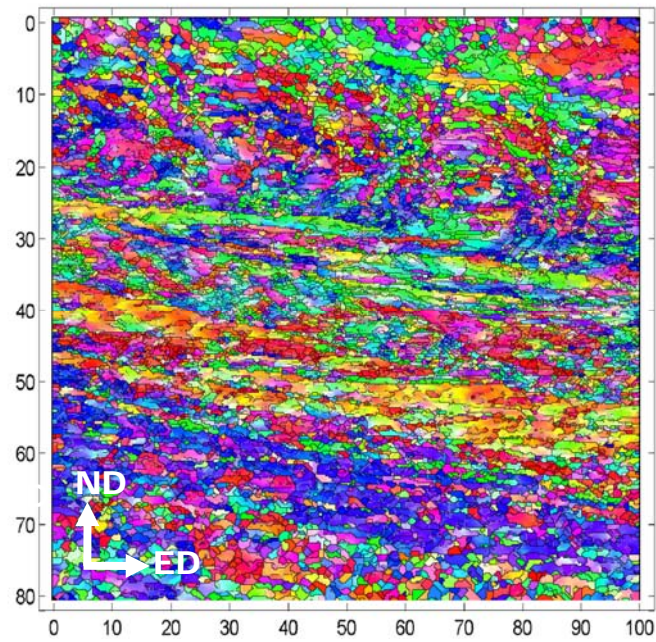


Figure 4-4. EBSD orientation map after two passes of pure copper in Route Bc. Size of map: $80 \times 100 \mu\text{m}$.

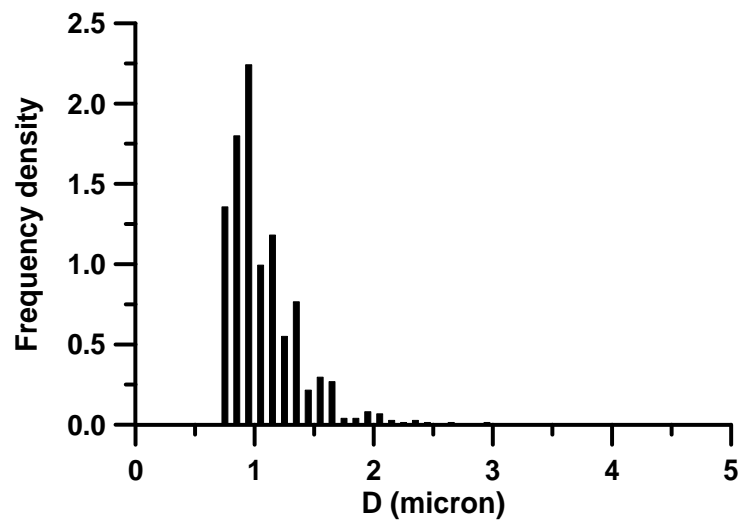


Figure 4-5. Measured grain size distribution for pure copper after two passes in route Bc.

EBSD maps are presented in Fig. 4-6 for three-pass ECAP-ed sample for two observation planes; on TD and ED. These maps are much larger than for the previous passes and

4: Grain Fragmentation in ECAP-ed Copper

present sufficient statistics in terms of number of grains. They will be analyzed for their misorientation distributions in Section 4.4.

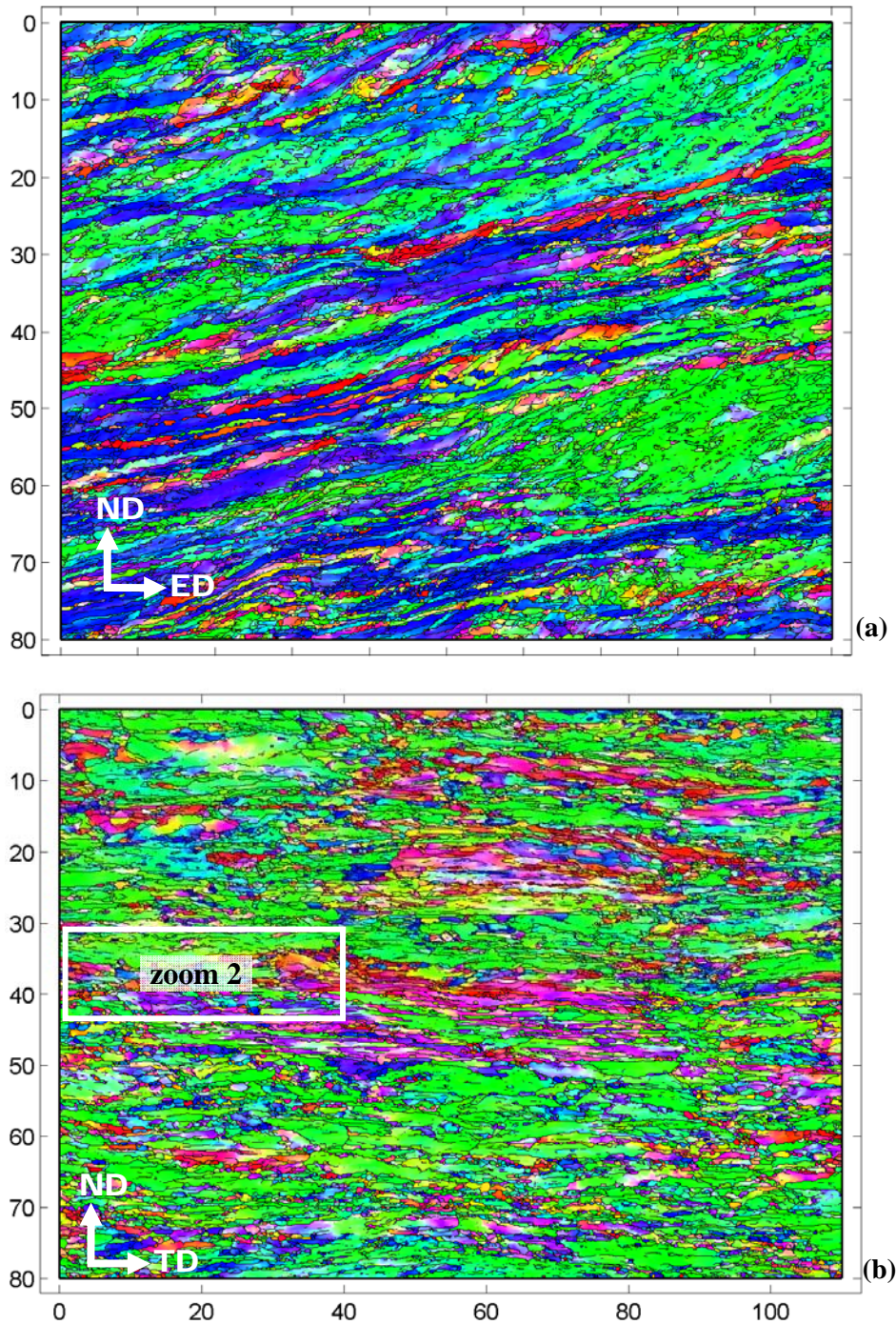


Figure 4-6. Orientation maps of 3 passes ECAP-ed copper: (a) TD plane and (b) ED plane. Boundaries with at least 5° misorientation are marked with black lines. The color code is the same as in Fig. 4-2, and scale is in micron (Zoom 2 refers to a later image, Figure 4-23).

4: Grain Fragmentation in ECAP-ed Copper

The same copper material was also rolled to strains given by the formula $\varepsilon = 2/\sqrt{3} \times \ln(T_0/T_f)$ with $T_0 = 2.0$ mm and thickness reduction of 60% and 84%, that are equivalent to one-pass ECAP (~1.06) and two-pass ECAP (~2.12) respectively. These samples contained a band-like lamellar structure with the long axis parallel to the rolling direction (Fig. 4-7). The average grain size was 2.63 ± 0.29 μm for the 60% rolled copper and 1.31 ± 0.13 μm and for the 84% rolled sample. In this study, the initial texture is nearly random, thus grain refinement difference between the two deformation mode is mainly caused by strain path effect.

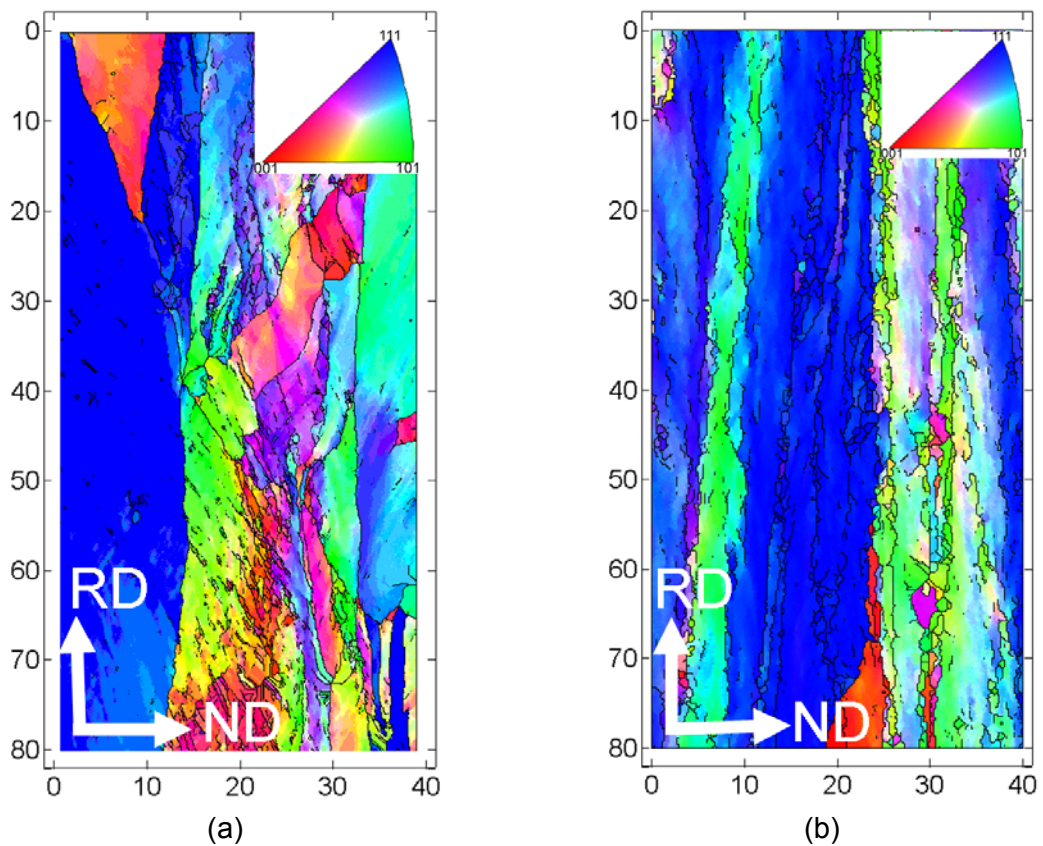


Figure 4-7. Deformation microstructure of OFHC copper deformed in rolling to a thickness reduction of 60% (a) and to 84% (b). Grain boundaries with misorientation larger than 5° are depicted by black lines. Scale is in μm .

4.1.3 Textures

The texture is shown in form of $\{111\}$ figures in Fig. 4-8 for the one-pass ECAP deformed copper sample obtained by two different measurement techniques; by X-ray and from EBSD orientation maps. The reason why the texture is examined by X-ray is to verify the representativeness of the textures obtained from EBSD. The texture intensity is

4: Grain Fragmentation in ECAP-ed Copper

statistically reliable when obtained by X-ray; however, this is not necessarily the case when it is measured by EBSD due to the much smaller area size examined. One can see that there are some deviations between the X-ray and EBSD textures (see, centre part in Fig. 4-8a and b): the difference can be minimized when big areas are measured and the number of grains are statistically representative. Nevertheless, the main characteristics obtained by X-ray or EBSD are the same. The one-pass texture shows the typical ideal orientations and fibres that appear after a shear strain of 2 and reported in [28].

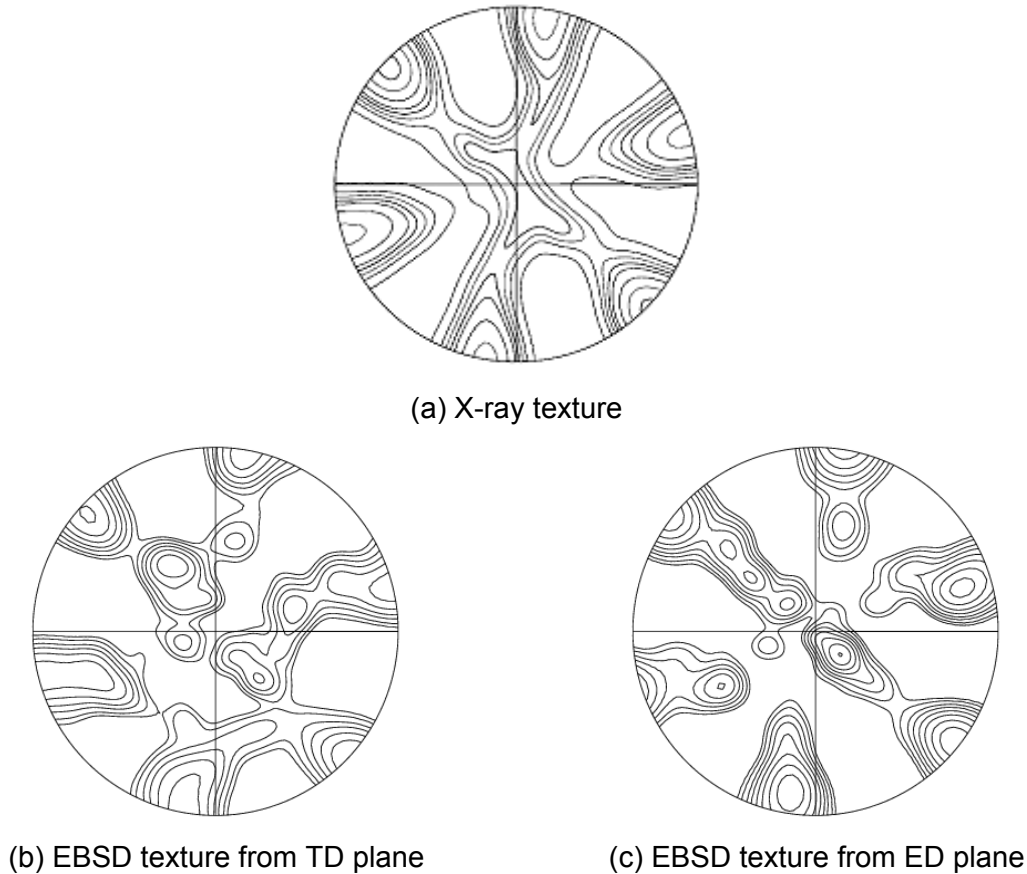


Figure 4-8. Measured textures for one-pass ECAP deformed copper in $\{111\}$ pole figures by X-ray (a) and by EBSD on the TD plane (b) and from the ED plane (c). All three textures are expressed in the same sample reference system: pressing ('extrusion') direction ED is to the right, and normal direction ND is vertical. Isolevels: 0.7, 1, 1.2, 1.4, 1.6, 2, 2.5, 3, 3.5, 4.

During the second ECAP pass in route Bc the texture intensifies significantly, see Fig. 4-9, measured by X-ray. It is characterised by a strong B component which is in off-position with respect to its ideal position. This measured texture agrees also very well with the measurements obtained by others, see in [28].

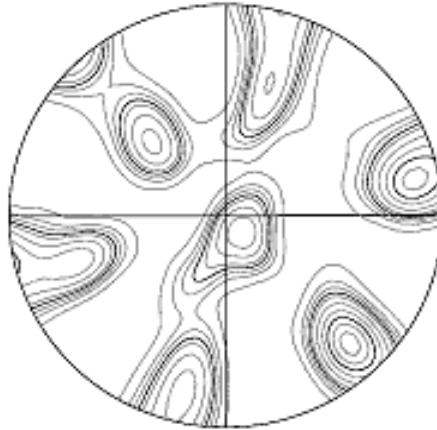


Figure 4-9. X-ray measured texture for two-pass ECAP route Bc deformed copper in $\{111\}$ pole figure. ED direction is to the right and normal direction ND is vertical. Isolevels: 0.7, 1, 1.2, 1.4, 1.6, 2, 2.5, 3, 3.5, 4.

The three-pass route A ECAP texture is presented in Fig. 4-10. The global texture was measured by synchrotron (thanks to Nils Scheerbaum, TU Dresden) which technique results in very good statistics of the bulk texture (Fig. 4-10a). The EBSD textures are also presented obtained from the TD and ED planes (Fig. 4-10b-c) but expressed both on the TD plane. One can see that the ED plane measurement is especially near to the synchrotron measurement but the TD plane texture is also acceptable.

For a relatively uniform deformation, if the local texture (Fig. 4-8c) is very close to the macroscopic texture (Fig. 4-8a), then the corresponding local microstructure should be representative as well. This is important, particularly for the statistics of misorientation angles, meaning that the experimental misorientation distributions obtained on different planes can be fully representative of the microstructure. As an example above, both textures are near to the expected texture after three pass, thus the microstructure are homogeneous in terms of grain fragmentation.

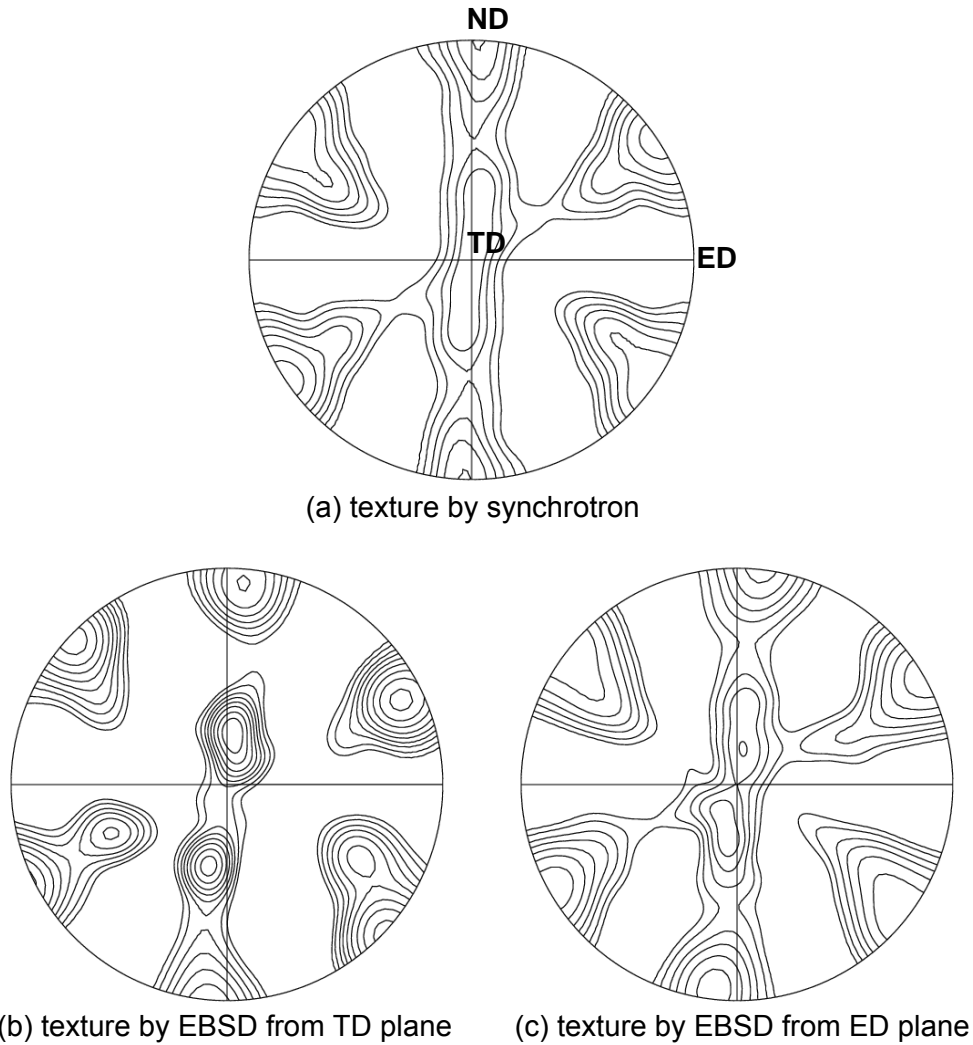


Figure 4-10. Measured textures for three-pass ECAP deformed copper in {111} pole figures by X-ray (a) and by EBSD on the TD plane (b) and from the ED plane (c). All three textures are expressed in the same sample reference system: ED to the right and normal direction ND is vertical. Isolevels: 0.7, 1, 1.2, 1.4, 1.6, 2, 2.5, 3, 3.5, 4.

4.1.4 Misorientation distributions

With the help of currently available commercial orientation mapping software codes (Channel 5 in HKL Technology and TSL) one can identify 'grain' boundaries using an imposed condition of minimum misorientation from pixel-to-pixel orientation measurements. From these boundaries, contingent regions formed by continuous closed boundaries can be defined; they are usually called grains if the minimum misorientation between the regions on the two sides of a boundary is sufficiently large (commonly 5° to 15°). Average orientations can also be assigned to the obtained grains as the averages over the orientations of the pixels that form the grain. Then the misorientation between two adjacent grains can be calculated from their average orientations. It is also of

4: Grain Fragmentation in ECAP-ed Copper

importance to analyze the distribution density function $\nu(\theta)$ of the misorientation angle θ of the grains that constitute the measured orientation map which will be subject of the present section. Such misorientation distribution is called next-neighbor misorientation distribution (NNMD). Mackenzie [133] has calculated the uncorrelated distribution density function $\nu(\theta)$ for a f.c.c. polycrystal with a random distribution of grain orientations, which is commonly referred to as the 'Mackenzie distribution' (solid black line in Fig. 4-11).

The identification of the grain structure after SPD is of importance as it can provide quantitative measures of the refined microstructure. The grain size distribution and the average orientation of the identified grains can be directly used in polycrystal plasticity modeling. These are readily calculated in the most widely used commercial orientation imaging software packages. However, the available package, such as HKL, does not necessarily produce the most relevant information about the structure. For example, they do not have the feature of displaying the frequency density function of the identified grain structure; they produce only the frequency distribution function of the adjacent pixels of the measurement. This information – however useful it may be for certain purposes – is very different from the NNMD function defined above. An example is displayed in Fig. 4-11 where both density functions are plotted for copper deformed in a 90° ECAP die after one pass (the map was taken on the TD plane from Fig. 4-2).

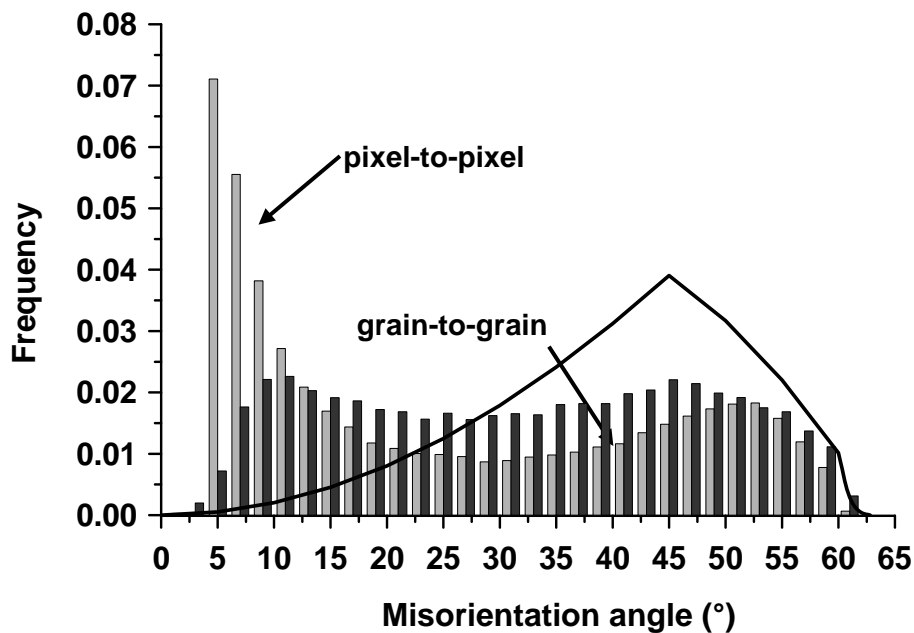


Figure 4-11. Comparison between pixel-to-pixel (light gray) and grain-to-grain (dark gray) misorientation distributions after one pass of copper in ECAP on the TD plane

4: Grain Fragmentation in ECAP-ed Copper

As can be seen, the pixel-to-pixel misorientation frequency distribution has a large peak at small angles while the NNMD based one - obtained for the identified grains (using the same 5° misorientation threshold) - displays a much larger fraction of high angle misoriented grains. It is important to point out further differences in the techniques used to construct these two kinds of distributions. In the case of pixel-to-pixel methodology, the detected misorientations do not necessarily correspond to a closed grain boundary delineating a grain (even if it is commonly called “Grain-boundary distribution”). The frequency value is also affected by the length of the detected boundaries as the number of pixel-misorientations along a boundary is proportional to its length. In case of NNMD, the misorientation values are all calculated between identified grains (with closed grain boundaries) and each grain (whether small or large) is counted with the same weight. Thus, in order to obtain insight in the misorientation frequency of polycrystals, the grain-based NNMD function is more suitable compared to the pixel-to-pixel misorientation distribution and will be employed in the present thesis. The minimum misorientation angle in identifying grains will be always 5° to fully identify subgrains, not dislocation cells/walls along the grain boundaries.

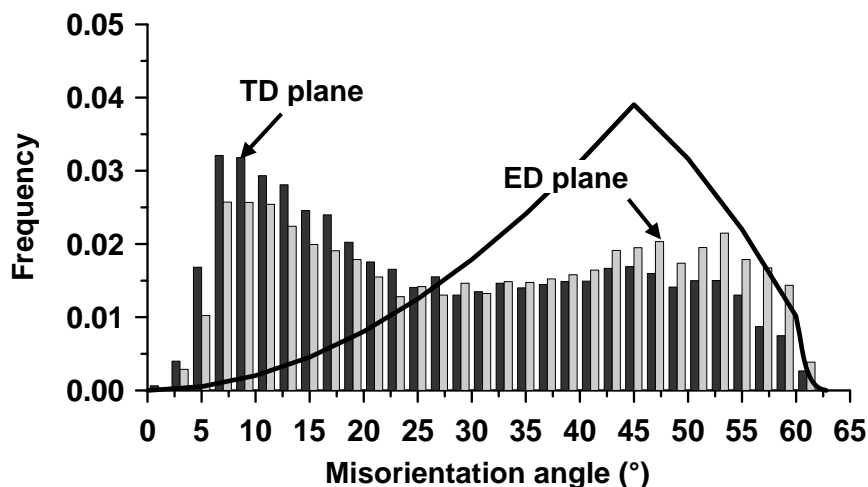


Figure 4-12. Grain-to-grain misorientation distributions measured on the TD as well as on the ED plane in pure copper deformed by ECAP after one pass. The minimum misorientation was set to 5° to identify grains.

Fig. 4-12 displays the NNMDs derived from the microstructures of the one ECAP-pass deformed copper sample from both the TD and ED plane measurements. They both show two peaks; one at lower angles and one at high misorientations. They are, however, clearly distinct; the frequency values are lower for the ED plane at low angles while they are higher at high angles. As will be shown below in Section 4.4, these differences can be

4: Grain Fragmentation in ECAP-ed Copper

explained by the different morphologies of the grains that can be seen in the two sections of observations.

Compare to one pass ECAP, Fig. 4-12, the NNMD does not change significantly after two ECAP passes in route Bc, see Fig. 4-13. In this case, the measurement was only carried out on the TD plane.

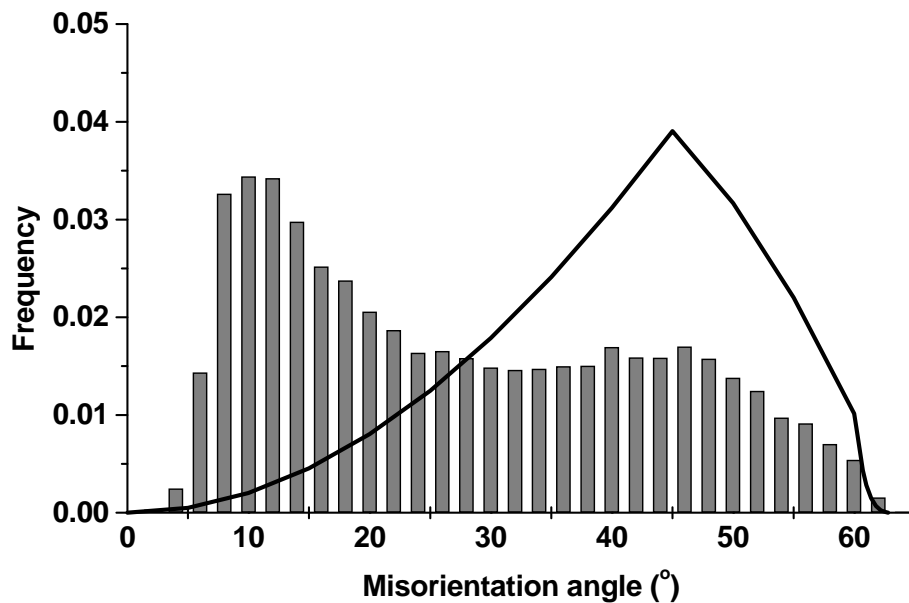


Figure 4-13. Grain-to-grain misorientation distribution measured on the TD plane in pure copper deformed by ECAP in route Bc two passes. The minimum misorientation was set to 5° to identify grains.

After three ECAP passes, see Fig. 4-14, the measured NNMDs become more even with respect to the one or two ECAP passes, see Fig. 4-12 and Fig. 4-13; the intensities of the two peaks become nearly the same. However, a small but systematic difference can be detected between the measurements of the two planes. The difference will be explained in Section 4.4.

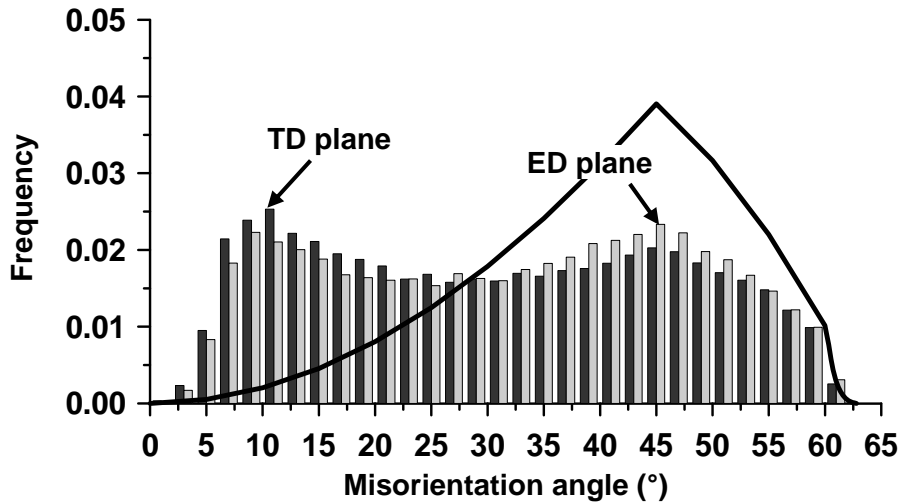


Figure 4-14. Grain-to-grain misorientation distributions measured on the TD as well as on the ED plane in pure copper deformed by ECAP in three passes in route A. The minimum misorientation was set to 5° to identify grains.

4.2 Grain Fragmentation Model Parameters

The deformation process for an ECAP die was first proposed to be simple shear according to the model of Segal [134] then later more sophisticated flow line approaches were developed for texture prediction after ECAP [28]. In the present modeling, the simple shear deformation model is used but it is known also to be able to provide reliable results for texture. It was shown in a recent work [135] that even if the flow lines are very much rounded, it is still possible to have near simple shear conditions in the material undergoing ECAP.

For the grain fragmentation polycrystal simulations, 500 orientations were selected from the measured initial texture, and grain sizes were also allocated from a range between 14 and 35 μm so that the simulated polycrystal closely approximated the experimental one: the models started at an average grain size of 24 μm and a nearly random texture. The grain size distribution was near to lognormal.

The simulation of the ECAP process was first tested only up to two passes (in route Bc), for the following reasons. First, three levels of embedded 'Rubik cubes' were used in the numerical code, which limited the minimum grain size to 1/27 of the initial one. Therefore, with the average grain size 24 μm , the minimum average grain size cannot become less than $24 \mu\text{m} / 27 = 880 \text{ nm}$ after three levels of grain subdivision. Furthermore, if one considers the smallest grain size in the population, i.e. 14 μm , the absolute minimum grain size attainable in the simulation is $16 \mu\text{m} / 27 = 590 \text{ nm}$. The measured average grain size

4: Grain Fragmentation in ECAP-ed Copper

after one pass was 1.86 μm and in two passes of route Bc ECAP it was 1.15 μm using a 5° misorientation criterion for grain identification in the modeling. In further passes, the experimental grain size decreased drastically (to about 230 nm after four passes), which is out of the range for the present simulation procedure. Thus, the computation was limited to strains corresponding to one or two passes. The other reason why larger strains were not aimed at in the first trial of the present model is that the Taylor model of polycrystal plasticity was used, which is known to fail at very large strains. Both the numerical constraints and the limitations of the polycrystal model will be overcome in future work. On the numerical side, one more level of 'Rubik-cube' subdivision is needed (so far it was restricted to three 'generations' because of a limitation with regard to the maximum number of possible dimensions in the FORTRAN language). As for the polycrystal model, it is expected that better texture predictions will be obtained by employing the self consistent viscoplastic code instead of the Taylor model.

This new grain refinement model has only one adjusting parameter but several simplifying hypotheses. One of the simplifying hypotheses is the width of the GB zone which controls the grain refinement. It was taken to be equal to the central zone of the grain. This might be a very rough approximation for grains with a very large size where it is expected that the effect of the GB is limited to a smaller region around the GB. As mentioned before, the present modeling is expected to be applicable below a certain grain size of about 30 μm . Many technically interesting materials have this characteristic grain size range. Obviously, this approximation becomes closer to the physical situation with ongoing grain refinement.

The only model parameter that has to be specified is μ which defines the retardation of the lattice rotation at the grain boundaries. A special value of μ is the one at which the lattice plane keeps its initial orientation at the GB. Using our circular shape assumption for the lattice distortion in the GB area (see Fig. 3-8), it can be seen that when the tangent to the curved lattice plane at the grain boundary is parallel to the initial orientation of the lattice plane then $\mu = 0.5$. It does not mean, however, that the lattice plane is pinned at the GB (that would happen at $\mu = 1$) because it has to be displaced along the GB. Another important element in the simplification is that the circular lattice distortion is approximated by a uniform rotation of the lattice in the GB region. This approximation implies that the subgrains within a GB are definitely not pinned to the GB but rather rotate at a rate determined by the value of μ . A tuning procedure permits to obtain the value of this single parameter and $\mu = 0.5$ gives satisfactory results assuming that there are no recovery

4: Grain Fragmentation in ECAP-ed Copper

processes which annihilate some of the curvature induced dislocations. For ECAP-ed copper the results presented below were simulated for $\mu = 0.5$.

4.3 Grain Fragmentation Modeling Results for ECAP

4.3.1 Predicted textures

Using the modeling parameters presented above, a fair agreement of the predicted texture from the proposed grain refinement model was obtained; see the simulated textures of Fig. 4-15 where the measurement is also displayed for easy comparison. The modeling result is better for one-pass ECAP than for two-pass route Bc. In both cases the calculated texture intensity is significantly higher than in the experiment. The maximum intensity is about twice as high as in experiment. Examining the two-pass simulated texture, one could find that all the components of the experimental texture are reproduced in the right positions. A small discrepancy is that an extra component appears in the simulation in an exaggerated proportion. The extra component is the rotated cube component whose position is indicated in the pole figures (Fig. 4-15). This discrepancy is caused by the use of the Taylor model. Simulation was performed by using the self-consistent model in its finite element tuned version by Toth et al. [132], confirming that the appearance of the cube component is associated with the use of the Taylor model.

It is important to see the effect of grain refinement on the predicted texture. For this purpose, simulations were also carried out with the simple Taylor model, without grain refinement (i.e. when $\mu = 0$). The result is displayed in Fig. 4-15. One can see that the textures are not much different. The main differences are actually in intensity. These values are much higher than those corresponding to the case when grain refinement was included in the simulation (see Fig. 4-15). This observation confirms the known effect of smoothing the textures by grain refinement [136], although in the present simulation this effect is not as strong as in experiment. The reason may lie in the coarseness of the approximation used, according to the curvature-related grain subdivision of a grain into three discrete regions for each dimension (corresponding to a 'Rubik cube' rule in 3D). In reality, the lattice curvature is continuous and smoothes out the texture more evenly. Thus, for $\mu = 0.5$, the maximum misorientation difference across a near-GB subgrain, which corresponds to an average misorientation of 5° with respect to the subgrain in the middle, is actually 10° .

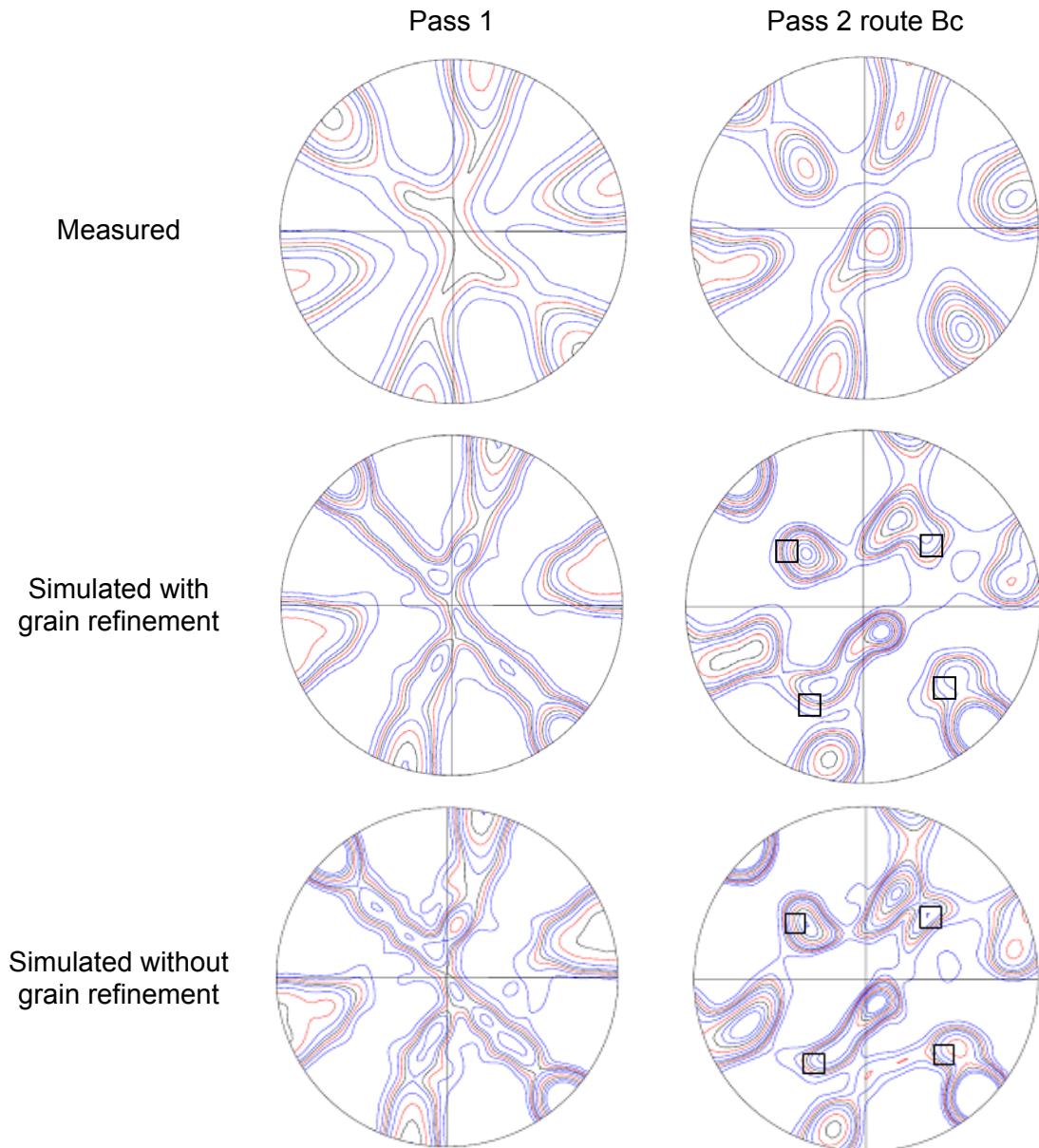


Figure 4-15. Measured and simulated textures for copper deformed by ECAP in route Bc represented by $\{111\}$ pole figures by X-ray. Pressing ('extrusion') direction ED is to the right, and normal direction ND is vertical. Isolevels: 0.7, 1, 1.2, 1.4, 1.6, 2, 2.5, 3, 3.5, 4. Open square symbols indicate a rotated cube position.

4.3.2 Predicted grain sizes

The frequency distribution of the grain size obtained by modeling for two-pass route Bc is displayed in Fig. 4-16. It shows a distribution fairly close to the experimental one: compare this figure to Fig. 4-5. Note that there are grain sizes that are larger than the scale in Fig. 4-16, however, due to their relatively small number with respect to the number of new

4: Grain Fragmentation in ECAP-ed Copper

grains (~6.5 millions), the frequency values are small. Such non-refined grains were also observed in experiments (refer to Fig. 4-5).

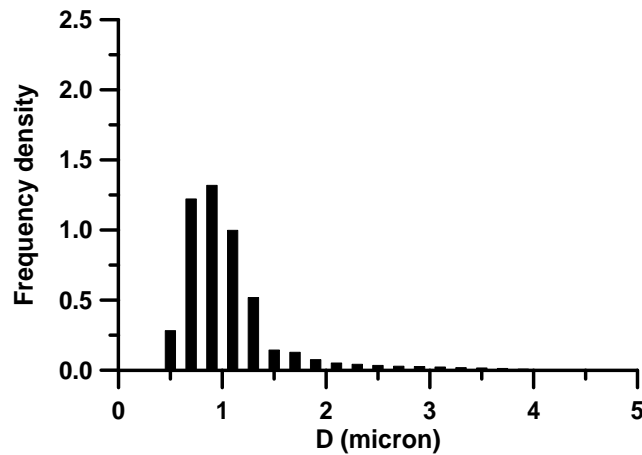


Figure 4-16. Predicted grain size distribution for pure copper after two passes in route Bc.

4.3.3 Predicted misorientation distribution

As the grain refinement model is topological, it is possible to obtain misorientation distribution of adjacent new grains. This can be done, however, only for the grain-interiors of the original grains because geometrical relations between the initial grains were not introduced in the model. In this way, the so-called ‘internal’ misorientation distribution can only be calculated for each initial grain, then, an average of these distributions can be made. The result of such calculation is displayed in Fig. 4-17 for two-pass route Bc copper together with the experimental measurement.

One can see in Fig. 4-17 that the grain fragmentation process produces grain misorientations up to 60° within the initial grains. There is a large maximum at lower grains. The measured NNMD shows important deviations with respect to the simulation. However, one has to consider that in the modeling only the ‘internal’ population of new grains is counted while in the measurement there are misorientations between new grains that belong to different initial grains being neighbours across the ‘old’ grain boundaries of the starting grains. The contribution of that population of new grains to the final NNMD is actually quite important and will be examined in detail in the last section of this chapter. The present modeling cannot predict that part of the NNMD which would actually increase very significantly the intensities at large angles in Fig. 4-17.

The effect of the texture on NNMD can be significant when the texture is strong. It is expected that the frequency of low misorientations increases in the NNMD while the large

4: Grain Fragmentation in ECAP-ed Copper

angle part of the NNMD is decreasing. The reason for it is that the probability that next neighbor grains belong to the same texture component is much higher when a texture component is very strong (nearly the same orientations belong to the same texture component).

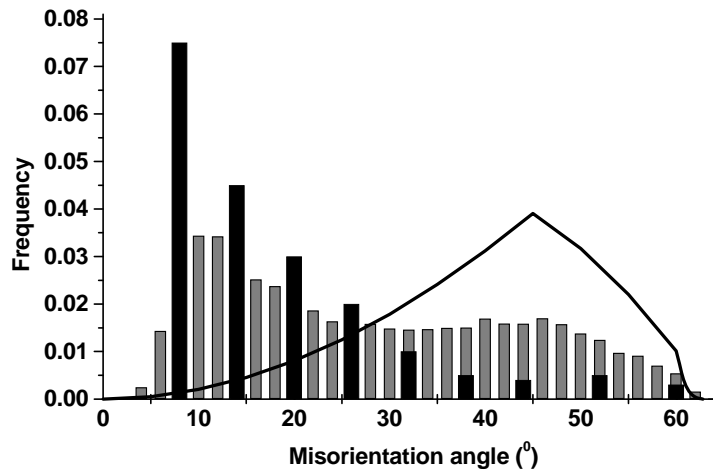


Figure 4-17. Comparison of predicted (black) and measured (gray) grain-to-grain misorientation distribution on the TD plane in pure copper deformed by ECAP in route Bc two passes. The minimum misorientation was set to 5° to identify grains.

4.3.4 Predicted geometrically necessary dislocation associated with lattice curvature

Lattice curvature cannot be maintained without geometrically necessary dislocation associated with lattice curvature. Simulated average density of lattice curvature induced dislocations is plotted as a function of strain in Fig. 4-18. The results show a rapid linear increasing up to a strain of about 0.2 while there is no grain refinement during this initial stage. At the end of this stage, subgrain misorientation reaches the value of 5° beyond which the subgrains are considered in the simulation to be new grains. Consequently, at that point the density of geometrically necessary dislocations associated with lattice curvature is set back to zero for these new grains. This is why a small drop can be seen after the initial linear part of the curve in Fig. 4-18. Following this, the geometrically necessary dislocations associated with lattice curvature density increases to about 10^{14} m^{-2} , which is much less than all other dislocation densities in the material (the cell-wall density can go up to $3.5 \times 10^{16} \text{ m}^{-2}$, see in [20]). This is understandable, as the dislocation density is accumulated only up to certain misorientation, and then all geometrically necessary dislocations associated with lattice curvature are supposed to be ‘consumed’ to produce new grain boundaries, thus being removed from the grain interiors. Since the rate

4: Grain Fragmentation in ECAP-ed Copper

of grain refinement is decreasing, the geometrically necessary dislocations associated with lattice curvature decreases as well, levelling off at a low value at the end of the second pass (Fig. 4-18).

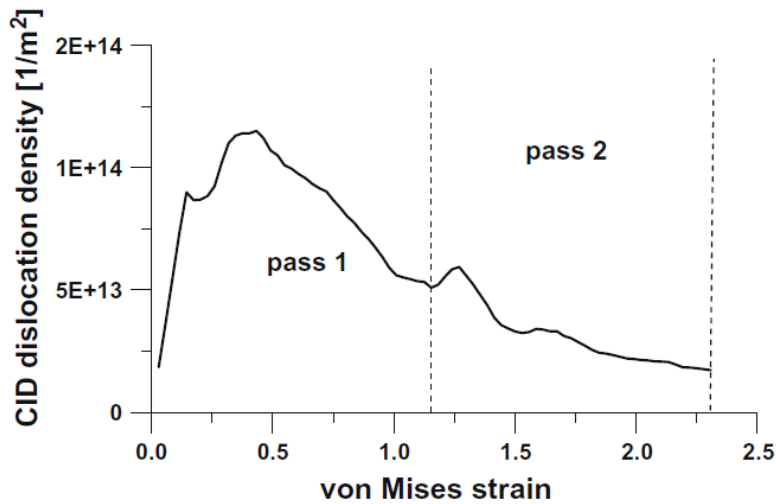


Figure 4-18. Predicted density of curvature induced dislocations in route Bc ECAP of copper

This tendency is a consequence of the hypotheses made in the present model relating the generation of geometrically necessary dislocations to the lattice rotation. As grain orientations approach the ideal texture positions, their lattice rotation decreases and so does the lattice plane curvature, which stems from the retardation of the lattice plane rotation at the grain boundaries. As a matter of fact, an initial rapid increase of the geometrically necessary dislocation density associated with lattice curvature can also be seen in Fig. 4-18 at the beginning of 2 passes. This is due to the repositioning of the sample in the die for the second pass. This rotation moves the grain orientations by 90° out of their positions in the Euler space into such a position where the lattice rotation is much higher.

4.4 Comparison of Grain Fragmentation Modeling between ECAP and Rolling

The results presented in the preceding section for modeling of fragmentation during ECAP deformation demonstrated the predictive capacity of the model. However, it has to be tested for different deformation modes in order to get convincing evidences for the pertinence of its main hypotheses. In this section, modeling results will be presented for a comparative study for the grain fragmentation process between ECAP and rolling. The

4: Grain Fragmentation in ECAP-ed Copper

experimental results for rolling were presented in Section 4.1.2. The rolling strains applied were the same as the equivalent strains in ECAP for one and two passes.

4.4.1 Elements of mechanics of ECAP and cold rolling

The present grain fragmentation refinement model is based on the main hypothesis that lattice rotation during SPD is the main driving force for the fragmentation. In grain refinement polycrystal modeling, the average lattice rotation rate can be computed from the individual lattice spins of the grains that constitute the polycrystal. Ignoring the direction of rotations, the scalar rate is the lattice rotation rate $|\dot{\Omega}|$ which was calculated for each crystal as follows:

$$|\dot{\Omega}| = \sqrt{\Omega_{12}^2 + \Omega_{23}^2 + \Omega_{13}^2} \quad (4-1)$$

where the $\dot{\Omega}_{12}$, $\dot{\Omega}_{23}$ and $\dot{\Omega}_{13}$ are the three components of the antisymmetric lattice rotation tensor. The average lattice rotation of the whole polycrystal was computed using the relative volume fractions of the grains.

Any comparison between two strain paths has to be made on a sound physical basis. For this reason, one has to choose physically equivalent strain rates in the two strain modes. The velocity gradients of the two tests from ECAP and cold rolling to the same equivalent strain used in the model are the following:

$$L_{ECAP} = \begin{pmatrix} \dot{\gamma}/2 & -\dot{\gamma}/2 & 0 \\ \dot{\gamma}/2 & -\dot{\gamma}/2 & 0 \\ 0 & 0 & 0 \end{pmatrix}_{(RD,ND,TD)}, \quad L_{rolling} = \begin{pmatrix} \dot{\epsilon} & 0 & 0 \\ 0 & -\dot{\epsilon} & 0 \\ 0 & 0 & 0 \end{pmatrix}_{(RD,ND,TD)} \quad (4-2)$$

Here $\dot{\gamma}$ is the shear rate on the shear plane of ECAP [28] and $\dot{\epsilon}$ is the strain rate in rolling. The corresponding strain rate tensors are:

$$D_{ECAP} = \begin{pmatrix} \dot{\gamma}/2 & 0 & 0 \\ 0 & -\dot{\gamma}/2 & 0 \\ 0 & 0 & 0 \end{pmatrix}_{(RD,ND,TD)}, \quad D_{rolling} = \begin{pmatrix} \dot{\epsilon} & 0 & 0 \\ 0 & -\dot{\epsilon} & 0 \\ 0 & 0 & 0 \end{pmatrix}_{(RD,ND,TD)} \quad (4-3)$$

These strain rate tensors are proportional to each other. Thus, the equivalence of strain requires that $\dot{\gamma} = 2\dot{\epsilon}$. It is not surprising that the strain rate tensors of rolling and shear

4: Grain Fragmentation in ECAP-ed Copper

can be exactly the same. The difference between the two tests is actually only in the imposed rigid body rotation rate $\dot{\beta}$ (the antisymmetric part of the velocity gradient), which is zero in rolling, while in ECAP it is:

$$\dot{\beta}_{ECAP} = \begin{pmatrix} 0 & -\dot{\gamma} & 0 \\ \dot{\gamma} & 0 & 0 \\ 0 & 0 & 0 \end{pmatrix}_{(RD,ND,TD)} \quad (4-4)$$

It can be also readily shown that the operating slip systems are the same in the two tests for crystals having the same orientation (assuming a Taylor deformation mode). Namely, according to the kinematics of slip, the macroscopic strain rate can be obtained from the crystallographic slips $\dot{\gamma}^s$ according to:

$$D_{ij} = \sum_{s=1}^n \frac{m_{ij}^s + m_{ji}^s}{2} \dot{\gamma}^s \quad (4-5)$$

Here $m_{ij}^s = b_i^s n_j^s$ is the Schmid orientation matrix with b^s and n^s being the slip direction and slip plane normal unit vectors, respectively, and n is the total number of slip systems. The Schmid tensor depends only on crystal orientation, thus, for identical orientations in ECAP or rolling the m_{ij}^s quantities are the same which means according to Eq. (4-5) that the slip rates $\dot{\gamma}^s$ are also the same. Initially, the grain orientations were identical in the two tests because the same initial texture was present in the samples. During plastic strain along different strain paths different textures develop, and thus, the orientations diverge. Nevertheless, the initial differences in lattice rotations are expected to be decisive in the early process of grain refinement.

4.4.2 Simulation results

From the dimensions of the sample and the extrusion speed the shear strain rate during ECAP can be estimated to be about 0.83 s^{-1} using Eq. (14) in Ref. [137]. The average strain rate during rolling was about 0.4 s^{-1} . The simulated variation of average grain size as a function is shown in Fig. 4-19. A grain is defined as an ensemble of subgrains whose mutual misorientations are less than 5° . The rate of grain refinement is very high during the first ECAP pass, after an 'incubation strain' of about 0.2. The deformation state of a material element during ECAP is such that there is elongation in the ED direction and compression in the ND direction [137], exactly like in rolling. The difference between the

4: Grain Fragmentation in ECAP-ed Copper

two deformation modes is only the presence of a large rigid body rotation during ECAP [137,28]. The predicted variation of the average grain size obtained by the grain refinement fragmentation modeling is consistent with the experimental observations for both deformation paths (Fig. 4-19) and the significantly larger grain sizes predicted for ECAP are also in good agreement with the measured values (see following section). This simple validation gives confidence in further exploration of the effect of strain path using the model.

The first stage consists in subdivision of the original grain at the first level of the 'Rubik cube'. The simulation algorithm is then activated at a lower level, at a strain of about 0.3 (Fig. 4-19). By the end of the first ECAP pass, the rate of subdivision has slowed down considerably, and the average grain size is close to 1 μm . The second pass begins at the von Mises strain of 1.15 and the end of the second pass the grain size is 0.9 μm and the grain population has increased from 500 to about 6 million.

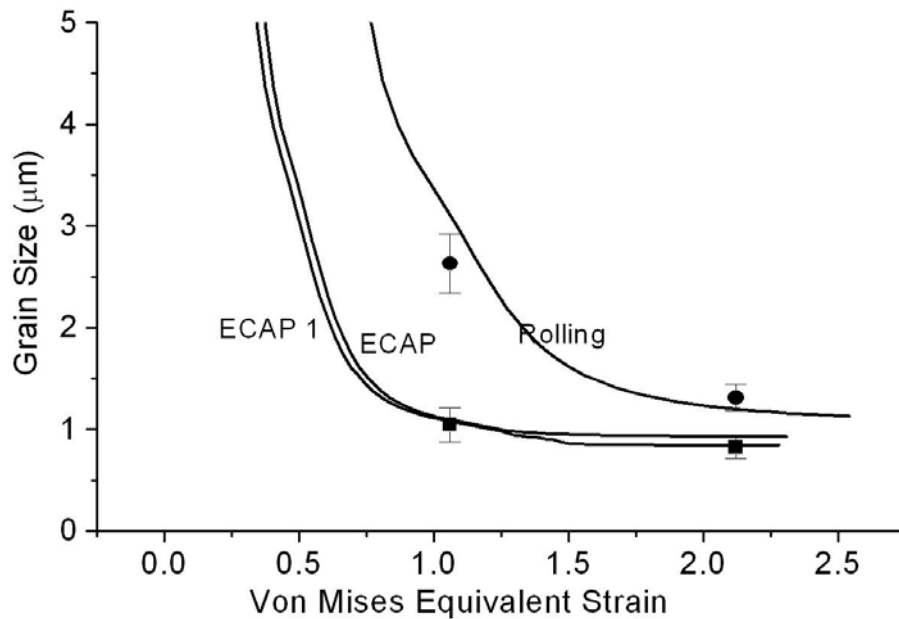


Figure 4-19. Simulated (continuous lines) and experimental (symbols) development of average grain size obtained in ECAP and rolling. Two simulations are shown for ECAP; the difference between them is the initial texture which was rotated by 90° for ECAP1.

4.4.3 Lattice rotation versus strain path

Orientation of initial texture with respect to the applied strain path

The simulation results presented in the preceding section show that the strain path is important in the grain refinement process. However, as the model is based on the lattice

4: Grain Fragmentation in ECAP-ed Copper

distortion due to its rotation, it must be sensitive to not only the strain path but also the initial texture. This means that to examine only the effect of strain path, the initial texture has to be oriented in the same manner for both ECAP and rolling. One can satisfy this condition by examining the deformation state for the two tests and then orient the texture accordingly.

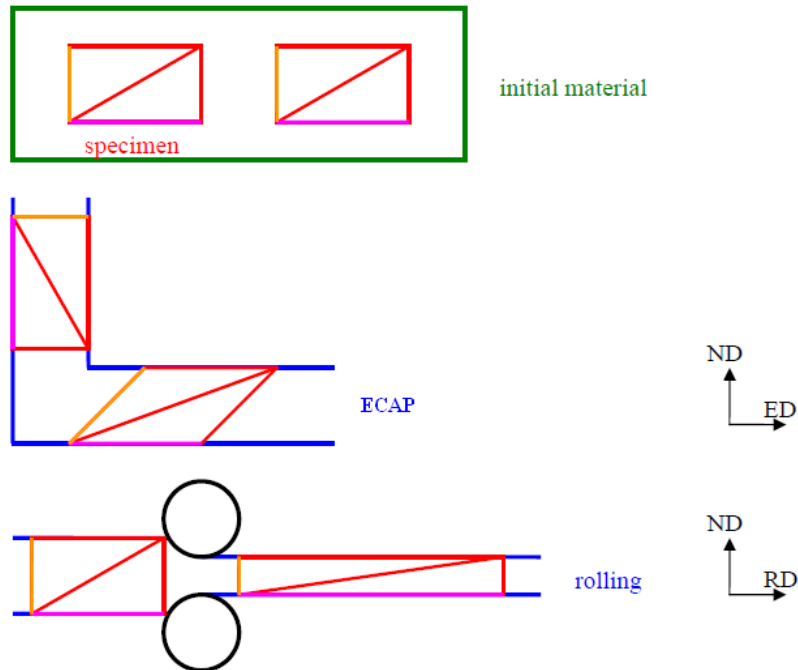


Figure 4-20. Analysis of the deformation processes in ECAP and rolling to show that the initial textures in the ECAP and rolling processes are 90° rotated with respect to the deformation (follow pink colored lines).

The deformation state of a material element during ECAP is such that there is elongation in the ED direction and compression in the ND direction [137], exactly like in rolling. The difference between the two deformation modes is only the presence of a large rigid body rotation during ECAP [28, 137]. In this study, the samples with the same geometry as for ECAP were rolled so that the initial rod axis direction coincided with the rolling direction (Fig. 4-20). The orientations of the transverse (TD) and normal directions (ND) were not necessary to be specified as the initial texture was very weak and the samples had a rotational symmetry around the longitudinal axis anyway. The specimens are subjected to the deformation procedure in the manner indicated in the sketch with the pink line initially vertically (for ECAP) and horizontally (for rolling), and both the two pink lines end horizontally along ED (ECAP) or RD (rolling), shown in Fig. 4-20. This represents a 90° rotation of the initial texture between the two tests.

4: Grain Fragmentation in ECAP-ed Copper

However, this 90° rotation of the initial texture should be only important for strong initial textures. In our study presented here, the texture intensity varied between 0.8 and 1.2 (Fig. 4-1) which can be considered as a nearly random texture. Therefore, it is expected that the effect of the initial texture is negligible meaning that the differences in the obtained microstructures mainly come from the differences in the applied strain paths. For verification purposes, the ECAP simulation was repeated with the initial texture rotated 90° around the TD axis. The result of that simulation is also shown in Fig. 4-19 (ECAP1). One can see that the result is very near to the non-rotated case (indicated by ECAP in the figure). For a strong initial texture the grain refinement can be significantly modified and it would be interesting to investigate such effect in future works.

Following the condition of $\dot{\gamma} = 2\dot{\epsilon}$ discussed above, the imposed strain rate was $\dot{\epsilon} = 0.4s^{-1}$ in rolling while the ECAP shear rate was set to $\dot{\gamma} = 0.8s^{-1}$ in the polycrystal grain refinement simulations. In this way, the lattice rotations could be directly compared for the two strain paths. The results obtained in this way for the lattice rotation are displayed in Fig. 4-21. Initially the lattice rotation rate in ECAP is about twice as high as in rolling (Fig. 4-21a). Lattice rotation rate decreases continuously during rolling but is always much smaller than in ECAP. Consequently, the integrated total lattice rotations are larger in ECAP with respect to rolling, see Fig. 4-21b.

After the first pass in ECAP, the lattice rotation rate becomes very large at the beginning of the second pass which appears as a kink in the curve of the total rotation, see Fig. 4-21b. This second feature can be explained by the non-monotonic nature of the strain path that the material experiences during ECAP. Namely, between each successive passes, a 90° rotation around the TD axis of the die is needed to re-position the sample into the die for the subsequent pass (this rotation about TD is common for all routes, including route A). This rotation brings the crystal orientations 90° away from their orientations achieved during the first pass [28, 138]. During the first pass orientations were converging towards the ideal positions. In ECAP, this process has to restart in the second pass. This non-monotonic nature of the ECAP process thus always involves large lattice rotations, much larger than in rolling, which is a monotonic strain path. Therefore, it is expected that the larger lattice rotations will lead to more efficient grain fragmentation, producing in this way significantly smaller grain sizes from the ECAP process.

4: Grain Fragmentation in ECAP-ed Copper

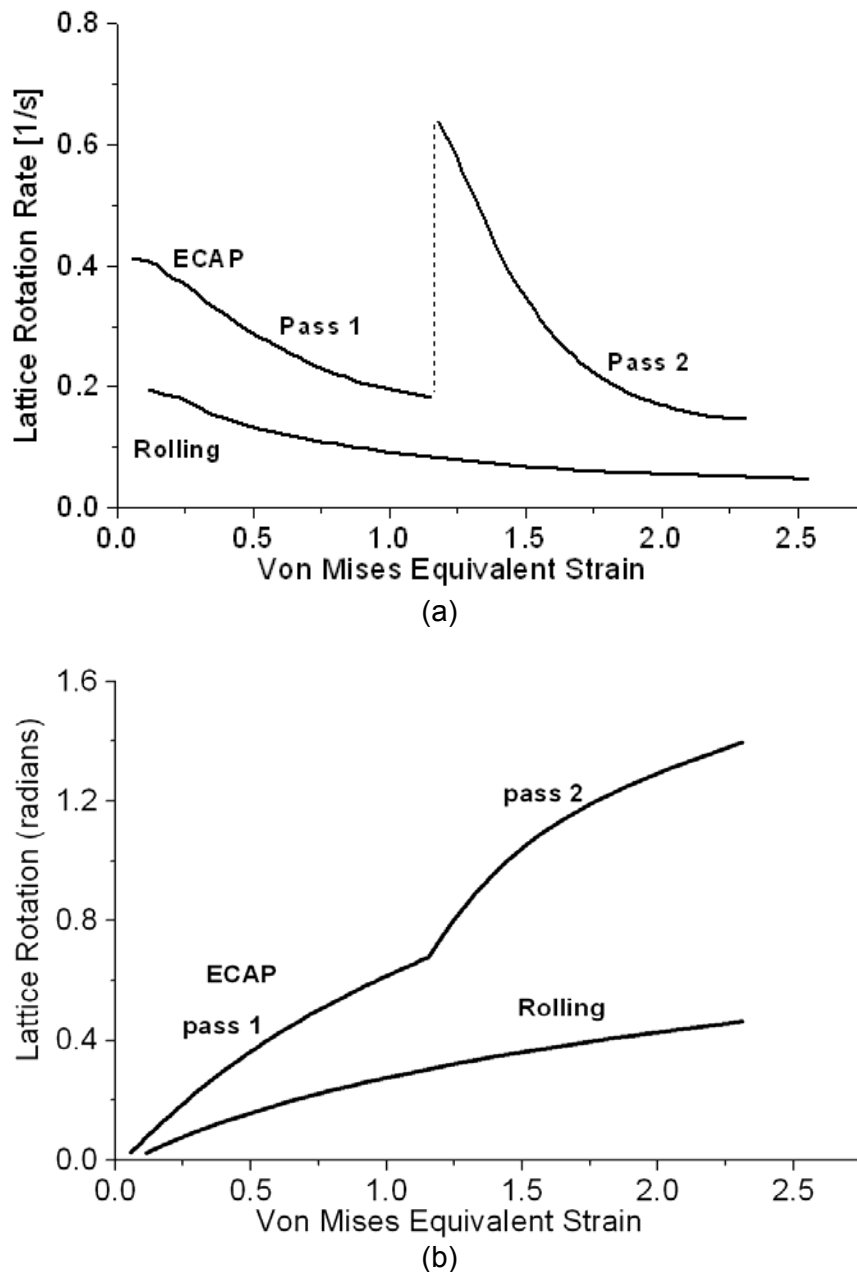


Figure 4-21. The average lattice rotation rate (a) and total lattice rotation (b) as a function of the equivalent strain obtained from the grain refinement simulation of ECAP as well as rolling.

Note that in the grain refinement model the occurrence of grain subdivision is controlled by the *absolute value* of the lattice rotation, not by the lattice rotation *rate* [20]. This is why there is no clearly visible abrupt change in the predicted average grain size in ECAP at the beginning of the second pass in Fig. 4-21 (there is, nevertheless, an increase in the negative slope, not easily visible in the figure). The larger the lattice rotation the more lattice curvature develops in the grains which accelerates the grain subdivision process [20]. Fig. 4-21b displays clearly a huge difference in the lattice rotations between ECAP

4: Grain Fragmentation in ECAP-ed Copper

and rolling which is increasing more at the beginning of the second pass. The 90° rotation of the sample between passes contributes significantly to the larger average value of the absolute lattice rotation which is responsible for the smaller grain size in ECAP.

This section has explained why the lattice rotation rate in general is smaller in rolling than in ECAP. To understand this, one has to consider the following relationship among the lattice rotation rate $\dot{\Omega}$, the rigid body rotation rate $\dot{\beta}$ and the plastic rotation rate $\dot{\omega}$ [139]:

$$\dot{\Omega} = \dot{\beta} - \dot{\omega} \quad (4-6)$$

When this relationship is used in ECAP, there is a large amount of rigid body rotation rate, which is displayed in Eq. (4-4). In rolling, however, $\dot{\beta}$ is absent, thus, the lattice rotation is directly equal to the plastic rotation rate:

$$\dot{\Omega}_{ECAP} = \dot{\beta} - \dot{\omega}, \quad \dot{\Omega}_{Rolling} = -\dot{\omega} \quad (4-7)$$

As shown above, the crystallographic slips of the crystals are the same in the present ECAP and rolling, thus, plastic rotation rates are also identical. It follows then from Eq. (4-7) that:

$$\dot{\Omega}_{ECAP} = \dot{\beta} + \dot{\Omega}_{Rolling} \quad (4-8)$$

Although this relation is valid only for individual crystals and with the same orientation in the two tests, it is clear that when the average of the absolute values for all the crystals are calculated the average lattice rotation rate is larger in ECAP compared to rolling. This is what explains the differences in the obtained final grain size which is significantly smaller for ECAP than for rolling at the same equivalent strain.

4.5 Split of Misorientation Distribution

It has been shown in section 4.3.3 above that the modeling can only predict misorientations between new grains of the same parent grain. In the present section, it will be shown how the experimental measured misorientation distribution can be split into two populations of grains for one of them being the 'internal' and the other is the 'grain-boundary' part that will be defined more precisely below.

4.5.1 Background

Two kinds of misorientation distributions are of interest: the so called correlated and uncorrelated distributions. The correlated one is defined in terms of the distribution density function of misorientations between neighboring grains, while the non-correlated one is calculated on the basis of misorientations between grains randomly selected from the grain population. The correlated distribution will be named in the present work as next-neighbor misorientation density ('NNMD') function.

This section mainly focuses on examining the correlated misorientation distribution density function $\nu(\theta)$ for neighboring grains in a microstructure produced as a result of ECAP. The population of neighboring grains changes substantially due to the grain refinement process at large strains. Any given original grain is replaced by a large number of smaller grains and all these 'daughter' grains have their origin within the 'parent' grain. For example, if we make a simplifying assumption of a cube-shaped parent grain being progressively subdivided into smaller cube-shaped grains, such a grain initially 20 μm in size will contain about 20^3 new grains when the refined grain size goes down to about 1 μm . The misorientation distribution between these daughter grains is expected to be very different from the one associated with the neighbors that are situated across the parent grain boundaries; that is, between grains that stem from different parent grains. When an EBSD measurement is carried out after a high degree of grain refinement, the original grain boundaries are not distinguishable from the newly emerged ones. Note that due to the large plastic strain in SPD processing, the initial grain boundaries cannot be distinguished from the new boundaries that are induced by the deformation process. Consequently, it appears impossible to obtain a separate misorientation distribution for the 'inner' grains, i.e. for those daughter grains within the same parent grain. In the following, a statistical technique is proposed which makes this distinction possible. The importance of obtaining such an intrinsic misorientation function is that it gives important information on the physics of the grain subdivision process.

4.5.2 Technique for obtaining the misorientation distributions

As described above, one can distinguish between two types of correlated grain-grain misorientations: (i) those between newly emerged daughter grains that originate within the same parent grain and (ii) those between daughter grains facing each other across an old grain boundary (GB) that separate distinct initial parent grains. In accordance with the definitions above, the first type will be called the 'internal' misorientation distribution and will be represented by the function $\nu_{\text{int}}(\theta)$, while the second type will be referred to as the

4: Grain Fragmentation in ECAP-ed Copper

'old boundary grain' misorientation distribution function, $\nu_{OBG}(\theta)$. Fig. 4-22 illustrates schematically these two populations. The measured total NNMD frequency is:

$$\nu_{total}(\theta) = f_{int}\nu_{int}(\theta) + f_{OBG}\nu_{OBG}(\theta) \quad (4-9)$$

Here f_{int} and f_{OBG} are the fractions of pairs of neighboring grains (one pair is defined as a grain and one of its neighbors) corresponding to the inner ("internal") grains and to the grains situated at the old GBs, respectively. These fractions will be determined below.

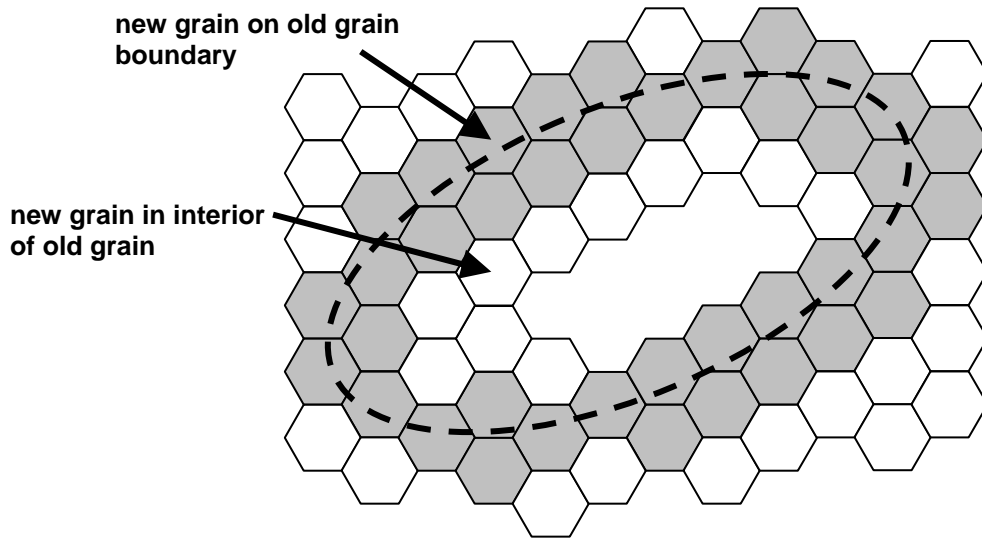


Figure 4-22. Schematic figure showing the trace of a boundary of an 'old' grain (broken line) together with the newly emerged finer grains represented by hexagons. New grains that are sitting at the old grain boundary are shaded.

A very similar decomposition was proposed by Pantleon [140], however, for another purpose: he examined the pixel-to-pixel misorientation distribution of the grain interiors and the same between the two sides of large angle boundaries. Here, grain-to-grain misorientations are examined and will be presented in the following:

The total number of pairs of grain neighbors N^p contained in the measurement plane indexed by p ($p = ND, TD$ or ED) can be calculated as:

$$N^p = n_{OG}^p \left(N_{int}^p + \frac{1}{2} N_{OBG}^p \right) \quad (4-10)$$

4: Grain Fragmentation in ECAP-ed Copper

where N_{int}^p and N_{OBG}^p are, respectively, the numbers of pairs within the inner part and across the boundaries of a parent grain. n_{OG}^p is the number of the original (or initial) grains covered in the measurement which is given by $n_{\text{OG}}^p = A_{\text{map}}^p / A_{\text{OG}}^p$ with A_{OG}^p being the theoretical area of the parent grains in their deformed state and A_{map}^p the map area. The division by 2 in the 'OBG' part of Eq. (4-10) is necessary as the misorientations across an 'old' grain boundary have to be counted only once for a pair of adjoining grains. Dividing by N^p on both sides of Eq. (4-10) leads to:

$$n_{\text{OG}}^p \frac{N_{\text{int}}^p}{N^p} + \frac{n_{\text{OG}}^p}{2} \frac{N_{\text{OBG}}^p}{N^p} = 1 \quad (4-11)$$

On the basis of this relation, the two fractions (or, in other words, the two weight factors) attributed to the two kinds of misorientations introduced in Eq. (4-9) can be defined as:

$$f_{\text{int}}^p = n_{\text{OG}}^p \frac{N_{\text{int}}^p}{N^p}, \quad f_{\text{OBG}}^p = \frac{n_{\text{OG}}^p}{2} \frac{N_{\text{OBG}}^p}{N^p} \quad (4-12)$$

The following relation between the fractions defined above is fulfilled:

$$f_{\text{int}}^p + f_{\text{OBG}}^p = 1 \quad (4-13)$$

Substitution of N^p from Eq. (4-10) in Eq. (4-12) yields the following expressions for the two fractions, or weight functions:

$$f_{\text{int}}^p = \frac{N_{\text{int}}^p}{N_{\text{int}}^p + \frac{1}{2} N_{\text{OBG}}^p}, \quad f_{\text{OBG}}^p = \frac{N_{\text{OBG}}^p}{2N_{\text{int}}^p + N_{\text{OBG}}^p} \quad (4-14)$$

The relative fractions of the two distributions introduced in Eq. (4-9) can be calculated from Eq. (4-14) if N_{int}^p and N_{OBG}^p are known. In the following, a procedure is presented which permits to obtain a good estimation of these quantities. It is sufficient to determine only one of them as Eq. (4-10) permits to obtain the other.

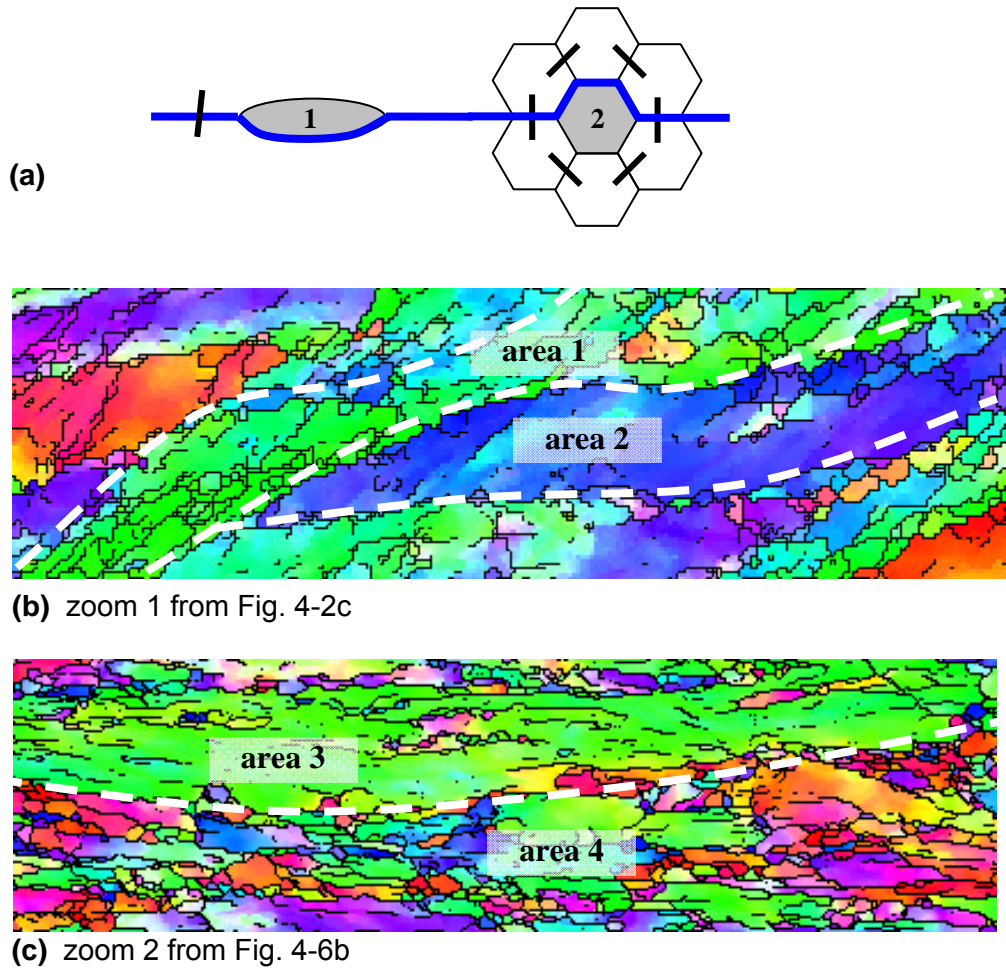


Figure 4-23. (a): Schematic illustration of the number of interconnected first neighbors around a grain for two “extreme” cases, the interconnections are indicated by short thick segments, and the blue line represents an old grain boundary; (b) and (c): Zooms in the EBSD map after 1 pass ECAP on the TD plane, and after 3 passes ECAP on the ED plane, respectively.

With the new OIM software of Beausir [123], it is possible to calculate from the experimental EBSD maps the following quantities that are of interest in the present analysis:

- the average boundary length between two neighbouring grains, $\langle l_g^p \rangle$;
- the average number of interconnected first neighbours around a grain, $\langle c_g^p \rangle$.

The average boundary length can give the approximate number of new grains located on one side of the original grain boundary by $L_{OGB}^p / \langle l_g^p \rangle$, where L_{OGB}^p is the average boundary length of the parent grain in its deformed state. The average number of

4: Grain Fragmentation in ECAP-ed Copper

interconnected grains $\langle c_g^p \rangle$ is a parameter borrowed from information technology (network system of computers [141]) which in its present use means the number of neighbours of a grain which are themselves neighbours (or can 'communicate with' in its IT meaning). For illustration, some special cases for this quantity are displayed in Fig. 4-23a.

When only one isolated new grain is situated along an original GB, then $\langle c_g^p \rangle = 1$. When a new grain is surrounded at all sides with other new grains in a hexagonal pattern, then $\langle c_g^p \rangle = 6$. Using the above defined quantities, the number of pairs of neighbours for one parent grain across its new boundary in the deformed state can be estimated as:

$$N_{OBG}^p = \frac{\langle c_g^p \rangle}{2} \frac{L_{OGB}^p}{\langle l_g^p \rangle} \quad (4-15)$$

The division by 2 in Eq. (4-15) expresses the assumption that for a given grain in the old GB region about half of the neighbor grains are situated on the opposite side of the initial GB.

One may argue that the above estimation could be used only for a relatively uniform microstructure. Indeed, the EBSD maps, especially at lower strain (after one pass ECAP), show features of non-uniformity. There are zones that contain few grains and others with many grains. Selected areas taken from the TD section EBSD map of pass 1 and from the ED section of three passes ECAP material are shown in Figs. 4-23b-c. The dotted lines delineate zones with very different microstructures. Independently of the number of passes the microstructure is inhomogeneous. Areas 1 and 4 are quite homogeneous in terms of grain refinement from experimental observation (Figs. 4-23b-c). On the contrary, Areas 2 and 3 display heterogeneous grains structure exhibiting many incomplete (non-closed) boundaries and a few isolated grains. These inhomogeneities are probably due to the orientation dependence of the grain fragmentation process; see recent modeling results based on such assumption in [20]. These diverse features have a significant effect on the two parameters introduced above, i.e., the number of interconnected neighbors $\langle c_g^p \rangle$ and the average boundary length between two neighboring grains $\langle l_g^p \rangle$, which are able to account for such a variability of the microstructures. Both parameters were actually measurement-plane dependent; their numerical values are compiled in Table 4-1.

4: Grain Fragmentation in ECAP-ed Copper

The last parameter of the present calculation is the boundary length of the initial ('old') grain L_{OBG}^p in its deformed state on different plane sections of the sample. It can be obtained from the geometry of the deformation process if the average initial grain size and the plane of the section are known (see the following description of relations for grain shape changes in ECAP route A).

Table 4-1. The average boundary length between two neighbouring grains, $\langle l_g^p \rangle$, and the average number of interconnected first neighbours around a grain, $\langle c_g^p \rangle$, measured from the EBSD maps on different planes of one-pass and three-pass deformed samples. The calculated 'internal' as well as the 'old boundary grain' type fractions are also indicated.

	$\langle l_g^p \rangle$ on TD	$\langle l_g^p \rangle$ on ED	$\langle c_g^p \rangle$ on TD	$\langle c_g^p \rangle$ on ED	f_{int}^{TD}	f_{OBG}^{TD}	f_{int}^{ED}	f_{OBG}^{ED}
Pass 1	1.1 μm	1.6 μm	2.5	5	0.726	0.274	0.509	0.491
Pass 3	0.57 μm	0.57 μm	5.4	7.0	0.517	0.483	0.351	0.649

Relations for grain shape changes in ECAP route A

The dimensions of the deformed initial grain can be obtained from the geometry of the process. The following formulas refer to route A processing. Assuming that the initial form of a grain is spherical, the simple shear process of ECAP transforms it into an ellipsoid. The semi-major axis a and the semi-minor axis b of the corresponding ellipse on the TD plane can be obtained from the following equations:

$$\frac{a}{b} = \frac{1}{2} \left(\gamma^2 + 2 + \gamma \sqrt{\gamma^2 + 4} \right), \quad c^2 = ab \quad (4-16)$$

where $\gamma = 2n$ is the total shear strain after n ECAP passes and $2c$ is the initial grain diameter. On the ED plane, the old grain boundaries appear as ellipses with major axes parallel to TD. The semi-minor axis of the ellipse on the ED plane, denoted l , can be obtained from the following relations:

$$\frac{c}{l} = \sqrt{\frac{b}{a} \sin^2 \alpha + \frac{a}{b} \cos^2 \alpha}, \quad \alpha = \frac{1}{2} \arctg \left(\frac{2}{\gamma} \right) \quad (4-17)$$

4: Grain Fragmentation in ECAP-ed Copper

where α is the orientation of the ellipse on the TD plane with respect to the ED plane, see Fig. 4-24. The major semi-axis is given by c on the ED plane.

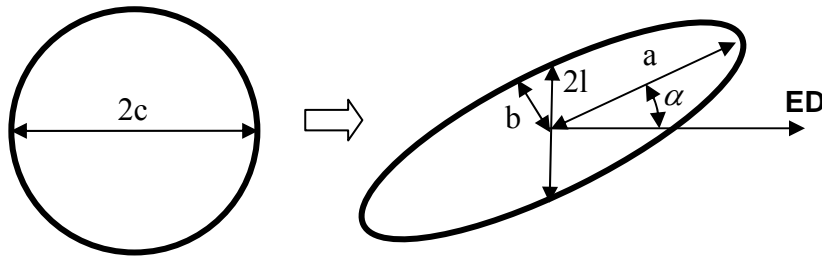


Figure 4-24. Geometry of an old grain on the TD plane in ECAP

Once the two semi-axes of the ellipse (a and b) are known, the perimeter of the ellipse, that is L_{OGB}^p , can be calculated using the approximation of Ramanujan [142] on both the ED and TD planes:

$$L_{OGB}^p = \pi \left[3(a+b) - \sqrt{(a+3b)(3a+b)} \right] \quad (4-18)$$

The variation in grain size is not considered here, only the average value. In this way, the calculated L_{OGB}^p value is also an average. However, using a single value for the deformed grain size does not mean that the Taylor approach of polycrystal plasticity is adopted in the present work. Individual grains may deform differently. Their average shape, however, always follows the shape change of the macroscopic sample.

Decomposition of NNMD

Note that all quantities in the above relations can be obtained from the orientation imaging maps and the geometry of the process. Now from Eq. (4-9), the internal part of the NNMD function is expressed as:

$$v_{\text{int}}(\theta) = \frac{v_{\text{total}}(\theta) - f_{OGB} v_{OGB}(\theta)}{f_{\text{int}}} \quad (4-19)$$

As mentioned above, two planes were selected for the EBSD measurements: the ED and TD planes. The ND plane was not used here as the corresponding statistics for old GB type misorientations was insufficient for that plane. Actually, in route A ECAP testing, the shape of an initial grain remains the same on the ND plane, so that only a small fraction of the new grains are situated along the old grain boundaries (its grain boundary does not

4: Grain Fragmentation in ECAP-ed Copper

stretch). Now we assume that both $\nu_{\text{int}}(\theta)$ and $\nu_{\text{OBG}}(\theta)$ are independent of the plane of measurement. Actually, it is not really an assumption since in this measurement we are dealing with two populations of misorientations which are not intermixed. The deviations between the measurements on different planes due to mixing of the two populations in different proportions depend on the plane. The misorientation values should not depend on which plane they are measured on, assuming that the orientation of the crystal lattice within a grain is uniform in 3D. Possible non-uniformities within the new grains are neglected in this approach, which is reasonable for the fine grained structure. Equation (4-19) can be used twice for two measurement planes, the ED and the TD:

$$\nu_{\text{int}}(\theta) = \frac{\nu_{\text{total}}^{\text{ED}}(\theta) - f_{\text{OBG}}^{\text{ED}} \nu_{\text{OBG}}(\theta)}{f_{\text{int}}^{\text{ED}}} \quad (4-20)$$

$$\nu_{\text{int}}(\theta) = \frac{\nu_{\text{total}}^{\text{TD}}(\theta) - f_{\text{OBG}}^{\text{TD}} \nu_{\text{OBG}}(\theta)}{f_{\text{int}}^{\text{TD}}} \quad (4-21)$$

The distribution density function $\nu_{\text{OBG}}(\theta)$ can be expressed from Eqs. (4-20) and (4-21) as:

$$\nu_{\text{OBG}}(\theta) = \frac{\nu_{\text{total}}^{\text{ED}}(\theta) f_{\text{int}}^{\text{TD}} - \nu_{\text{total}}^{\text{TD}}(\theta) f_{\text{int}}^{\text{ED}}}{f_{\text{OBG}}^{\text{ED}} f_{\text{int}}^{\text{TD}} - f_{\text{OBG}}^{\text{TD}} f_{\text{int}}^{\text{ED}}} \quad (4-22)$$

All quantities entering Eq. (4-22) are known, which permits calculating $\nu_{\text{OBG}}(\theta)$. Once $\nu_{\text{OBG}}(\theta)$ is known, $\nu_{\text{int}}(\theta)$ is obtained from Eqs. (4-9), (4-20) or (4-21).

4.5.3 NNMD implementation

Figs. 4-12 and 4-14 showed the measured NNMDs obtained on the ED and TD planes of the one- and three-pass ECAP samples. For the one-pass sample, several measured maps were considered in the construction of the NNMD. The Mackenzie distribution is also traced to enable comparison of the measured NNMD with a random distribution.

Using the procedure described above, the experimental misorientation functions shown in Figs. 4-2 and 4-6 were split into two distributions; the ‘internal’ and the ‘old boundary grain’ types. The results obtained are shown in Figs. 4-25 a-b for copper that went through one and three ECAP passes, respectively.

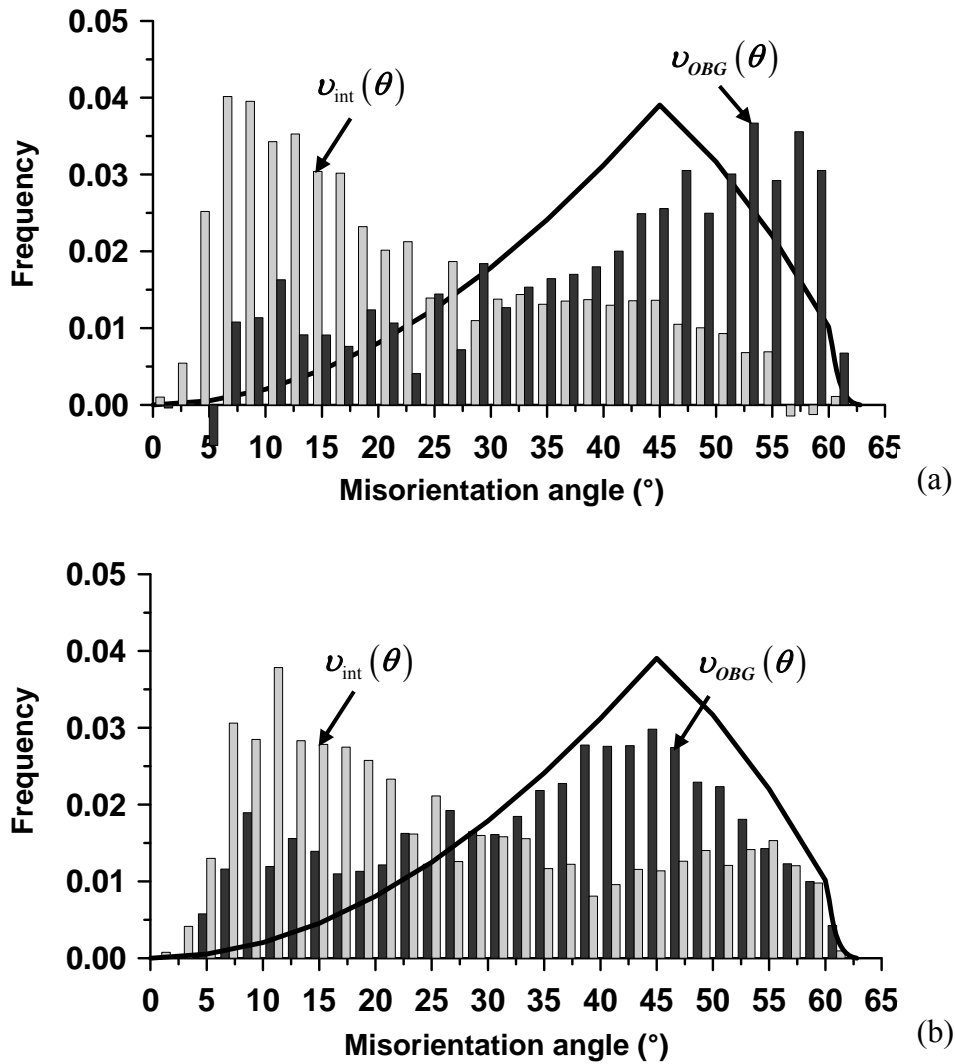


Figure 4-25. Split NNMDs for one pass (a) and three-pass (b) ECAPed copper; in light gray the old grain-interior frequency distribution ($\nu_{int}(\theta)$) and in dark gray the old boundary layer grain distribution ($\nu_{OBG}(\theta)$).

It should be emphasized again that the distributions shown in Figs. 4-25a-b were calculated on the basis of misorientations between identified neighboring grains, not between measurement pixels, as it is common in the literature, see above. For this purpose a special software, already mentioned before, was developed by Beausir [123].

4.5.4 Discussions on NNMD

As can be seen from Figs. 4-25, the ‘internal’ and ‘old-grain-boundary’ misorientation distributions are radically different. Within the parent grain interiors, the misorientation frequency is high for low angles while the misorientations across old grain boundaries

4: Grain Fragmentation in ECAP-ed Copper

occur with high frequencies for large angles. It is also clear that there exists a large population of new grains adjacent to grain boundaries that have relatively low misorientation angles. This may be a result of the development of the texture which promotes such lower misorientation angles [140]. The internal misorientation distribution can also be interpreted in terms of a mechanism of progressive grain subdivision by dislocation cell formation within parent grains with gradual accumulation of misorientation between cells separated by dislocation cell walls. In the recent model of grain refinement [20], when interpreting the obtained misorientation distribution, it was assumed that the part of the misorientation distribution associated with old grain boundaries was random. The present results show that such hypothesis is actually a rather crude approximation.

There are also some negative frequency values the present analysis returned, cf. Fig. 4-25), which need discussion. Of course, such values are unphysical; however, as these distributions were obtained from calculations, this may happen in certain circumstances, as analysis that Eq. (4-20) shows. With the present experimental data for the pass one sample, see Table 4-1, the denominator in Eq. (4-22) is positive, and hence only a negative value of the numerator can lead to a negative $\nu_{OBG}(\theta)$. Using again the experimental values for the weight factors obtained for the one pass sample, one can see that for the frequencies to be positive the difference between $\nu_{total}^{ED}(\theta)$ and $\nu_{total}^{TD}(\theta)$ must not exceed 30% of the smaller of the quantities. This requirement, however, is violated in some cases in experiment. This may be the result of a deficiency in the statistics in a particular range of misorientation angles, meaning that the experimental misorientation distributions obtained on different planes are not fully representative of the microstructure. It was discussed in the experimental results that the textures can be used as indicators of the quality of the statistics, which was not perfectly satisfactory in the EBSD maps for the one pass sample on the TD plane. Generally, it was estimated that in order to obtain statistically valid results with the present analysis, at least 10000 pairs of neighbor grains should be present in an EBSD map for each section. For the one pass sample maps, the number of grains was 10473 on the TD plane and 11589 on the ED plane. Better statistics was achieved for the sample that underwent three ECAP passes where these numbers were 28946 and 31727, respectively. This statistics is important in a particular range of misorientation angles, meaning that the experimental misorientation distributions obtained on different planes in the proposed NNMD technique can be fully representative for the actual microstructure.

4: Grain Fragmentation in ECAP-ed Copper

The technique proposed for deconvoluting the experimental NNMDs into grain interior and grain boundary fractions may be of great significance for understanding the mechanism of grain refinement. For example, in ECAP the parent grains in the ED section become extremely flat for large numbers of ECAP passes with the consequence that the fraction of the old grain boundary part of the misorientation function becomes the major element in the total misorientation distribution function. Table 4-1 shows that already after the first ECAP pass, the fraction of misorientations across the grain boundary of the parent grains is 49% on the ED plane. This value increases to about 65% after the third pass. Thus, the shift of the total distribution towards large angles can be simply a consequence of the geometry-driven changes in the shape of the parent grains. Such results with respect to the overall misorientation distribution were already observed as early as in 1996 [143].

In the grain refinement model presented in [20] it is suggested that fragmentation begins at the grain boundaries due to a slow-down of lattice rotation in those regions, which produces lattice curvature. The present analysis supports that hypothesis providing experimental evidence for large misorientations in the boundary regions of the initial grains. New grains also emerge in the interior of the parent grains with a misorientation distribution which has a high peak at low angles without showing large development with strain. A comparison of the $\nu_{\text{int}}(\theta)$ distributions for the one- and three-pass deformed samples testify that the differences in the misorientation distribution fractions stemming from the two regions ('old boundary' and 'internal') are documented in their characteristics presented in Table 4-1. For the most part, though, they are due to the geometry variation of the initial grains.

4.6 Summary

Grain refinement modeling in ECAP-ed and rolled copper has been studied in this Chapter. The main findings are the following:

- i) A comparative experimental and simulation study of ECAP-ed one-pass and two pass has been performed. It was found that the microstructure in the ECAP deformed one pass copper was much more refined on the TD plane than on the other orthogonal planes. The grain size from both passes observed experimentally can be fairly well predicted by the grain fragmentation model. From our observation, texture does not change greatly from the effect of grain refinement. Similar conclusions were also confirmed by existing simulation work carried out without consideration of grain refinement [28]. Those simulations also led to a

4: Grain Fragmentation in ECAP-ed Copper

good agreement with experimental texture development. The reason behind this is that grain refinement slightly changes the orientation of a subgrain with respect to the parent grain but the overall deformation mode still remains the same. Texture components are formed in the convergent regions of the velocity field in the orientation space and do not move away from its original stable position, even if misorientations build up due to subgrain formation.

- ii) The grain fragmentation process is more effective in ECAP compared to rolling at the same equivalent strain. It is the larger lattice rotation in ECAP which is responsible for marked differences in the grain sizes. The simulation results confirmed the basic hypothesis of the grain refinement model, namely, larger lattice rotation rate leads to smaller grain size, is in agreement with experimental observations. In this way, this proposed grain fragmentation modeling was convincingly validated and gave the great confidence to characterize UFG materials used in micro-forming.

- iii) Next-neighbour misorientation distribution functions measured on copper samples severely deformed by ECAP in route A up to three passes. It has been found that the misorientation distributions depend on the measurement plane. This dependence, as well as other details of the evolution of the misorientation distribution, was interpreted in terms of the geometry changes of the initial grains. This new statistical type technique permits us to split the misorientation distribution into the grain interior and the grain boundary related constituents, without a need to identify the old grain boundaries in actual experiment. It has been also shown that the shift of the misorientation distribution towards large misorientation angles caused by grain fragmentation under severe plastic deformation is mostly due to the geometry changes of the initial grains constituting the polycrystal. It has been found that the new grains created in the interior of the parental grains mostly contribute to the range of relatively small misorientation angles. Oftentimes it is claimed that a large number of ECAP passes are needed to increase the fraction of large angle grain boundaries. In light of the above considerations, the observed shift towards large misorientation angles in a grain structure may be a result of sheer geometry of grain deformation, rather than a genuine, intrinsic rise in the misorientation between two newly-formed grains separated by an inner boundary. We consider this as an important corollary of the considerations presented in this work.

5

TEXTURE ANALYSIS DURING MICRO DEEP DRAWING

5. TEXTURE ANALYSIS DURING MICRO DEEP DRAWING

The previous Chapter studied the effect of lattice rotation on the different strain path – ECAP and cold rolling – with a main focus on the role of grain refinement under different strain. This Chapter will use the measured and predicted data to look especially at the texture changes during micro deep drawing. It aims to study how texture is varying during micro-forming when an already initially textured UFG material is used for forming. ECAP-ed grain sizes are commonly around 250 nm, and in most cases micro-forming allows a t/D ratio far greater than the critical value at which individual orientations play a significant role, and thus these materials are promising candidates for micro-forming processes. However, since the optimal starting microstructure for micro-forming is not obvious, it is necessary to investigate the influence of the number of ECAP passes on the bi-axial ductility in a micro deep-drawing test [19].

5.1 Deep Drawing Experiments

5.1.1 Tensile properties of ECAP-ed copper

The CG as-received copper had a relatively low strength and a total elongation strain of 50% and upwards, whereas the ECAP-ed samples showed a significant increase in strength but a considerable decrease in ductility (see Fig. 3-5 in Chapter 3). The maximum or peak stress was achieved within 1–2% of uniform elongation; however, there was a relatively high post-uniform elongation of about 8–9%. The sample subjected to four ECAP passes had the poorest ductility but maximum tensile strength (see Fig. 3-5). Fig. 5-1 shows another analysis of the tensile behaviour, as a function of number of passes. As can be seen, the tensile strength is gradually increasing up to four passes while the total elongation is decreased. For more passes, the peak stress decreased while the total elongation increased very significantly.

5: Texture Analysis During Micro Deep Drawing

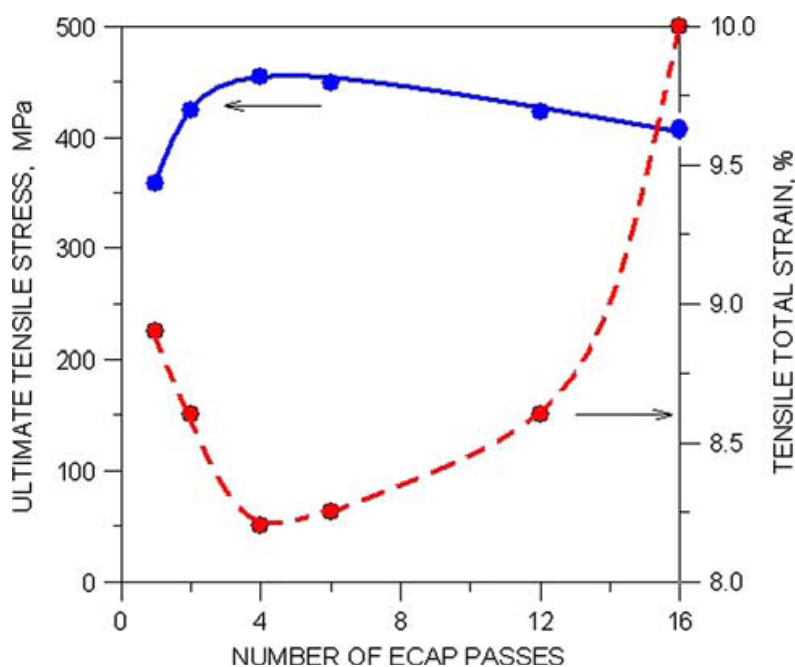


Figure 5-1. Tensile strength (solid line) and tensile ductility (dash line) as a function of number of ECAP passes

5.1.2 Deep drawability of ECAP-ed copper

Several typical drawn cups are shown in Fig. 5-2 with decreasing the blank sizes from the left to the right hand side. The LDR versus number of ECAP passes is shown in Fig. 5-3 for the as-received and one pass ECAP-ed materials. The material processed by one ECAP pass has a low LDR (below 1.9) due to the poorest tensile ductility. A slight increase in LDR can be seen with number of passes increasing up to four (Fig. 5-4), confirming an improvement in deep drawability, perhaps, due to increased normal plastic anisotropy, r value, as observed for UFG aluminium [144]. (r value was not, however, measured for the present copper case). Starting from four passes, the LDR remained fairly constant, in spite of the increase in tensile ductility (Fig. 5.1). Nevertheless, the LDR values for UFG copper for the cups of Fig. 5-2 drawn from blanks with four different diameters from copper pre-processed by one and four ECAP passes are fairly close to the range of 2.0–2.2 as seen in the normal scale deep drawing process with traditional coarse grained materials [145]. It is important to note that despite the big decrease in tensile ductility from about 50% for annealed copper to below 10% for ECAP processed copper, LDR of those materials differs insignificantly and, therefore, the drawability suffers insignificantly from grain refinement because more even properties can be achieved along the surface of the material by decreasing the grain size.

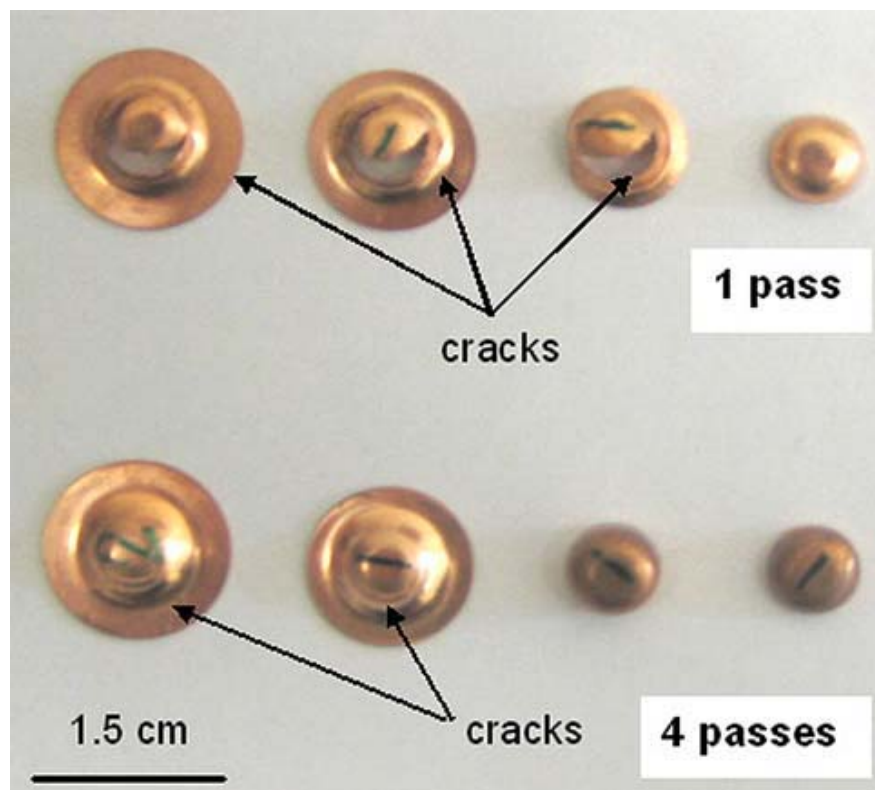


Figure 5-2. Cups drawn from blanks with four different diameters from copper pre-processed by one and four ECAP passes

5: Texture Analysis During Micro Deep Drawing

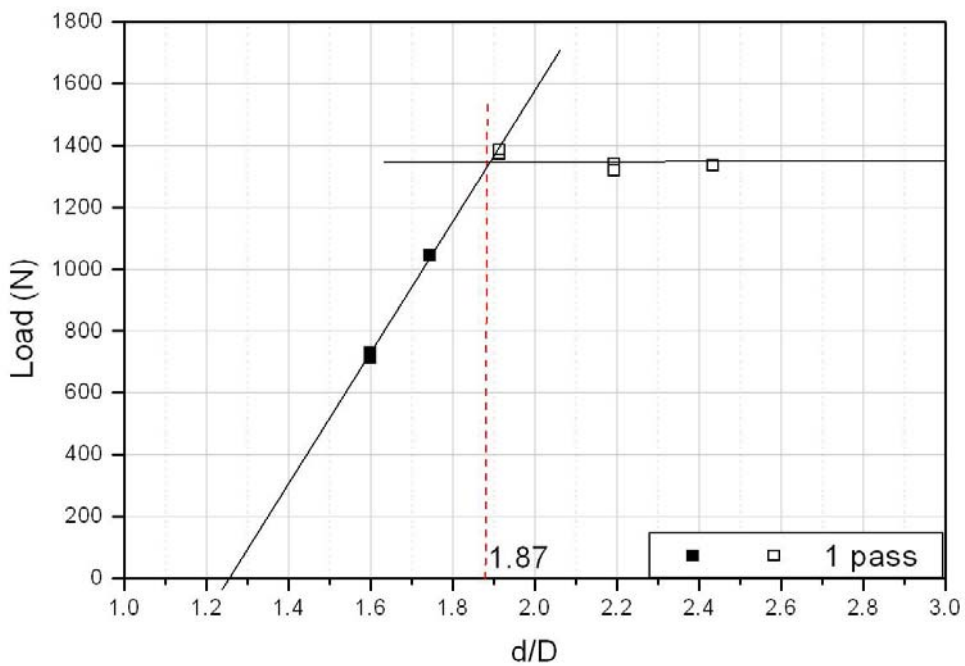
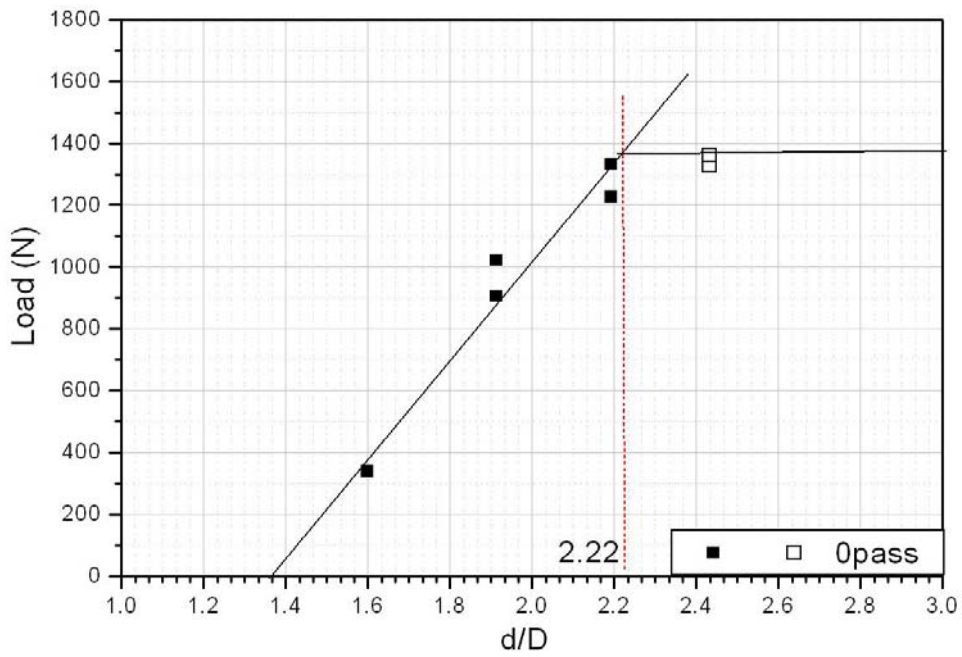


Figure 5-3. Load versus d/D for number of ECAP passes (experimental). Full and open symbols are used for non cracked and cracked samples, respectively.

5: Texture Analysis During Micro Deep Drawing

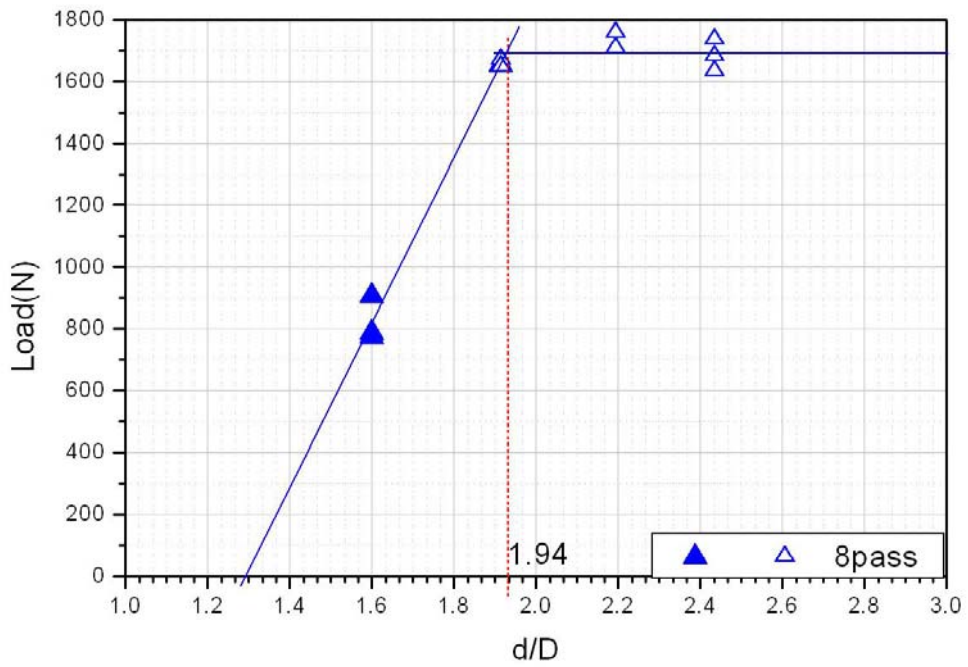
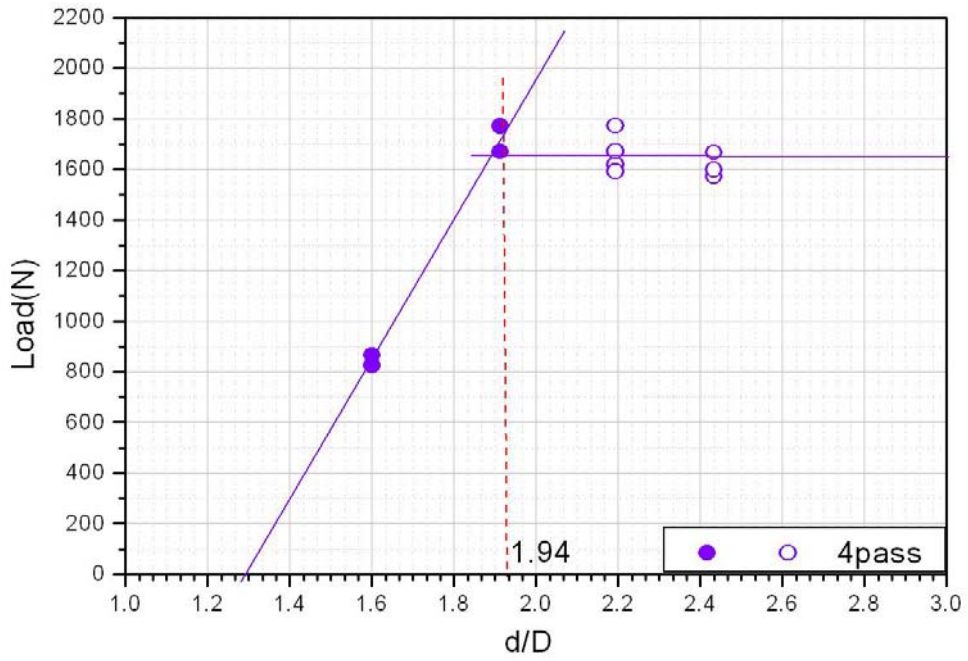


Figure 5-3. Continued

5: Texture Analysis During Micro Deep Drawing

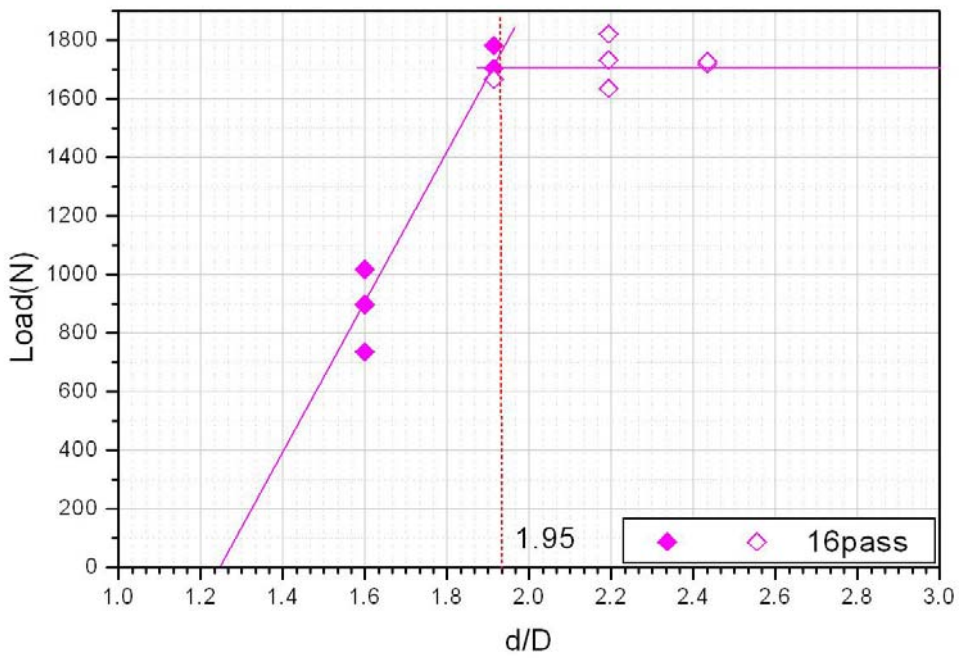
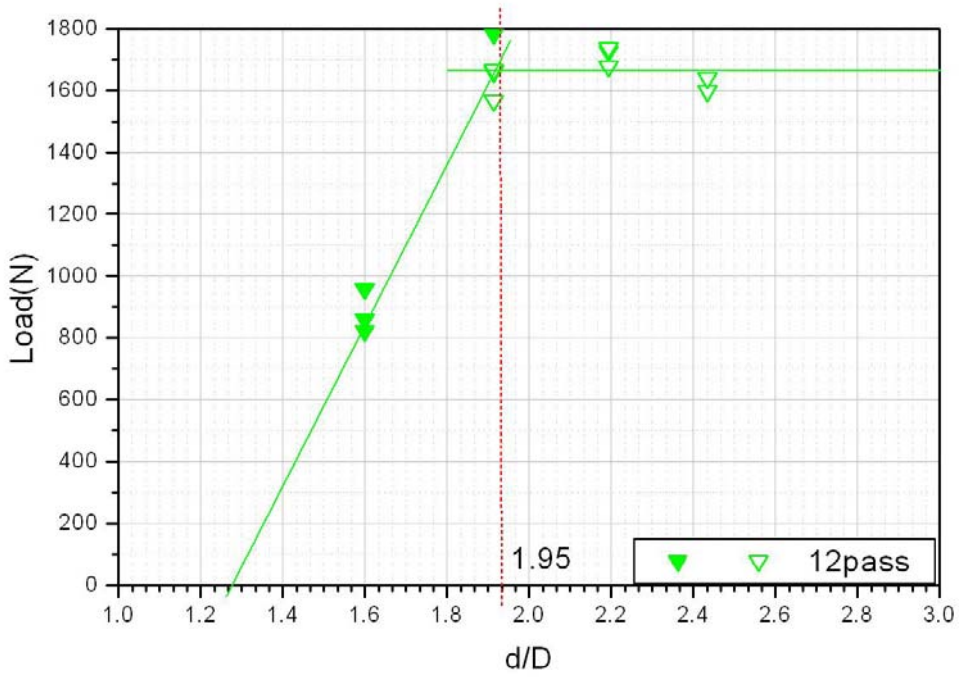


Figure 5-3. Continued

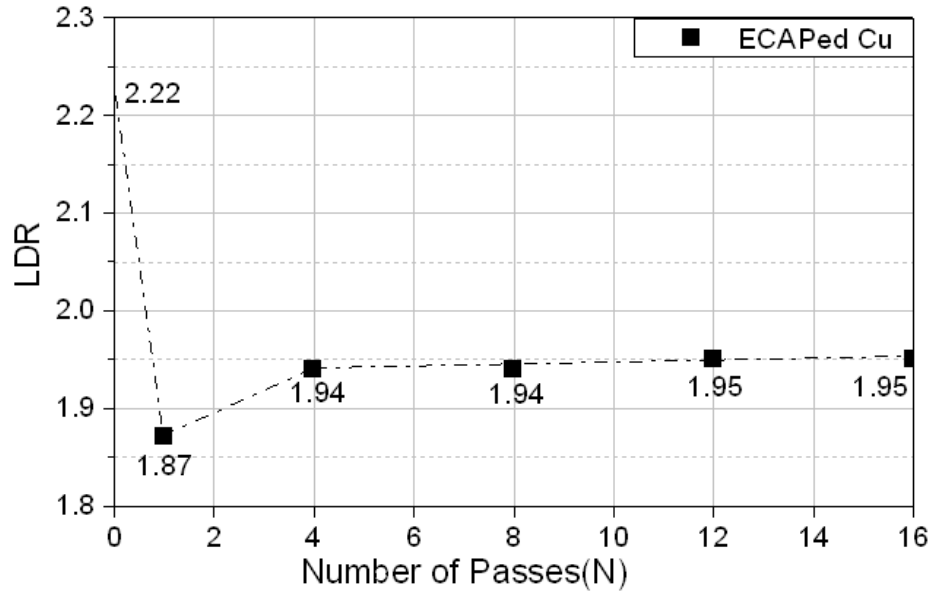


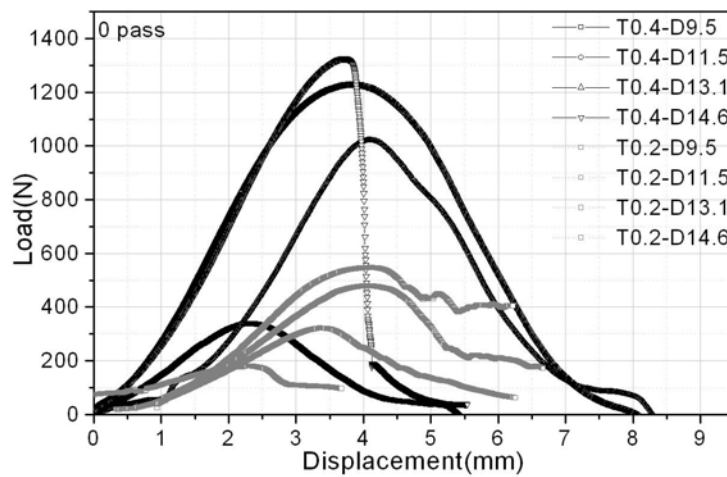
Figure 5-4. Limit drawing ratio versus number of ECAP passes (experimental)

5.1.3 Initial thickness effect on deep drawability of ECAP-ed copper

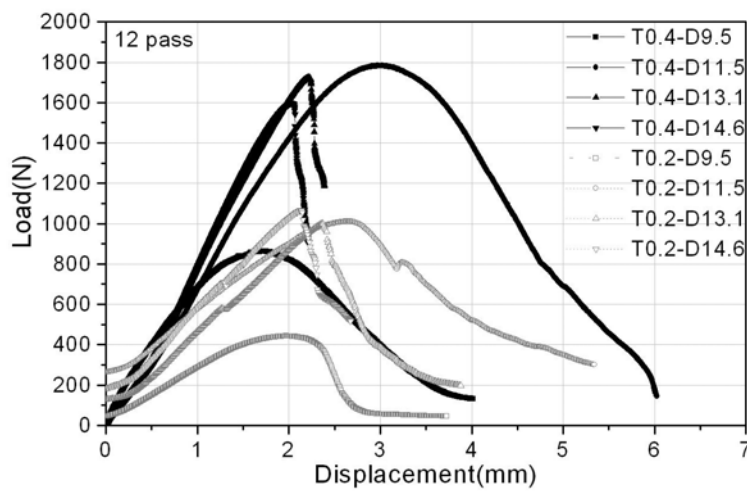
In this section it will be shown that the different initial thickness on drawability of the UFG specimen is minor. Concerning the maximum loading force, however, it is natural that it is reduced significantly when the thickness is smaller, see Fig. 5-5. The same trend was also observed by Chen et al. [146]. For CG copper, a further decrease in maximum load is observed. This decrease can be readily explained with the lower strength of the material. Fig. 5-6 shows a comparison of the measured LDR ratios for the 0.4 and 0.2 mm cases for the as received material and for the twelve pass ECAP pre-deformed samples. One can see that the limiting LDR is slightly larger for the as-received samples for 0.2 mm thickness while it is exactly the same for the twelve pass samples which have an UFG microstructure before cup drawing. Using the grain size and thickness, one can obtain that the volume fraction of the bulk grains decreased from 87.5% to 75% when the thickness is reduced from 0.4 mm to 0.2 mm for the present UFG structure. This is not very significant. As reported in Chapter 1.1 size effect occurs when the sheet thickness falls below the level of $15D$ [16, 17], where D is the grain size. In the present case, this critical limit is not reached. Because the UFG copper has such a large number of grains in its cross-section a thickness reduction of the blank from 0.4 mm to 0.2 mm leads to negligible effect in material behaviour mainly because the surface grains' contribution still remains small. Therefore, the observed decrease in drawing force is not related to a thickness effect [51] (Fig. 5-6). However, the mechanical behaviour of a material such as its strength depends on texture. When the thickness decreases relative to the grain size ($t/d < 15$) (Fig. 5-7), the texture will approach the local grain orientation, and orientation changes that take

5: Texture Analysis During Micro Deep Drawing

place during deformation are a consequence of the fact that deformation occurs on the most favourably oriented slip or twinning systems. For this reason, the grain structure of the deformed metal acquires a preferred orientation or texture. Therefore, it is interesting to investigate the texture evolution underlying observed t/d after micro-forming.



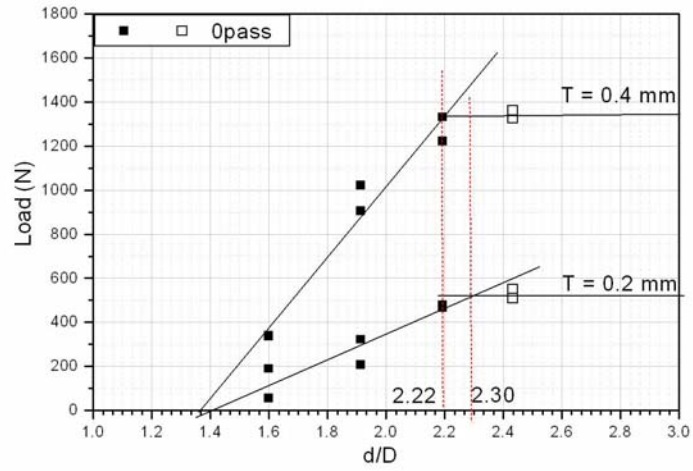
(a)



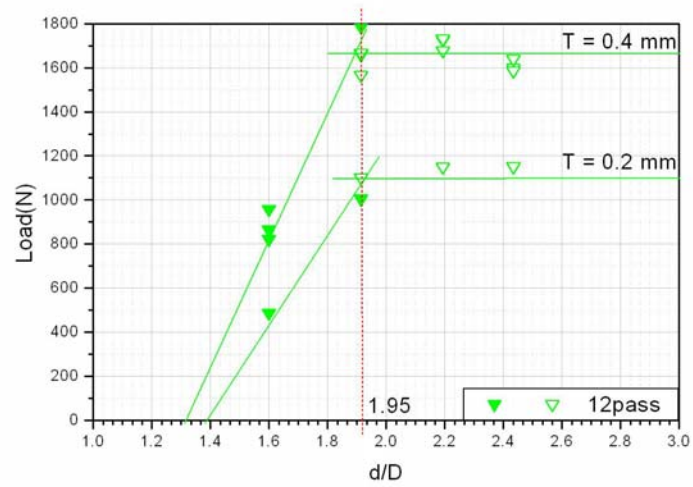
(b)

Figure 5-5. Load-displacement curves for CG (a) and UFG (b) copper at the different thicknesses of 0.4 mm and 0.2 mm (experimental)

5: Texture Analysis During Micro Deep Drawing



(a)



(b)

Figure 5-6. Experimental load versus drawing ratio for the 0-pass and for the 12-pass ECAP-ed samples at 0.4 and 0.2 mm sheet thicknesses. Full and open symbols are used for non cracked and cracked samples, respectively.

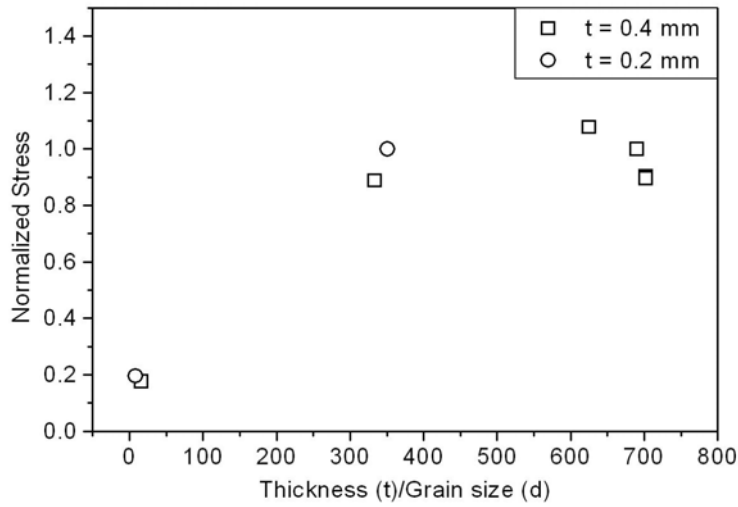


Figure 5-7. Normalised yield stress vs thickness/grain size for ECAP-ed copper.

5.2 Experimental Textures

5.2.1 Textures after ECAP and before micro drawing

According to the typical reference [81], (see Fig. 2-4 and Table 2-2), the ideal orientations of the textures developed in ECAP can be derived from the condition of negative simple shear (SS) that is taking place at the intersection plane of the channels (i.e., at 45° in our study) Experimental work has been conducted by X-ray to measure the textures after ECAP. They are presented in forms of $\{111\}$ pole figures in Fig. 5-8 and in ODF space in Fig. 5-9. The projection plane of the pole figures is the ED plane and a key figure for the ideal orientations and fibers is also provided in Fig. 5-8. One can see in the pole figure that after the first ECAP pass the texture components are closely aligned with the ideal orientations. The texture consists of a partial $\langle 110 \rangle_\theta$ fiber (where $\langle 110 \rangle_\theta$ is parallel to the shear direction) running from C_θ to $A_\theta / \bar{A}_\theta$ through $B_\theta / \bar{B}_\theta$ and a partial $\{111\}_\theta$ fiber (where $\{111\}_\theta$ is parallel to the normal of the shear plane) extending from $A_{1\theta}^*$ to $A_{2\theta}^*$ through $A_\theta / \bar{A}_\theta$. A relatively high intensity is found for the C_θ and $A_{1\theta}^*$ components. A stronger $A_{1\theta}^*$ compared to $A_{2\theta}^*$ is a direct result of the sign of the shear, which is negative. This is also in accordance with the observation from Li et al. [81]. According to [81], texture components can be concentrated along three fibers defined as f1, f2 and f3, and a monoclinic sample symmetry with respect to the TD axis can exist for the first pass (Fig. 5-9). The f1 fibers comprise $A_{1\theta}^* - A_\theta / \bar{A}_\theta - A_{2\theta}^*$ and consist solely of the $\{111\}_\theta$

5: Texture Analysis During Micro Deep Drawing

partial fiber. The f2 fiber runs along $C_\theta - \bar{B}_\theta / B_\theta - \bar{A}_\theta / A_\theta - A_{1\theta}^*$ and comprise both $C_\theta - \bar{B}_\theta / B_\theta - \bar{A}_\theta / A_\theta$ or $\langle 110 \rangle_\theta$ and $\bar{A}_\theta / A_\theta - A_{1\theta}^*$ or $\{111\}_\theta$ partial fibers, respectively. Symmetrical to the f2 fiber, the f3 fiber contains $C_\theta - \bar{B}_\theta / B_\theta - \bar{A}_\theta / A - A_{2\theta}^*$ which can be subdivided into $C_\theta - \bar{B}_\theta / B_\theta - \bar{A}_\theta / A_\theta$ or $\langle 110 \rangle_\theta$ and $\bar{A}_\theta / A_\theta - A_{1\theta}^*$ or $\{111\}_\theta$ partial fibers, respectively.

The fibers can be well distinguished in the ODF presentation in Fig. 5-9. After one pass, approximately uniform orientation densities are observed along all three fibers with the developed orientations close to their ideal positions (Fig. 5-8). Just like in the pole figures, slightly stronger intensity is seen in the ODF for the C_θ component and relatively weaker intensity was recorded for the $A_{2\theta}^*$ component (Fig. 5-9a). After four passes (Fig. 5-9b), the near-monoclinic sample symmetry along the fibers is absent. The f1 and f3 fibers appear incomplete and less uniform. The overall texture intensity is reduced. Compared to the one-pass copper, four passes result in significant weakening of the intensities around the $A_{2\theta}^*$ and C_θ components while a stronger $A_{1\theta}^*$ appears.

For the further eight and sixteen passes, the characteristics of the textures are quite similar to the four-pass case, only intensity variations can be seen. Particularly, the texture is the strongest after eight passes. Concerning some details of the textures, one can see in the ODFs that the $A_{1\theta}^*$ and \bar{B}_θ components are significantly shifted away from their ideal orientation position.

5: Texture Analysis During Micro Deep Drawing

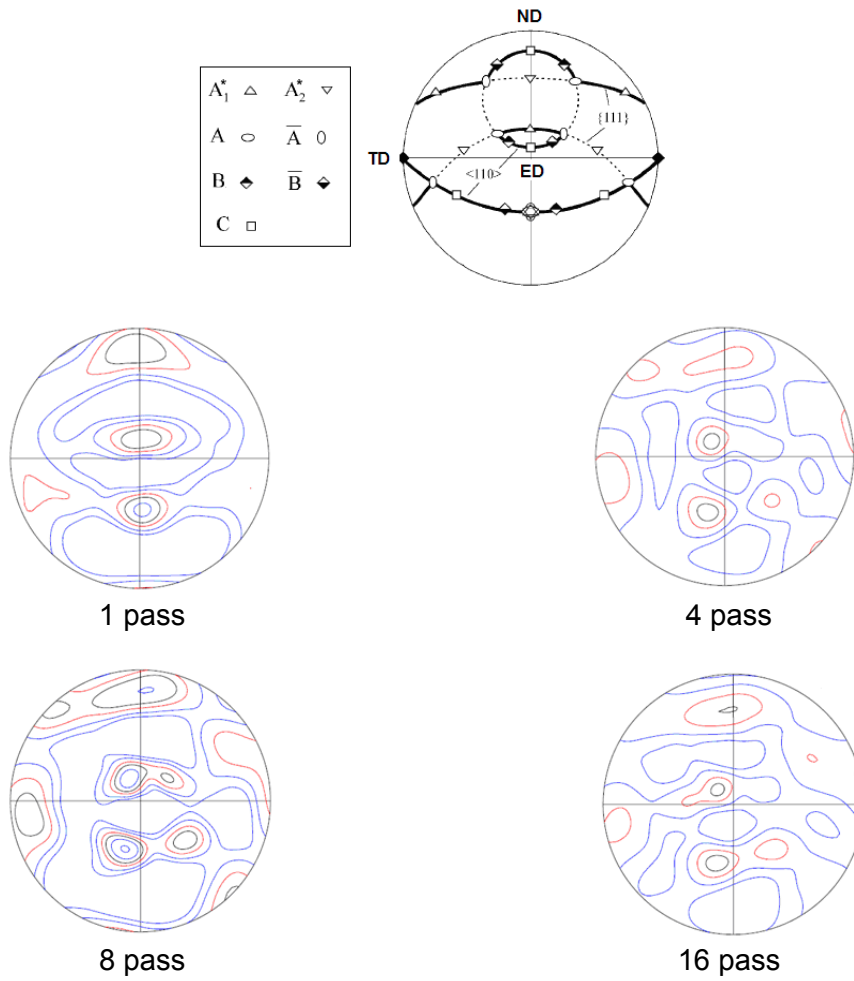


Figure 5-8. Experimental textures in $\{111\}$ pole figures after 1, 4, 8 and 16 ECAP passes in route Bc. Isolevels: 0.7, 1.0, 1.5, 2.0, 2.8, 4.0.

5: Texture Analysis During Micro Deep Drawing

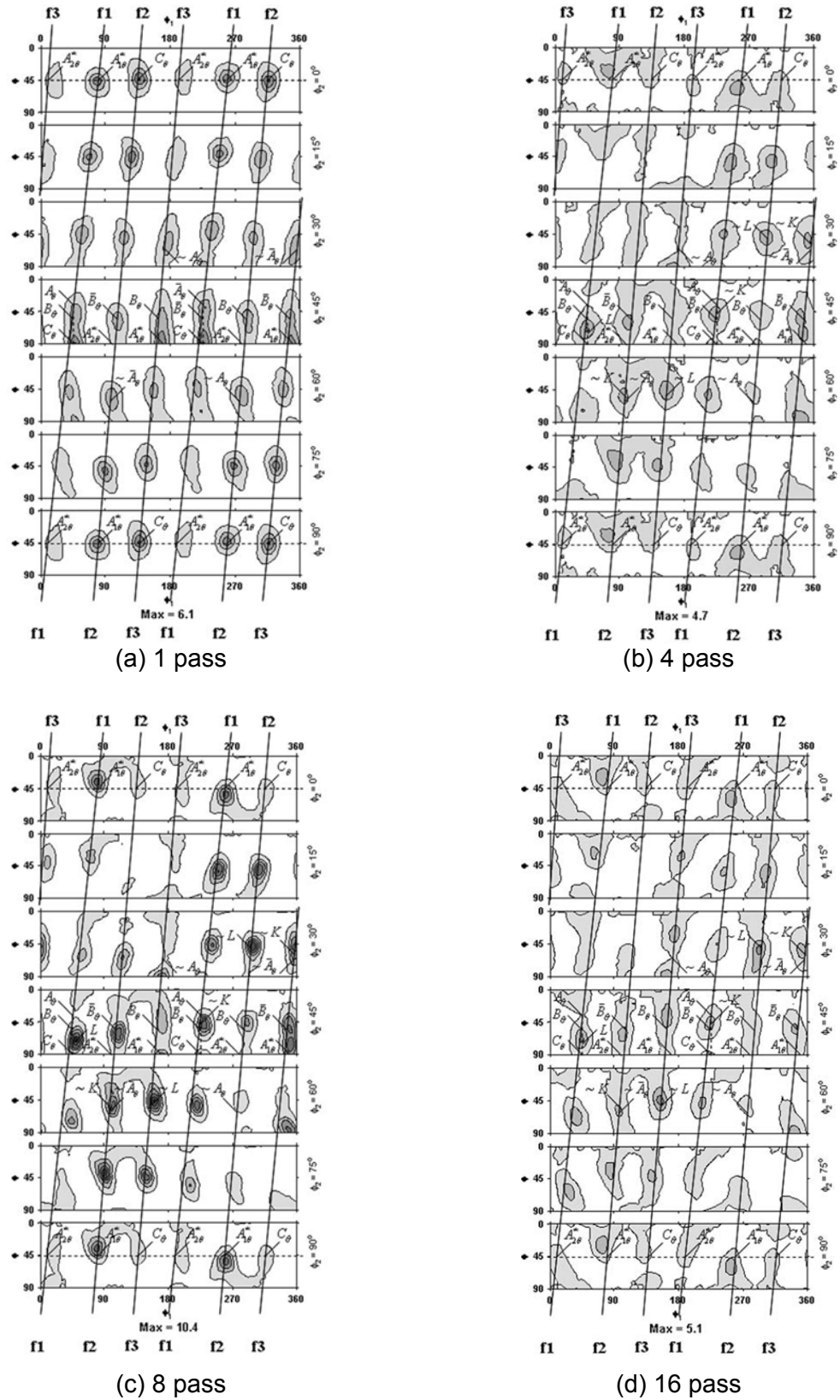


Figure 5-9. Constant ODF sections of ECAP-ed copper (a) 1 pass, (b) 4 pass, (c) 8 pass and (d) 16 pass. Contour step size: 1.65 times [147].

5.2.2 Textures after micro drawing

The textures measured after the cup-drawing tests by X-ray in the form of {111} pole figures were also projected on the ED plane; see Fig. 5-10. The texture of the annealed copper was nearly isotropic and remained practically the same after micro drawing (compare the first pole figure in Fig. 5-10 to Fig. 4-1). This is also the case for the other ECAP passes; the measured textures at the bottom of the drawn cups are nearly the same as the one right after ECAP (compare the textures in Fig. 5-10 to those in Fig. 5-8).

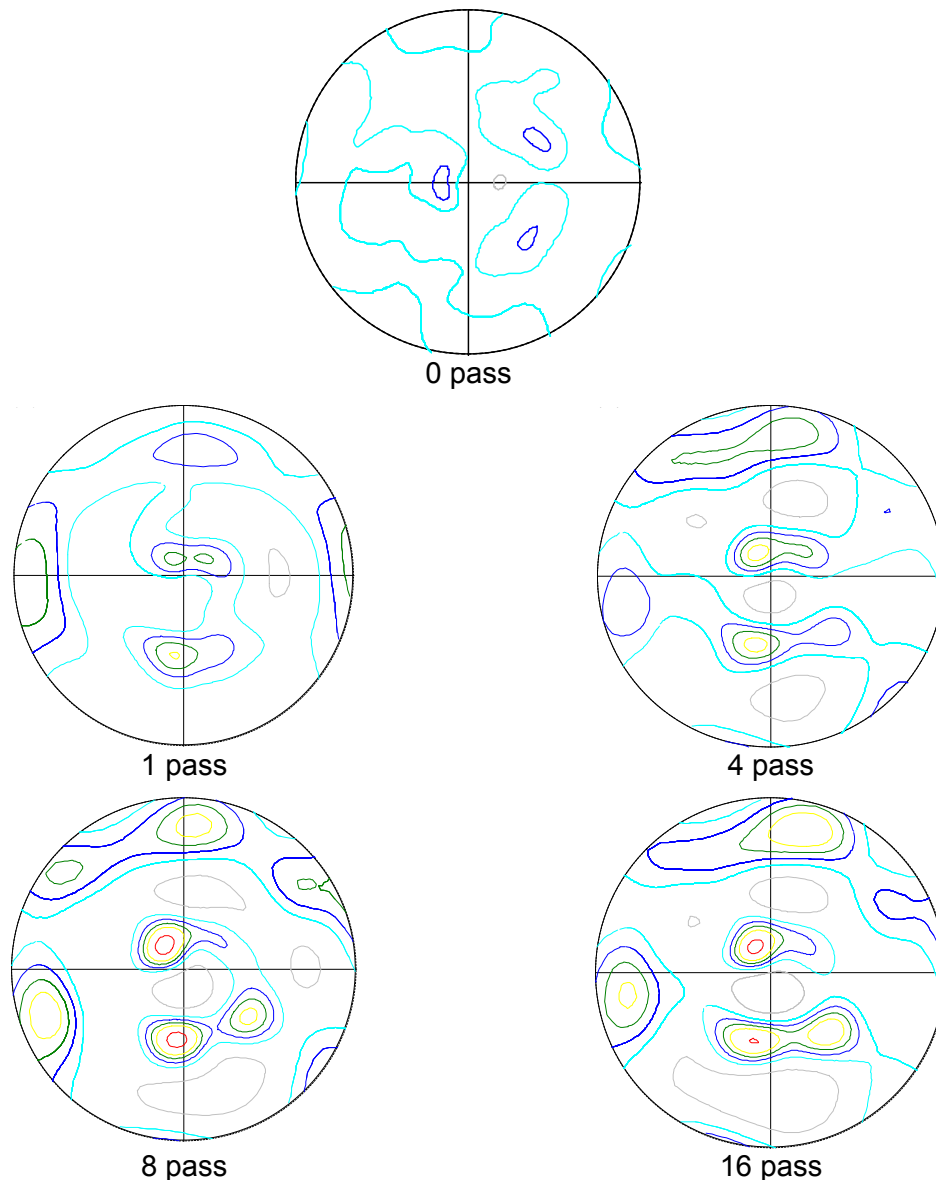


Figure 5-10. Textures ({111} pole figures) measured by X-ray at the base of the cups after cup micro-drawing for the sample with initial blank diameter of 14.6 mm. The number of ECAP passes prior to drawing are indicated under each pole figure. Isolevels: 0.7, 1, 1.2, 1.4, 1.6, 2. The reference system is the same as in Fig. 5-8.

5: Texture Analysis During Micro Deep Drawing

The local textures on the 16 pass ECAP-ed sample were also measured by EBSD after deep drawing from an initial blank diameter of 14.6 mm. The measurements were done in the ND section and plotted in Fig. 5-11 in $\{111\}$ pole figures. The six positions where the textures were examined are indicated in Fig. 5-11 for the 1-pass deformed material but the positions are similar for the 16-pass sample (with points 3 and 4 shifted towards the flange).

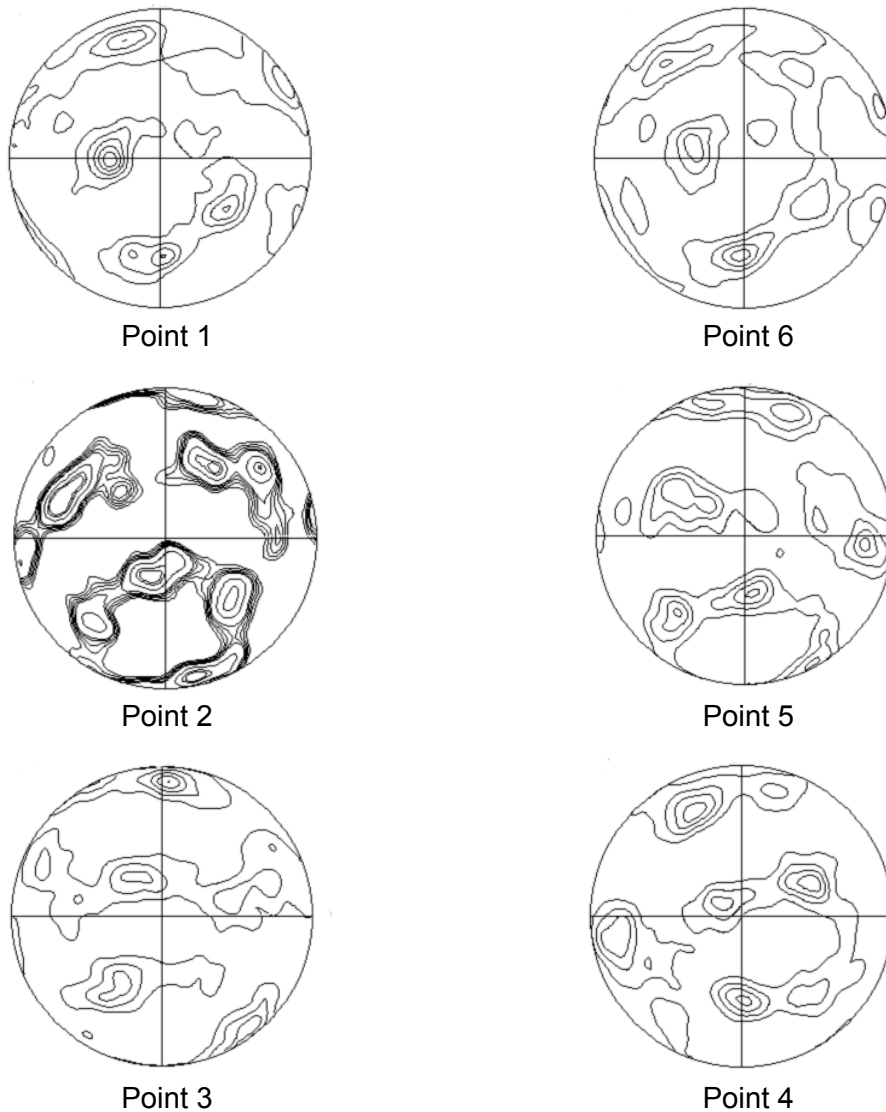


Figure 5-11. Textures measured by EBSD after cup-drawing in $\{111\}$ pole figures for the 16-pass ECAP after cup micro-drawing for the sample with initial blank diameter of 14.6 mm at six selected points in the cup. The projection plane is ED, and ND and TD axes are at the top and on the left of each pole figure, respectively. Isolevels: 0.7, 1, 1.2, 1.4, 1.6, 2, 2.5.

5: Texture Analysis During Micro Deep Drawing

Concerning the texture measured by EBSD at the bottom part of the cup (point 1) one can see that it is basically the same as the one measured by X-ray (Fig. 5-10, 16 passes) apart from an about 10° rotation to the left. One can interpret this deviation as a result of possible differences in the relative intensities of the components which makes the impression of a rotation. Also, a local EBSD measurement might not have reliable statistics to represent the perfect intensity proportions. Moreover, an apparent rotation might be also explained by a small deviation in cutting and alignment of the EBSD sample. The sample-cut might not go through precisely the center of the cup which can produce a rotation of the texture.

In EBSD, the texture was measured at six points, near to the internal as well as the external surfaces of the wall. Concerning the bottom part of the cup, for points 1 and 6 in Fig. 5-11, the texture does not change across the wall. For the other measurements by EBSD presented in Fig. 5-11, the through-thickness variations are evident. In order to discuss them, however, it is first useful to see into the texture modeling results, see the following section 5.3.

Similar to texture evolution, microstructure was found no change at the measured six points (Fig. 5-12), and the subgrain size lies in the range from $\sim 0.39 - 0.44 \mu\text{m}$ (Fig. 5-13), with the average of approximately $0.42 \mu\text{m}$ with 5° misorientation criteria. The grain size distribution (Fig. 5-13) shows that only small grains, and these grains are more uniform in the areas measured. The misorientation distribution shows a bimodal distribution typical of UFG materials (Fig. 5-14).

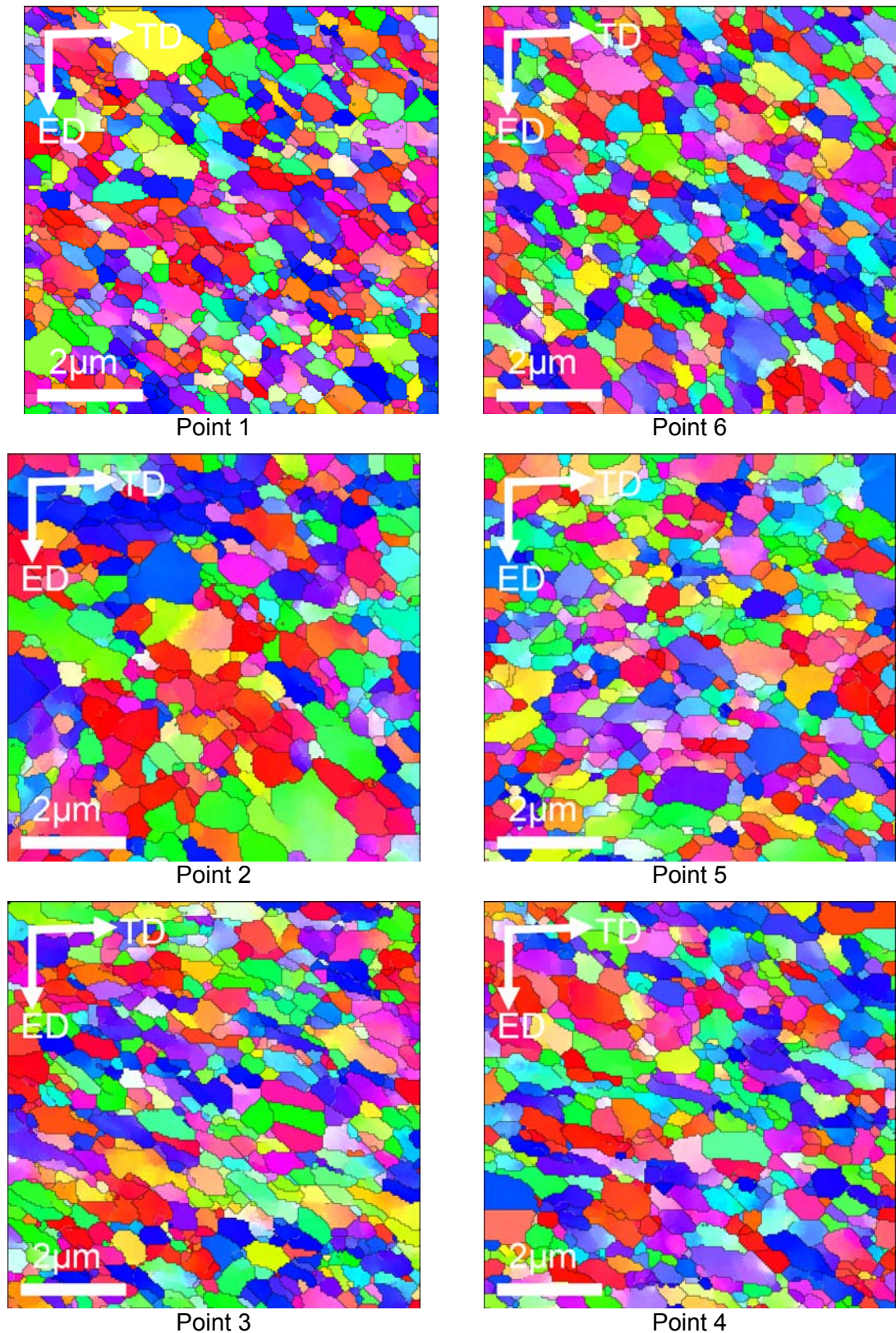


Figure 5-12. EBSD after cup-drawing for the 16-pass ECAP after cup micro-drawing for the sample with initial blank diameter of 14.6 mm at six selected points in the cup. Boundaries with at least 5° misorientation are marked with black lines. The colour code for the orientation of the axis perpendicular to the image is shown in an insert.

5: Texture Analysis During Micro Deep Drawing

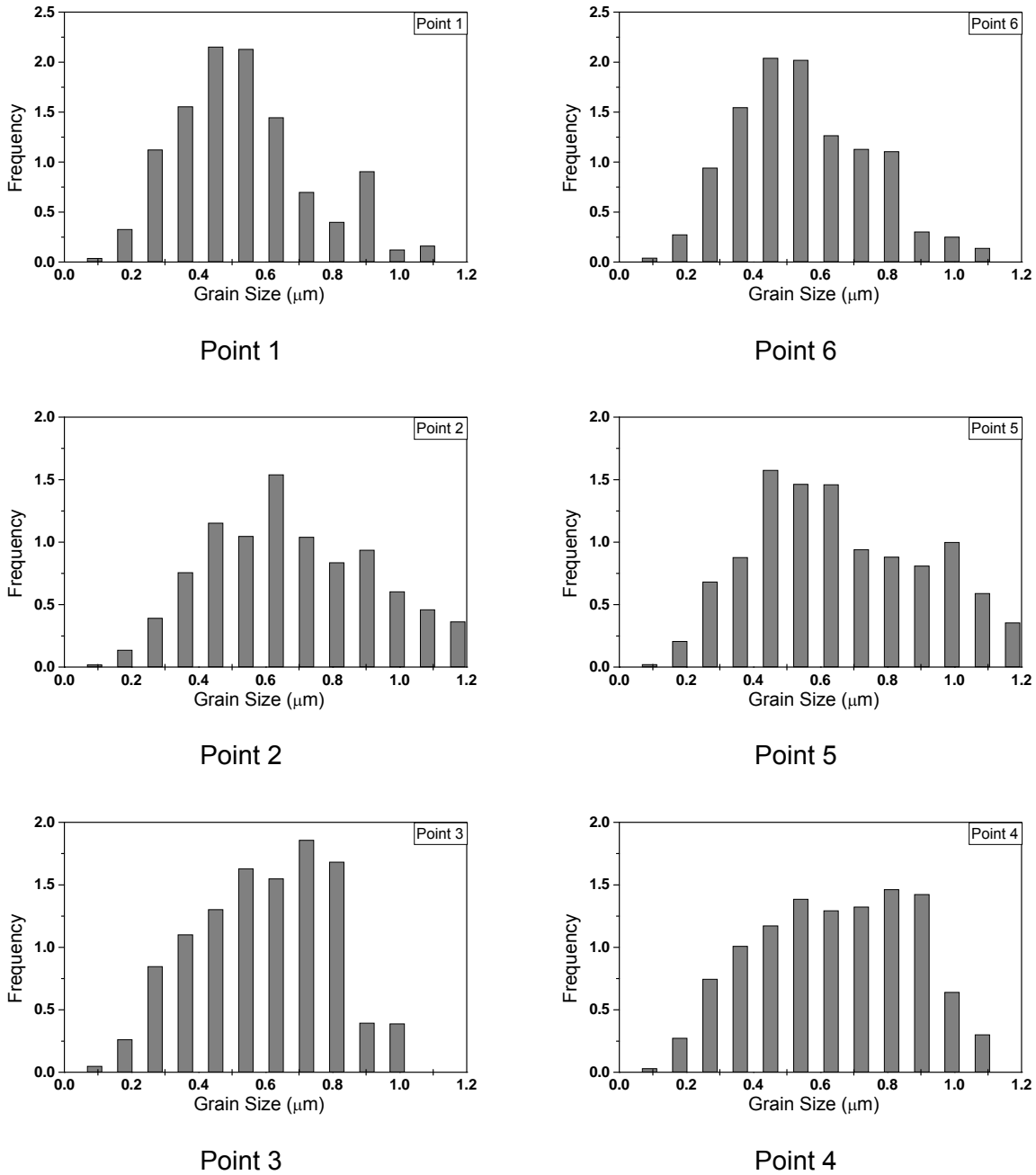


Figure 5-13. Grain size distribution of the 16-pass ECAP after cup micro-drawing for the sample with initial blank diameter of 14.6 mm at six selected points in the cup.

5: Texture Analysis During Micro Deep Drawing

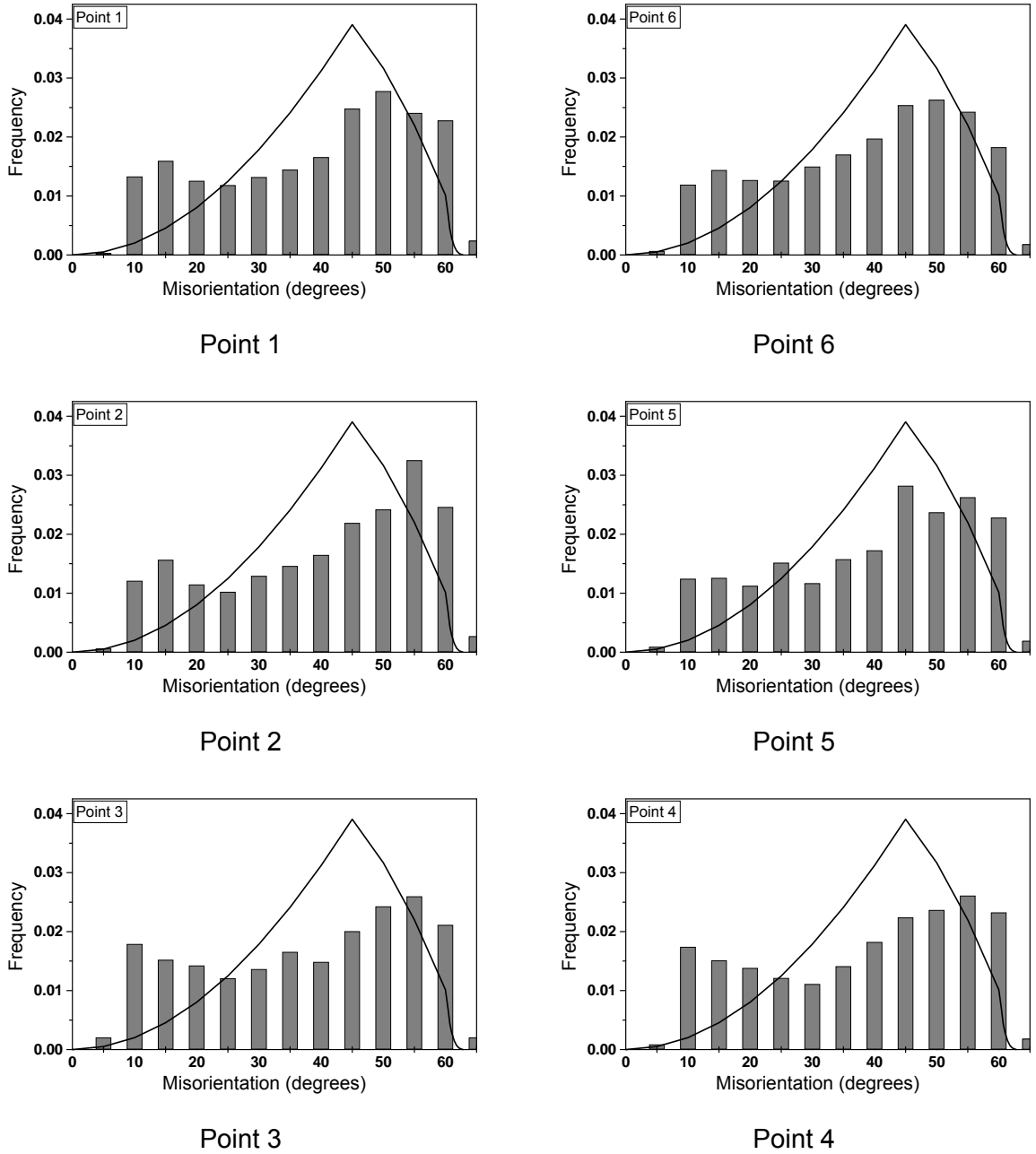


Figure 5-14. Neighbour-to-neighbour misorientation distribution of the 16-pass ECAP after cup micro-drawing for the sample with initial blank diameter of 14.6 mm at six selected points in the cup.

5.3 Texture Modeling in Cup Drawing

Before texture modeling, FE simulations of the cup-test were carried out by A. Molotnikov [148]. These simulations provided the so-called deformation gradients along selected flow lines of material elements at the six simulation points that are identified in Fig. 5-15. The self-consistent viscoplastic polycrystal code [149] in its FE tuned version [150] was used to simulate texture development along the selected flow lines. It was important to use the experimental textures after ECAP as they were strong textures, see previously. Thus, the initial textures were introduced as input textures for the cup drawing polycrystal simulations with the help of 3000 grain orientations. In order to generate these orientations, the discretization technique published in [151] was used. In the polycrystal code, the usual 12 $\{111\} \langle 110 \rangle$ f.c.c. slip systems of copper were considered. In these simulations the hardening was not modeled, for the reason that there is usually little effect on the texture development when hardening is taken into account. One of the most important parameter in the polycrystal code is the viscoplasticity index m which was taken to be 0.1; this is a typical value for the purpose of texture simulations [152]. The grain shape and its evolution can be taken into account in self consistent simulations. However, for the initial state, the grains were considered to be equiaxed in this modeling, which is a reasonable approximation for grain shape after route Bc in ECAP (especially after 4, 8 and 16 passes, where each time the initial grain shape is recovered). In the cup-drawing simulations the grain shape was allowed to evolve.

In order to reduce the number of computations (and to save space), three examples were selected from the five initial cases (0, 1, 4, 8 and 16 ECAP passes): the 0, 1 and 16 passes. The simulation results are displayed in $\{111\}$ pole figures in Figs. 5-16, 5-17 and 5-18, for the 0, 1 and 16 passes, respectively. One can see that the predicted textures show characteristic development as a function of location within the cup and of the initial blank diameter. One general observation is that the strength of the simulated texture increases monotonically as a function of plastic strain (see Table 5-1 for the strain values).

5: Texture Analysis During Micro Deep Drawing

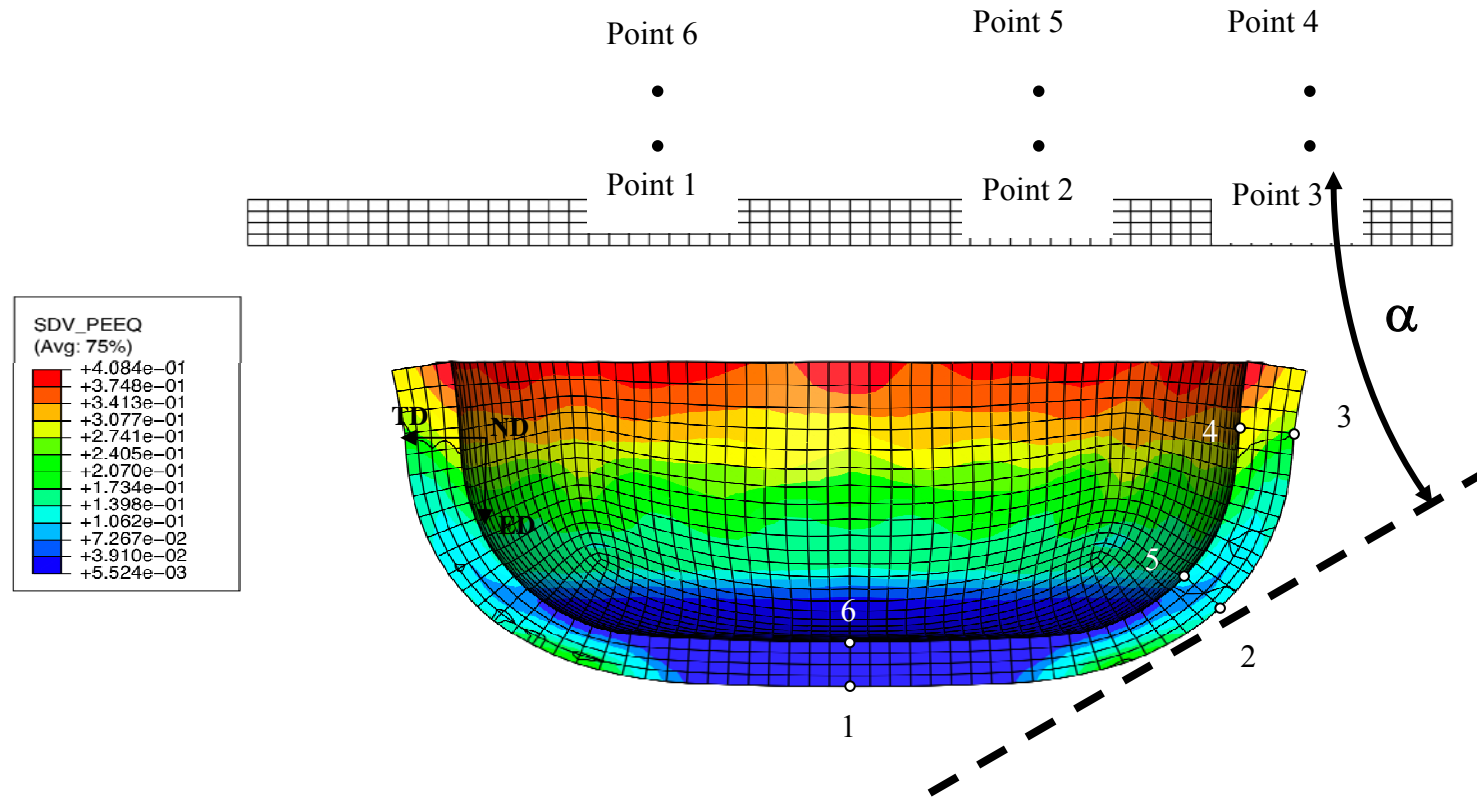


Figure 5-15. FE predicted shape and von Mises strain map of the one-pass ECAPed sample with initial blank diameter of 9.5 mm. Numbers indicate the six points selected for texture simulation and measurement at their initial positions and after drawing. The rotation angle of the deformed surface with respect to the undeformed is indicated by α at point 2 (30°) [153].

5: Texture Analysis During Micro Deep Drawing

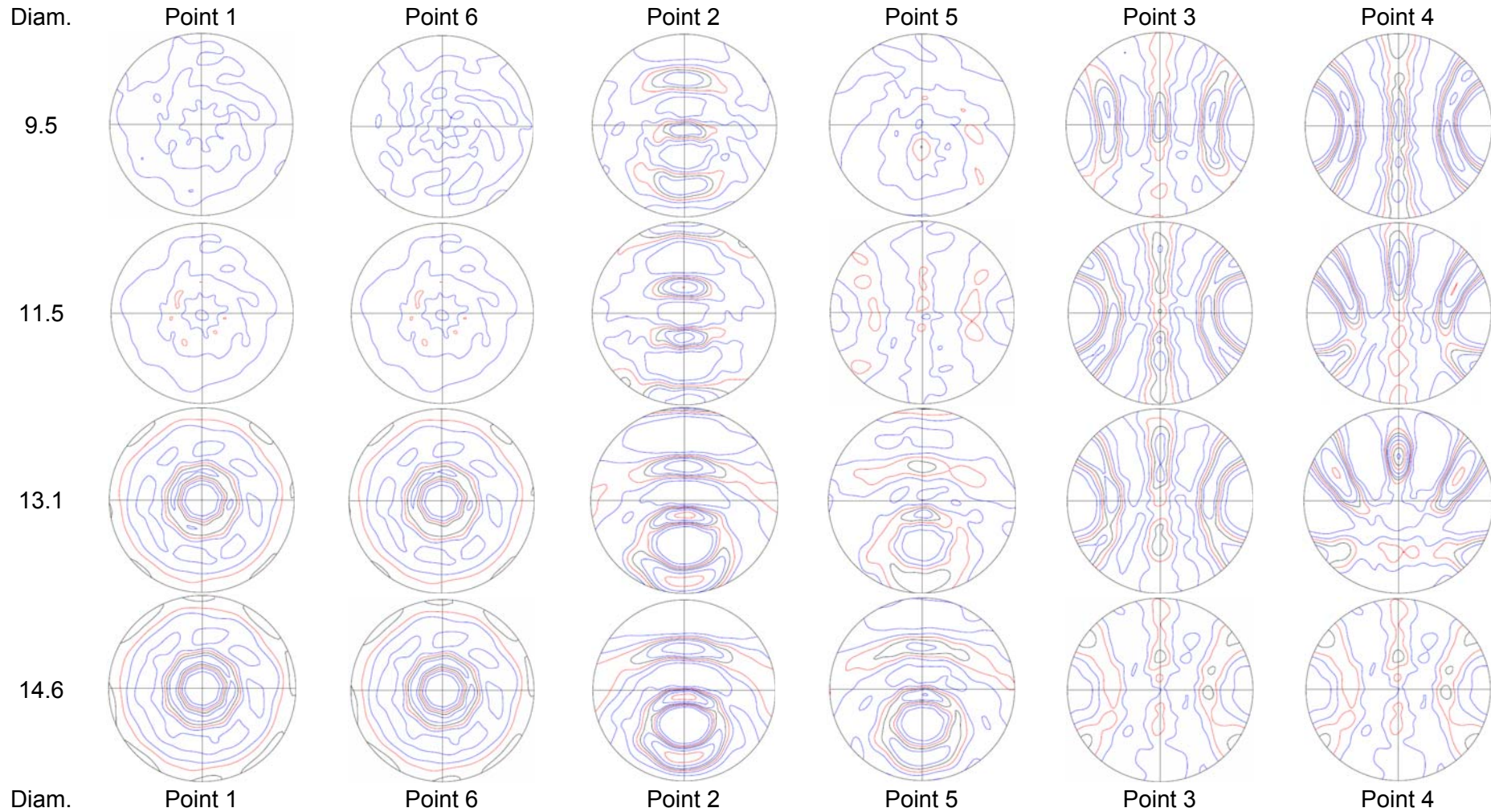


Figure 5-16. Simulated textures in $\{111\}$ pole figures for the 0-pass ECAP cup-drawing as a function of blank diameter and position in the drawn cup. The projection plane is ED, and axes ND and TD are at the top and on the left of each pole figure, respectively. Isolevels: 0.7, 1, 1.2, 1.4, 1.6, 2, 2.5, 3, 3.5, 4. [153]

5: Texture Analysis During Micro Deep Drawing

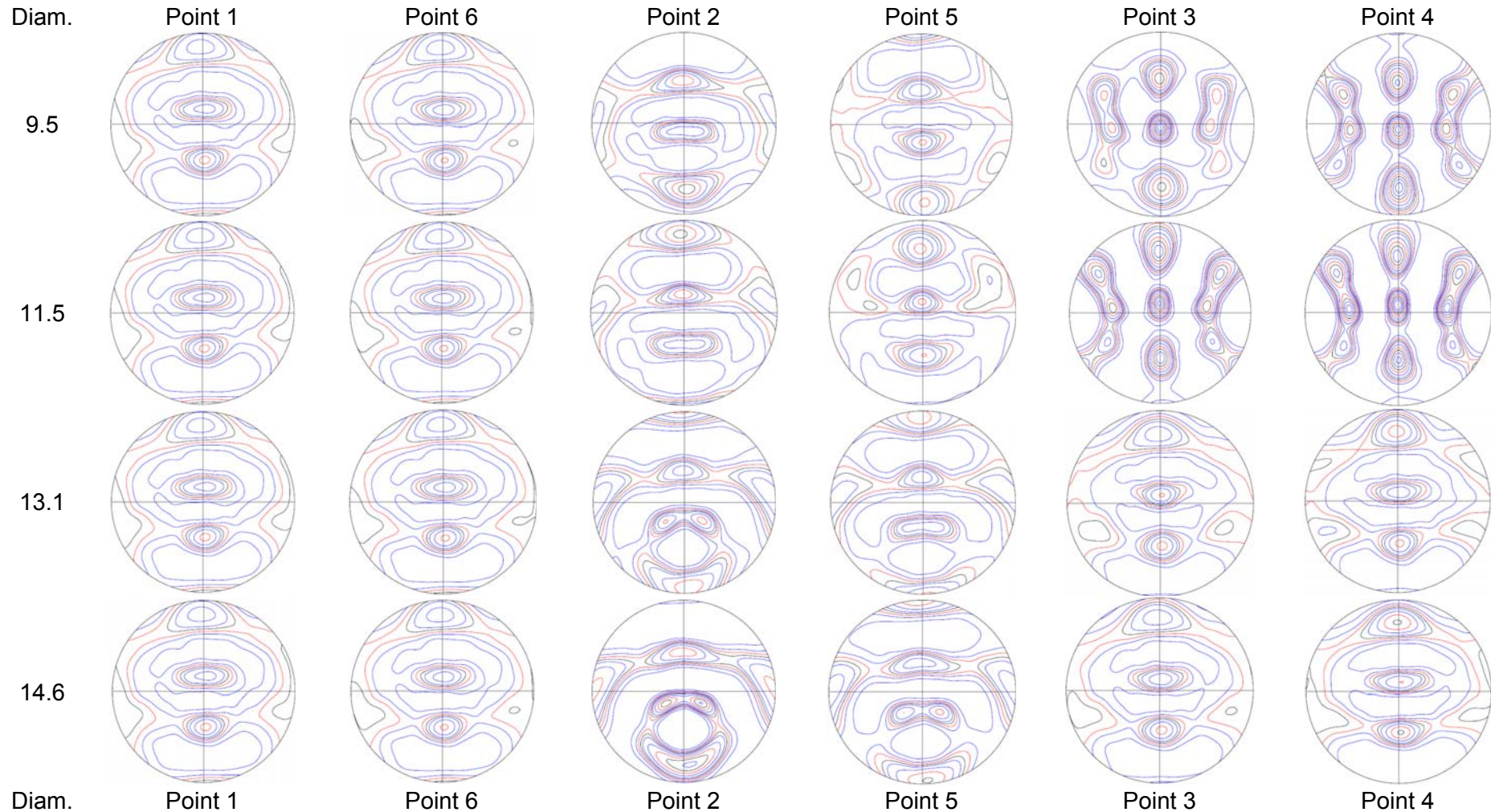


Figure 5-17. Simulated textures in {111} pole figures for the 1-pass ECAP cup-drawing as a function of blank diameter and position in the drawn cup. The projection plane is ED, and axes ND and TD are at the top and on the left of each pole figure, respectively. Isolevels: 0.7, 1, 1.2, 1.4, 1.6, 2, 2.5, 3, 3.5, 4. [153]

5: Texture Analysis During Micro Deep Drawing

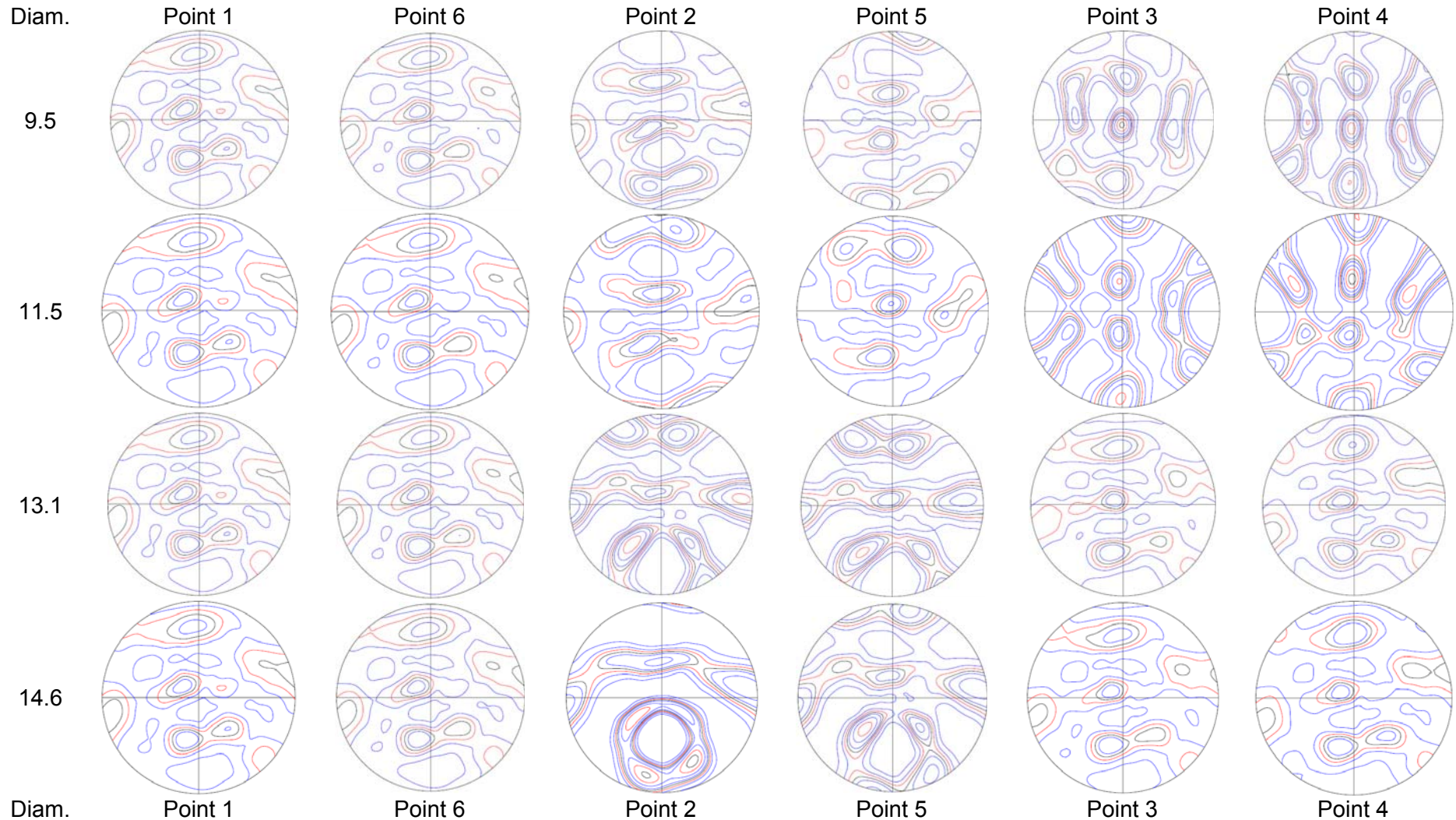


Figure 5-18. Simulated textures in $\{111\}$ pole figures for the 16-pass ECAP cup-drawing as a function of blank diameter and position in the drawn cup. The projection plane is ED, and axes ND and TD are at the top and on the left, respectively. Isolevels: 0.7, 1, 1.2, 1.4, 1.6, 2, 2.5, 3, 3.5, 4.[153].

5: Texture Analysis During Micro Deep Drawing

Table 5-1. The von Mises accumulated strains from the FE simulations at six points in cup drawing tests

Point:	D = 9.5 mm ($\times 10^{-2}$)						D = 11.5 mm ($\times 10^{-2}$)						D = 13.1 mm ($\times 10^{-2}$)						D = 14.6 mm ($\times 10^{-2}$)					
	1	6	2	5	3	4	1	6	2	5	3	4	1	6	2	5	3	4	1	6	2	5	3	4
Pass-0	4	2	19	6	26	35	6	7	24	8	28	34	20	21	37	20	27	36	22	23	41	25	19	19
Pass-1	4	3	19	4	27	37	3	2	19	5	41	50	3	3	18	11	4	5	3	2	39	23	4	15
Pass-16	4	3	46	28	7	13	3	3	18	6	27	33	4	3	26	21	4	6	3	3	46	28	7	13

5: Texture Analysis During Micro Deep Drawing

As expected, there is little texture development at points 1 and 6 for all four blank diameters. From the experimental results, these points are situated in the inner and outer surfaces of the bottom of the cup. The texture at the base of the cup drawn from the non-ECAP-ed sample remains nearly random for the two smaller blank diameters (9.5 and 11.5 mm) in the simulations while a fibre-type relatively weak texture develops for the two larger diameters (Fig. 5-16). This fibre is of the type $\langle 110 \rangle \parallel ED$. It is due to the thinning of the cup at the bottom which can take place for these larger samples. This thinning effect can be verified in Table 5-1 where one can see that the strain at points 1 and 6 is much larger for the two larger blank diameters compared to the two smaller ones. For the larger diameters the strain amounts to about 0.22, which seems to be enough to orient grains near to the ideal fiber and the obtained fiber is of the same kind as for axisymmetric compression of f.c.c. polycrystals.

One can explain the larger strain in the non-ECAP-ed sample in the following way. As this sample is not pre-deformed in ECAP it can undergo considerable strain hardening during drawing. The same does not take place in the samples which are pre-deformed by ECAP. During forming of the non-ECAP-ed samples, the part of the sample which is initially between the bottom and the flange (the wall of the cup) strengthens by strain hardening. However, once the wall is hardened significantly, the bottom of the cup will flow as well because the flange will be retained longer due to its initially large diameter. Looking into the texture evolution of the pre-ECAP-ed samples, one cannot see a similar effect. The textures at the base of the cups are practically identical to the textures before drawing for the one or 16 ECAP-ed samples; compare Fig. 5-8 with Figs. 5-16 and 5-18. The reason for this is that hardening was already saturated during the ECAP deformation so only the cup wall can deform. This reasoning is well supported by the strain data in Table 5-1.

One common feature for all textures in the lower corner region of the cups (points 2 and 5) that they are radically different from the initial textures in all cases. They are also much stronger than in the flat base. This high texture strength at point 2 is due to the large strain at this point (see Table 5-1 and Fig. 5-17). Very important to point out also the variations of the texture across the cup-wall from point 2 to point 5: the texture is much weaker inside the wall than in the outside region. Again, this difference is due to the differences in plastic strains, see Table 5-1. The differences in the textures are most significant between the inner and outer points for cups drawn from the as-received copper (0 pass). This can be attributed again to the significant thinning of the bottom and corner part due to the effect of large strain hardening. This thinning effect leads to more differences at the outer surface. In all three cases, the texture is of a fibre character for the two larger blank

5: Texture Analysis During Micro Deep Drawing

diameters (13.1 and 14.6 mm) with a fibre axis that is located about halfway between the ED and –ND directions. All these fibres are of <110> types. Actually, the strain state is near plain strain compression locally perpendicular to the surface of the sheet in the corner region. For such strain state, the textures are not complete fibres. They are actually similar to rolling textures of copper at these points (this observation can actually be verified if a suitable rotation is carried out around the ND axis to account for the rotated orientation of the wall).

It is important to point out that the textures that develop at points 3 and 4 originate from the flange part of the blank. The initial material point is drawn into the cup for the 9.5 and 11.5 mm blanks, while it remains in the flange region for larger initial diameters. Consequently, in the first case, the texture is very different from the initial texture and very strong due to the large plastic strain. In the second, the drawn texture is basically the same as the initial texture. Another consequence is that the through-thickness variation of the texture is less pronounced in these regions (points 3 and 4) when compared to the corner region that contain the simulation points 2 and 5.

5.4 Discussions

As observed above, the texture of ECAP-ed f.c.c. metals can be adequately compared with the textures obtained by simple shear [154], although clear differences still exist between these two cases [155]. ECAP-ed textures are close to their ideal positions in our study. However, slight shifts are observed from 4 passes and onward. Aside from post processing errors, the rigid body rotation was inherent in SS-type deformation are responsible for the shift. Specific to the case of ideal simple shear, the number of operative slip systems is limited resulting in overall negation of the tilt effect for the intermediate strain range [156, 157]. Contrarily, in the ECAP case, the operation of multi slip from the first pass and onward – as seen in previous viscoplastic self-consistent modeling results [155] – causes the texture components to rotate up to 10 deg in the direction of the rigid body rotation [158]. As a result, i) slip system activity coupled with ii) differences in entry texture due to a prescribed route and iii) the deformation necessitated by additional passes leads to variations in the orientation position and stability of individual ideal components within the bulk texture [158].

Our texture measurements are in contradiction with Li et al [155], where an increase in texture strength after 4 and 8 passes was found. Mainly, these disparities allude to heterogeneity of the as-deformed billet due to varying friction conditions at the billet-die

5: Texture Analysis During Micro Deep Drawing

interface [159] and also the degree of difficulty in locating exact center of the billet stable length (from where the ED plane copper was cut) for equivalently similar texture scans with increasing passes. However, other differences such as the starting texture of the materials and the area of the sample over which the texture scan was performed [160] also mean that direct comparison of the measurement with those found in literature must be made with care. Over all, the method of texture index first suggested by Bunge et al. [161] should be used when quantifying end-texture strength.

In our study, texture evolution with increasing strain leads to the following observations, monoclinic sample symmetry is lost as distinct non-uniformity and incompleteness in orientation density along the various fibers, process via route Bc yields less fiber like texture components, which can be segregated into f1, f2 and f3 fibers comprising $\{111\}_\theta$ and $\langle 110 \rangle_\theta$ partials, respectively. This is in agree with the equiaxed grain structure after four passes observed by TEM and EBSD [147]. Under conditions of negative simple shear, the end of each route Bc ECAP cycle – every four passes- returns substantially weaker $A_{2\theta}^*$ and C_θ components in comparison to other ideal orientations. Such variations in the relative intensities of different texture components were also found with changes in strain level by other SPD methods [162, 163]. Increased strain accumulation during multi pass ECAP also results in an increased spread of orientation density and tendency of nonsymmetric orientation flow away from their ideal positions in the sense of shear. One can see that the basic features are similar; however, there are large differences as well, and these differences must be due to the relatively large plastic strain at these points.

Micro deep drawing, It was pointed out from the experimental results that because of the low plastic strain in the cup base, there is no evolution in texture at that location, and this is observed in both the X-ray and EBSD studies. In the latter case, the texture was examined at simulation points 1 and 6 (Fig. 5-16) with no discernable difference within the expected scatter of the measurement. In contrast, in the FE simulation, the plastic strain is much larger at the bottom corner simulation points 2 and 5 (see Table 5-1 and Fig. 5-15) and these simulation results confirm the EBSD measurements presented in Fig. 5-11. As can be seen, there is a fairly good correspondence between the measurement (Fig. 5-8) and the FE simulated textures (Fig. 5-17, bottom row). It is also confirmed by EBSD that the texture is stronger at point 2 which is the outer part of the corner and is in good

5: Texture Analysis During Micro Deep Drawing

agreement with the simulation. Even the small rotation difference between the through-thickness textures is validated by the experimental results.

There are two ingredients that can change the crystallographic texture of the material in a forming process: the plastic strain and the rigid body rotations. These are both included in the velocity gradient that was implemented from the FE simulation into the crystal plasticity modeling. However, it is useful to see the effects that are caused separately by rigid rotation and strain in a cup drawing test. For this purpose, the effect of material rigid rotation was examined at selected points in the process. There are significant material rotations at points 2 and 5 as these points are in the bottom corner region of the part. We have selected the case of 1-pass ECAP-ed sample with the 9.5 mm blank size as a demonstration. At the end of the forming process, the shape of the cup as obtained from the FE simulation is shown in Fig. 5-19.

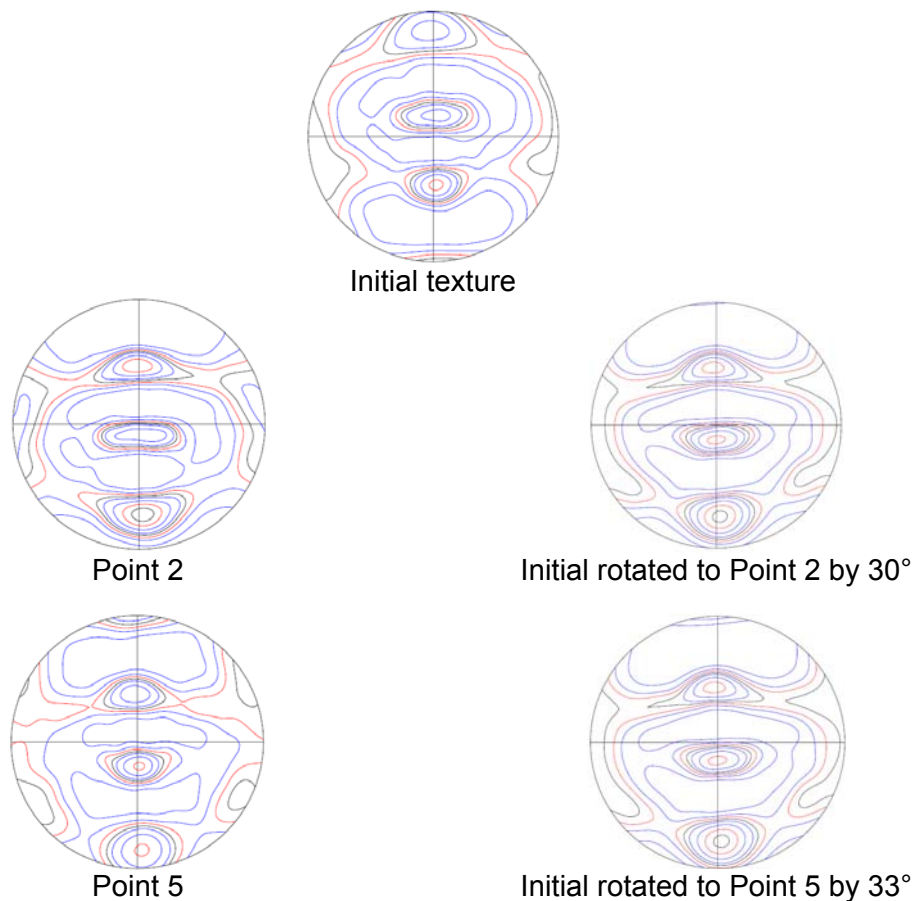


Figure 5-19. Simulated textures in the one-pass ECAP drawn cup compared to the initial texture that is simply rotated around the TD axis at four positions. Isolevels: 0.7, 1, 1.2, 1.4, 1.6, 2, 2.5, 3, 3.5, 4.

5: Texture Analysis During Micro Deep Drawing

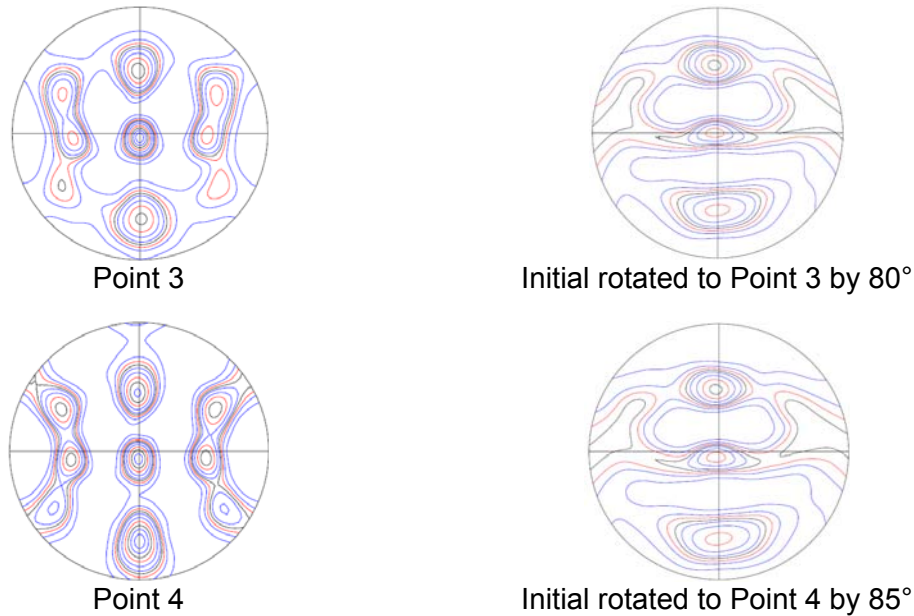


Figure 5-19. Continued

The material rotation around the ND axis is shown in Fig. 5-19 for point 2 by the angle, which is 30° . For point 5, the same rotation is 33° . Applying then these rotations to the initial one-pass ECAP textures, we projected the so-obtained pole figures on the ND plane for comparison with the predicted textures at these points. As can be seen in Fig. 5-19, the simply rotated pole figure is very near to the predicted texture at both points. This agreement means that most of the texture changes are due to simple material rigid body rotations. The effect of the plastic strain on the texture is not that significant as the strains are actually relatively small.

As can be seen in Table 5-1, the von Mises equivalent strains amount to only 0.19 and 0.04 at points 2 and 5, respectively. Similarly, the initial texture was rotated by 80° for point 3 and by 85° for point 4. Comparing these rotated textures with the simulated texture (Fig. 5-18), one can see that the basic features are similar; however, there are large differences as well, and these differences must be due to the relatively large plastic strain at these points.

The von Mises strains (Table 5-1) are 0.27 and 0.37 at points 3 and 4, respectively, which are much larger than at points 2 and 5. The reason for the larger strains is that these points were originally on the flange and then drawn into the vertical wall of the cup.

5: Texture Analysis During Micro Deep Drawing

Finally, it is important to point out that local texture measurements that are presented above using the EBSD technique are possible to carry out even on a very small sample while they are virtually impossible to do by X-ray. This is why texture was only measured at the bottom part of the drawn cups with X-ray. On the contrary, EBSD permitted to explore even the texture gradients at regions where local curvature of the sample was very important. This was the case at points 2 and 5 in the above presented results.

5.5 Summary

Texture evolution during micro-forming has been studied in this Chapter. The main objective is to understand the evolution of the texture and explore through-thickness variations for the UFG case. Measurements along with extensive simulation work have been carried out on copper which was pre-deformed to large strains by ECAP. A simulation technique is established by combining FE simulation with polycrystal modeling. Given the fact that the FE model does not consider crystal plasticity, the posteriori FE flow lines has been integrated into the self consistent viscoplastic polycrystal model to predict the texture evolution at selected points during cup forming. The predictions were faithfully validated by the texture measurements carried out using X-ray and EBSD techniques. It was shown that rigid rotation during the drawing process play an important role in the evolution of the texture. Through-thickness variations in the texture were found by both simulations and experiments. Such variations are important in cup forming if the grain size is very small. For large grain size, such variations are not predictable due to the small wall thickness while they can be well simulated if the grain size is very small. The agreements between the FE simulation and measurements confirm the above results.

6

MICRO-EXTRUDED UFG AND CG COPPER

6. MICRO-EXTRUDED UFG AND CG COPPER

This Chapter builds on the detailed finding during micro-extrusion on the thermal stability. Thermal stability during further processing is one of the main concerns in the application of UFG materials for micro-forming. Micro-extruded copper with a range of grain sizes, spanning from CG to UFG copper, have been studied at different extrusion speeds. It was clear that the grain size after micro-extrusion depends on the processing speed and was always larger than the grain size expected from purely geometrical considerations of the process. Differential scanning calorimetry, dislocation density measurements and hardness all support the occurrence of dynamic recrystallization (DRX) of the UFG copper – but importantly not the CG copper – during micro-extrusion at the highest extrusion speed of 25mm/min. To determine the strain path in micro-extrusion, the analytic flow line model of Altan was used and validated by the finite element calculation. The viscoplastic self consistent (VPSC) polycrystal modelling was employed for understanding the texture evolution during micro-extrusion. The effect of recovery was incorporated in the grain refinement model by changing the curvature induced dislocation density represented by an adjustable parameter in model for CG copper at the low speed micro-extrusion of 1 mm/min. Good agreement with the experimental observation was obtained. Importantly, although the CG copper was micro-extrudable, the thermal stability of UFG copper was superior after high speed micro-extrusion because of the dynamic recrystallization and this justifies the use of UFG copper in this case..

6.1 Force and Displacement during Micro-extrusion

For each strain rate, at least two samples were extruded in order to check repeatability. Fig. 6-1 shows that the extrusion force required for the UFG copper is higher than the CG copper at the same speed. This trend is in accordance with the Hall-Petch relationship, because the flow stress required to deform larger grain size materials is less than that to deform smaller grain size materials. Therefore, a lower extrusion force is required. By changing the strain rate, it can be seen for the UFG copper that the required force is higher with higher strain rate, while for CG copper, the required force does not show evident changes with different strain rates. The reasons for these trends are being investigated with further experiments. The buckle in Fig 6-1 is caused by the filling specimens into the conical die.

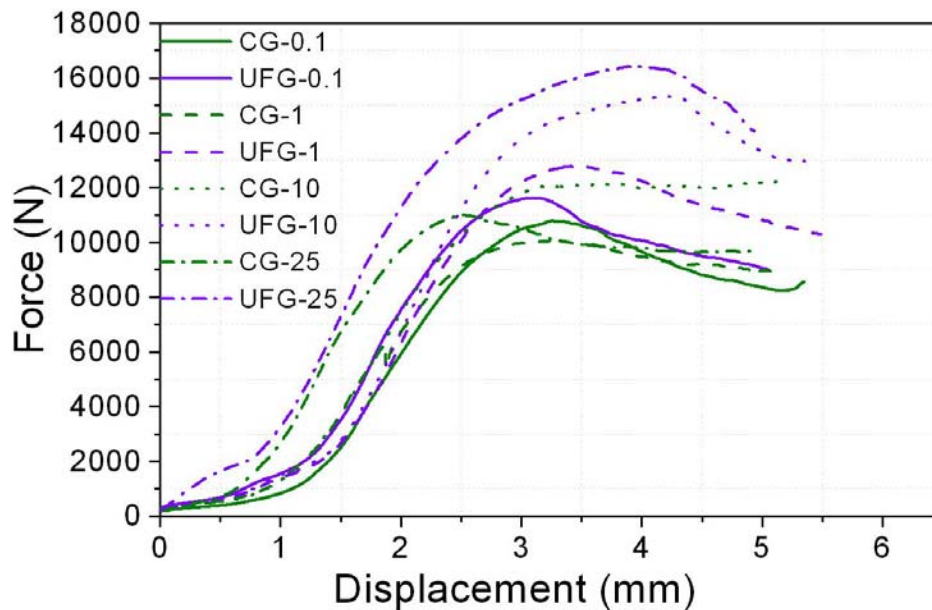


Figure 6-1. Force-displacement response for micro-extruded UFG and CG copper

6.2 Microstructure of UFG and CG Copper after Micro-extrusion

Considerable grain coarsening took place in the specimen annealed at 600°C (Fig. 6-2a). The initial average grain size was 24 μm with a broad distribution (Fig. 6-3a). The misorientation distribution of the initial material (Fig. 6-3b) shows a high peak at 60° which is due to the numerous annealing twins present in the material (see Fig. 6-2a). For CG materials after extrusion at the speed of 1 mm/min., the microstructure of the CG copper is very much elongated in the extrusion, as expected (Figs. 6-2b-c). The average subgrain size of the CG copper after extrusion is 0.9 μm at the intermediate, $C = 0.6$ position and 1.4 μm at the centre, $C = 0$ position (Fig. 6-4) using the 5° misorientation criteria (the C parameter is defined as the ratio of the actual radial distance from the centre of the specimen and the total radius in the Fig. 6-17 described later using the analytical flow line entering at position $C = 0.6$ ($C = 0$ is the centre) identified by the arrow. The first neighbour misorientation distribution shows a peak at about 12° and at larger angles and has a form similar to the Mackenzie curve (Fig. 6-4b). For CG at different extrusion speeds, the subgrain size lies in the range of ~0.9-0.98 μm at 5° misorientation criteria and does not change with the extrusion speeds (Fig. 6-5).

6: Micro-extruded UFG and CG Copper

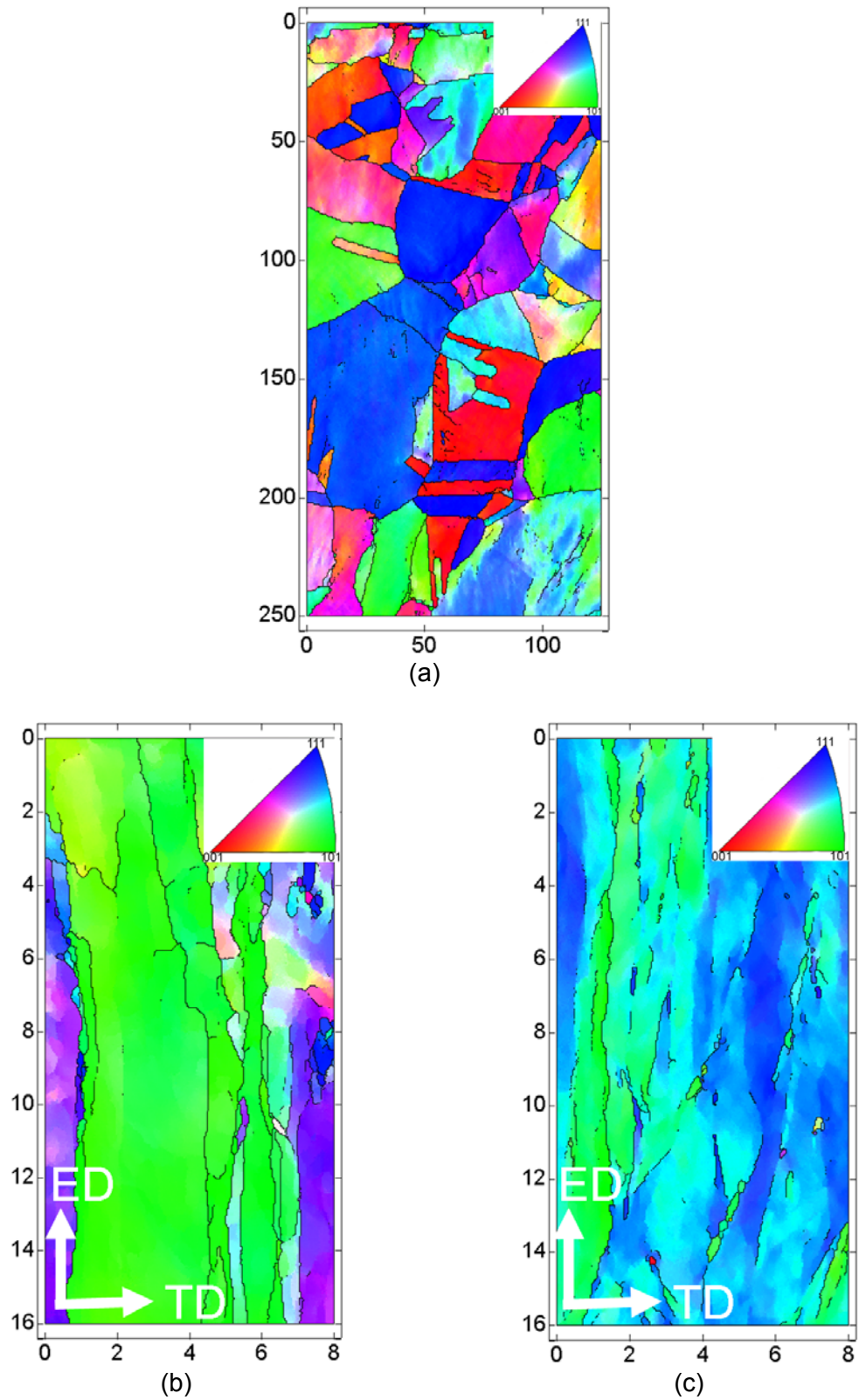
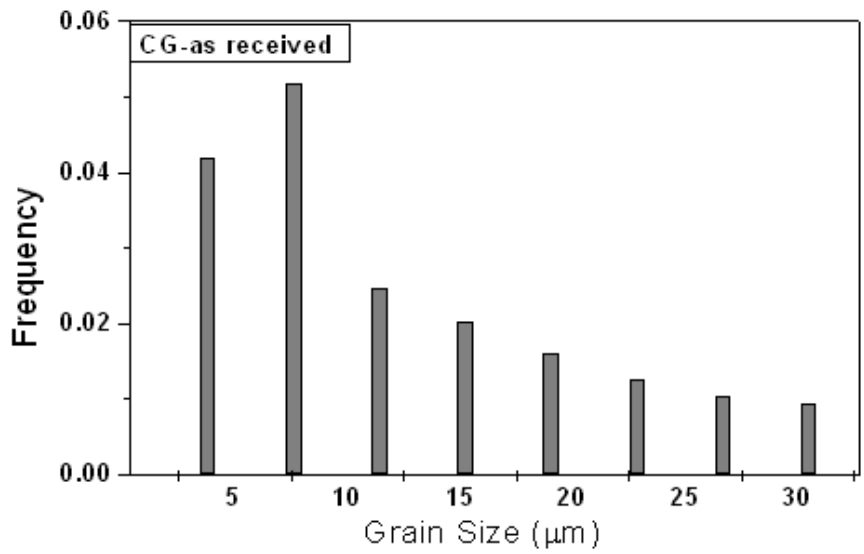
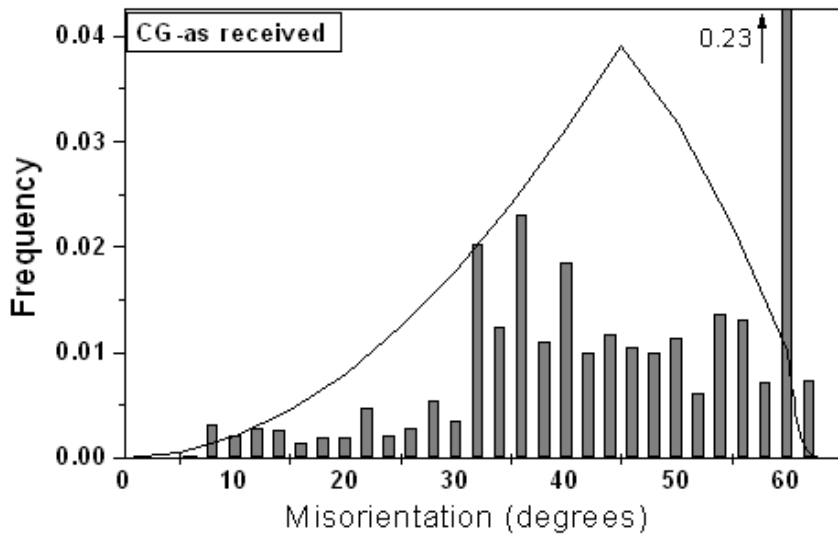


Figure 6-2. Examples of orientation maps after micro-extrusion in CG copper: (a) as-received; (b) $C = 0.6$ and (c) $C = 0$. Boundaries with at least 5° misorientation are marked with black lines. The colour code for the orientation of the axis perpendicular to the image is shown in an insert. Coordinates are in μm .

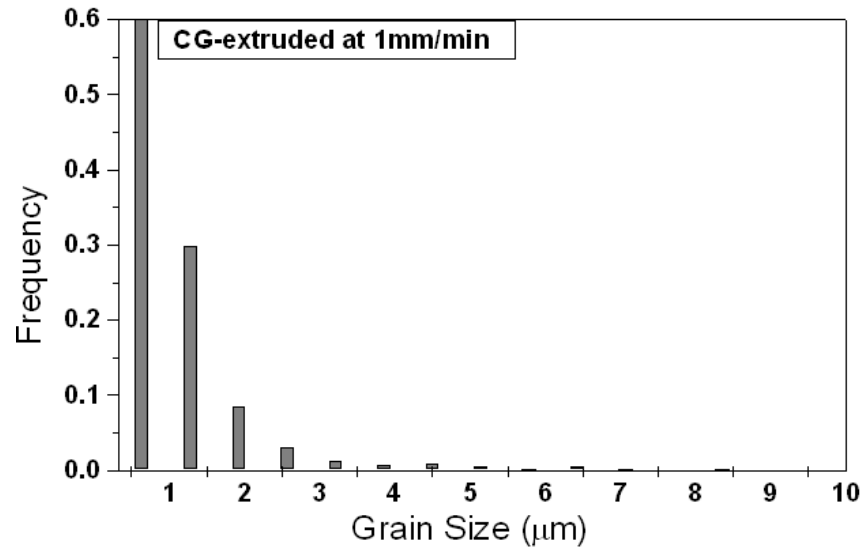


(a)

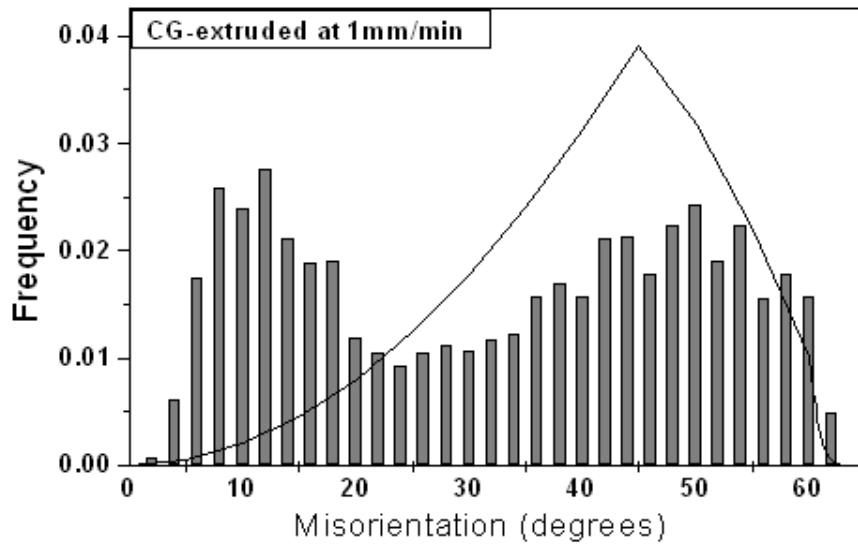


(b)

Figure 6-3. Grain size (a) and neighbour-to-neighbour misorientation distribution (b) in CG as-received copper.

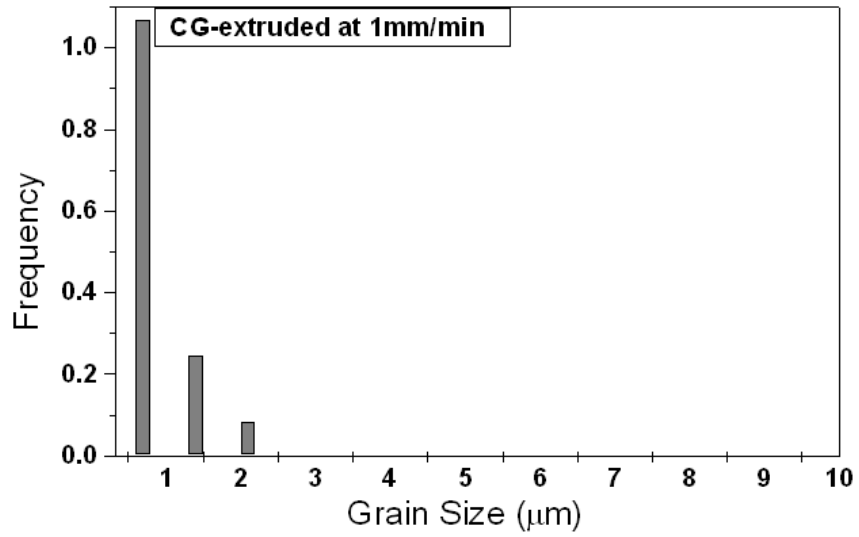


(a)

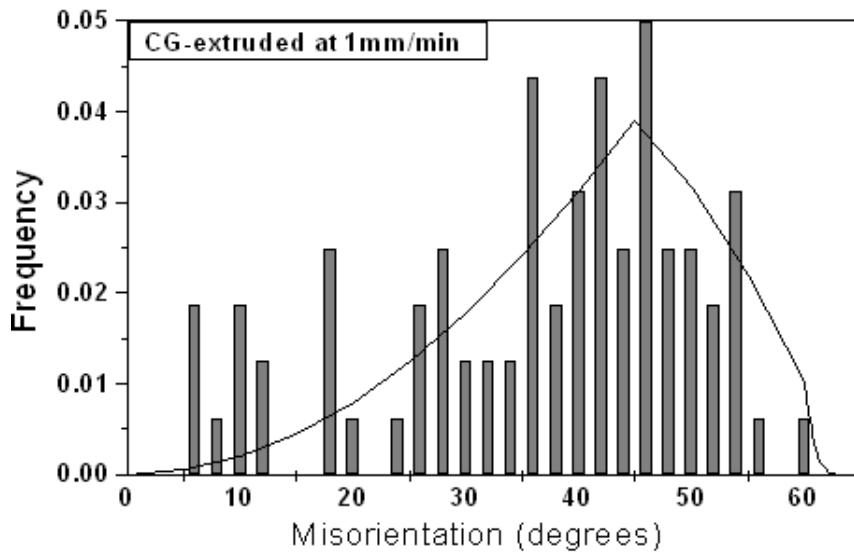


(b)

Figure 6-4. (a) Grain size; (b) neighbour-to-neighbour misorientation distribution at position $C = 0.6$; and (c) Grain size and (d) neighbour-to-neighbour misorientation distribution at $C = 0$ in CG copper after micro-extrusion.



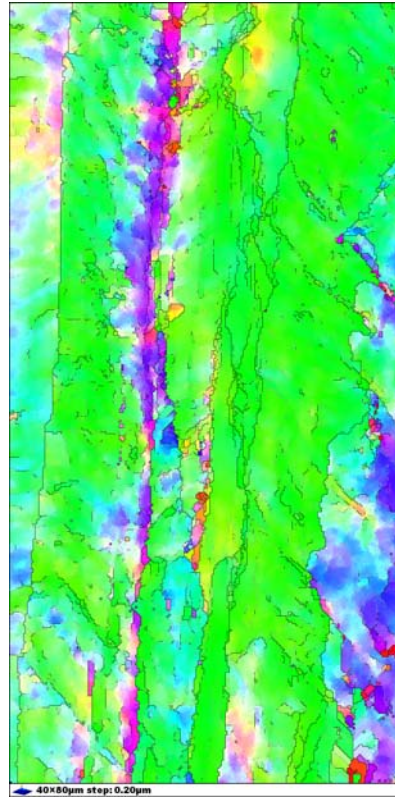
(c)



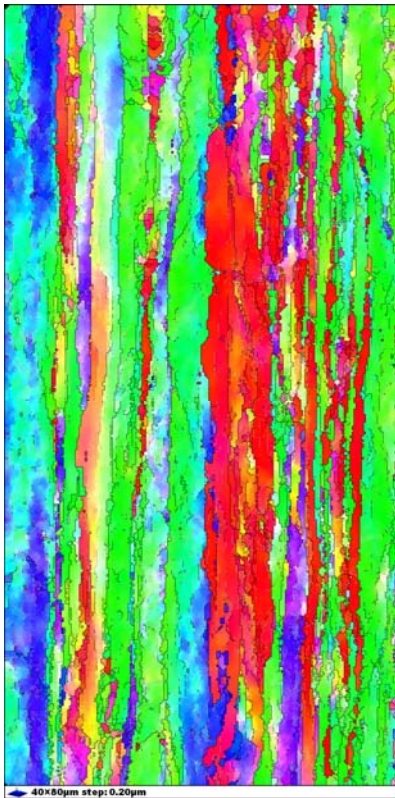
(d)

Figure 6-4. Continued

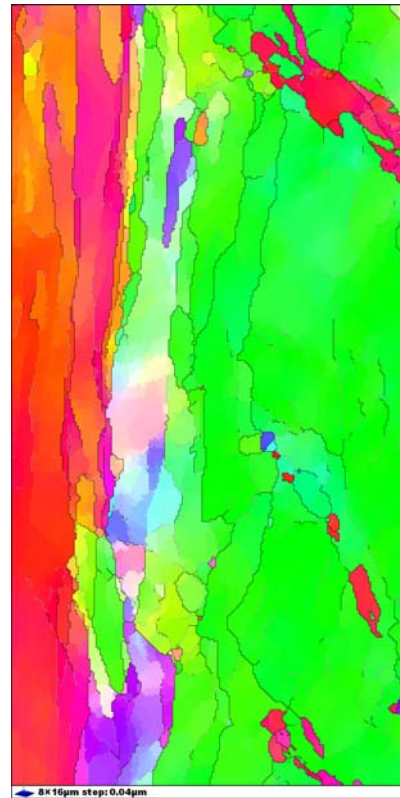
6: Micro-extruded UFG and CG Copper



(a)



(b)



(c)

Figure 6-5. Microstructure of CG copper extruded at different speeds: (a) CG extruded at 0.1 mm/min; (b) at 10 mm/min and (c) at 25 mm/min. Scale bar and ED are the same as Fig. 6-2.

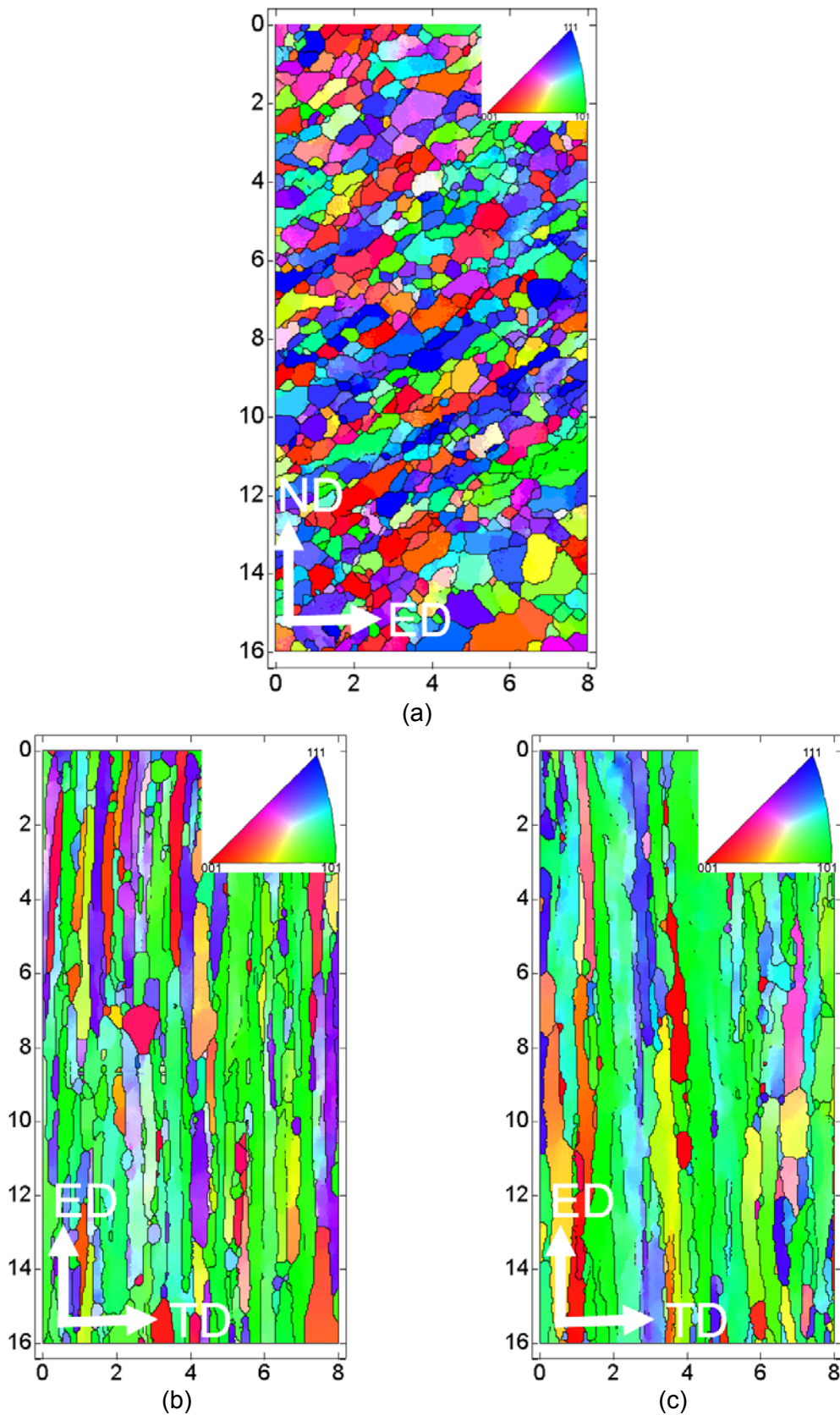
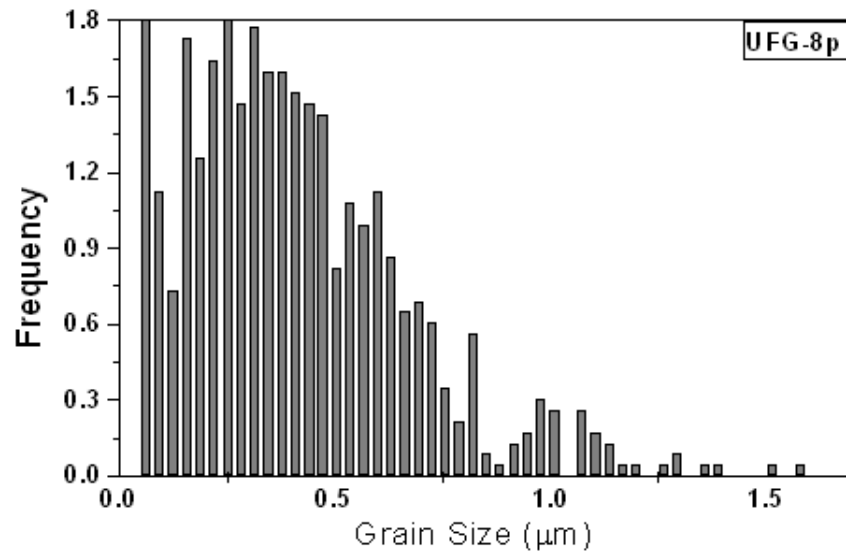


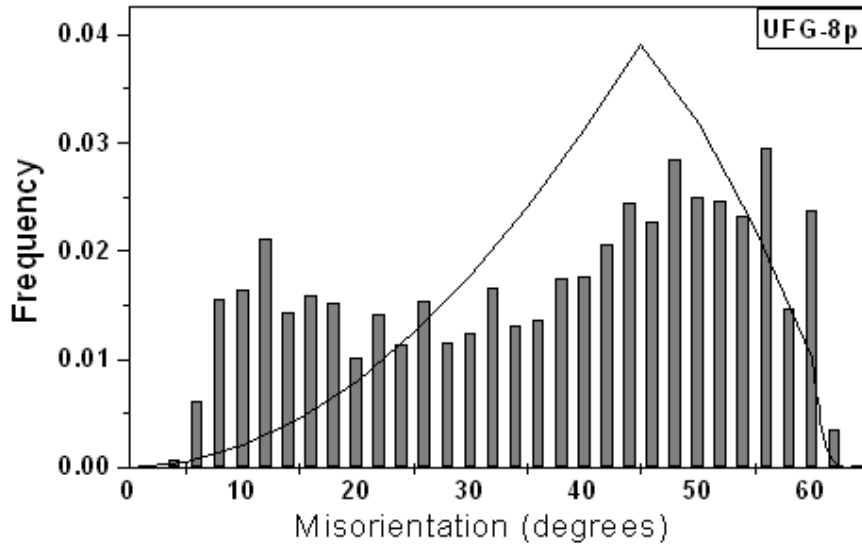
Figure 6-6. Examples of orientation maps after micro-extrusion in UFG copper: (a) as-received, (b) at $C = 0.6$ and (c) at $C = 0$. Boundaries with at least 5° misorientation are marked with black lines. The colour code is shown in an insert. Coordinates are in μm .

6: Micro-extruded UFG and CG Copper

For UFG materials, a band-like lamellar structure can be seen in the deformed structure of initial UFG specimen, with the long axis parallel to macro-shear direction imposed by the ECAP process (Fig. 6-6a). The average grain size was $\sim 0.4 \mu\text{m}$ using the 5° misorientation criteria. The grain size distribution (Fig. 6-7a) shows that there are only small grains; large size grains are totally absent. The misorientation distribution shows a bimodal distribution typical of UFG materials (Fig. 6-7b).



(a)



(b)

Figure 6-7. (a) Grain size and (b) neighbour-to-neighbour misorientation density distributions in UFG copper.

6: Micro-extruded UFG and CG Copper

After extrusion at 1 mm/min, an elongated microstructure is prevalent (Fig. 6-6b-c). The grain size based on the linear intercept method perpendicular to the extrusion direction is $\sim 0.49 \mu\text{m}$ at both intermediate, $C = 0.6$ and centre $C = 0$ positions which are larger than the initial grain size (Fig. 6-8a and 6-8b). The misorientation distribution presents the usual bimodal character (Fig. 6-8b) with intensity at large angles higher than the distribution before extrusion. Subgrain sizes ($\sim 0.47\text{-}0.49 \mu\text{m}$) at 5° criteria are approximately constant when UFG copper has been extruded at the speeds of 0.1 and 10 mm/min (Fig. 6-9a and b), but elongated grains have clearly expanded at 25 mm/min with the average subgrain size of $0.65 \mu\text{m}$ (Fig. 6-9c). The percentage of high-angle boundaries in UFG/ECAP-ed copper was $\sim 35\%$ is, close to the reported value of $\sim 25\%$ [14, 15].

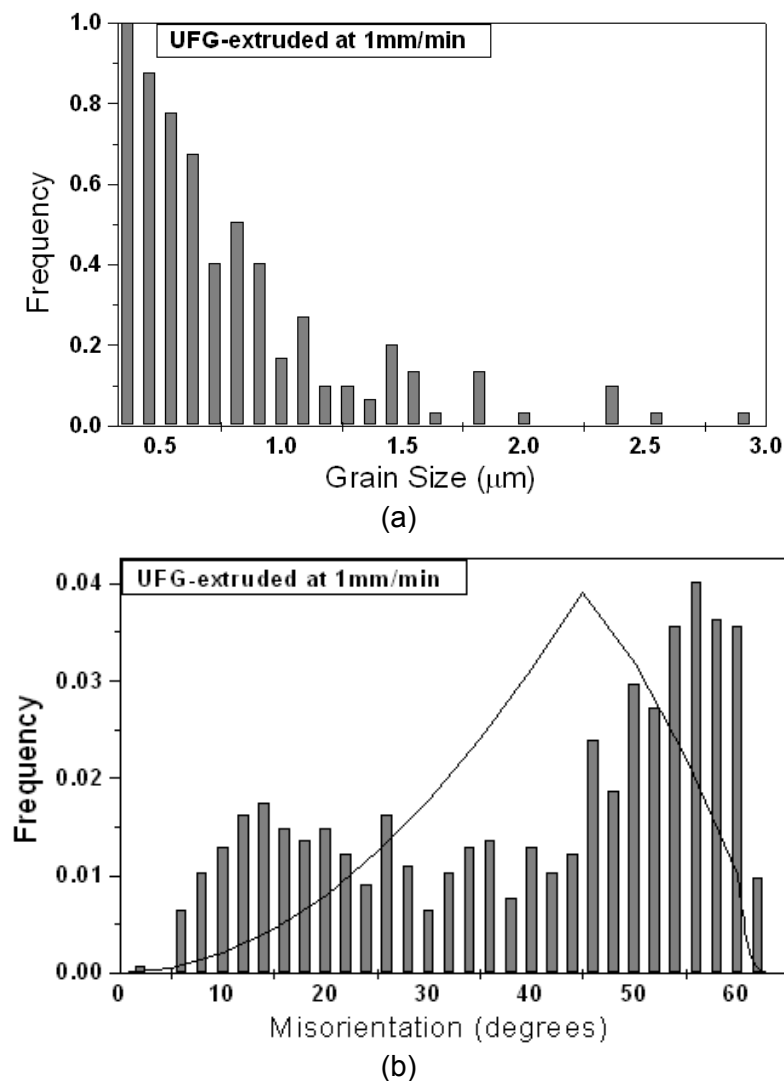


Figure 6-8. (a) Grain size; (b) neighbour-to-neighbour misorientation distribution at position $C = 0.6$; (c) Grain size and (d) neighbour-to-neighbour misorientation distribution at position $C = 0$ in UFG copper after micro-extrusion.

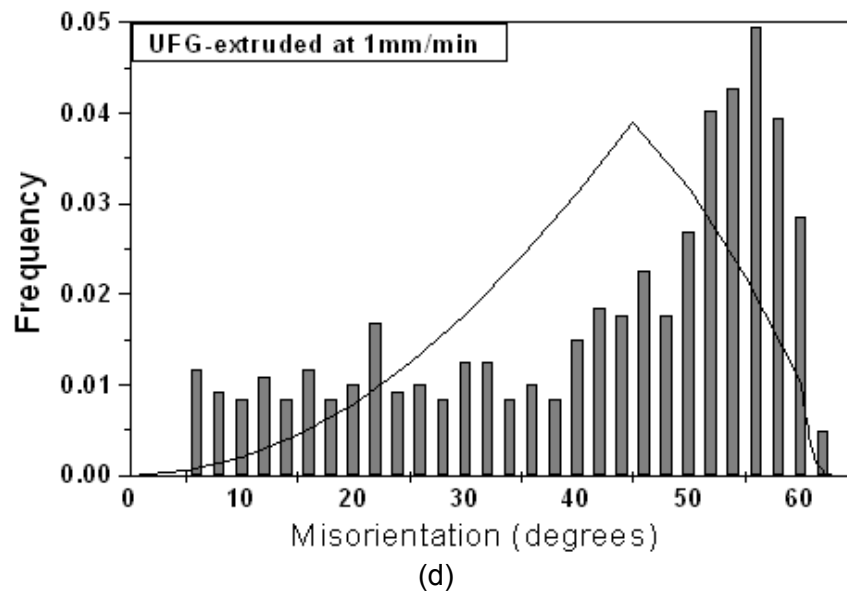
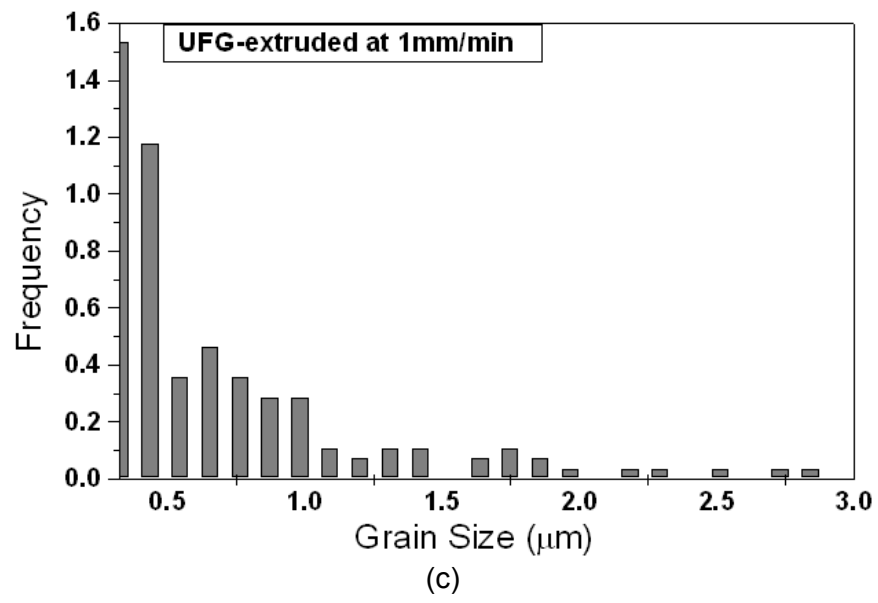
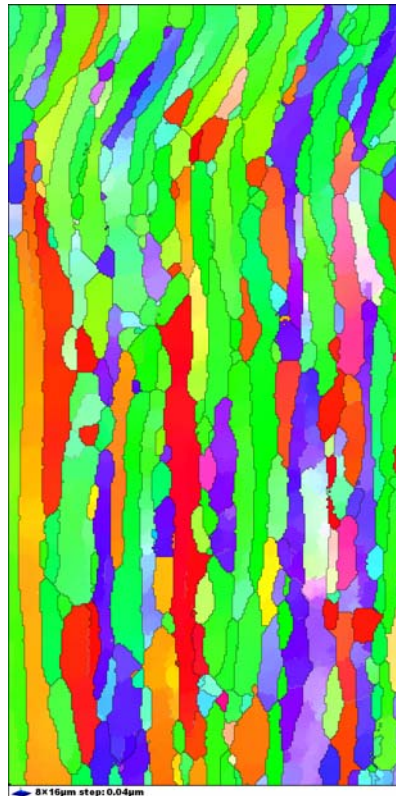
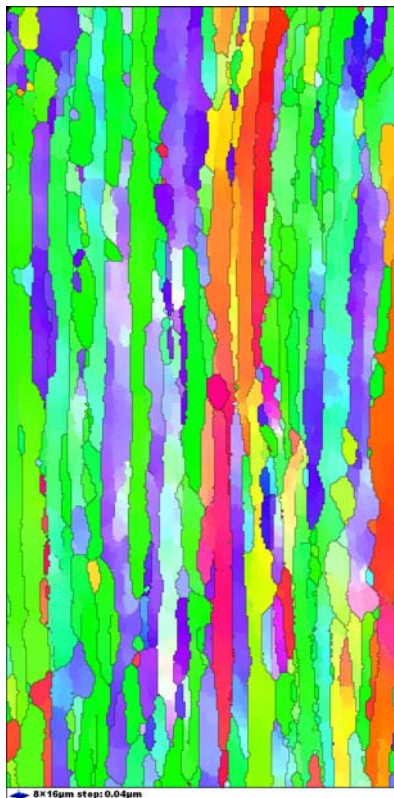


Figure 6-8. Continued

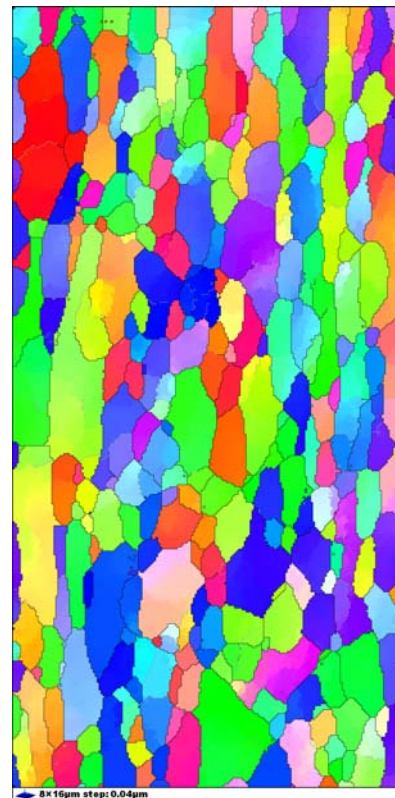
6: Micro-extruded UFG and CG Copper



(a)



(b)



(c)

Figure 6-9. Microstructure of UFG copper extruded at different speeds: (a) UFG extruded at 0.1 mm/min; (b) at 10 mm/min and (c) at 25 mm/min. Scale bar and ED are the same as in Fig. 6-6.

6.3 Texture Evolution of UFG and CG Copper after Micro-extrusion

Instead of the entire orientation distribution functions, the inverse pole figures are particularly useful for deformation processes such as extrusion, which require the specification of only a single axis, i.e., the extrusion direction. However, the texture has no axial symmetry with respect to the longitudinal axis of the specimen for the UFG initial material which was pre-processed by ECAP, thus transverse direction was also shown (Fig. 6-11a). The texture for the initial CG material (Fig. 6-10a) shows a $\langle 100 \rangle$ fiber together with a $\langle 110 \rangle$ and a spreading of this component towards $\langle 111 \rangle$. The UFG initial sample has a more complex texture because it is a shear texture which was made by eight-pass ECAP on the 45° plane of the extruded sample. This is why there are intensities everywhere in the inverse pole figures of the UFG sample, except at positions near to $\langle 111 \rangle \parallel \text{ED}$ and $\langle 110 \rangle \parallel \text{TD}$. The reason for this that the $\langle 111 \rangle$ planes are preferably parallel to the shear plane (which is 45° away from ED) and the $\langle 110 \rangle$ directions are preferential along the shear direction (which is also at 45° with respect to the ED) and in no way parallel to the TD direction. After different speeds micro-extrusion, a double fibre texture $\langle 111 \rangle$ and $\langle 110 \rangle$ forms for both UFG and CG. For CG, two sharp fibre textures $\langle 111 \rangle$ and $\langle 100 \rangle$ are developed during extrusion (Figs. 6-10b-e). Similar results are reported for extrusion of f.c.c. metals [164-167]. For UFG copper, approximately constant fiber components are found, where higher intensity in 0.1, 1 and 10 mm/min (Figs. 6-11b-d) was found when comparing with CG. A dependence of stacking fault energy (SFE) on the fiber type has been reported in [168]: materials with a high SFE depict a strong $\langle 111 \rangle$ fiber whereas materials with a low SFE depict a strong $\langle 100 \rangle$ fibre. After extrusion at 25 mm/min in UFG specimen, a dramatically decreased intensity the texture is obtained moving towards the $\langle 100 \rangle$ component (Fig. 6-11e).

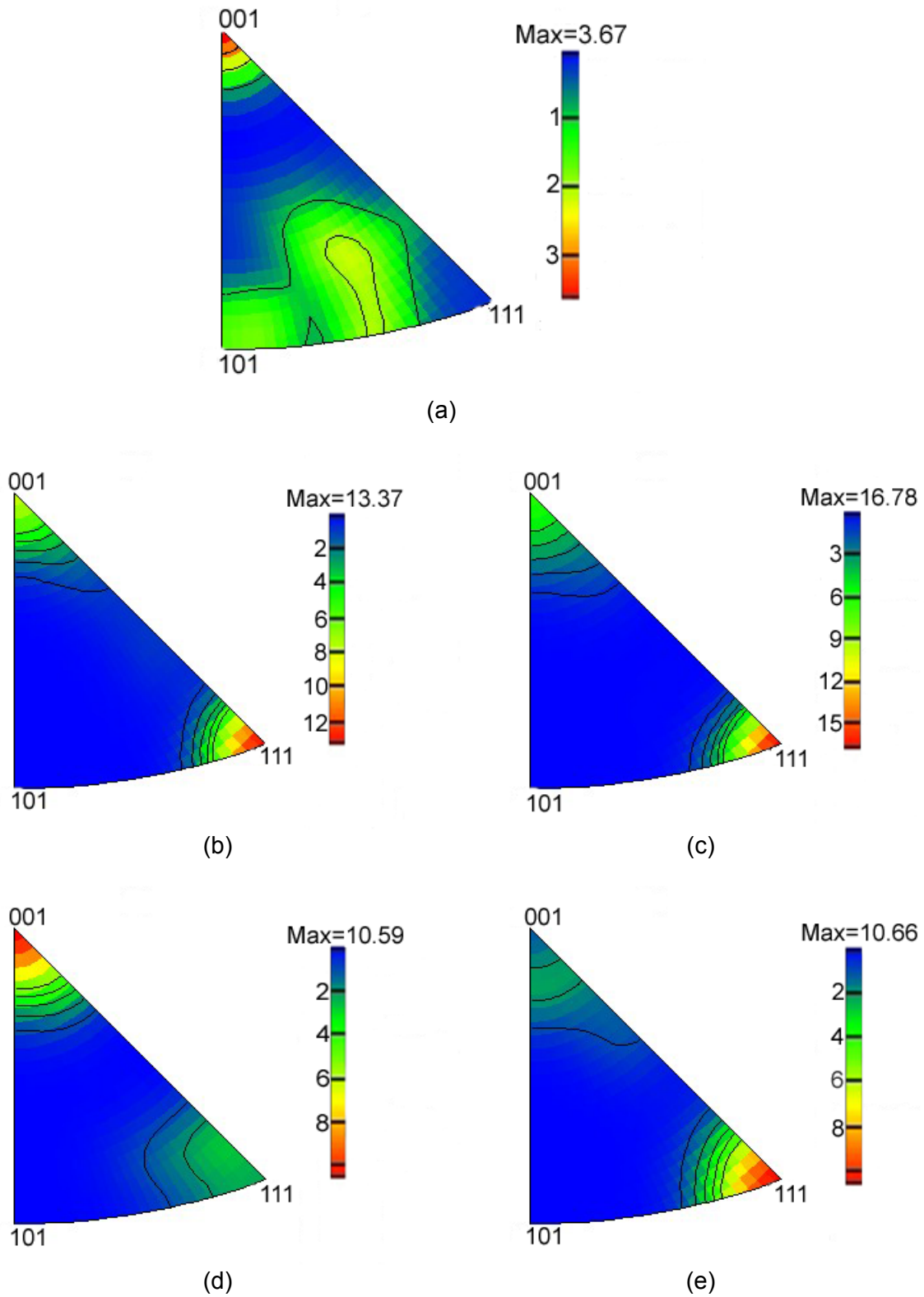


Figure 6-10. IPFs of CG as-received (a), and CG copper extruded at different speeds: (b) CG extruded at 0.1 mm/min; (c) at 1 mm/min; (d) at 10 mm/min and (e) at 25 mm/min.

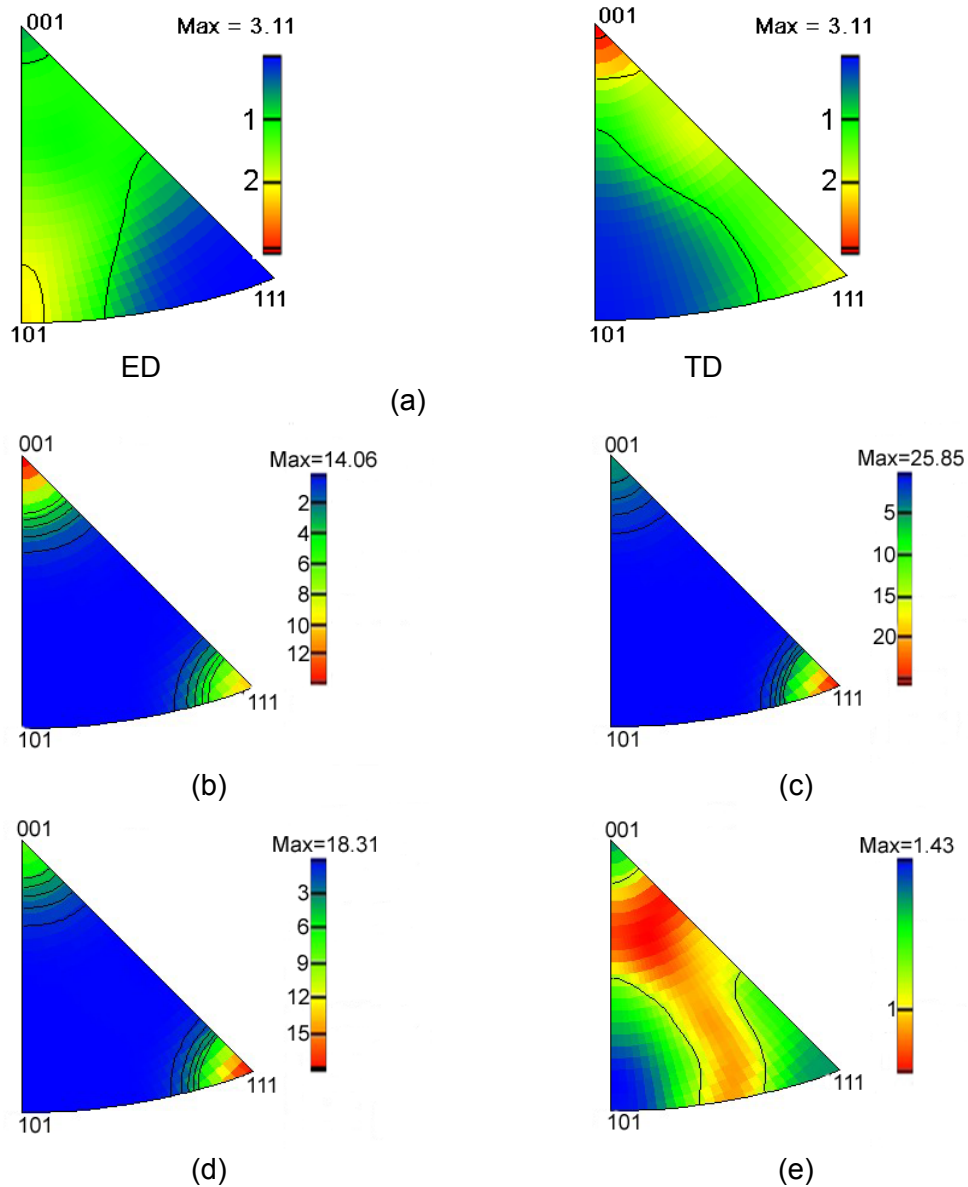


Figure 6-11. IPFs of UFG initial (a) and UFG copper extruded at different speeds: (b) UFG extruded at 0.1 mm/min; (c) at 1 mm/min; (d) at 10 mm/min and (e) at 25 mm/min.

6.4 Differential Scanning Calorimetry

The differential scanning calorimetry (DSC) curves in Fig. 6-12 show an exothermic peak at about 163°C after 8 pass ECAP, and at 202°C after extrusion at 0.1 mm/min. The peak decreases with increasing extrusion speed to 177°C after extrusion at 25 mm/min (Fig. 6-13a). Similar to the changing trend of peak temperature (T_p), the stored energy decreases with increasing extrusion speed. It is approximately 0.95 ± 0.05 J/g after 8 pass ECAP (Fig. 6-13b), which is close to the values for copper processed by ECAP to similar strains [169, 13], whereas after extrusion at the speed of 25 mm/min, the stored energy

6: Micro-extruded UFG and CG Copper

decreases to 0.71 ± 0.03 J/g. Same observation was found by others [170, 171]. For CG, the stored energy measured at different extrusion speeds remains roughly constant at 0.75 ± 0.05 J/g, which is ~20% lower than the value of the initial UFG samples (Figs. 6-12 and 6-13b), and there is no obvious shift in peak temperature (Figs. 6-12 and 6-13a).

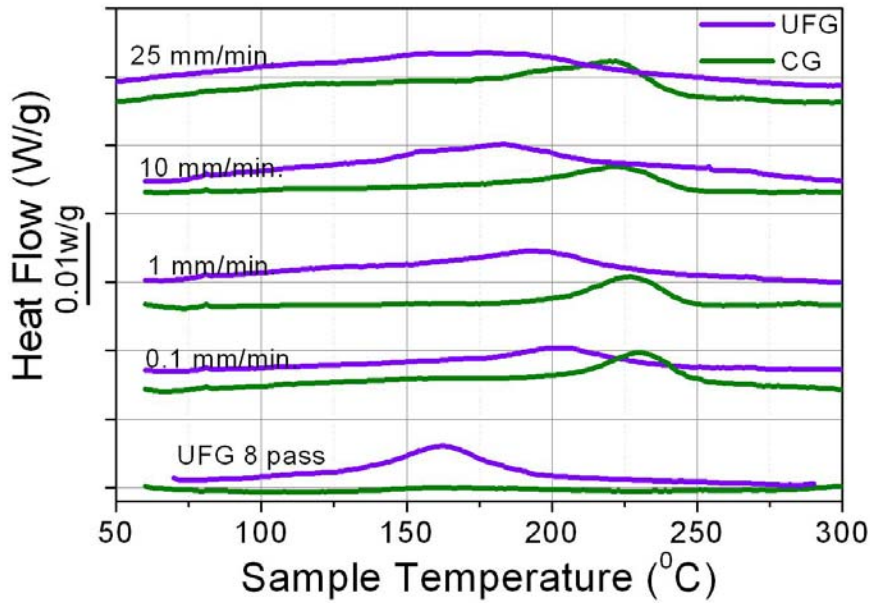


Figure 6-12. Exothermic DSC curves of UFG and CG copper extruded at 0.1, 1, 10, and 25 mm/min. Samples were scanned at a linear heating rate of 10 K/min. (The very bottom scans are for the un-extruded starting materials).

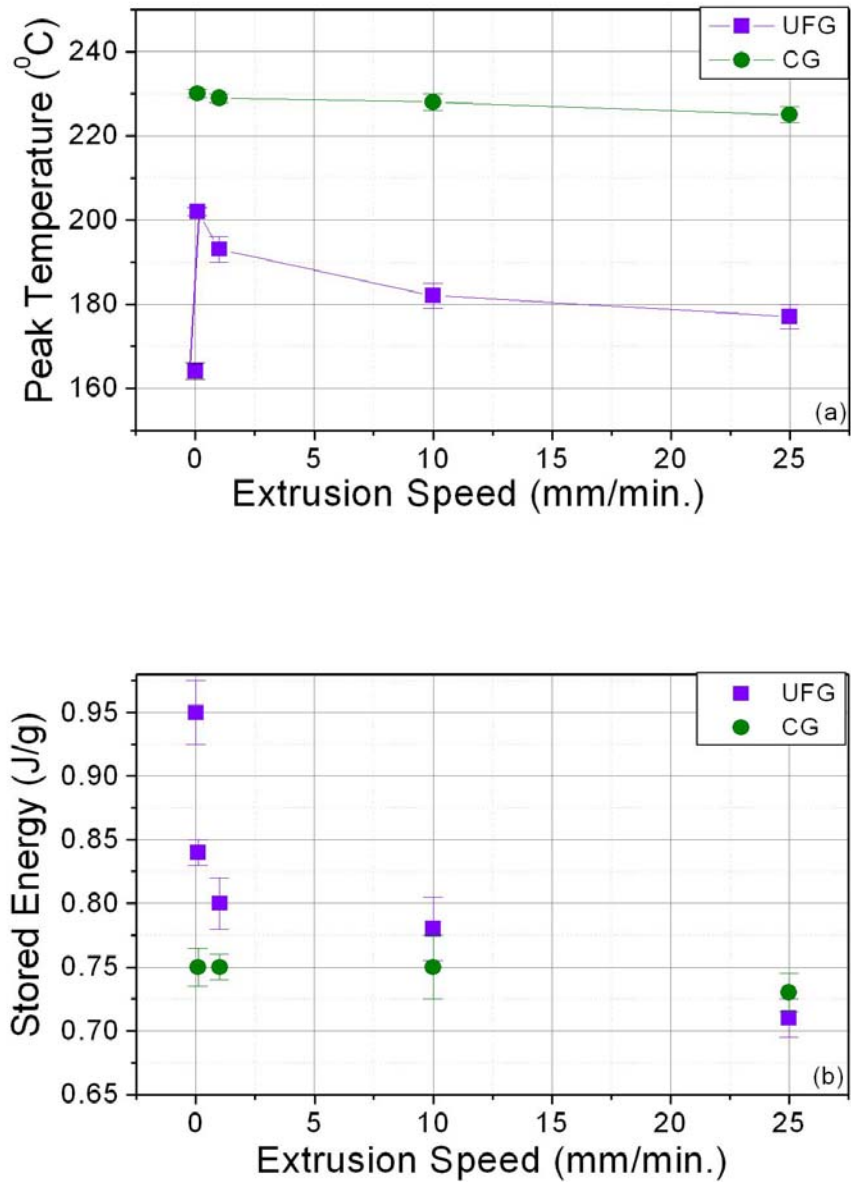


Figure 6-13. (a) Peak temperatures from DSC measurement for UFG and CG copper and (b) Stored energy from DSC measurement for UFG and CG copper. Values for the un-extruded starting material in both cases are shown as an extrusion speed of zero for comparison.

6.5 Nano-indentation

Both UFG and CG copper at different extrusion speeds were subjected to nano-indentation under a maximum 5000 μN load (Fig. 6-14).

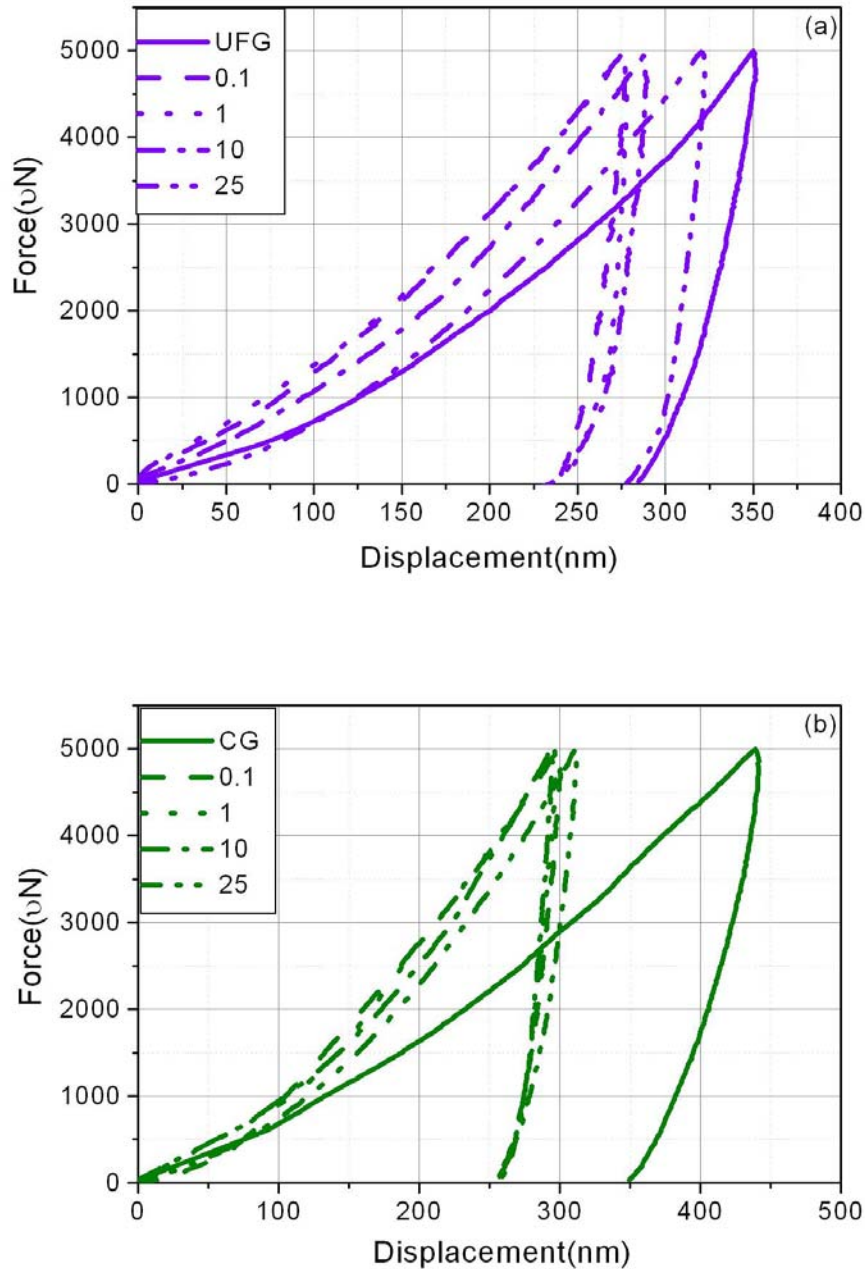


Figure 6-14. Load and displacement curves from nano-indentation experiments performed at 100 µN/sec: (a) UFG and (b) CG.

After 8 pass ECAP, the hardness (1.7 ± 0.01 GPa) measured in this study is close to the reported values for UFG copper [93]. The hardness increased rapidly when extruded at the low speeds of 0.1 and 1 mm/min, and a remarkable decrease in hardness was observed after extrusion at 25 mm/min (Fig. 6-15). For CG, the hardness remains approximately constant, declining only slightly after extrusion at 25 mm/min (Figs. 6-14b

6: Micro-extruded UFG and CG Copper

and 6-15). The dislocation density (Fig. 6-16) of the UFG copper ($19.56 \pm 0.38 \times 10^{14} \text{ m}^{-2}$) is similar to the reported values [172, 173] and followed the same trend as the hardness data. An obvious decrease in dislocation densities was found in UFG copper and only slight decrease in CG copper ($13.8 \pm 0.5 - 10.2 \pm 1.1 \times 10^{14} \text{ m}^{-2}$).

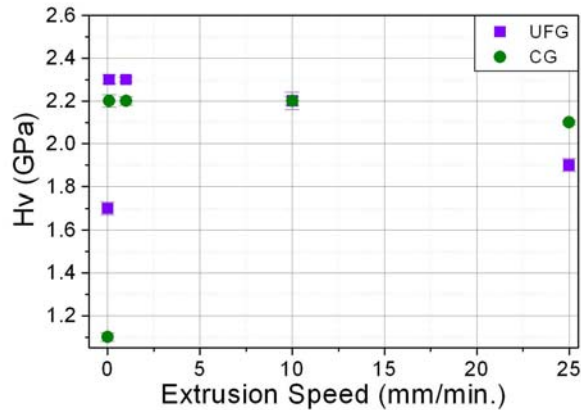


Figure 6-15. Nano-indentation hardness variation for extruded UFG and CG copper. Values for the un-extruded starting material in both cases are shown as an extrusion speed of zero for comparison.

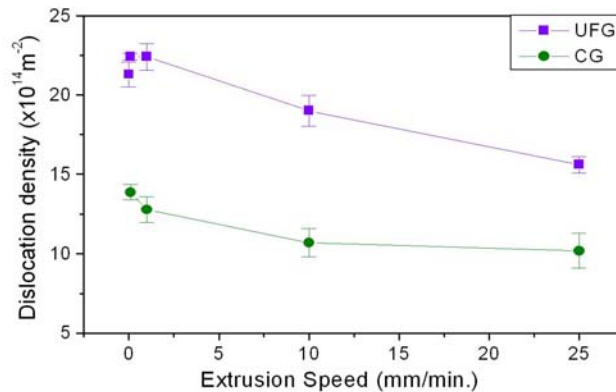


Figure 6-16. Dislocation density calculation from XRD measurement for extruded UFG and CG copper. Values for the un-extruded starting material in both cases are shown as an extrusion speed of zero for comparison.

6.6 Flow Line Model

Based on the upper bound theorem Avitzur [174] and Altan et al [175] proposed analytical flow line functions for axisymmetric extrusion in a cylindrical die to determine the strain path. The model introduced by Altan et al [175] has been successfully used for the drawing of pearlitic steel [175] and also has been adopted in this study. It was also

6: Micro-extruded UFG and CG Copper

The constant C defines selected flow lines with values of $0 \leq C \leq 1$; $C = 0$ for a line at the centre and $C = 1$ at the surface, respectively. The shape of a selected flow line can be plotted from Eq. (6-1) using the formula:

$$r = C \left[R_2 + \frac{R_1 - R_2}{A^3} z^2 (3A - 2z) \right] \quad (6-2)$$

In order to validate the analytic flow line model, a finite element simulation was carried out. The simulation was performed using the commercial package Q-Form [177] by Dr. Rimma Lapovok. The software is based on the flow formulation which relates the stresses to the plastic strain increments and the material is an incompressible rigid-viscoplastic continuum. The flow stress for copper was represented as a function of strain in a table form. The friction coefficient was taken to be 0.2 which is a value commonly used for forming processes in FE simulations. The distribution of equivalent strain and strain rate, mean stress and equivalent stress were obtained as result of simulation. Four equally-spaced horizontal and five vertical flow lines were considered during extrusion. The result of the FE simulation is also shown in Fig. 6-18. The nearest flow line with respect to the experiment was situated at the initial position 0.62R (0.6R in the experiment). As can be seen, the analytic flow line corresponds very well to the flow line image obtained from the FE simulation.

From the flow line function, the components of the velocity vector can be obtained as the partial derivatives of $f(r, z)$:

$$V_r = \lambda \frac{\partial f(r, z)}{\partial z} = -V_f \left(\frac{R_2}{R_1 - R_2} A^3 \right)^2 6rz(A - z) \left[z^2(3A - 2z) + \frac{R_2}{R_1 - R_2} A^3 \right]^{-3} \quad (6-3)$$

$$V_\theta = 0 \quad (6-4)$$

$$V_z = -\lambda \frac{\partial f(r, z)}{\partial r} = -V_f \left(\frac{R_2}{R_1 - R_2} A^3 \right)^2 \left[z^2(3A - 2z) + \frac{R_2}{R_1 - R_2} A^3 \right]^{-2} \quad (6-5)$$

Here λ is a parameter defined by the boundary conditions and V_f is the absolute value of the exit velocity of the material. In a polycrystal plasticity simulation, the velocity gradient is needed; in cylindrical coordinates it is defined as:

6: Micro-extruded UFG and CG Copper

$$L = \begin{bmatrix} \frac{\partial V_r}{\partial r} & \frac{1}{2} \left(\frac{\partial V_\theta}{\partial r} - \frac{V_\theta}{r} + \frac{1}{r} \frac{\partial V_r}{\partial r} \right) & \frac{1}{2} \left(\frac{\partial V_z}{\partial r} + \frac{\partial V_r}{\partial z} \right) \\ \frac{1}{2} \left(\frac{\partial V_\theta}{\partial r} - \frac{V_\theta}{r} + \frac{1}{r} \frac{\partial V_r}{\partial r} \right) & \frac{V_r}{r} + \frac{1}{r} \frac{\partial V_\theta}{\partial \theta} & \frac{1}{2} \left(\frac{\partial V_\theta}{\partial z} + \frac{1}{r} \frac{\partial V_z}{\partial \theta} \right) \\ \frac{1}{2} \left(\frac{\partial V_z}{\partial r} + \frac{\partial V_r}{\partial z} \right) & \frac{1}{2} \left(\frac{\partial V_\theta}{\partial z} + \frac{1}{r} \frac{\partial V_z}{\partial \theta} \right) & \frac{\partial V_z}{\partial z} \end{bmatrix}_{r,\theta,z} \quad (6-6)$$

From Eqs. (6-3) – (6-6), the velocity gradient can be obtained as:

$$L = \begin{bmatrix} \frac{\partial V_r}{\partial r} & 0 & \frac{\partial V_r}{\partial z} \\ 0 & \frac{V_r}{r} & 0 \\ 0 & 0 & \frac{\partial V_z}{\partial z} \end{bmatrix}_{r,\theta,z} \quad (6-7)$$

Finally, using Eqs. (6-3) – (6-5), the non-zero components of the velocity gradient can be expressed as:

$$L_{rr} = -V_f \left(\frac{R_2}{R_1 - R_2} A^3 \right)^2 6z(A-z)G^{-3} \quad (6-8)$$

$$L_{\theta\theta} = L_{rr} \quad (6-9)$$

$$L_{zz} = -2L_{rr} \quad (6-10)$$

$$L_{r\theta} = -6rV_f \left(\frac{R_2}{R_1 - R_2} A^3 \right)^2 \left[(A-2z)G^{-3} - 3z^2(A-z)^2G^{-4} \right] \quad (6-11)$$

where G is introduced to simplify the equations, and is defined as:

$$G = z^2(3A-2z) + \frac{R_2}{R_1 - R_2} A^3 \quad (6-12)$$

The velocity gradient components obtained for the present experimental conditions along the flow line defined by $C = 0.6$ (Fig. 6-18) show that the deformation speed increases drastically near to the exit point of the die. Actually, the tension component (L_{zz}) obtained from Eqs. (6-8) - (6-10) using the extrusion speed of 1 mm/min increases up to 0.6 s^{-1} . The shear component also becomes significant, up to 0.4 s^{-1} , just before the flow line exits the deformation zone. It also goes through a sign change during deformation. From the FE simulation it was possible to track the evolution of the equivalent strain rate (not the

individual components) and this is also plotted in Fig. 6-18. As can be seen, the equivalent strain rate shows a very similar evolution to the development of the velocity gradient components.

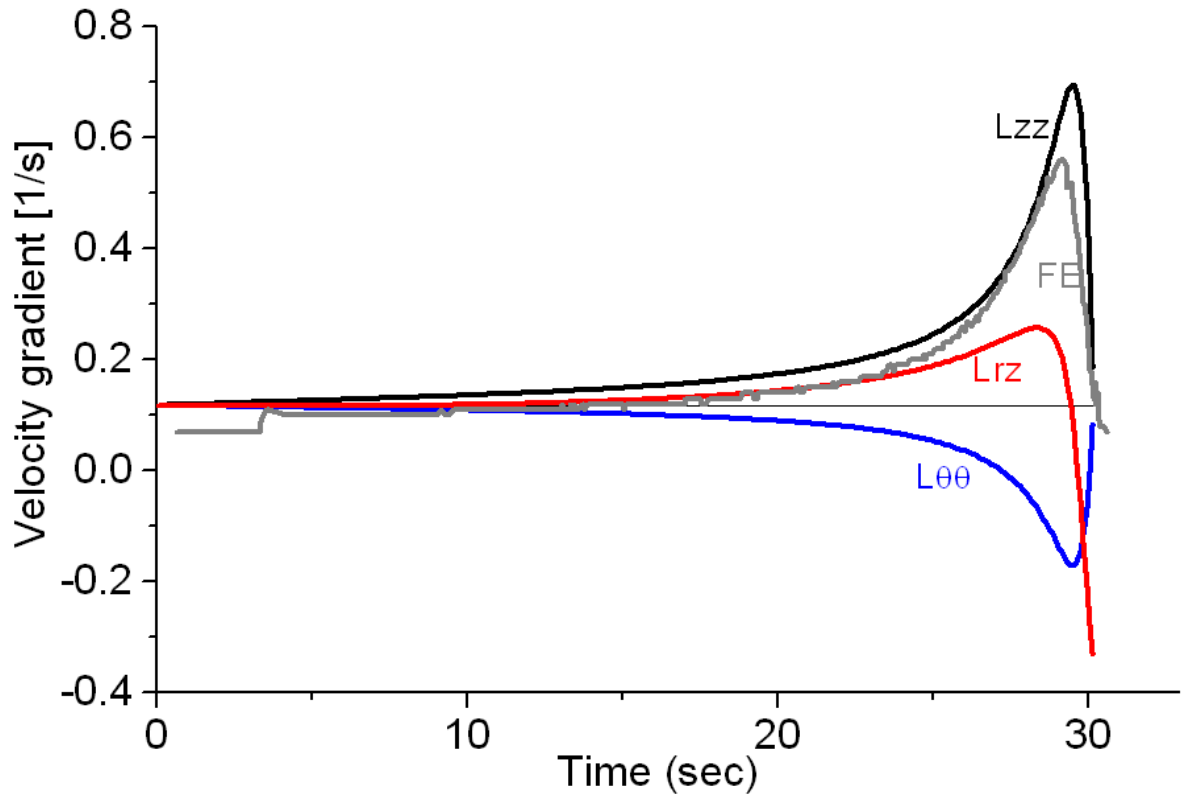


Figure 6-18. Evolution of the components of the velocity gradient as a function of time along the flow line selected at position $C = 0.6$ ($C = 0$ is the centre). The equivalent strain rate obtained from the FE simulation is superimposed (it corresponds to initial position $C = 0.62$).

6.7 Polycrystal Modeling

In order to understand the texture evolution during micro-extrusion one must apply a polycrystal model coupled to an accurate representation of the velocity gradient through the container and die. The viscoplastic self consistent model (VPSC) polycrystal model was used. An analytical representation of the velocity gradient is the simplest way to insert the velocity gradient into the VPSC model, but first we validated it with a finite element simulation. In addition to the texture simulations the recently developed grain refinement and VPSC model [20] were used for the coarse-grained material only.

Two polycrystal models were applied in the present work: the VPSC model in its version of [132] as well as the grain refinement model [20]. Grain refinement modeling was only

possible for the initially CG material where the average grain size was 24 μm . The UFG material had already 0.4 μm grain size before extrusion which was too small for the grain refinement model. For that material, the VPSC model was used without grain refinement simulation. 500 randomly oriented grain orientations were generated as input for the extrusion of the CG material with an average grain size of 24 μm and with a lognormal distribution for the grain size. In the UFG case, 1000 grain orientations were selected from the texture of the ECAP-deformed material. In both simulations, the velocity gradient derived from the flow line model was used; the material element containing the initial texture was moved and deformed along the flow line. Two flow lines were considered: one in the centre line of the sample ($C = 0$) and one at an intermediate position defined by $C = 0.6$.

6.8 Discussions

6.8.1 Textures

The CG $\{100\}$ pole figures measured before and after extrusion at speed of 1 mm/min (Fig. 6-19) is characteristic of an EBSD measurement of samples with relatively large grains. They are quite spotty due to the small number of grains in one map (note that the pole figures are taken from one EBSD map, whereas the grain statistics are an aggregate of three or four maps). This illustrates well the difficulties that can arise for the statistics when CG materials are used with respect to UFG materials.

For the UFG material, the textures before and after extrusion at speed of 1 mm/min are presented in Fig. 6-20. The initial texture is typical of the route Bc texture of copper after eight passes. Fig. 6-20 shows the textures after extrusion in $\{100\}$ pole figures. The $\{100\}$ pole figure is shown because in this presentation the $\langle 100 \rangle$ and $\langle 111 \rangle$ fibres that are characteristic of extrusion of copper can be well distinguished. The $\langle 100 \rangle$ fibre component appears in the middle horizontal line as well on the top and bottom of the pole figure while the $\langle 111 \rangle$ appears about half-way between these reflections. As can be seen, the $\langle 111 \rangle$ fibre is always strong while the $\langle 100 \rangle$ fibre appears only in the central part of the sample and much weaker than the $\langle 111 \rangle$. Furthermore, in the intermediate position between the centre and the surface of the sample, the texture seems to be slightly rotated around the tangential direction. A pronounced non-uniform distribution is present along the fibres in both the centre and intermediate positions. This kind of texture is frequent in drawing or extrusion and is called the 'cyclic' texture. In the intermediate position it originates from the shear component that appears in extrusion, which will be explained in the following section.

6: Micro-extruded UFG and CG Copper

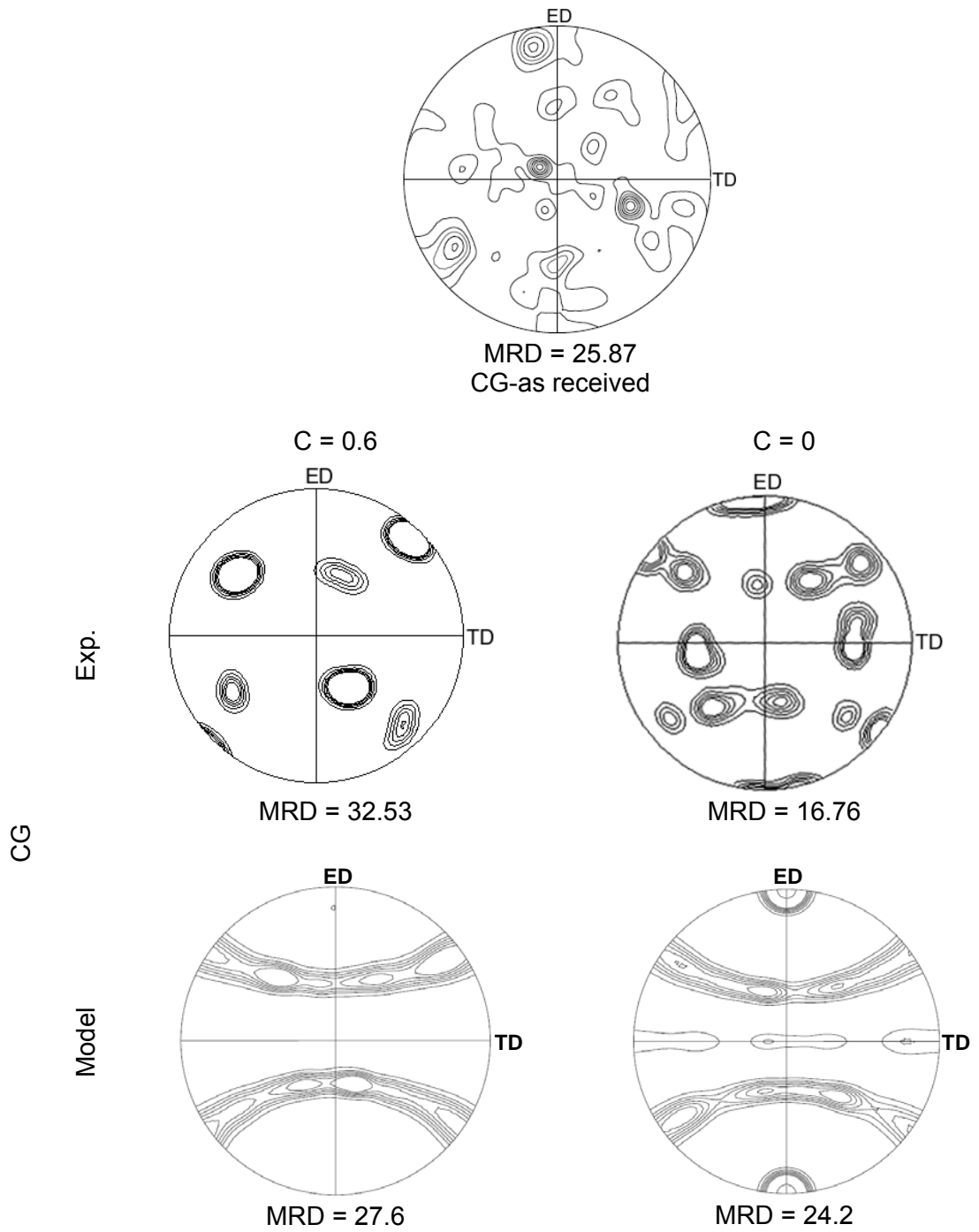


Figure 6-19. Experimental and predicted $\{100\}$ pole figures of $C = 0$ and $C = 0.6$ within the extrudates for CG copper; Isolevels: 1.2, 2.0, 2.5, 3.0, 3.5, 4, 8, 12, 20, 30.

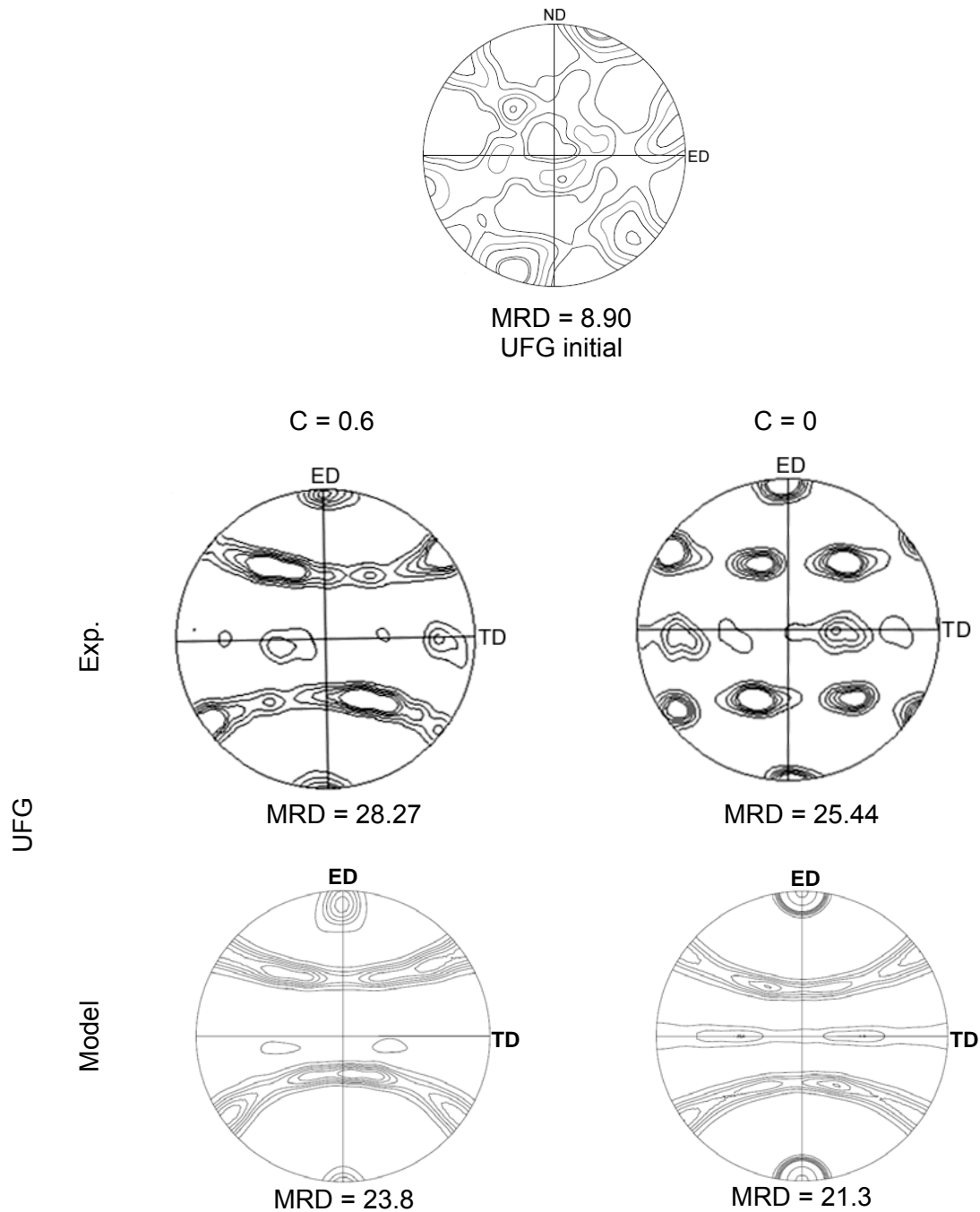


Figure 6-20. Experimental and predicted $\{100\}$ pole figures for positions $C = 0$ and $C = 0.6$ within the extrudates for UFG copper; Isolevels: 1.2, 2.0, 2.5, 3.0, 3.5, 4, 8, 12, 20, 30.

The statistics could have been better in the CG EBSD maps and textures (Fig. 6-2). However, we deliberately have chosen the same map size for both the CG and UFG materials to clearly demonstrate the differences. The main difference is the number of grains present in the same cross section. The predicted texture for the initially CG material (Fig. 6-19) shows that there is only one fibre in the intermediate position; this is the $\langle 111 \rangle$

6: Micro-extruded UFG and CG Copper

fibre and it appears in a position rotated around the circumferential axis (TD in the figure). This tilt of the texture is produced by the shear component of the extrusion process which is traced in Fig. 6-18. This shear component is first positive, and then just before leaving the die it becomes large and negative. The sense of the tilt of the texture is related to the sense of the shear. One can readily identify that the tilt corresponds to the *negative* part of the shear component. The reason why only the $\langle 111 \rangle$ fibre is present is related to the instability of the $\langle 100 \rangle$ component in the presence of shear. Without shear, the $\langle 100 \rangle$ fibre is stable, as can be seen in the texture measured in the central part of the sample. The $\langle 100 \rangle$ cube texture component is shown [178] to be unstable under shear and rotates quickly with the speed of the rigid body spin, and therefore, dissolves.

Starting with the initial CG texture the evolution of texture and grain size was obtained using the grain refinement model in Chapter 3. During the simulations, the initially 500 grains were subdivided into nearly 7 million new grains with an average grain size of 0.92 μm in the intermediate position. The measured average grain size was 0.9 μm , thus the simulation agrees very well with the measurement. The simulation in the centre position led to only 255656 new grains with an average grain size of 1.66 μm . The experimental grain size along the centre line was 1.4 μm , which is also in good agreement with the simulation result. However, in order to obtain this good agreement, one had to tune the grain refinement model in Chapter 3. There is only one parameter to change in the model which defines the degree of retardation of the lattice rotation by the grain boundaries producing the curvature of the lattice (μ , see in [20]). In the first application of the model, μ was taken to be 0.5 in the simulation of grain refinement during ECAP. In the present case, it was chosen to be 0.22 at the intermediate position and 0.4 along the centre line. This tuning of the lattice curvature can actually be explained by considering that significant heating happened during micro extrusion as discussed above. Taking a friction coefficient of 0.2 (the same as the one used in the FE simulation), when temperature rises dislocations can annihilate more easily, and this happens also to those dislocations that are producing the lattice curvature. Therefore, the density of curvature induced dislocations should be less in case recovery processes become more important. The μ parameter is in direct relation with the lattice curvature (see in [20]). It is then physically plausible that μ should be decreased when temperature increases. This is the reason why smaller μ value led to better agreement for the grain size. Note that different μ values were used for the intermediate and central regions (see above). This difference can be justified by taking into account the possible temperature gradient within the sample. Namely, due to the large strain rate at the exit (see Fig. 6-18), the temperature cannot be equalized so it is expected that the temperature is significantly smaller in the central

6: Micro-extruded UFG and CG Copper

region. Consequently, a larger μ value should be used, which was the case in the simulations. Note that the above reasoning about the effect of heat only causes a certain recovery of the dislocation structure, not a dynamic recrystallization. The existence of the temperature gradient could be confirmed in finite element calculations if heat effects due to friction and plastic straining are properly taken into account.

In case of the UFG starting material it was not possible to employ the grain refinement model because initially there was such a small grain size which was out of the range of the grain refinement model. In this case the initial texture was strong and 1000 orientations representing the texture were selected from the measured ECAP texture. The simulated textures are shown in Fig. 6-20. These predicted textures are comparable to those predicted for CG-material (compare to Fig. 6-19) with the difference that there is a clear cyclic-nature of the texture in the central region for the UFG material. The same pattern along the experimental $\langle 111 \rangle$ fibre can be detected. In the intermediate position, the predicted and measured textures also have the same pattern. The main difference is that in the latter case the measured pole figure is spotty for the reasons of statistics which could have been better measuring larger zones on the samples by EBSD.

6.8.2 Thermo mechanical behaviour

For the thermo mechanical behaviors, the dislocation densities determined by X-ray measurement are close to the dislocation densities obtained by others [169, 172, 173, 179-182] for copper of similar or unknown purity processed by severe plastic deformation (Fig. 6-21).

From these data one can calculate the stored energy and compare with the stored energy from all boundaries, which can be computed from the EBSD data. There is some difference due to dislocations between boundaries, but this contribution is small, as the density between boundaries has previously been shown to be an order of magnitude lower than the values calculated from XRD [29]. Eqs. (6-13) and (6-14) are used to determine the stored energies from the dislocation density (XRD) and boundary contribution (EBSD), respectively.

$$E_d = \frac{1}{2} \rho G b^2 \quad (6-13)$$

$$E_b = \frac{2\bar{\gamma}}{d_{\theta \geq 1^\circ}} \quad (6-14)$$

6: Micro-extruded UFG and CG Copper

where G is the shear modulus (for copper 48.3 GPa), b Burger's vector (2.56×10^{-10} m²), and ρ is the dislocation density. The dislocation calculated from X-ray peak broadening by using the method described in Chapter 3. From equation (6-13), we can obtain the stored energy from dislocations between boundaries walls. The stored energy resulting from the boundary energy can be calculated by using equation (6-14), $\bar{\gamma}$ can be calculated based on EBSD measurement [183]. Applying Eqs. (6-13) and (6-14), one can find that the stored energies are consistent within experimental error (Table 6-1). The remaining discrepancy with the DSC stored energy is a contribution from vacancies [184, 185, 186].

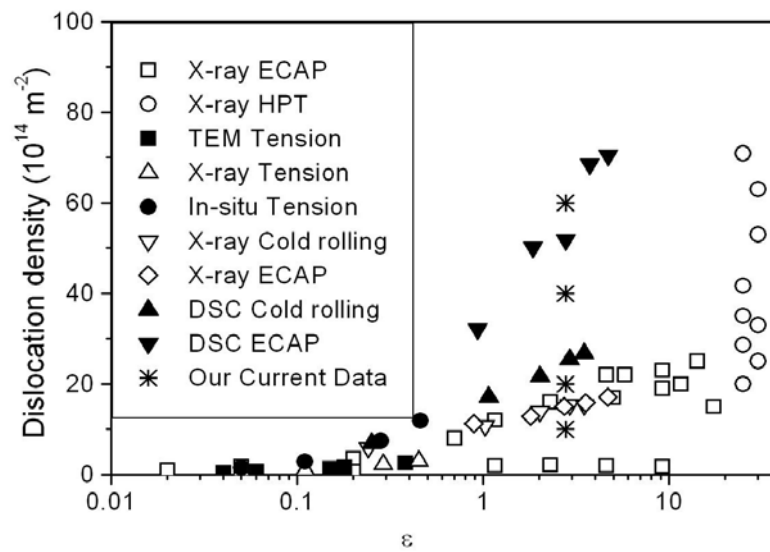


Figure 6-21. Comparison of the deformation induced dislocation densities in severe plastic deformed copper by X-ray measurement [169, 172, 173, 179], DSC measurement [180] and TEM [181, 182].

The mechanical properties of the CG material and their proxy (dislocation density) are consistent with the annealing response during DSC. The hardness and dislocation densities barely change with the increasing extrusion speed, and this trend is mirrored in the annealing measures (stored energy and peak temperature). However, in the case of the UFG material, the trend in DSC response with the increasing extrusion speed is unusual. Whereas the stored energy declines in concert with the hardness and dislocation density, the peak temperature also unexpectedly declines. The hypothesis is that deformation heating during micro-extrusion of the UFG copper is sufficient to initiate restoration mechanisms, which then serve to reduce the stored energy and peak temperature during subsequent post-extrusion before DSC. To justify this hypothesis one

6: Micro-extruded UFG and CG Copper

must explore the factors controlling the kinetics of recrystallization and whether the temperature rise during extrusion is sufficient to induce restoration processes.

The kinetics of recrystallization is governed by the relation

$$X \propto \dot{N} \dot{G} \quad (6-15)$$

where X is the volume fraction of recrystallization, \dot{N} the rate of nucleation, and \dot{G} the interface migration rate which is described as:

$$\dot{G} \propto MP \quad (6-16)$$

where P is the driving force, and M the mobility of the recrystallization front [187].

In this exposition, one first looks at the factors that control recrystallization during the continuous heating DSC experiment, and then seek to explain the effect of prior restoration mechanisms on these factors. The DSC response is connected to the recrystallization kinetics by the peak temperature T_p , which is the temperature where 50% recrystallization takes place. During continuous heating, accelerated recrystallization leads to a lower peak temperature [188]. Thus, in order to observe a decreased peak temperature either \dot{N} must increase and/or \dot{G} must increase (Eq. 6-15).

One can eliminate an increase in the interface migration rate by looking at the factors that control \dot{G} (Eq. 6-16). In order to induce an increase in the interface migration rate, either the stored energy P , or the mobility M must increase. Fig. 6-12 has shown that the energy stored during extrusion and released by recrystallization during continuous heating DSC decreases for UFG copper, and thus one would expect on this basis that the interface migration rate should also decrease, leading to a higher T_p . Turning to mobility, it is assumed that mobility is an increasing function of misorientation for low angle boundaries and constant for high angle boundaries [187]. The average misorientation for low angle boundaries remains approximately constant (Fig. 6-22), and thus for a common DSC heating rate the mobility is likely to increase at the same rate for each extrusion

6: Micro-extruded UFG and CG Copper

condition. Therefore, one expects the growth rate to decrease, which would also lead to a higher T_p .

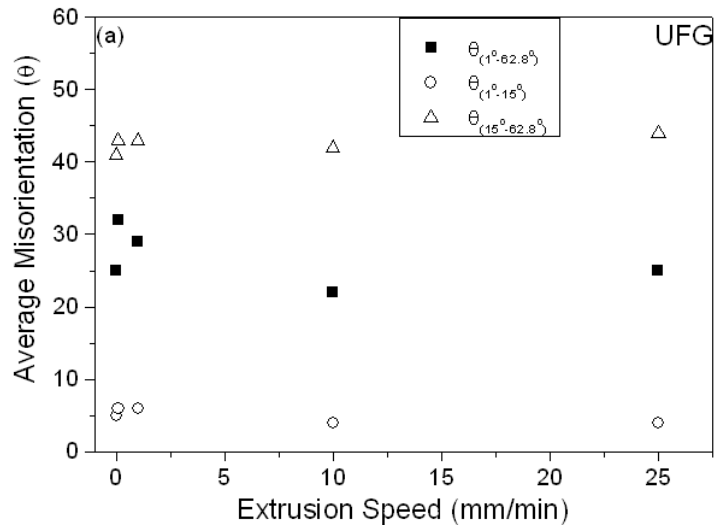


Figure 6-22. Variation of average misorientation for initial UFG and UFG copper extruded at different speeds.

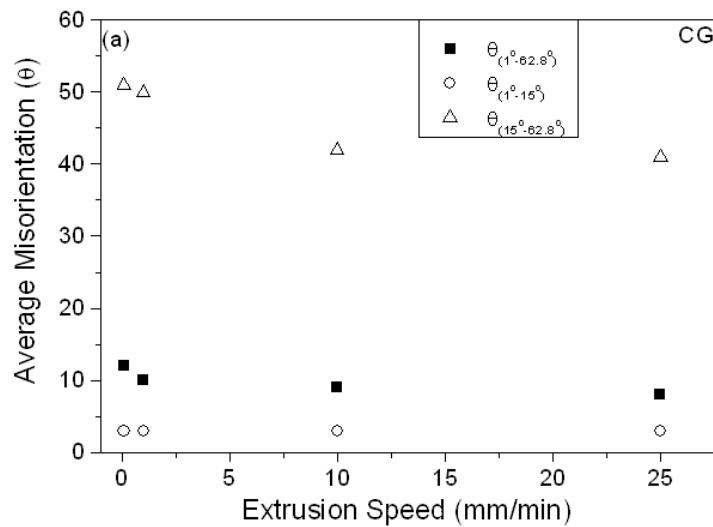


Figure 6-23. Variation of average misorientation for initial CG and CG copper extruded at different speeds.

6: Micro-extruded UFG and CG Copper

Table 6-1. Stored energy calculation from EBSD and XRD measurements of UFG and CG copper extruded at different speeds

mm/min.	UFG					CG			
	8 passes	0.1	1	10	25	0.1	1	10	25
EBSD									
d_{ECD} (μm)	0.26 ± 0.02	0.33 ± 0.01	0.33 ± 0.02	0.26 ± 0.03	0.53 ± 0.01	0.38 ± 0.01	0.33 ± 0.03	0.31 ± 0.04	0.4 ± 0.05
$\bar{\gamma}$ (J/m^2)	0.5	0.52	0.54	0.55	0.56	0.4	0.41	0.42	0.43
E_b (J/g)	0.43	0.35	0.37	0.47	0.24	0.23	0.28	0.30	0.24
XRD									
E_d (J/g)	0.34	0.40	0.40	0.32	0.28	0.25	0.23	0.19	0.18

6: Micro-extruded UFG and CG Copper

The remaining possibility is that the nucleation term must benefit from prior restoration mechanisms and our experimental evidence, bolstered by the literature, supports this conclusion. If grains were to nucleate during micro-extrusion we would expect to observe several differences after extrusion between the high speed and low speed extrusions: i) an increase in the mean grain size; ii) a decrease in the stored energy because dislocations have been eliminated; iii) a decrease in the dislocation density; and iv) an increase in the average misorientation of low angle boundaries. The first three of these four predictions are found in this work, and the absence of the fourth is explained in terms of relative rates of restoration. The mean grain size does indeed increase for UFG, but not for CG. The stored energy (Fig. 6-12 and 6-13) and dislocation density (Fig. 6-16) decreases after extrusion of the UFG. However, the misorientation barely changes (Fig. 6-22a and 6-23a). This can be explained by the rate of formation of grains with high angle boundaries forming from low angle boundaries being faster than the rate of rotation of subgrains to higher misorientations. i.e., grains are leaving the low angle boundary class faster than the misorientation is increasing. The work of Lefevre-Schlick et al. supports this argument [189], showing that the incubation time for the nucleation of recrystallization by grain boundary bulging in copper is about three times faster than the incubation time for the nucleation of recrystallization by sub-grain rotation in the bulk of the grains. Furthermore, the effect of prior restoration on recrystallization kinetics is found in work on Al-2.5%Mg [190], where a clear shift of T_p to lower temperature is found due to prior recrystallization.

Thus the hypothesis is shown to be plausible: during continuous heating a decrease in growth rate is offset by enhanced nucleation as a result of restoration mechanisms operating during extrusion, and this serves to reduce both the stored energy and peak temperature during subsequent post-extrusion before DSC. The remaining question is whether the temperature rise is sufficient during micro-extrusion to allow formation of nuclei/prior recrystallization. For copper, which has a low stacking fault energy, one can reasonably expect dynamic recrystallization if the temperature is high enough during micro-extrusion. Although the temperature rise cannot be measured directly due to the complexity of the extrusion die, one can estimate the temperature rise at the different speeds used in this experimental campaign. Also, it is necessary to explain how recrystallization comes about in the UFG material and not in the CG. Contributions to the heat rise during extrusion are from i) deformation work; ii) friction between the billet and the container wall; and iii) friction at die land [191]. The latter two of these contributions

6: Micro-extruded UFG and CG Copper

are primarily at the surface of the extrudate. The temperature rise during extrusion can be evaluated by summing all these components.

The rise in mean temperature ($\Delta\bar{T}_1$) due to the first component can be calculated as [191]:

$$\Delta\bar{T}_1 = \frac{\bar{\sigma} \ln ER}{\sqrt{3}(\rho \times s)} \quad (6-17)$$

where $\ln ER$ is the homogeneous strain and the mean flow stress, $\bar{\sigma}$ is based on the yield stress taken from previous tensile tests [147], and s and ρ are the specific heat (for copper, $372 \text{ J}(kgK)^{-1}$) and density (8930 kgm^{-3}), respectively [192].

The temperature rise caused by the second and third components $\Delta\bar{T}_2$ and $\Delta\bar{T}_3$ are estimated by [191]:

$$\Delta\bar{T}_2 = \frac{\bar{\sigma}}{4\sqrt{3}(\rho \times s)} \sqrt{\frac{V_R L_B}{\alpha}} \quad (6-18)$$

and

$$\Delta\bar{T}_3 = \frac{\bar{\sigma}}{4\sqrt{3}(\rho \times s)} \sqrt{\frac{V_E L_D}{\alpha}} \quad (6-19)$$

where V_R is the ram velocity, L_B the billet length, α the thermal diffusivity (for copper, $\alpha = 1.174 \times 10^{-4} \text{ m}^2 \text{ S}^{-1}$), V_E the exit speed, and L_D the die land length.

The sum of Eqs. (6-17), (6 - 18) and (6 - 19) at various extrusion speeds is the maximum temperature rise possible at the surface of the extrudate. In this case, the contributions at the surface (Equations 6-18 and 6-19) are relatively minor and the maximum temperature rise during extrusion of the UFG material ranges from approximately 108 °C at the lowest extrusion speed to 112 °C at the highest extrusion speed, whereas for the CG material the temperature rise is between 45 °C and 47 °C. This difference is due to the much larger flow stress of the UFG material. Under 112 °C, the initiation of recrystallization during micro-extrusion is possible for the UFG material [193] but is certainly not possible for the CG. Furthermore, if we take into account the time of the test, at the lower speeds there is

6: Micro-extruded UFG and CG Copper

sufficient time for the heat to dissipate to the die block, whereas at the highest speed with a test duration of 12 s this is unlikely. Here, this argument is not rigorous as it neglects changes in the flow stress due to the contrary effects of softening as a result of the rise in temperature and strain hardening. Nonetheless, this argument does explain the experimental observations, and microstructural evolution during micro-extrusion confirms this explanation.

Finally, the grain size variations due to extrusion of the UFG material should be discussed. The initial grain size was 0.4 μm while after extrusion it became slightly larger; 0.49 μm . These grain size measures were determined using the line intercept technique, in the direction perpendicular to the sample axis. Actually, one could predict from the geometry of the extrusion process that the grain size should be 16 times smaller due to the elongation of the sample. Thus, there is very significant grain coarsening during the extrusion of the UFG material. An interpretation of this effect can be formulated as follows. The initial material not only had a very small grain size but it also had a very high strength due to the eight ECAP pass before the extrusion. Therefore, the temperature rise produced by the plastic work and the friction with the die have been much more significant in the UFG material than in the CG case leading to dynamic recrystallization (DRX) of the sample [194, 195] and it has been discussed above. The occurrence of recovery and dynamic recrystallization is also discussed in [196] where the relative proportion of the $\langle 111 \rangle$ and $\langle 100 \rangle$ fibres were examined in the copper matrix of a Cu-Nb wire composite. Those authors have found that the $\langle 100 \rangle$ fibre decreases during large strain possibly due to dynamic recrystallization induced by large strain. In our case, the UFG material underwent 8 passes in ECAP route Bc which represents a shear strain of ~ 8 already before micro extrusion (equivalent strain of 4.6), thus the total plastic strain (4.6 + 2.8) is in the same range as in [196]. In conclusion, both DRX and the shear component of the strain decrease the $\langle 100 \rangle$ fibre intensity and this can be the reason why there is still a qualitatively good agreement between the measured and predicted textures the latter taking into account only the effect of shear. In order to describe the texture changes, 3 maps which cover at least 700 grains per map were chosen to separate the recrystallized from the un-recrystallized grains (Fig. 6-24). The obtained recrystallization fraction was $\sim 25\%$ using the 15° misorientation criterion for measurement. This result is consistent with the nano-indentation measurements presented in section 6.5 (Fig. 6-15) and justified by the microstructure observation in Fig. 6-9.

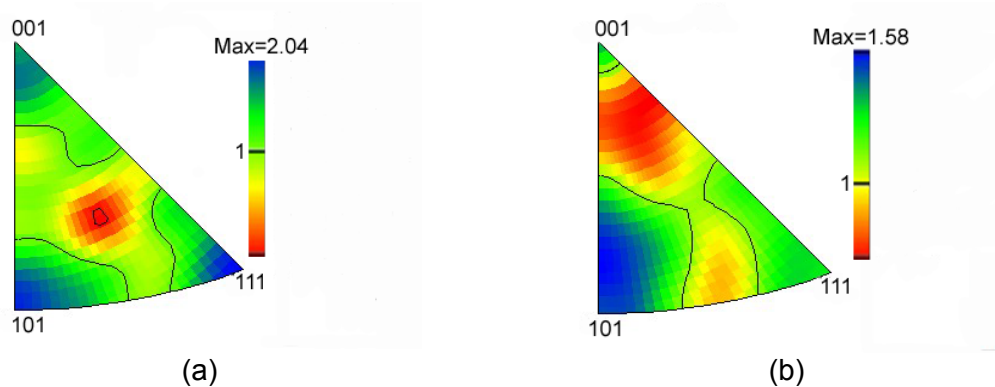


Figure 6-24. IPFs of UFG micro-extruded at 25 mm/min: (a) recrystallized component and (b) un-recrystallized component.

6.9 Summary

For texture evolution of UFG and CG copper after micro-extrusion, significant texture variations along the cross-section of the extruded sample for both UFG and CG copper have been found. A rotation of the ideal $\langle 111 \rangle$ fibre has been identified in a region near the surface which was shown to be the result of the shear component during the process. During micro-extrusion, a grain coarsening was observed for UFG copper which was attributed to dynamic recrystallization.

The thermal stability of UFG copper is improved by extrusion, declines with extrusion speed and is always poorer than CG copper. The stored energy of CG copper remains approximately constant with extrusion speed and there is no obvious change in peak temperature. In contrast, micro-extrusion of the UFG copper results in a reduction of stored energy concurrent with an unexpected reduction in peak temperature at high extrusion speeds. This is in accord with the microstructure measurement.

For the modeling, an analytic flow line model was adopted to describe the deformation mode during extrusion. Finite element results were also used to validate the results of the analytic approach. A large increase in the strain rate was obtained in the die just before the exit of the material. Polycrystal simulations were performed to obtain the variations in the texture using the velocity gradient of the analytic flow line function.

The grain refinement model in Chapter 3 was also employed to predict the average grain sizes. It helped to explain the microstructural evolution. The obtained results agree well

6: Micro-extruded UFG and CG Copper

with the measurements provided that the heat effect is taken into account in the refinement modeling for CG copper. For UFG, however, this grain refinement is limited at this stage due to small initial grain size (0.4 μm). Therefore, the present modeling is not able to model such small initial grain size as mentioned in Chapter 3, it is expected to be used for the application below a certain grain size and roughly to be 30 μm . For such small initial grain size and final grain size below 100 nm, the diffusion component needs to be considered for the deformation mechanism together with the crystallographic slips of grain fragmentation. Such research will be pursued in future work.

7

SUMMARIES, CONCLUSIONS AND FUTURE WORK

7. SUMMARIES, CONCLUSIONS AND FUTURE WORK

7.1 Summaries

Micro-forming technologies should permit mass production, low-cost procedures and quality controlled processes when one or more dimensions of the part are less than 1 μm . Its scale is the margin between conventional precision manufacturing and silicon-based technology. So far, a large number of investigations have been reported in this field but they do not reach the same conclusions. It should be noted that it is not possible to apply the know-how of conventional forming processes to the field of micro-metal forming due to the so-called size effects – dimensional ratio of thickness / grain size of ~ 15 . Given the fact that micro parts made from CG materials can lead to non-uniform materials flow and lack of repeatability of products during micro-forming, one important question to answer is:

Are UFG materials the best candidate for micro-forming? In any forming operation an important aim is to obtain uniform properties of the formed products. When grain size is large, however, local properties vary at a scale which is equal to the component size. The larger the grain size, the larger the variation is in properties related to surface behaviors (friction, wear and corrosion, etc.). The reason for this is that the anisotropy of a crystalline material is maximum for a single crystal. Therefore, by decreasing the grain size, more uniform properties can be achieved along the surface of the material. This argument is also valid for the part thickness. If the thickness is limited, which is very much the case in micro forming, uniformity of the thickness requires many grains along the surface and across through the thickness. This condition can only be satisfied if the grain size is as small as possible; that is, using UFG materials.

A new grain refinement model based on the retarded lattice rotation near the grain boundary region of a grain of the polycrystal was used. This model is based on the assumption that crystal rotation inherent in plastic deformation is not uniform within the grain. In its grain boundary area, the lattice rotation is slowed down as an effect of the grain boundary due to the neighboring grains. Although the model contains several simplifying hypotheses, it captures the main effects produced by grain fragmentation and permits us the success in predicting grain size distribution, texture development after large strain deformation, and misorientation distribution of neighboring grains.

This research work presents the comparative study of initial UFG copper for the different strain paths: ECAP and cold rolling. Grain refinement modeling demonstrated that the

7: Summary, Conclusions and Future Work

smaller grain sizes in ECAP than in rolling are attributed to different lattice rotation rates in ECAP and cold rolling.

This research work has led to an interesting modeling which concerns the EBSD analysis of the microstructure when next-neighbor misorientation distributions (NNMDs) are measured. It was found experimentally that the NNMD is different when measuring on different sections of the deformed sample. The new model was used to provide an explanation for this novel experimental finding, that is, the deviation is caused by the different proportions of two populations of new grains: those that are in the interior of their parent grains and those that are neighbors across the old grain boundaries. The reason behind is that the old grain boundaries appear in different proportions on the different sections of the sample. The use of this new split technique related to NNMD into the internal and grain boundary part permitted to clarify that the internal new grains contribute much less to the total grain refinement than the new grains at the grain boundary of the initial grains. This is also a fundamental issue in the understanding of the grain refinement process due to large plastic strains.

Another interesting and important issue in this study is the question: *Is texture development important during micro-forming?* Clearly, UFG materials are needed for micro-forming. During their production – for example via severe plastic deformation processes – strong crystallographic textures appear, which will be the input textures for the subsequent micro forming process. Moreover, these textures are usually such that their symmetry (if any) does not agree with the symmetry of the micro forming process. Such deviations lead to texture developments during the forming operation which results in different textures for different locations within the sample even if the strain mode is the same. Consequently, all the properties that texture is dependent on will be varying strongly within the sample and not obey the symmetry of the formed piece. This, of course, has to be avoided, if possible, or if not, at least the extent of the variation of the texture has to be known within the micro formed piece. This can be done by experimental analysis, such as EBSD. This can also be conducted by using simulation tools such as polycrystal plasticity. In addition, texture gradients are also important within the wall thickness. In fact, the use of UFG microstructure as input material for micro-forming may lead to variations in the texture development within the wall. This is also important to know quantitatively in order to estimate its possible impact on material behaviors.

7: Summary, Conclusions and Future Work

Related to the latter issue *the thermal stability of the microstructure* was studied experimentally using X-ray, DSC and EBSD after large deformation of the samples by varying the speeds during micro-extrusion. Measured grain sizes larger than those expected from the geometry of the process from grain fragmentation simulation indicated that recovery was operating for CG copper during deformation. The recovery process was considered even in the fragmentation modeling, which results in smaller curvatures of the crystal lattice when the CIDs (curvature induced dislocations) are partially removed by recovery leading to larger grain sizes for CG copper after micro-extrusion. For the UFG copper, significant grain coarsening during micro-extrusion was from dynamic recrystallization, and DSC and dislocation density measurements permitted us to quantify these processes.

7.2 Conclusions

According to the results obtained, the following major conclusions can be drawn:

- i) To approach described grain size effect during micro-forming, a new grain fragmentation model was used for SPD process. The concept in this model is that grain subdivision is associated with accumulation of lattice curvature during the deformation process. The basic assumption is that lattice rotation within an individual grain is impeded near the grain boundaries by the constraining the effect of the neighboring grains, which gives rise to lattice curvature. On this basis, the starting UFG material was obtained by equal channel angular pressing (ECAP) and micro-extrusion were the two micro-forming processes investigated. These experiments were supported by application of a grain fragmentation model coupled to a viscoplastic self consistent (VPSC) simulation in ECAP and micro-extrusion.
- ii) The strain path effect that makes the difference between ECAP and cold rolling copper at the same equivalent strain was studied in this work experimentally and by simulations. The simulation results confirmed the basic hypothesis of the grain refinement model, namely, larger lattice rotation rate leads to smaller grain size, is in accord with experiments. Consequently, the proposed grain fragmentation modeling was convincingly validated and gave the great confidence to characterize UFG materials used in micro-forming.
- iii) A new statistical type technique has been developed that permits to split the misorientation distribution into the grain interior and the grain boundary related constituents, without a need for identifying the old grain boundaries in actual

7: Summary, Conclusions and Future Work

experiment. The present work has examined in detail the misorientation distribution functions measured on copper samples severely deformed by ECAP in route A up to three passes. It has been found that the misorientation distributions depend on the measurement plane. This dependence, as well as other details of the evolution of the misorientation distribution, was interpreted in terms of the geometry changes of the initial grains. It has been shown that the shift of the misorientation distribution towards large misorientation angles caused by grain fragmentation under severe plastic deformation is mostly due to the geometry changes of the initial grains constituting the polycrystal. Against the common belief, the grains emerging in the interior of the parental grains only contribute to small misorientation angles.

- iv) The investigation of the number of ECAP passes on the bi-axial ductility in micro deep drawing has been investigated by experimental measurements. Tests showed that a much higher drawing force was required for high strength UFG copper compared to annealed material. The limit drawing ratio of ECAP processed copper was in the range of 1.9 – 2.0, while a higher value of 2.2 was observed for the coarse grained copper. A higher LDR is preferred during manufacturing. However, this consideration has to comprise all aspects for the final products, such as surface quality and formability. The decrease in LDR value was insignificant for UFG copper regardless the number of passes, compared to the significant loss of tensile ductility from 50% to below 10%. Texture evolution is also important because it related directly the formability during micro-forming. The main objective was to understand the evolution of the texture and explore through-thickness variations for the ultrafine-grained case. Measurements along with extensive simulation work were carried out on copper which was pre-deformed to large strains by ECAP. The simulation technique involved FE and polycrystal modeling. Although the FE model did not include crystal plasticity, it was possible to integrate a posteriori the FE flow lines into the self-consistent viscoplastic polycrystal model and predict the texture evolution at selected points during cup forming. The texture measurements that were carried out using X-ray and EBSD techniques were faithfully validated by the prediction. It was shown that rigid rotation during the drawing process plays an important role in the evolution of the texture. Through-thickness variations in the texture were found by both simulations and in experiments. Such variations are important in cup forming if the grain size is very small as in the present study. For large grain size, such variations are not predictable due to the small wall thickness while they can be well simulated if the grain size is very small. The good agreements between the simulations and the measurements obtained in the present study confirm this main conclusion.

7: Summary, Conclusions and Future Work

- v) Four different extrusion speeds of 0.1, 1, 10 and 25 mm/min were chosen to investigate the strain rate effect with respect to the thermal stability, mechanical properties, and microstructure, as well as the texture changes after micro-extrusion of UFG and CG copper, spanning CG (25 μm) to UFG copper (230 nm). Each starting material was micro-extruded at room temperature at different speeds mentioned above to a strain of 2.77. The stored energy of the UFG copper decreased with extrusion speed from a value of 0.95 ± 0.05 J/g for the starting material to 0.71 ± 0.03 J/g for material extruded at 25 mm/min. The peak temperature decreased from 202°C for material extruded at 0.1mm/min to 177°C for material extruded at 25 mm/min. However, stored energy and peak temperature values for the CG copper were approximately constant with extrusion speed at around 0.75 ± 0.03 J/g and 230°C. The lower stored energy and lower peak temperature of the UFG copper compared to CG copper is attributed to recrystallization commencing during micro-extrusion. It is clear that the grain size after micro-extrusion depends on the processing speed and always larger than the one expected by pure geometry of the process. This effect of recovery for CG copper was taken into account in the modeling work, where it was modeled by changing the curvature induced dislocation density through the only parameter (μ) of the grain refinement model, and in accord with the experimental observation. UFG copper, however, could not be modeled by the grain fragmentation model. Importantly, although the CG copper was micro-extrudable, the thermal stability of UFG copper was superior after high speed micro-extrusion because of the dynamic recrystallization and this justifies the use of UFG copper in this study.

7.3 Future Work

The future research will continue to improve the proposed grain fragmentation model. The model presented in Chapter 3 is limited to a small grain size in terms of computational performance, and it does not consider large strains due to the use of the polycrystal model which fails at large strains. Both the numerical constraints and the limitations of the polycrystal model will be overcome in the future. The computational performance could be improved to by conducting one more level of 'Rubic-cube' subdivision. The limitation of the polycrystal model could be improved by using the VPSC model to achieve better texture predictions. For grain size below 100 nm, the diffusion component needs to be considered for the deformation mechanism together with slip of grain fragmentation. In addition, the further evidences for direct corroboration of the hypothesis used in the model also need to be sought in the future. Care needs to be taken to follow the orientation from its initial position, as large gradients may develop at an early stage of deformation when the grain

7: Summary, Conclusions and Future Work

rotates faster, eventually ending up near an ideal position so that its rotation rate will become slow. Therefore, it cannot be ruled out that final orientations near the ideal position correspond to large lattice curvature which is in apparent contradiction with the basic hypothesis. Suitable analysis techniques will be developed to evaluate EBSD measurements to find out grain size vs orientation relations. Three dimensional observations using dual-beam EBSD equipment will be also used to explore 3D topological features of the grain refinement process.

Concerning ECAP, EBSD analysis on all the orthogonal billet planes will be carried out at various passes for different routes to understand the grain refinement mechanism. The split-technique of the misorientation distribution presented in this thesis for the two populations of misorientations (mother grain interior and grain boundary type) will be applied for this purpose.

Despite a significant amount of texture studies in the past decades, understanding texture evolution in SPD is still in its early stage. Especially, texture evolution in low symmetry metals needs further study. Measuring, predicting and controlling texture are important components in processing, synthesis and design of SPD materials, and texture evolution will be studied by incorporating accurate grain substructure evolution information to the polycrystal VPSC code based on experimental measurements. The VPSC model will be developed iteratively to determine parameter sets for the texture results of different SPD-processed metals and alloys. Modeling and analysis will be conducted to predict deformation texture and the transition from deformation texture to recrystallization texture over a range of temperatures of micro-extrusion/micro deep drawing at different strains and strain rates for copper or other f.c.c. metals. The experimentally validated microstructures, textures and grain boundary properties for recrystallization during micro forming will be identified through precise modeling prediction.

Deformation twinning plays an important role in the development of crystallographic texture and in the grain refinement process. However, the processes involved in the nucleation and growth of twins are not as well understood as those for slip. The argument for twinning in UFG materials is the high stresses caused by the small surrounded UFG grains. While annealing could potentially be used to tailor materials properties, it has yet to be optimized. Future research will study the role of twins in the deformation behavior of nano-scale microstructure as one of the strengthening mechanisms, and also the grain boundary engineering for annealing twins in severely deformed UFG metals and alloys.

7: Summary, Conclusions and Future Work

Experimental results for different grain sizes and geometric scales together with theoretical interpretations will be conducted for insightful understanding of the specimen size effect by monitoring the mechanical properties over a range of grain sizes. Sheet-forming will be performed through ECAP/rolling both CG and UFG copper to different thicknesses. Although the yield stress of large grains follows the expected modeling behavior, specimens with small grains below a critical dimension ratio of thickness / grain size of ~ 15 exhibit unexpected results. Therefore, it is expected to detect different mechanical behaviors for geometrical reasons and it will be pursued in the future work.

REFERENCES

- [1] M. Geiger, M. Kleiner, R. Eckstein, N. Tiesler, U. Engel, *CIRP Ann* 50 (2001) 445-462.
- [2] U. Engel, R. Eckstein, *J Mater Process Technol* 125-126 (2002) 35-44.
- [3] S. Miyazaki, K. Shibata, H. Fujita, *Acta Metallurgica* 27 (1979) 855-862.
- [4] J. F. Michel, P. Picart, *J Mater Process Technol* 141 (2003) 439-446.
- [5] N. Krishnan, J. Cao, K. Dohda, *J. Manuf. Sci. Eng.* 129 (2007) 669-676.
- [6] A. Rosochowski, W. Presz, L. Olejnik, M. Richert, *Int J Adv Manuf Technol* 33 (2007) 137-146.
- [7] R. Z. Valiev, N. A. Krasilnikov, N. K. Tsenev, *Mater Sci Eng A* 137 (1991) 35-40.
- [8] R. Z. Valiev, R. K. Islamgaliev, I. V. Alexandrov, *Progr Mater Sci* 45 (2000) 103-189.
- [9] A. Gholinia, P. B. Prangnell, M. V. Markushev, *Acta Mater* 48 (2000) 1115-1130.
- [10] M. Richert, Q. Liu, N. Hansen, *Mater Sci Eng A* 260 (1999) 275-283.
- [11] V. M. Segal, *Mater Sci Eng A* 197 (1995) 157-164.
- [12] R. Z. Valiev, T. G. Langdon, *Progr Mater Sci* 51 (2006) 881-981.
- [13] W. H. Huang, C. Y. Yu, P. W. Kao, C. P. Chang, *Mater Sci Eng A* 366 (2004) 221-228.
- [14] A. L. Etter, T. Baudin, C. Rey, R. Penelle, *Mater Charac* 56 (2006) 19-25.
- [15] O. V. Mishin, D. Juul Jensen, N. Hansen, *Mater Sci Eng A* 342 (2003) 320-328.
- [16] Y. Xiang, J. J. Vlassak, *Acta Mater* 54 (2006) 5449-5460.
- [17] R. P. Vinci, E. M. Zielinski, J. C. Bravman, *Thin Solid Films* 262 (1995) 142-153.
- [18] N. Hansen, *Acta Metallurgica* 25 (1977) 863-869.
- [19] X. Ma, R. Lapovok, C. Gu, A. Molotnikov, Y. Estrin, E. V. Pereloma, C. H. J. Davies, P. D. Hodgson, *J Mater Sci* 44 (2009) 3807-3812.
- [20] L. S. Tóth, Y. Estrin, R. Lapovok, C. Gu, *Acta Mater* 58 (2010) 1782-1794.
- [21] J. Keepler, What is a good number, in: *Fastener Technology International* Oct. 1999 www.coldheadermachinecorp.com.
- [22] M. Geiger, E. Egerer, U. Engel, *Production Engineering* (2001) 101-104.
- [23] N. Tiesler, *Wire* 1 (2002) 34-38.
- [24] A. Messner, U. Engel, R. Kals, F. Vollertsen, *J Mater Process Technol* 45 (1994) 371-376.
- [25] J. Cao, N. Krishnan, Z. Wang, H. Lu, W. K. Liu, A. Swanson, *J. Manuf. Sci. Res. Eng.* 126 (2004) 642-652.
- [26] E. O. Hall, *Physical Society - Proc.* 64 (1951) 747-753.
- [27] F. Vollertsen, Z. Hu, H. S. Niehoff, C. Theiler, *J Mater Process Technol* 151 (2004) 70-79.
- [28] I. J. Beyerlein, L. S. Tóth, *Progr Mater Sci* 54 (2009) 427-510.
- [29] F. Vollertsen, *Metal Forming: Microparts*, *Encyclopaedia of Materials, Science and Technology* 2001.
- [30] Y. Saotome, K. Yasuda, H. Kaga, *J Mater Process Technol* 113 (2001) 641-647.
- [31] K. Nagasaka, Y. Umeki, M. Sugimoto, *J. Jpn. Soc. Technol. Plasticity* 11 (1970) 38.
- [32] H. Ikeda, H. Komatsu, in: *Proceedings of the 34th Japanese Joint Conference on Technology of Plasticity*, 1983, p. 93.
- [33] N. Witulski, H. Justinger, G. Hirt, *Validation Of FEM-Simulation For Micro Deep Drawing Process Modeling*, in: S. Ghosh, J. C. Csatro, J. K. Lee (Eds.), *NUMIFORM*, American Institute of Physics 2004.

References

- [34] J. Wang, Y. Iwahashi, Z. Horita, M. Furukawa, M. Nemoto, R. Z. Valiev, T. G. Langdon, *Acta Mater* 44 (1996) 2973-2982.
- [35] E. O. Hall, in: *Proc. Phys. Soc., Ser. B*, vol 64, 1951, pp. 747-753.
- [36] N. J. Petch, *J. Iron and Steel Institute* (1953) 25-28.
- [37] L. V. Raulea, A. M. Goijaerts, L. E. Govaert, F. P. T. Baaijens, *J Mater Process Technol* 115 (2001) 136-141.
- [38] T. A. Kals, R. Eckstein, *J Mater Process Technol* 103 (2000) 95-101.
- [39] N. J. Petch, *Iron and Steel Institute* 174 (1953) 25-28.
- [40] M. Geiger, M. Kleiner, R. Eckstein, N. Tiesler, U. Engel, *Microforming*, in: 51st General Assembly of CIRP, , vol 50, Nancy, 2001, pp. 445-462.
- [41] J. S. Stölken, A. G. Evans, *Acta Mater* 46 (1998) 5109-5115.
- [42] N. A. Fleck, G. M. Muller, M. F. Ashby, J. W. Hutchinson, *Acta Metall et Mater* 42 (1994) 475-487.
- [43] G. Kim, J. Ni, M. Koc, *J. Manuf. Sci. Res. Eng.* 129 (2007) 470-476.
- [44] N. Hansen, *Adv. Eng. Mater.* 7 (2005) 815-821.
- [45] E. C. Aifantis, *Mechanics of Materials* 35 (2003) 259-280.
- [46] H. Gao, Y. Huang, W. D. Nix, J. W. Hutchinson, *J. Mech. Phys. Solids* 47 (1999) 1239-1263.
- [47] Y. Huang, H. Gao, W. D. Nix, J. W. Hutchinson, *J. Mech. Phys. Solids* 48 (2000) 99-128.
- [48] R. Lapovok, F. H. Dalla Torre, J. Sandlin, C. H. J. Davies, E. V. Pereloma, P. F. Thomson, Y. Estrin, *J. Mech. Phys. Solids* 53 (2005) 729-747.
- [49] Y. Estrin, A. Molotnikov, C. H. J. Davies, R. Lapovok, *J. Mech. Phys. Solids* 56 (2008) 1186-1202.
- [50] Y. Estrin, H. S. Kim, F. R. N. Nabarro, *Acta Mater* 55 (2007) 6401-6407.
- [51] A. Molotnikov, R. Lapovok, C. H. J. Davies, W. Cao, Y. Estrin, *Scripta Mater* 59 (2008) 1182-1185.
- [52] R. Z. Valiev, *Mater Sci Eng A* 234-236 (1997) 59-66.
- [53] Y. Iwahashi, J. Wang, Z. Horita, M. Nemoto, T. G. Langdon, *Scripta Mater* 35 (1996) 143-146.
- [54] F. Dalla Torre, R. Lapovok, J. Sandlin, P. F. Thomson, C. H. J. Davies, E. V. Pereloma, *Acta Mater* 52 (2004) 4819-4832.
- [55] J. T. Wang, Y. Zhang, Q. L. Jin, *Continuous recrystallization phenomenon in high purity copper during equal channel angular pressing up to high strain at room temperature*, in: vol 584-586 PART 2, Trans Tech Publications Ltd, Goslar, Germany, 2008, pp. 929-937.
- [56] Q. R. Liu, N. Hansen, *Mater Sci Eng A* 260 (1999) 275-283.
- [57] M. J. Zehetbauer, J. Kohout, E. Schafner, F. Sachslehner, A. Dubravina, *J Alloys Compd* 378 (2004) 329-334.
- [58] M. Zehetbauer, H. P. Stuewe, A. Vorhauer, E. Schafner, J. Kohout, *Adv. Eng. Mater.* 5 (2003) 330-337.
- [59] T. C. Lowe, R. Z. Valiev, *Investigations and Applications of Severe Plastic Deformation*, Kluwer Academic Publishers, 2000.
- [60] Y. T. Zhu, T. G. Langdon, R. S. Mishra, S. L. Semiatin, M. J. Saran, T. C. Lowe, *Ultraine Grained Materials II*, in: Annual Meeting and Exhibition, TMS, 2002.
- [61] K. Neishi, Z. Horita, T. G. Langdon, *Mater Sci Eng A* 325 (2002) 54-58.
- [62] D. H. Shin, B. C. Kim, Y.-S. Kim, K.-T. Park, *Acta Mater* 48 (2000) 2247-2255.
- [63] D. Jia, Y. M. Wang, K. T. Ramesh, E. Ma, Y. T. Zhu, R. Z. Valiev, *Appl Phys Lett* 79 (2001) 611.
- [64] K.-T. Park, Y.-S. Kim, J. G. Lee, D. H. Shin, *Mater Sci Eng A* 293 (2000) 165-172.

References

- [65] H. S. Kim, M. H. Seo, S. I. Hong, *J Mater Process Technol* 113 (2001) 622-626.
- [66] E. A. El-Danaf, *Mater Sci Eng A* 492 (2008) 141-152.
- [67] Y. Iwahashi, Z. Horita, M. Nemoto, T. G. Langdon, *Acta Mater* 46 (1998) 3317-3331.
- [68] M. Furukawa, Y. Iwahashi, Z. Horita, M. Nemoto, T. G. Langdon, *Mater Sci Eng A* 257 (1998) 328-332.
- [69] N. Tsuji, Y. Saito, H. Utsunomiya, S. Tanigawa, *Scripta Mater* 40 (1999) 795-800.
- [70] J. Y. Huang, Y. T. Zhu, H. Jiang, T. C. Lowe, *Acta Mater* 49 (2001) 1497-1505.
- [71] S. V. Zherebtsov, G. A. Salishchev, R. M. Galeev, O. R. Valiakhmetov, S. Y. Mironov, S. L. Semiatin, *Scripta Mater* 51 (2004) 1147-1151.
- [72] M. Richert, H. P. Stüwe, M. J. Zehetbauer, J. Richert, R. Pippan, C. Motz, E. Schafner, *Mater Sci Eng A* 355 (2003) 180-185.
- [73] R. Z. Valiev, E. V. Kozlov, Y. F. Ivanov, J. Lian, A. A. Nazarov, B. Baudelet, *Acta Metall et Mater* 42 (1994) 2467-2475.
- [74] Y. T. Zhu, J. Y. Huang, J. Gubicza, T. Ungar, Y. M. Wang, E. Ma, R. Z. Valiev, *J Mater Res* 18 (2003) 1908-1917.
- [75] Y. M. Wang, E. Ma, M. W. Chen, *Appl Phys Lett* 80 (2002) 2395.
- [76] J. Cizek, I. Prochazka, R. Kuzel, M. Cieslar, R. Islamgaliev, *Journal of Metastable and Nanocrystalline* 17 (2003) 37-44.
- [77] U. Andrade, M. A. Meyers, K. S. Vecchio, A. H. Chokshi, *Acta Metall et Mater* 42 (1994) 3183-3195.
- [78] G. Mohamed, B. Bacroix, *Acta Mater* 48 (2000) 3295-3302.
- [79] P. L. Sun, C. Y. Yu, P. W. Kao, C. P. Chang, *Scripta Mater* 47 (2002) 377-381.
- [80] S. Kobayashi, S. Tsurekawa, T. Watanabe, G. Palumbo, *Scripta Mater* 62 294-297.
- [81] S. Li, I. J. Beyerlein, M. A. M. Bourke, *Mater Sci Eng A* 394 (2005) 66-77.
- [82] S. Li, I. J. Beyerlein, D. J. Alexander, *Mater Sci Eng A* 431 (2006) 339-345.
- [83] V. Randle, O. Engler, *Introduction to texture analysis: macrotexture, microtexture and orientation mapping*, 2000.
- [84] I. J. Beyerlein, L. S. Toth, C. N. Tome, S. Suwas, *Philosophical Magazine* 87 (2007) 885-906.
- [85] H. S. Kim, Y. Estrin, *Mater Sci Eng A* 410-411 (2005) 285-289.
- [86] Y. H. Zhao, Y. T. Zhu, X. Z. Liao, Z. Horita, T. G. Langdon, *Appl Phys Lett* 89 (2006).
- [87] C. C. Koch, *Scripta Mater* 49 (2003) 657-662.
- [88] R. Z. Valiev, I. V. Alexandrov, Y. T. Zhu, T. C. Lowe, *J Mater Res* 17 (2002) 5-8.
- [89] P. S. Follansbee, U. F. Kocks, *Acta Metallurgica* 36 (1988) 81-93.
- [90] D. Torre, E. V. Pereloma, C. H. J. Davies, *Scripta Mater* 51 (2004) 367-371.
- [91] Q. Wei, S. Cheng, K. T. Ramesh, E. Ma, *Mater Sci Eng A* 381 (2004) 71-79.
- [92] Y. F. Shen, L. Lu, M. Dao, S. Suresh, *Scripta Mater* 55 (2006) 319-322.
- [93] L. Lu, R. Schwaiger, Z. W. Shan, M. Dao, K. Lu, S. Suresh, *Acta Mater* 53 (2005) 2169-2179.
- [94] Y. M. Wang, E. Ma, *Appl Phys Lett* 83 (2003) 3165-3167.
- [95] J. Chen, L. Lu, K. Lu, *Scripta Mater* 54 (2006) 1913-1918.
- [96] S. Cheng, E. Ma, Y. M. Wang, L. J. Kecskes, K. M. Youssef, C. C. Koch, U. P. Trociewitz, K. Han, *Acta Mater* 53 (2005) 1521-1533.
- [97] R. K. Guduru, K. L. Murty, K. M. Youssef, R. O. Scattergood, C. C. Koch, *Mater Sci Eng A* 463 (2007) 14-21.
- [98] M. Zehetbauer, *Acta Metall et Mater* 41 (1993) 589-599.
- [99] C. Gu, J. Lian, Z. Jiang, Q. Jiang, *Scripta Mater* 54 (2006) 579-584.
- [100] C. Gu, J. Lian, Z. Jiang, *Adv. Eng. Mater.* 8 (2006) 252-256.

References

- [101] C. Langlois, S. Guérin, M. Sennour, M. J. Hÿtch, C. Duhamel, Y. Champion, *J Alloys Compd* 434-435 (2007) 279-282.
- [102] Y.-H. Zhao, J. F. Bingert, X.-Z. Liao, B.-Z. Cui, K. Han, A. V. Sergueeva, A. K. Mukherjee, R. Z. Valiev, T. G. Langdon, Y. T. Zhu, *Advanced Materials* 18 (2006) 2949-2953.
- [103] Y. Wang, M. Chen, F. Zhou, E. Ma, *Nature* 419 (2002) 912-914.
- [104] Y. H. Zhao, J. F. Bingert, Y. T. Zhu, X. Z. Liao, R. Z. Valiev, Z. Horita, T. G. Langdon, Y. Z. Zhou, E. J. Lavernia, *Appl Phys Lett* 92 (2008).
- [105] D. G. Morris, M. A. Muñoz-Morris, *Acta Mater* 50 (2002) 4047-4060.
- [106] W. Q. Cao, A. Godfrey, W. Liu, Q. Liu, *Mater Sci Eng A* 360 (2003) 420-425.
- [107] R. Z. Valiev, *Mater. Sci. Forum* 584-586 (2008) 22-28.
- [108] N. A. Fleck, J. W. Hutchinson, *J. Mech. Phys. Solids* 49 (2001) 2245-2271.
- [109] E. Ma, *JoM* 58 Apr. (2006) 59.
- [110] W. S. Zhao, N. R. Tao, J. Y. Guo, Q. H. Lu, K. Lu, *Scripta Mater* 53 (2005) 745-749.
- [111] L. Lu, X. Chen, X. Huang, K. Lu, *Science* 323 (2009) 607-610.
- [112] V. Randle, G. Owen, *Acta Mater* 54 (2006) 1777-1783.
- [113] D. P. Field, R. C. Eames, T. M. Lillo, *Scripta Mater* 54 (2006) 983-986.
- [114] R. Z. Valiev, Y. Estrin, Z. Horita, T. G. Langdon, M. J. Zehetbauer, Y. T. Zhu, *JoM* 58 (2006) 33-39.
- [115] S. C. Baik, Y. Estrin, H. S. Kim, R. J. Hellmig, *Mater Sci Eng A* 351 (2003) 86-97.
- [116] Y. Estrin, L. S. Toth, Y. Brechet, H. S. Kim, *Modelling of the evolution of dislocation cell misorientation under severe plastic deformation*, in: vol 503-504, Trans Tech Publications Ltd, Fukuoka, Japan, 2006, pp. 675-680.
- [117] Y. Estrin, L. S. Tóth, A. Molinari, Y. Bréchet, *Acta Mater* 46 (1998) 5509-5522.
- [118] L. S. Toth, A. Molinari, Y. Estrin, *Journal of Engineering Materials and Technology, Transactions of the ASME* 124 (2002) 71-77.
- [119] W. Pantleon, N. Hansen, *Acta Mater* 49 (2001) 1479-1493.
- [120] M. R. Barnett, F. Montheillet, *Acta Mater* 50 (2002) 2285-2296.
- [121] D. Raabe, Z. Zhao, S. J. Park, F. Roters, *Acta Mater* 50 (2002) 421-440.
- [122] D. Raabe, Z. Zhao, W. Mao, *Acta Mater* 50 (2002) 4379-4394.
- [123] B. Beausir, *Software for Orientation Image Mapping*, in: <http://benoitbeausir.free.fr/>, 2010.
- [124] R. Hielscher, H. Schaeben, *J. Appl. Cryst.* 41 (2008) 1024-1037.
- [125] G. Ribárik, *Modeling of diffraction patterns based on microstructural properties*, in: *Physics Doctorate School*, vol PhD, Eotvos Lorand University, 2008.
- [126] S. R. Skjervold, N. Ryum, *Acta Metall et Mater* 43 (1995) 3159-3176.
- [127] B. L. Li, A. Godfrey, Q. Liu, *Scripta Mater* 50 (2004) 879-883.
- [128] D. P. Field, P. B. Trivedi, S. I. Wright, M. Kumar, *Ultramicroscopy* 103 (2005) 33-39.
- [129] J. F. Nye, *Acta Metallurgica* 1 (1953) 153-162.
- [130] B. S. El-Dasher, B. L. Adams, A. D. Rollett, *Scripta Mater* 48 (2003) 141-145.
- [131] S. K. Mishra, P. Pant, K. Narasimhan, A. D. Rollett, I. Samajdar, *Scripta Mater* 61 (2009) 273-276.
- [132] A. Molinari, L. S. Tóth, *Acta Metall et Mater* 42 (1994) 2453-2458.
- [133] J. K. Mackenzie, *Biometrika* 45 (1958) 229.
- [134] V. M. Segal, *Mater Sci Eng A* 271 (1999) 322-333.
- [135] A. Hasani, L. S. Tóth, *Scripta Mater* 61 (2009) 24-27.
- [136] L. Delannay, O. V. Mishin, D. J. Jensen, P. Van Houtte, *Acta Mater* 49 (2001) 2441-2451.

References

- [137] L. S. Tóth, R. Arruffat Massion, L. Germain, S. C. Baik, S. Suwas, *Acta Mater* 52 (2004) 1885-1898.
- [138] J. De Messemaeker, B. Verlinden, J. Van Humbeeck, *Acta Mater* 53 (2005) 4245-4257.
- [139] K. S. Havner, *Acta Mechanica* 14 (1982) 183-187.
- [140] W. Pantleon, *Problems in Materials Science* 52 (2007) 13-23.
- [141] S. H. Strogatz, *Nature* 410 (2001) 268-276.
- [142] S. Ramanujan, *Ramanujan's Collected Works*, Chelsea, New York, 1962.
- [143] O. V. Mishin, V. Y. Gertsman, R. Z. Valiev, G. Gottstein, *Scripta Mater* 35 (1996) 873-878.
- [144] R. Lapovok, I. Timokhina, P. W. J. McKenzie, R. O'Donnell, *J Mater Process Technol* 200 (2008) 441-450.
- [145] Z. Marciniak, J. L. Duncan, S. J. Hu, *Mechanics of sheet metal forming*, Butterworth-Heinemann, Oxford, 2002.
- [146] C. H. Chen, R. S. Lee, J. T. Gau, *Journal of Strain Analysis for Engineering Design* 45 283-299.
- [147] F. Dalla Torre, A. A. Gazder, C. F. Gu, C. H. J. Davies, E. V. Pereloma, *Metall Mater Trans A* 38A (2007) 1080-1095.
- [148] A. Molotnikov, *Size and strain gradient effects in dislocation based constitutive modelling*, in: vol PhD, Monash University, Melbourne, 2010.
- [149] A. Molinari, G. R. Canova, S. Ahzi, *Acta Metallurgica* 35 (1987) 2983-2994.
- [150] A. Molinari, L. S. Toth, *Acta Metall et Mater* 42 (1994) 2453-2458.
- [151] L. S. Tóth, P. Van Houtte, *Textures and Microstructure* 19 (1992) 229-224.
- [152] L. S. Toth, A. Molinari, *Acta Metall et Mater* 42 (1994) 2459-2466.
- [153] L. S. Tóth, R. Lapovok, A. Molotnikov, C. Gu, J. J. Fundenberger, C. H. J. Davies, *Mater Sci Eng A* 527 (2010) 4633-4640.
- [154] S. R. Agnew, J. R. Weertman, *Mater Sci Eng A* 242 (1998) 174-180.
- [155] S. Li, I. J. Beyerlein, D. J. Alexander, S. C. Vogel, *Acta Mater* 53 (2005) 2111-2125.
- [156] L. S. Toth, *Adv. Eng. Mater.* 5 (2003) 308-316.
- [157] L. S. Toth, K. W. Neale, J. J. Jonas, *Acta Metallurgica* 37 (1989) 2197-2210.
- [158] L. S. Toth, P. Gilormini, J. J. Jonas, *Acta Metallurgica* 36 (1988) 3077-3091.
- [159] S. Li, I. J. Beyerlein, C. T. Necker, D. J. Alexander, M. Bourke, *Acta Mater* 52 (2004) 4859-4875.
- [160] S. Ferrasse, V. M. Segal, S. R. Kalidindi, F. Alford, *Mater Sci Eng A* 368 (2004) 28-40.
- [161] H. J. Bunge, *Texture Analysis in Materials Science: Mathematical Methods*, Butterworth & Co. Berlin, 1982.
- [162] J. Baczynski, J. J. Jonas, *Acta Mater* 44 (1996) 4273-4288.
- [163] F. Montheillet, M. Cohen, J. J. Jonas, *Acta Metallurgica* 32 (1984) 2077-2089.
- [164] D. Merz, G. Wassermann, *Zeitschrift fuer Metallkunde* 56 (1965) 516-522.
- [165] H. Gertel-Kloos, H. G. Brokmeier, H. J. Bunge, *Mater. Sci. Forum* 157-6 (1994) 685-692.
- [166] N. Inakazu, Y. Kaneno, H. Inoue, *Mater. Sci. Forum* 157-6 (1994) 715-720.
- [167] D. N. Lee, Y. H. Chung, M. C. Shin, *Scripta Metall* 17 (1983) 339-342.
- [168] C. S. Batrrett, T. B. Massalski, *Structure of Metals*, McGraw-Hill, New York, 1966, p. 543.
- [169] L. Balogh, J. Gubicza, R. J. Hellmig, Y. Estrin, T. Ungár, K. Z., *Suppl.* 23 (2006) 381-386.
- [170] S. Suwas, A. Eberhardt, L. S. Toth, J. J. Fundenberger, T. Grosdidier, *Mater. Sci. Forum* 467-470 (2004) 1325-1330.

References

- [171] J. Gubicza, L. Balogh, R. J. Hellmig, Y. Estrin, T. Ungár, *Mater Sci Eng A* 400-401 (2005) 334-338.
- [172] J. Gubicza, S. Dobatkin, Z. Bakai, N. Q. Chinh, T. G. Langdon, *Mater. Sci. Forum* 567-568 (2008) 181-184.
- [173] J. Gubicza, C. Nguyen Quang, T. G. Langdon, T. Ungar, *Microstructure and strength of metals processed by severe plastic deformation*, in: TMS (The Minerals, Metals & Materials Society), Warrendale, PA, USA, 2006, pp. 231-236.
- [174] B. Avitzur, *Metal Forming: Processes and Analysis*, MacGraw-Hill, New York, 1968.
- [175] S. B. Altan, N. Antar, E. Gultekin, *J Mater Process Technol* 33 (1992) 263-272.
- [176] C. F. Gu, L. S. Loth, R. Lapovok, C. H. J. Davies, *Philos Mag* 91 (2011) 273-290.
- [177] in: *Q-Form User's Guide*, Quantor Ltd. 2000.
- [178] L. S. Tóth, J. J. Jonas, *Textures and Microstructures* 10 (1989) 195-209.
- [179] M. J. Zehetbauer, G. Steiner, E. Schafler, A. Korznikov, E. Korznikova, *Deformation induced vacancies with severe plastic deformation: Measurements and modelling*, in: vol 503-504, Trans Tech Publications Ltd, Fukuoka, Japan, 2006, pp. 57-64.
- [180] T. Ungár, E. Schafler, P. Hanák, S. Bernstorff, M. Zehetbauer, *Mater Sci Eng A* 462 (2007) 398-401.
- [181] E. Göttler, *Philos Mag* 28 (1973) 1057-1076.
- [182] M. Wilkens, M. O. Bargouth, *Acta Metallurgica* 16 (1968) 465-468.
- [183] A. Godfrey, N. Hansen, Q. Liu, *Metall. Mater. Trans. A* 36 (2005) 2371-2378.
- [184] W. Q. Cao, C. F. Gu, E. V. Pereloma, C. H. J. Davies, *Mater Sci Eng A* 492 (2008) 74-79.
- [185] R. Kužel, M. Janeček, Z. Matěj, J. Čížek, M. Dopita, O. Srba, *Metall Mater Trans A* DOI: 10.1007/s11661-009-9895-0 (2009).
- [186] E. Schafler, G. Steiner, E. Korznikova, M. Kerber, M. J. Zehetbauer, *Mater Sci Eng A* 410-411 (2005) 169-173.
- [187] F. J. Humphrey, M. Hatherly, *Recrystallization and related annealing phenomena*, Elsevier Science Inc., NY, 1996, p. 219.
- [188] M. J. Starink, A. M. Zahra, *Thermochimica Acta* 292 (1997) 159-168.
- [189] F. Lefevre-Schlick, Y. Brechet, H. S. Zurob, G. Purdy, D. Embury, *Mater Sci Eng A* 502 (2009) 70-78.
- [190] B. Decreus, H. S. Zurob, J. Dunlop, Y. Brechet, *Mater. Sci. Forum* 550 (2007) 381-386.
- [191] T. Sheppard, *Extrusion of Aluminium Alloys*, Kluwer Academic Publishers, London, 1999, p. 51.
- [192] G. J. Richardson, D. N. Hawkins, C. M. Sellars, *Worked Example in Metalworking*, 1985.
- [193] X. Molodova, G. Gottstein, M. Winning, R. J. Hellmig, *Mater Sci Eng A* 460-461 (2007) 204-213.
- [194] C. F. Gu, C. H. J. Davies, *Mater Sci Eng A* 527 (2010) 1791-1799.
- [195] D. Juul Jensen, K. H. J. Buschow, W. C. Robert, C. F. Merton, I. Bernard, J. K. Edward, M. Subhash, V. Patrick, *Annealing Textures*, in: *Encyclopedia of Materials: Science and Technology*, Elsevier, Oxford, 2001, pp. 319-323.
- [196] E. N. Popova, V. V. Popov, E. P. Romanov, N. E. Hlebova, A. K. Shikov, *Scripta Mater* 51 (2004) 727-731.